SCANNING AND POST-PROCESSING PARAMETER OPTIMIZATION FOR CT DIMENSIONAL METROLOGY

Ye Tan

Supervisor:

Prof. Dr. Ir. Jean-Pierre Kruth
Prof. Dr. Ir. Wim Dewulf

Members of the Examination Committee:

Prof. Dr. Ir. Martine Wevers
Prof. Dr. Ir. Bert Lauwers
Dr.Ir. Jun Qian
Prof. Dr. Ir. Leonardo De Chiffre
Prof. Dr. Ir. Carlo Van de Casteele

Dissertation presented in partial fulfilment of the requirements for the degree of PhD in Engineering

April 2015

Uitgegeven in eigen beheer, Ye Tan, Heverlee 3001, Belgium

Preface

The works presented in this thesis are the results of my research activities at Mechanical Engineering Department and Campus Group T – KU Leuven.

First of all, I would like to express my greatest acknowledgements to my promotors: Prof. Jean-Pierre Kruth and Prof. Wim Dewulf. Your profound knowledge, experience, structured and creative thinking guided me through the darkest moments of my PhD research. More importantly, your passion for scientific research and positive attitude when facing challenges will give me a far-reaching influence for my entire life. These valuable years of being your students will be forever appreciated.

Then, I want to address my sincere appreciations to Prof. Martine Wevers, Prof. Bert Lauwers, Dr. Jun Qian, Prof. Leonardo De Chiffre and Prof. Carlo Van de Casteele for their guidance, support and constructive suggestions to the thesis.

Furthermore, I appreciate all the colleagues I have worked together with during this period: Min Zhang, Kim Kiekens, Frank Welkenhuyzen, Bart Boeckmans, Gabriel Probst, Evelina Ametova, Frederik Vogeler, Eddy Smets, Jo Van Kriekingen, Haibin Zhao and many others. Thank you for all your kind help. It was an honor for me to be part of this team and it was nice experience working together with all of you.

Besides, I want to say a big "thank you" to all my close friends (Zhibin Sun, Tingting Wang, Lin Zhang, Yue Peng, Yansong Guo, Ying Xie, Yelin Deng, Taorui Wen, Yue Zhao) and other Chinese colleagues that I have met in Belgium during these years. Thank you for your friendship and for all the happy moments we have spent together.

最特别的感谢致与我远在中国的亲人们：我的父亲（谭会民）、母亲（胡晓华）、姐姐（谭雯文）、姐夫（张志强）以及我可爱的小侄女（张睿涵）。感谢你们一直以来的信任、鼓励与无私的帮助。

Special thanks go to my Belgian family (Edwin, Marleen, Sarah, Dorien,…). I wouldn't be able to get so far without your support. Thank you for always being there whenever I need advice and help.

Elke, my love, meeting you and marrying you was the best thing that ever happened to me in my life. You are the source of my strength when I feel weak and the source of my happiness when I feel blue. I know I don't often say "thank you" to you, but I hope you know how much I appreciate you and how important you are to me.

At last, I would like to thank my little daughter Sophie; despite of all the sleepless nights and countless Pampers, a smile on your face would be my best comfort.

Thus, doing a PhD can actually mean a lot of fun. The condition is that if you can have all the above mentioned awesome people around you. Although my PhD will end, the fun will continue.

Ye Leuven, 2015.4

Abstract

Industrial CT, as an emerging technology for dimensional quality control, is increasingly favoured by industry due to its capabilities to provide geometric information of inner and hidden structures of complex or assembled parts. However, industrial CT has not been widely accepted as an accurate measurement tool due to its high operator dependency and lack of traceability.

This PhD study investigates various influence factors and their correlations throughout the entire measurement loop of CT dimensional metrology, including the workpiece’s properties, the scanning settings and the post-processing parameters. Based on the results of this PhD research, optimization strategies in term of parameters for scanning and post-processing have been proposed.

Except for measuring academic test workpieces, a case study of an ABS (anti-lock breaking system) module from an automotive company is presented. In this study, a complex industrial component has been used to investigate the measurement accuracy, the measurement, the repeatability and other challenges in dimensional CT metrology. In addition to the influencing factors mentioned above, the influence of the alignment system has also been studied in depth.

Korte Samenvatting

Industriële CT komt, als opkomende technologie voor dimensionele kwaliteitscontrole, steeds meer in de gunst van de industrie vanwege zijn mogelijkheden om geometrische gegevens te verschaffen van inwendige en verborgen structuren van complexe of samengestelde onderdelen. Het wordt echter niet algemeen aanvaard als een nauwkeurig meetinstrument door de hoge operator-afhankelijkheid en het gebrek aan traceerbaarheid.

Deze doctoraatsstudie onderzoekt verschillende invloedsfactoren en hun correlaties doorheen de volledige metingscyclus van CT dimensionele metrologie, waaronder de eigenschappen van het werkstuk, de scaninstellingen en de post-processing parameters. Op basis van de resultaten van deze doctoraatsstudie, worden er optimalisatiestrategieën voorgesteld voor de parameters tijdens het scannen en de nabewerking.

Naast meetresultaten voor academische teststukken, wordt er ook een casestudy voorgesteld van een ABS-module (antiblokkeersysteem) van een automobielbedrijf. In deze casestudy werd een complexe industriële component gebruikt om de meetnauwkeurigheid, de meting, de herhaalbaarheid en andere uitdagingen van dimensionale CT-metrologie te onderzoeken. Naast de reeds genoemde invloedsfactoren wordt ook de invloed van het uitlijnsysteem diepgaand bestudeerd.

List of Abbreviations

ABS: anti-lock breaking system

AM: additive manufacturing

BH: beam hardening

BHC: beam hardening correction

CAD: computer aided design

CMM: coordinate measurement machine

DOE: design of experiments

EPS: expanded polystyrene

FBP: filtered back-projection

FDD: focal spot – X-ray detector distance

FOD: focal spot – object distance

GPS: geometrical product specifications

HVL: half value layer

LINAC: linear accelerator

MPE: maximum permissible error

MTR: minimum transmission ratio

NDT: non-destructive testing

PBT: polybutylene terephthalate

PE: polyethylene

PEEK: polyether ether ketone

PET: positron emission tomography

PPS: polyphenylene sulfide

ROI: region of interest

SLS: selective laser sintering

SNR: signal to noise ratio

SPECT: single-photon emission computed tomography

SPM: scanning probe microscope

X-ray CT: X-ray computed tomography

List of Definitions

Additive Manufacturing: refers to a process by which digital 3D design data is used to build up a component in layers by depositing material. *[International Committee F42 for Additive Manufacturing Technologies, ASTM]*

Beam Hardening Effect: Beam hardening is seen with polychromatic X-ray sources. As the X-ray passes through the body, low energy X-ray photons are attenuated more easily, and the remaining high energy photons are not attenuated as easily. Thus, beam transmission does not follow the simple exponential decay seen with a monochromatic X-ray. *[Hsieh J., 2003]*

Bremsstrahlung Radiation: bremsstrahlung is a German word used in physics to describe the electromagnetic radiation emitted by a high speed charged particle (e.g. electron) when decelerated by another charged particle. It yields a continuous X-ray spectrum from very low energies up to the full energy (i.e. applied keV) of the impacting electron. *[Gargaud M. et al., 2011]*

Characteristic Radiation: the discrete forms of radiation that are emitted from atoms when electron transitions occur in the orbitals of electrons. *[Gargaud M. et al., 2011]*

Compton scattering: also known as incoherent scattering, in this process, the photon abruptly changes direction and transfers a portion of its original energy to the electron from which it scattered, producing an energetic recoil electron. The fraction of the photon energy that is transferred depends on the scattering angle. When the incoming photon is deflected only slightly, little energy is transferred to the electron. Maximum energy transfer occurs when the incoming photon is backscattered from the electron and its original direction is reversed. [*Encyclopedia Britannica Online Academic Edition*. Encyclopedia Britannica Inc., 2014]

Dimensional Metrology: the science of calibrating and using physical measurement equipment to quantify the physical size of or distance from any given object. *[Connie L. D., 2006]*

Filtered Back-Projection: an image reconstruction method which combines the back projection and ramp filtering. It is based on the "Linear Integral Transformation" developed by J. Radon in 1917. *[Herman G.T., 2009]*

Half Value Layer: the thickness of the material at which the intensity of radiation entering it is reduced by one half. *[Jerrold T. B. et al., 2011]*

Histogram: graphical representation of the empirical relationship between the values of a characteristic and their frequencies or their relative frequencies. *[ISO 3534-1]*

Linear Attenuation Coefficient: the fraction of photons removed from a mono-energetic beam of X-rays or gamma rays per unit thickness of material is called the linear attenuation coefficient (μ), typically expressed in units of inverse centimeters (cm^{-1}). *[Jerrold T. B. et al., 2011]*

Look up Table: an array that replaces runtime computation with a simpler array indexing operation. *[Campbell-Kelly M. et al., 2003]*

Maximum Permissible Error: extreme value of the measurement error, with respect to a known reference quantity value, permitted by specifications or regulations for a given measurement, measuring instrument, or measuring system. *[International Vocabulary of Metrology - Basics and General Concepts and Associated Terms]*

Measurement Repeatability: precision under specific conditions where independent test results are obtained with the same method on identical test items in the same laboratory by the same operator using the same equipment within short intervals of time. *[ISO 3534-1]*

Minimum transmission ratio: expressed in percentage, which describes the X-ray transmission through the highest X-ray attenuation path when scanning an object. *[ISO 15708:2002, Non-destructive testing - Radiation methods - Computed tomography; part 2 chapter 7.3.1]*

Measurement Uncertainty: it is a parameter, associated with the result of a measurement, which characterizes the dispersion of the values that could reasonably be attributed to the measurand. *[International Vocabulary of Metrology - Basics and General Concepts and Associated Terms]*

Partial Volume Effect: the loss of apparent activity in small objects or regions because of the limited resolution of the imaging system. *[Hoffman E. J., 1979]*

Photoelectric Absorption: in this process, the incident X-ray or gamma-ray photon interacts with an atom of the absorbing material, and the photon completely disappears; its energy is transferred to one of the orbital electrons of the atom. *[Encyclopedia Britannica Online Academic Edition. Encyclopedia Britannica Inc., 2014]*

Repeatability: closeness of the agreement between the results of successive measurements of the same measurand carried out under the same conditions of measurement. *[VIM 3.6]*

Reproducibility: closeness of the agreement between the results of measurements of the same measurand carried out under changed conditions of measurement. *[VIM 3.7]*

Selective Laser Sintering: an additive technique in which powdered material is selectively melted, or sintered, when exposed to a laser beam. *[ISO/TC XXX/SC N, 2010-09-17]*

Signal to Noise Ratio: a measure used in science and engineering that compares the level of a desired signal to the level of background noise. It is defined as the ratio of signal power to the noise power, often expressed in decibels. *[ISO 12232: 1997 Photography]*

Solarization: a physical phenomenon that describes materials undergoes temporary/permanent change in color after being subjected to high energy electromagnetic radiation, such as ultraviolet light or X-rays. Clear glass and many plastics will turn amber, green or other colors when subjected to X-radiation, and glass may turn blue after long term solar exposure in the desert. *[Moncke D., 2001]*

Surface Roughness: a parameter derived from the primary surface profile by suppressing the long wave component using the short wave Gaussian profile filter with a cut-off wavelength value L_c. *[ISO 4287]*

Thresholding (Segmentation): the process which determines the respective interfaces between different materials and surrounding air. *[Gonzalez R. C. & Woods R. E., 2002]*

Waviness: a parameter derived by suppressing the long wave component using the "profile filter L_f", and suppressing the short wave component using the long wave Gaussian profile filter with a cut-off wavelength value of L_c. *[ISO 4287]*

X-ray attenuation: the removal of photons from a beam of X-rays as it passes through matter. *[Jerrold T. B. et al., 2011]*

X-ray Computed Tomography (X-ray CT): a technology that uses computer-processed X-rays to produce tomographic images (virtual 'slices') of specific areas of the scanned object, allowing the user to see what is inside it without cutting it open. Digital geometry processing is used to generate a three-dimensional image of the inside of an object from a large series of two-dimensional radiographic images taken around a single axis of rotation. *[Herman G. T., 2009]*

X-ray: electromagnetic radiation of high energy and very short wavelength (between about 0.01 and 10 nanometers), capable of passing through many substances opaque to light, and widely used in medical diagnosis and treatment and in many analytical techniques. *[Oxford English Dictionary, 2005]*

Table of Contents

CHAPTER 4: Influence of Scan Settings Parameters... 65

CHAPTER 1

Introduction

This chapter gives a short introduction on the X-ray computed tomography (CT) technology, starting from the discovery of X-ray, the birth of the first CT scanner until its recent developments and modern application fields. Additionally, the current status of CT dimensional metrology is discussed; together with a short discussion on the two "inter-laboratory comparison" projects, in which the achievable accuracy and the uncertainty of dimensional measurements using industrial CT equipment are addressed.

1.1 X-ray CT technology

1.1.1 What is industrial CT?

X-ray computed tomography (X-ray CT) is a technology that applies X-rays to produce tomographic images (virtual "slices") of a scanned object. Digital image processing can be used to generate a three-dimensional voxel model of the object from a large number of two-dimensional projection images taken around a single axis of rotation. Because X-ray CT is the most common form of CT in various contexts, the term computed tomography (CT) is often used to refer to it alone. However, other types of "CT" exist, such as: single-photon emission computed tomography (SPECT) and positron emission tomography (PET) *[Herman G. T., 2009]*.

The key difference between a medical and an industrial CT scanner lays in their configurations. In a medical CT system, the X-ray source and detector are rotating around the patients; while in an industrial CT system, the object is placed on a rotation stage and it rotates between the fixed X-ray source and the detector (Fig 1.1). Moreover, the achievable resolution of an industrial CT scanner is significantly better than that of a medical CT scanner, due to the possibility of using a variable and high magnification, a smaller spot size and longer acquisition time.

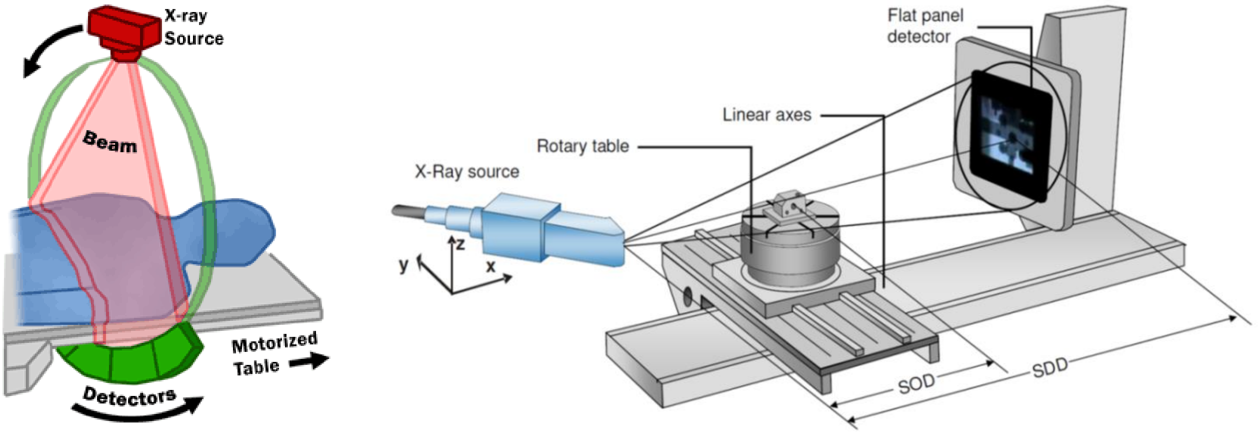

(a) *(b)*

Figure 1.1 *Left: basic configuration of a typical medical CT system [http://www.fda.gov]; Right: an industrial CT system with cone-beam X-ray source and flat panel detector [Schmitt R. et al., 2011]*

1.1.2 The evolution of X-ray CT technology

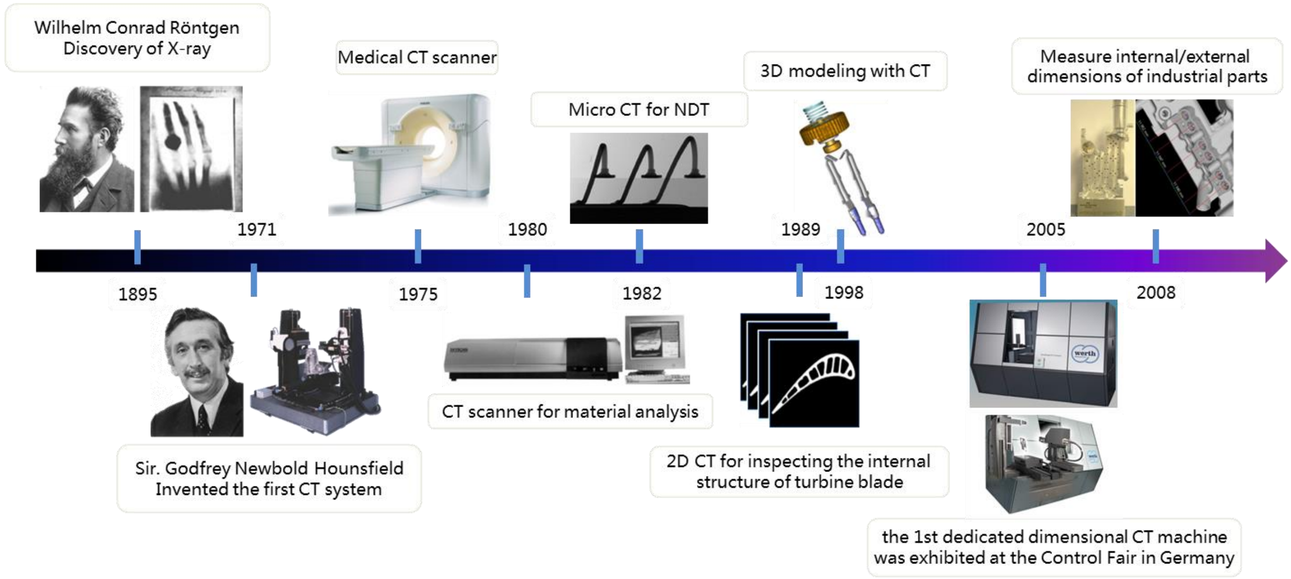

Figure 1.2 *The evolution of X-ray CT technology [Based on "Schmitt R. et al., 2011"]*

Although the existence of X-rays has been noticed by many researchers since the invention of experimental discharge tubes around 1875, the German physicist Wilhelm Röntgen was the first to systematically study its effect and thus regarded as the discoverer of X-ray in 1895. The prototype of the first medical CT scanner was developed by Sir. Godfrey Hounsfield in the early 1970's. Since then, CT has been widely used for medical diagnosis and has become one of the most important techniques for medical imaging *[Aaron G. F., 2009]*. Starting from 1980, industrial CT has become a popular tool for material analysis and non-destructive testing (NDT), where cross sections of objects can be visually inspected: e.g. for observing the inner structure or for detecting defects in the materials *[Reimers P. et al., 1983]*. In the late 1990s, 3D modeling and quantitative analysis using industrial CT became possible due to the fast development of image processing techniques. The 1st dedicated CT scanner for dimensional metrology was exhibited at the Control Fair in Germany in 2005 *[Kruth J.P. et al., 2011]*. Since then, Industrial X-ray CT systems are increasingly used as dimensional measuring tools for acquiring external and internal dimensional information of complex industrial parts.

1.2 Modern application fields

1.2.1 Industrial CT for material analysis and non-destructive testing

Nowadays, material analysis and non-destructive testing (NDT) (e.g. checking the internal cooling channels of turbine blades and detecting delamination of carbon fiber based structures) are major applications of industrial CT. As illustrated in Fig.1.3 and 1.4, X-ray CT has an excellent performance as an NDT technique in terms of combining penetration depth, resolution and geometrical complexity. *[Bergmann R. B., 2004]*

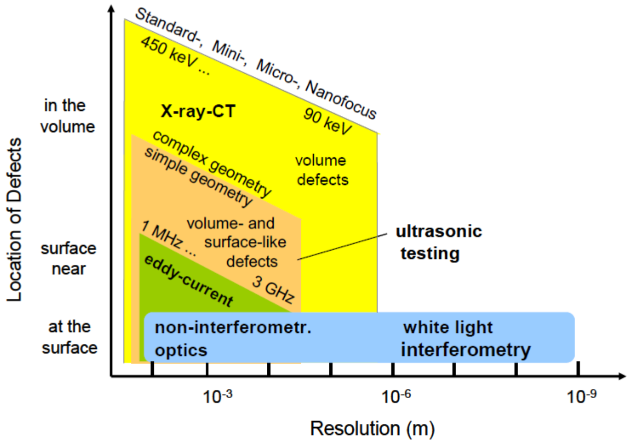

Figure 1.3 *Classification and comparison of chosen NDT techniques and optical measurement techniques according to detectable defect location and spatial resolution. [Bergmann R. B., 2004]*

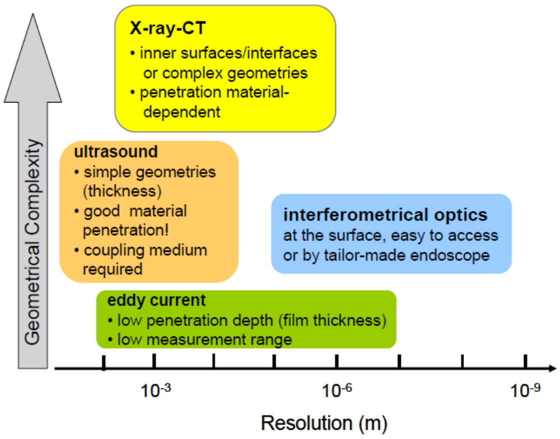

Figure 1.4 *Classification of chosen NDT techniques according to geometrical complexity and resolution. [Bergmann R. B., 2004]*

More recently, industrial CT is increasingly applied by the additive manufacturing industry due to its capability of checking complex internal cavities, performing failure analysis and porosity assessment of “3D printed” parts (Fig.1.5 and 1.6).

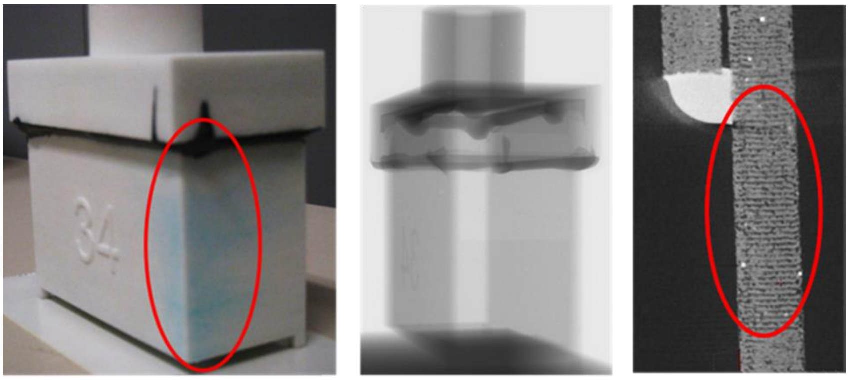

Figure 1.5 *Failure analysis of an additive manufactured ink box. During the testing phase, one side of the box shows obvious ink leakage. CT scan of this ink box reveals larger layer spacing on the leakage side. Moreover, denser metal powder inclusions can also be noticed (bright white particles).*

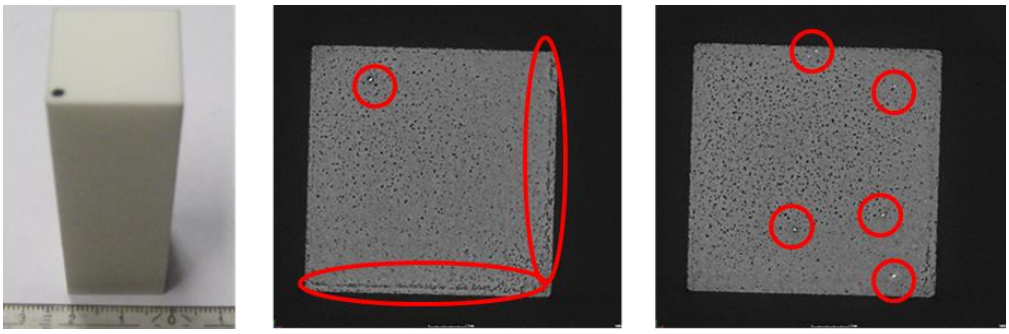

Figure 1.6 *Porosity assessment of an additive manufactured cuboid. Certain building defects are clearly noticeable at the edge, in addition, denser metal power inclusions are also revealed.*

1.2.2 Industrial CT for dimensional metrology

Accurate measurements, control of dimensional and geometric tolerances are essential elements for manufacturing industry. Nowadays, multi-function integration dramatically increases the complexity of industrial components; Multi-material assemblies can also be made out of one injection molding step; moreover, with the help of additive manufacturing techniques, parts with complex internal structures can be easily produced. However, the dimensional tolerances of these complex features, assemblies and internal structures are very difficult to be controlled non-destructively in the traditional way. Since 2005, the manufacturing industry started showing great interest in CT for dimensional quality control purposes, due to its capability to provide geometric information of inner and hidden structures non-destructively and to combine qualitative (e.g. voids and crack) and quantitative (e.g. density, porosity, dimensions and tolerances) checks in one measurement task *[Kruth J.P. et al., 2011]*. Fig 1.7 and 1.8 demonstrate the evolution of measurement devices in manufacturing metrology and the typical resolution and measuring range plots for optical sensors, tactile probing systems, computed tomography and scanning probe microscopes.

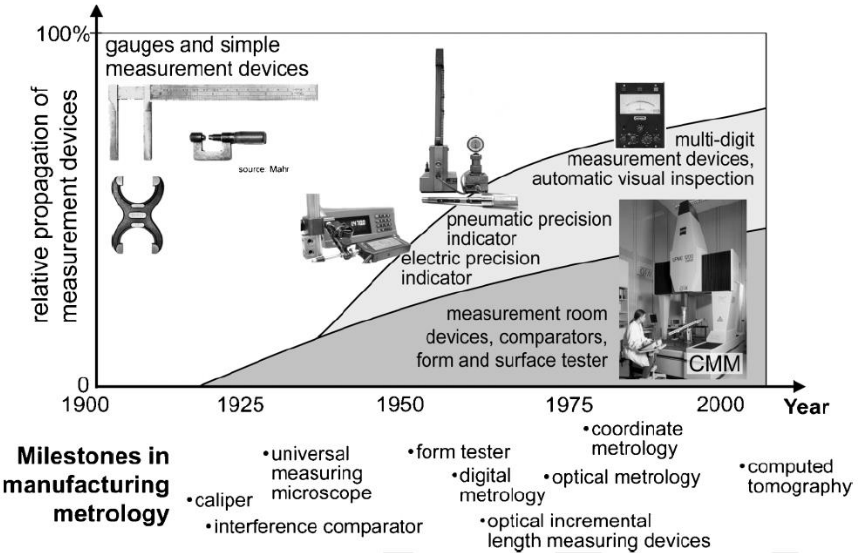

Figure 1.7 *Development of measuring devices [Weckenmann A. et al., 2009]*

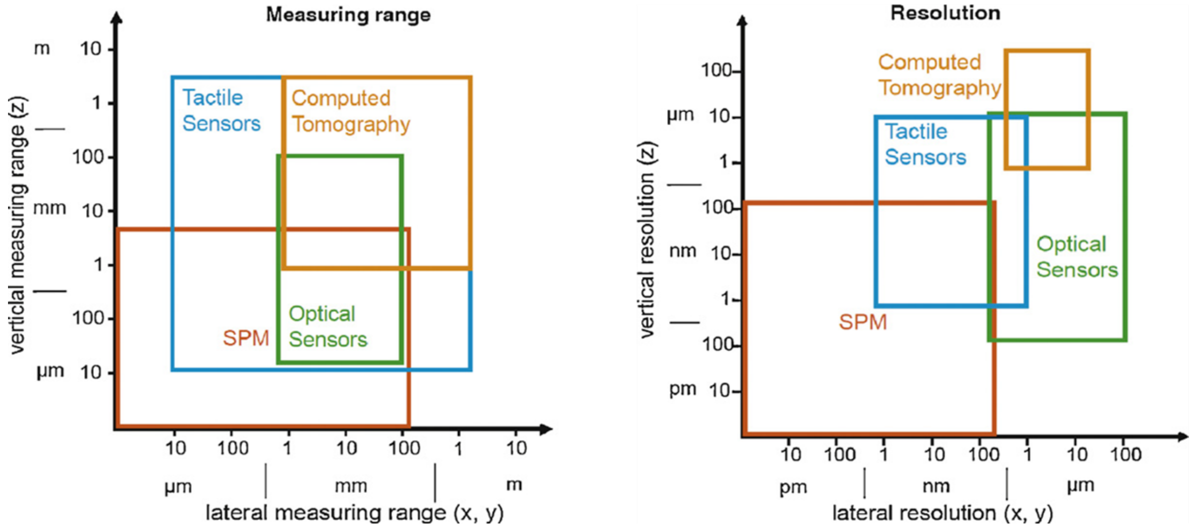

Figure 1.8 *Typical measuring range and resolution plots for optical sensors, tactile probing systems, computed tomography and scanning probe microscopes (SPM). [Weckenmann A. et al., 2009]*

1.2.3 Achievable accuracy: inter-laboratory comparison projects

Today, micron level dimensional measurement accuracy and MPE (maximum permissible error) value have been claimed by various industrial CT manufactures; however, the current methods for calculating the MPE value of industrial CT systems are mostly based on measuring simple geometries, such as sphere center distances. Due to numerous error sources and the lack of standardization, it is very difficult to make a direct link between the claimed MPE value and the uncertainty of actual dimensional measurements when performing the CT dimensional metrology on complex industrial components. Thus, "which accuracy can CT dimensional metrology achieve at this moment?" remains a challenging question. This is one of the main reasons of the limited consideration of CT as a valid measuring tool in current industrial practice *[Carmignato S., 2012]*.

In order to evaluate the metrological performance of industrial CT systems worldwide and to investigate the traceability of measurement results obtained by experienced users of CT systems for dimensional metrology, two inter-laboratory comparison projects have been organized which involved various laboratories in Europe, America and Asia. Participants were selected among the most experienced users of CT systems for dimensional metrology including national metrology institutes, research institutes, CT system manufacturers, and industrial users. The first project was organized by prof. Simone Carmignato (University of Padova, Italy) from 2009 till 2011; a second project was organized by prof. Leonardo De Chiffre (Technical University of Denmark), which started in May 2012 and ended in September 2013. In total 6 objects have been analyzed: the 4 items involved in the first inter-laboratory comparison project are dedicated calibration objects coming from academic institutes and research centers (Fig 1.9); the 2 items used in the second inter-laboratory comparison project comes from industry (Fig 1.10).

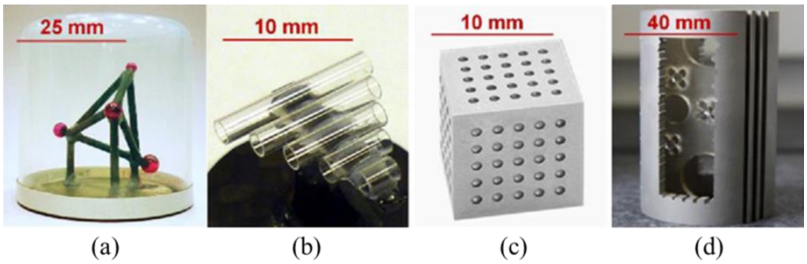

Figure 1.9 *The four items used in the first inter-laboratory comparison project: (a) CT Tetrahedron – ruby spheres supported by carbon fiber frames, (b) pan flute gauge – five borosilicate glass tubes supported by a carbon fiber frame, (c) calotte cube – a hollow titanium cube, with 75 spherical calottes on three sides of the cube, (d) QFM cylinder – a hollow titanium cylinder with embodied calotte spheres and containing micro structures; a ball plate carrying five sapphire spheres is clamped into the cylinder [Carmignato S., 2012]*

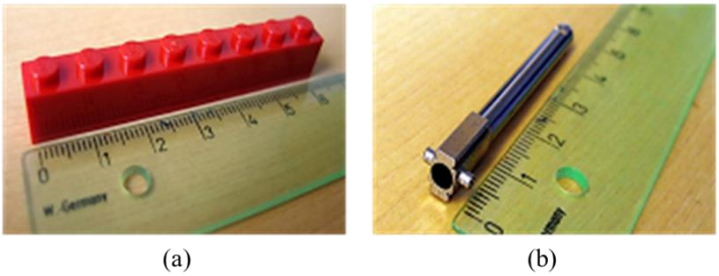

Figure 1.10 *The two objects used for the second inter-laboratory comparison project: (a) polymer brick from LEGO, made of Acrylonitrile Butadiene Styrene, (b) metallic tubular component from the medical industry [Angel J. et al., 2013]*

The above mentioned items were circulated and measured by all participants using industrial CT systems; their measuring procedures and dimensional measurement results were compared and analyzed. Several general conclusions can be drawn from both projects *[Carmignato S. et al., 2011] [Angel J. et al. 2013]*:

a) Large deviations are observed from form error measurements.

b) Measuring the dimensions of standard features (e.g. spheres’ center distance, cylinder diameter, wall thickness etc.) is more reliable. However, uncertainty calculation remains challenging, even for experienced users.

c) Operator influence is significant; the dimensional measurement results are largely influenced by the selected measuring strategy (machine settings, reconstruction, beam hardening correction, thresholding, calibration methods ...)

It can also be seen that, besides enhancing the related hardware to improve the performance of industrial CT systems, it is essential to develop advanced measuring and calibration procedures. Furthermore, standardizing the methods for evaluating the metrological properties of industrial CT systems (e.g. calculation for the MPE value, measurement uncertainty estimation…) is of utmost importance.

CHAPTER 2

Influence Factors in CT Dimensional Metrology & Study Aims

In this chapter, the basic principle, hardware and software of a typical industrial CT system are briefly explained. Moreover, the operation steps of using an industrial CT system for dimensional metrology are described, including various influence factors for each step. This also leads to the most important goal of this PhD study: investigating different influence factors for CT dimensional metrology and searching for a practical and reliable strategy for optimizing these parameters.

2.1 Basic principle: technical systems and components

2.1.1 Hardware

As introduced in Section 1.1, modern industrial CT's hardware system mainly includes 3 parts: the X-ray source, the kinematic system and the X-ray detector.

- **X-ray source**

There are many types of X-ray sources, such as X-ray tubes which evolved from experimental Crookes tubes, linear accelerator (LINAC) X-ray sources and large synchrotron radiation facilities that can also be used to generate X-ray for CT applications. The commonly installed X-ray source on industrial CT systems is the Coolidge tube; its basic configuration is shown in Fig 2.1 (a): electrons are generated by the thermionic effect from a filament (cathode of the tube) heated by an electric current. A high voltage potential is applied between the cathode and the anode, so that the electrons are accelerated up to very high speed ($a = q \times E/m$ where "a" is the acceleration; "q" is the charge of an electron; "E" is the electric field determined by the cathode and the anode voltages; "m" is the mass of an electron).A deflection unit is implemented to control the convergence of the electron beam, and magnetic lenses are used for focusing the electron beam onto the target. When hitting the target material, the electron beam will experience a sudden deceleration, causing energy to be converted into heat (more than 99%) and X-ray (less than 1%). The radiation produced in this way has a polychromatic spectrum, which consists of both Bremsstrahlung radiation and characteristic radiation (Fig 2.1 (b)). Bremsstrahlung is an X-ray generation process which yields a continuous X-ray spectrum from very low energies up to the full energy of the impacting electrons. Characteristic radiation is caused by electrons changing rotating orbit, thus is dependent on the target material and is characterized by line spectra.

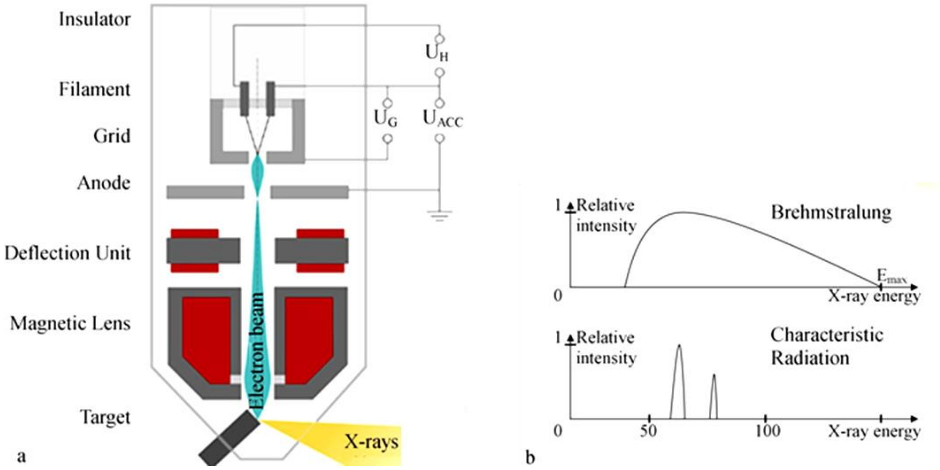

Figure 2.1 *(a) Schematic of a typical X-ray tube for industrial CT systems, (b) example of radiation spectra [Kruth J.P. et al., 2011]*

- **X-ray attenuation**

Attenuation is the process by which X-ray beams lose energy as they travel through matter and interact with it. Different mechanisms might take place during this process, including Thomson (or Rayleigh) scattering, photoelectric absorption, Compton scattering, pair production and photodisintegration. As shown in Fig 2.2, the relative contribution of these mechanisms to the total attenuation is influenced by the incident photon energy.

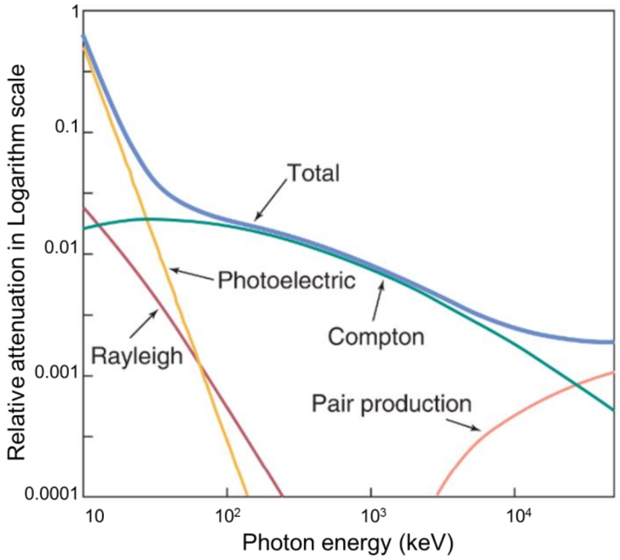

Figure 2.2 *General probability of different attenuating processes [Jerrold T. B., 2011]*

Thomson scattering (also known as Rayleigh or coherent scattering) occurs without change of internal energy of the interacted atom, nor of the incident X-ray photon. Pair production can only happen when the X-ray photon energy is greater than 1.02 MeV; similarly, photodisintegration requires even higher X-ray energy. Thus, for a common industrial CT system, the two major processes that may occur resulting in the attenuation of X-rays are: photoelectric absorption and Compton scattering. Table 2.1 gives an example of the probability of these two attenuation processes for water at different X-ray photon energies *[http://www.e-radiography.net]*:

X-ray photon energy	Photoelectric absorption	Compton scattering
10 keV	95%	5%
25 keV	50%	50%
60 keV	7%	93%
150 keV	0	100%
200 keV	0	100%

Table 2.1 *Probability of X-ray attenuation processes in water at different X-ray photon energies*

The basic principles of photoelectric absorption and Compton scattering are shown in Fig 2.3:

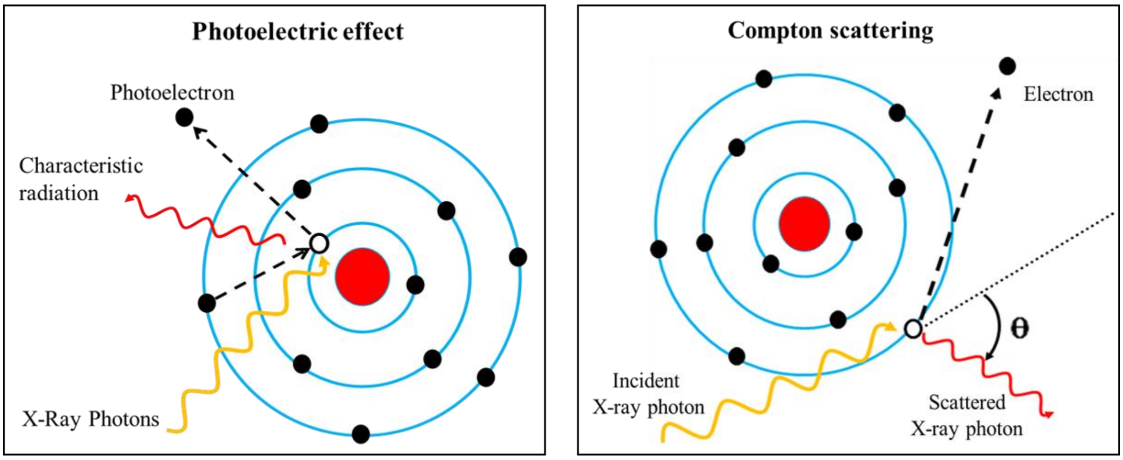

***Figure 2.3** Photoelectric absorption and Compton scattering*

During the photoelectric absorption process, the incident X-ray interacts with an atom of the absorbing material and the photon completely disappears; its energy is transferred to one of the orbital electrons of the atom. In Compton scattering process, the photon abruptly changes direction and transfers a portion of its original energy to the electron from which it scattered, producing an energetic recoil electron. The fraction of the photon energy that is transferred depends on the scattering angle. When the incoming photon is deflected only slightly, little energy is transferred to the electron. Maximum energy transfer occurs when the incoming photon is backscattered from the electron and its original direction is reversed. *[Encyclopedia Britannica Online Academic Edition, 2014]*

In addition, it needs to be mentioned that scanning industrial components with X-ray CT isn't without any risk. Certain interactions might occur between the incident X-ray and the scanned materials; "solarization" belongs to one of these interactions. It concerns materials undergoing temporary/permanent change in color after being subjected to high energy electromagnetic radiation, such as ultraviolet light or X-rays *[http://www.cmog.org/article/solarized-glass]*. Clear glass and many plastics will turn amber, green or other colors when subjected to X-radiation. A few examples are shown in Fig 2.4 and 2.5:

Figure 2.4 *Streetlight globes that have solarized to a purple color [http://www.cmog.org/article/solarized-glass]. Note that the screw threads have not turned purple because they were shielded from sunlight by the metal fixture.*

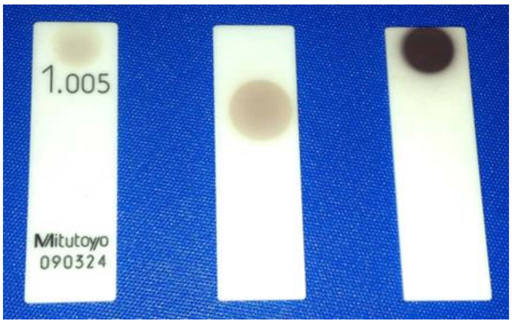

Figure 2.5 *Ceramic (ZrO_2) end gauge after local X-ray radiations: they were very close to the X-ray source, radiated at 185KV for 10 minutes. Left: 1 year after radiation. Middle: six month after radiation. Right: 2 minutes after radiation.*

It is believed that solarization is caused by the formation of internal defects called color centers, which selectively absorb portions of the light spectrum. Color center absorption can often be reversed by heating the glass to high temperatures (a process called thermal bleaching) to restore the glass to its initial transparent state.

The most problematic effect of solarization is that a material's physical or mechanical properties can be permanently degraded: X-ray irradiation can induce significant changes to properties of ceramic materials, such as strength, electrical and thermal conductivities, dielectric response and optical behavior. Solarization is also one of the mechanisms involved in the breakdown of plastics within the environment *[Linn W. H. et al., 1994]*. Many industrial CT systems contain glass fiber components in the encoder system of their axes or in the X-ray detector system, the property of these components might degrade over time and causes instability for the entire system.

- **Kinematic system**

In an industrial CT system, the X-ray source and detector are usually fixed, while the object is placed on a rotary table. During CT scanning, the object rotates around a single rotation axis between the X-ray source and detector, as indicated in Fig 1.1. The rotary table can rotate continuously or stepwise (for minimizing the ring artifacts); translational movement along the vertical axis is also required for 3D CT with a linear detector or for performing a helical CT scan.

The achievable resolution is primarily determined by the focal spot size, the detector pixel size and the magnification. Nowadays, most metrological CT systems are using micro focus X-ray tubes. Depending on the applied X-ray power, the focal spot size typically ranges from 3 µm to more than 100 µm. Magnification is determined by the source to object and source to detector distances. In an ideal case, a higher magnification yields a better resolution. However, due to the finite focal spot size, the edges of an object are blurred when moving towards the X-ray source, as shown in Fig 2.6. In addition, along with larger magnification (larger open scan angle), the cone artifacts will also become much severer *[Weckenmann A. et al., 2009]*.

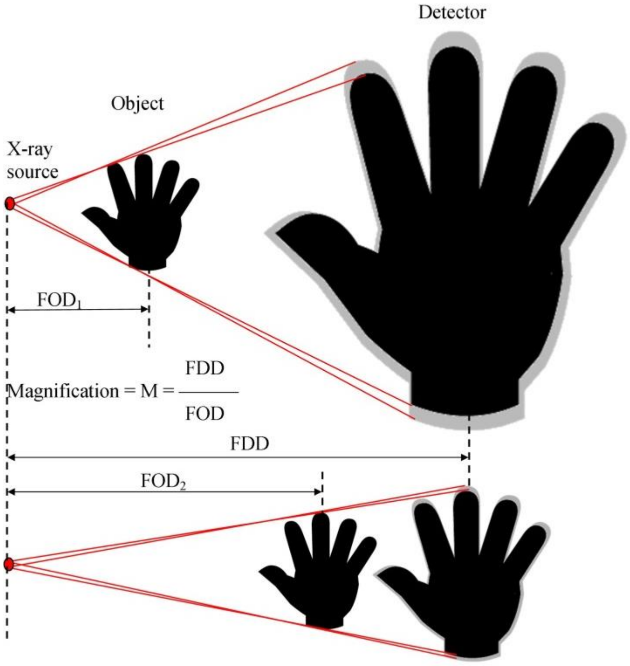

Figure 2.6 *Image magnification and blurring by moving part towards the X-ray source. FOD: focal spot – object distance. FDD: focal spot – X-ray detector distance. [Kruth J.P. et al., 2011]*

- **X-ray detector:**

Nowadays, digital X-ray detectors are much more popular than analog film X-ray detectors due to their lower price and possibilities for various image processing. Among all digital X-ray detectors, the flat panel detectors are accepted as the main stream elements for nowadays digital X-ray technology. As shown in Fig 2.7, there are different designs for a flat panel detector; the most successful and widely used type is a so-called “indirect” detector. They are based on amorphous silicon TFT/photodiode arrays coupled to X-ray scintillators. The basic X-ray conversion process is demonstrated in Fig 2.7 and 2.8. X-ray photons strike the scintillator layer and are converted into visible light. This light then reaches the photodiodes and generates electrons. The electrons can activate the pixels in a layer of amorphous silicon. The activated pixels generate electronic data that can be converted into a high quality projection image of the scanned object.

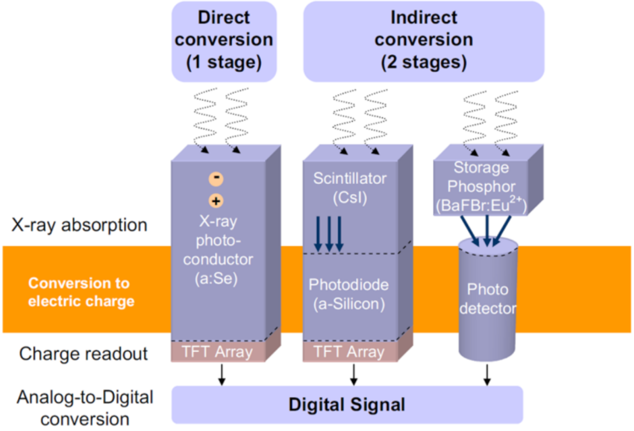

Figure 2.7 *General model for digital X-ray technologies (adapted from reference) [Chotas H.G. et al., 1999]*

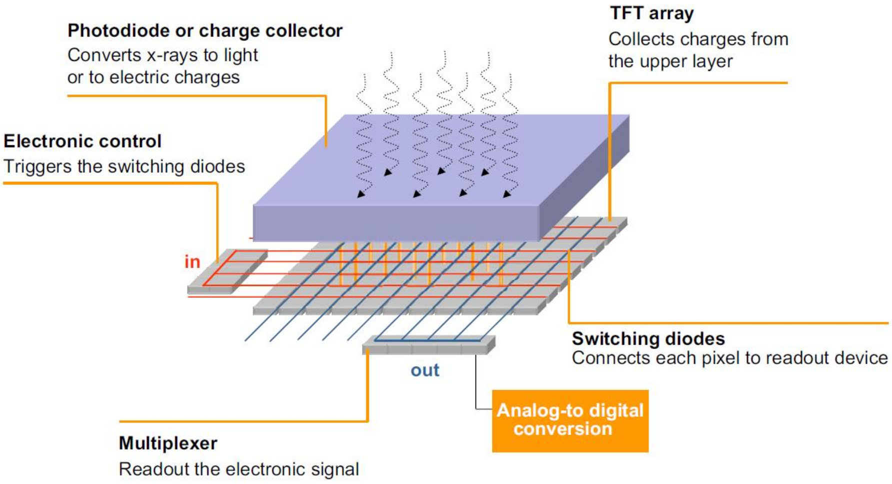

Figure 2.8 *Flat-panel structures [Luis L. et al., 2009]*

2.1.2 Software

Apart from the hardware, image processing also plays an essential role in CT dimensional metrology.

- **Image reconstruction**

Among various reconstruction algorithms (analytical and adaptive reconstruction etc.), filtered back-projection (FBP) is the most widely applied method in industry. It is based on the linear integral transformation (Radon transformation) and uses a model which describes the attenuation of X-ray when passing through an object with varying linear attenuation coefficient “µ”:

$$I = I_o \exp\left[-\int \mu(x)dx\right] \tag{1}$$

In which, “I” stands for the energy summation of the detected X-ray per pixel after passing through materials; “I_0” stands for the energy summation of the detected X-ray without any attenuation; “x” stands for the penetration lengths per material along the propagation path. The linear attenuation coefficient is determined by the X-ray photon energy and the property of the scanned material. Typically, FBP reconstruction involves three basic steps:

1. Multiply the projection data by a weighting filter
2. Convolve the weighted projection data using their Fourier transforms
3. Each weighted projection is back-projected over the three dimensional reconstruction grids. Usually, interpolation is applied when creating voxels *[Kak A. C. et al., 2001] [Feldkamp L. et al., 1984]*.

- **3D modelling and data analysis**

The 3D reconstruction is followed by the thresholding process which determines the respective interfaces between different materials and surrounding air, as shown in Fig 2.9. This is a crucial step because it influences the surface quality of the 3D model and affects the geometries to be measured. However, the thresholding process is complicated by the partial volume effect. As shown in Fig 2.10, the partial volume effect is caused by the inherent resolution limitations of the industrial CT hardware (pixel size, finite focal spot size etc.). As a result, the gray value of voxels that comprise more than one material will represent a weighted average of their properties. Various techniques exist to identify the object/material edges and many of them apply sub-voxel interpolation to compensate the resolution limitations. Generally speaking, two types of thresholding techniques exist: single gray value global thresholding and adaptive local thresholding. The advantages and disadvantages of different thresholding techniques are investigated in Chapter 5.

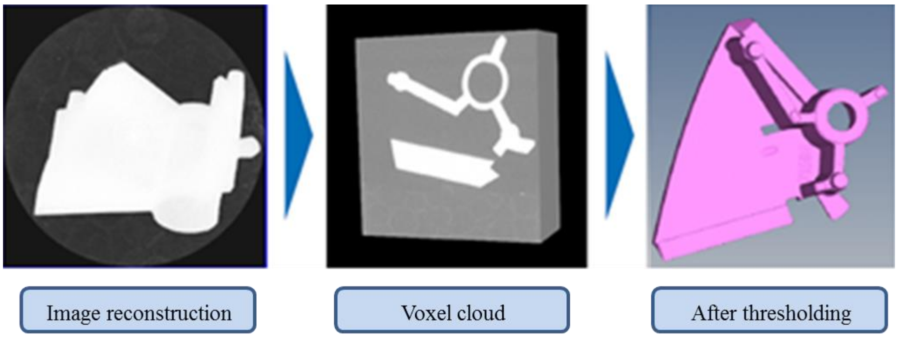

***Figure 2.9** From voxel cloud to 3D model [Based on Schmitt R. et al., 2011]*

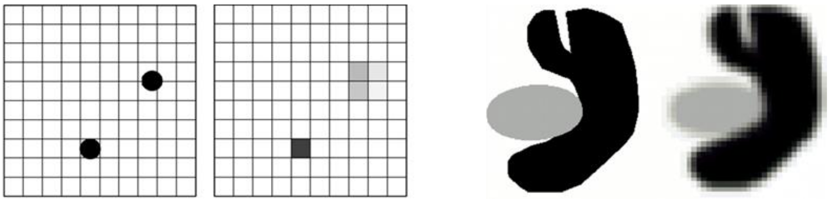

Figure 2.10 *Examples of partial volume effect. The left side images represent the actual objects; the right side images represent the blurring results due to the partial volume effect. [http://www.scanco.ch]*

As shown in Fig 2.11, the data analysis for CT dimensional metrology typically includes:

1. Individual measurand assessment, such as coordinate alignment, point position, dimensions and tolerances of standard features (e.g. plane distance, circle and cylinder diameter, etc.). Least square fitting is mostly applied for defining these features. The software structure for this kind of analysis is very similar to the ones that are used for tranditional tactile CMM.
2. Actual-to-nominal CAD comparison. This is often performed for analyzing the deviation of measured complex parts to a nominal CAD representation.
3. Other analyses include wall thickness analysis, void detection, porosity and density assessment etc.

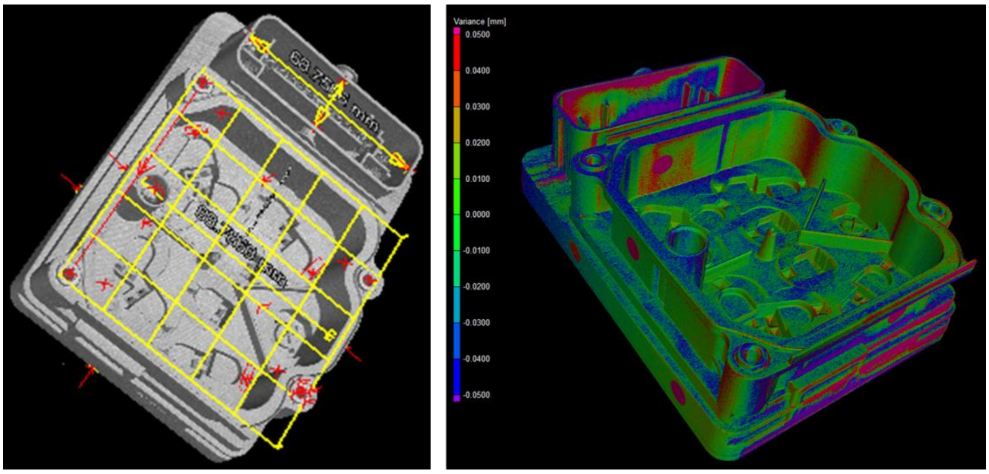

Figure 2.11 *Example of dimensional analysis using CT 3D model*

2.2 Working procedure, influence factors and measurement uncertainty for CT dimensional metrology

The basic operation process for CT dimensional metrology can be divided into four steps, as depicted in Fig 2.12: 2D projection image acquisition, 3D voxel cloud reconstruction, surface determination for creating a 3D model and metrological analysis (e.g. feature measurement, CAD comparison, porosity assessment etc.)

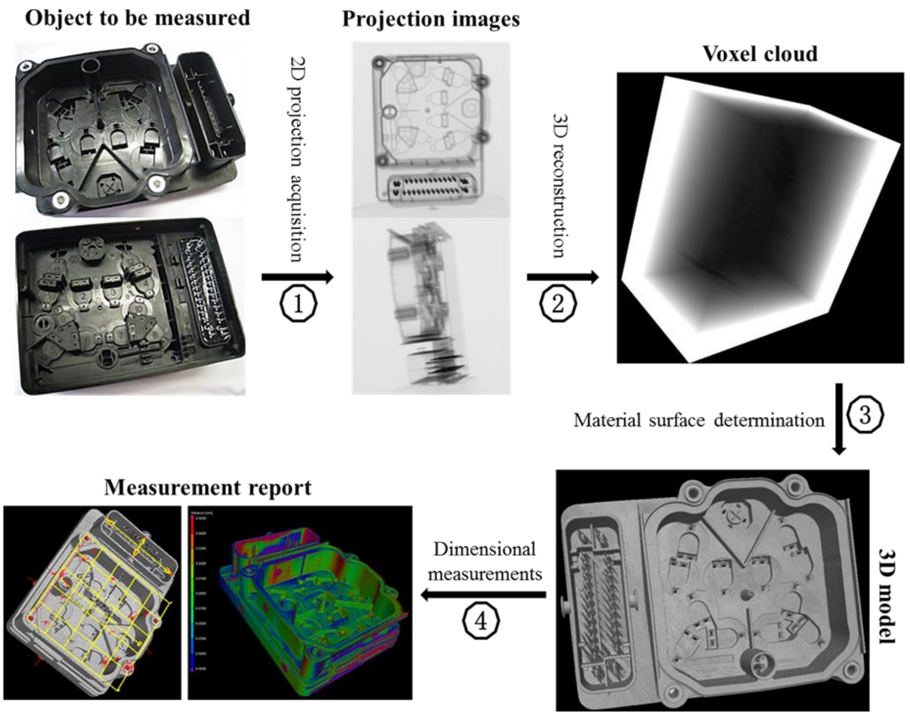

Figure 2.12 *Basic processes for CT dimensional metrology*

For dimensional metrology applications, the measurement uncertainty is an essential element. It is a positive value characterizing the dispersion of the values attributed to a measured quantity *[International vocabulary of metrology – Basic and general concepts and associated terms (VIM), 3rd edition, 2008]*. The uncertainty has a probabilistic basis and reflects incomplete knowledge of the quantity. All measurements are subject to uncertainty and a measured value is only complete if it is accompanied by a statement of the associated uncertainty. Along with entering the dimensional metrology application field, the need for measurement uncertainty assessment also arises for industrial CT. However, there are more than 30 measurement uncertainty contributors throughout its entire process chain *[VDI/VDE 2630, Computed tomography in dimensional measurement]*. These influence factors are categorized into four groups as indicated in Fig 2.13.

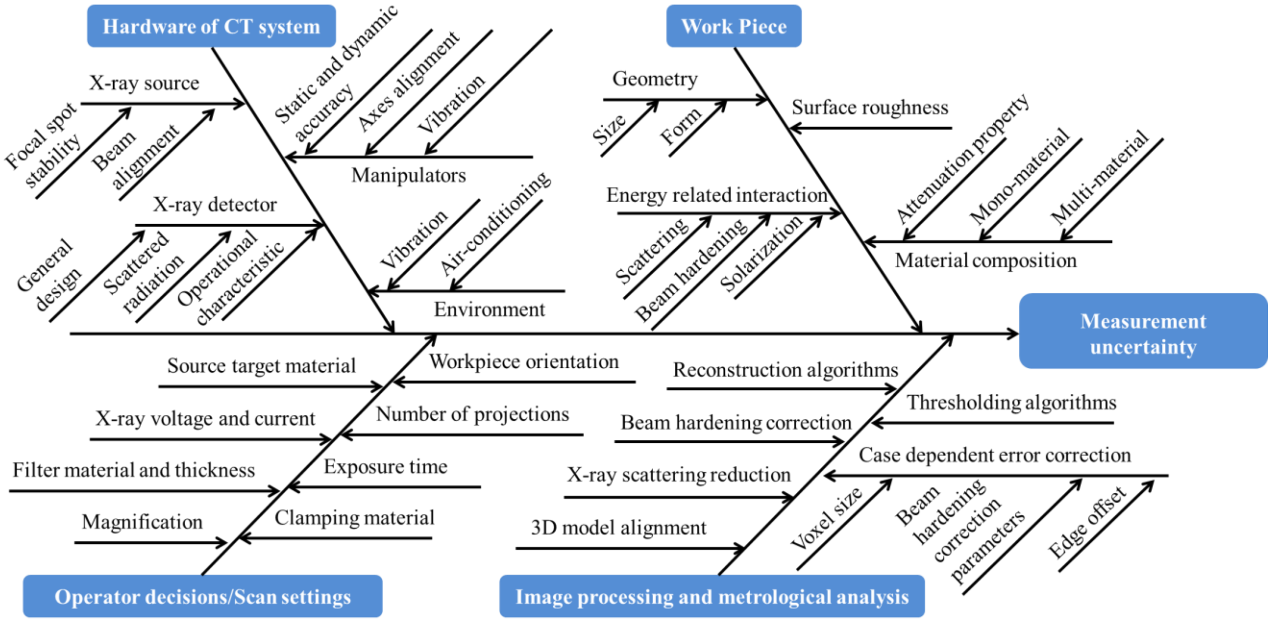

Figure 2.13 *Influence factors for CT dimensional metrology [Based on Schmitt R. et al., 2011] [VDI/VDE 2630, Computed tomography in dimensional measurement]*

Many studies have been conducted by different research groups to assess the influence of these factors on CT dimensional metrology. Vogeler F. et al. studied the X-ray focal spot drifting and temperature variations on a 225 kV industrial CT system using 2D stationary images and proposed an experimental way to compensate the related dimensional measurement errors *[Vogeler F. et al., 2011]*. Welkenhuyzen F. et al. investigated the accuracy of the kinematic system of a 450 kV industrial CT system and its influence on CT dimensional metrology applications; this study revealed that misalignment and inaccuracy of manipulator axes can result in significant dimensional measurement errors *[Welkenhuyzen F. et al., 2014]*. Kiekens K. et al. evaluated the influence of the X-ray power settings and the object size on the accuracy of CT dimensional measurements. It was found that the accuracy of CT dimensional measurement is dependent on both the X-ray power settings (voltage and current) and the object's size *[Kiekens K. et al., 2011]*. VDI/VDE 2630 has suggested using standard artefacts similar to real measurement objects for estimating the material influence *[VDI/VDE 2630–1.3/VDI/VDE 2617-13:2009. Computed tomography in dimensional measurement – guideline for the application of DIN EN ISO 10360 for coordinate measuring machines with CT-sensors]*. However, in practice, it will be difficult to judge whether the similarity is enough and the validity of the characteristics is satisfying *[Weckenmann A. et al., 2013]*. Weckenmann A. et al. investigated three major operator settings during the preparation of a CT scan: orientation of the workpiece, magnification (voxel size) and number of projections. This study proves that the orientation of the workpiece in the measurement volume is vital for the quality of the measurements; using higher magnification can in general improve the measurement accuracy; increasing the number of projections has very limited influences on the dimensional measurement results as long as the minimal required number of projections is ensured *[Weckenmann A. et al, 2009]*. Due to various image artifacts arising from the FBP reconstruction and the possibility of fast computing and image processing using multiple GPUs, many iterative/analytical reconstruction methods have been developed in recent years *[Batenburg K.J. et al., 2011]*. However, taking into account the efficiency and availability, currently, most industrial CT users are still using FBP as their main reconstruction method. Beam hardening correction algorithms have been developed and improved since the early 1970s to reduce various image artifacts. For mono-material objects, linearization techniques are often applied, which are based on estimation of the relation between a propagated path length within the object and corresponding measured intensity *[Ramakrishna K. et al., 2006] [Joseph P.M. et al., 1997]*. A referenceless beam hardening correction technique has been developed for the correction of multi-material objects *[Krumm M. et al., 2008]*. Dewulf W. et.al investigated the influence of beam hardening correction parameters on the diameter of a calibrated steel pin in different experimental set-ups and pointed out that inappropriate beam hardening correction can result in local dimensional measurement errors *[Dewulf W. et al., 2012]*. Accurate thresholding is one of the main challenges for CT dimensional metrology. In the past, global thresholding was often applied for determining the material's surface. However, this method is very vulnerable to local gray value variations, not applicable for dealing with multi-material objects and incapable of producing traceable dimensional measurement results under changing scanning conditions *[Kroll J. et al., 2012]*. Many local thresholding techniques have been developed to overcome these drawbacks: Abutaleb et al. suggested a local thresholding method which depends on the joint (2D) entropy of a pixel neighborhood *[Abutaleb A.S. et al., 1989] [Brink A.D., 1992];* Similarly, White and Rohrer developed a method in which the pixel's gray value is compared with the average of the gray values in its neighborhood *[White J.M. et al., 1983]*. Nowadays, for mono-material object, a local thresholding method is commonly applied which starts from an isosurface contour and then further adapt the material's edge based on the changing gradient of the local gray values *[Tan Y. et al., 2011]*. More recently, a multi-material thresholding method was proposed by Shammaa M.H., et al., which uses a modified and combined method of two well-known algorithms: region growing and graph-cut *[Shammaa M.H. et al., 2010]*.

These numerous influence factors make the uncertainty determination for CT dimensional metrology very challenging. Although draft standard (VDI/VDE 2630) exists which lists potential contributors for measurement uncertainty, due to its highly case dependent nature, there is no general standard for evaluating the metrological performance of industrial CT systems. Many studies have been made by different research groups to estimate the measurement uncertainty of CT dimensional metrology, they are based on simulations *[Wenig P. et al., 2006] [Welkenhuyzen F. et al., 2012]*, experiments *[Bartscher M. et al., 2010] [Weckenmann A. et al., 2009] [Müller P. et al.,* *2011] [Kiekens K. et al., 2011 and 2012] [Dewulf W. et al., 2013]*, or a combination of both *[Schmitt R. et al., 2010]*. Analytical assessments of the metrological performance of CT systems are commonly based on the procedures described in the guideline ISO/TS 15530-3 *[ISO/TS 15530-3 2004 Geometrical Product Specifications (GPS) — Coordinate measuring machines (CMM): Technique for determining the uncertainty of measurement — Part 3: Use of calibrated workpieces or standards]*. In which the expanded uncertainty is divided into three main contributors: workpiece, calibration and measurement procedure.

For CT dimensional metrology, most of the above mentioned influence factors are correlated. The relative importance of each influence factor varies from case to case. Thus, it is not only necessary to understand how these influence factors affect the dimensional measurement results, but also of utmost importance to know the magnitude of their influences and their co-relations.

2.2 Aims and structure of this thesis

As stated in the title, the aim of this PhD study is to investigate and “optimize” various influence factors throughout the entire process chain of CT dimensional metrology. The general approach includes three steps: 1. Identify and categorize the factors; 2. Investigate the influence of different factors and their correlations; 3. Based on the findings from the previous steps, establish a practical strategy for optimizing these factors.

Following this approach, each of the following chapters tackles one category of influence factors: Chapter 3 investigates the influence of the workpiece properties. Chapter 4 looks into the impacts of operator’s decisions on the dimensional measurement results and proposes a best practice for machine setting optimization. Chapter 5 studies the influence of the image processing algorithms and how to set these parameters in order to obtain the “optimal” dimensional measurement results. Chapter 6 presents a case study performed on a multi-material assembly from automotive industry, aiming at transferring academic research knowledge to industrial applications.

CHAPTER 3

Influence of Workpiece Properties

This chapter investigates the influence of two major workpiece properties: the material composition and the surface roughness. Furthermore, the effects of the object's orientation, feature types and their correlation with the material composition are also discussed.

3.1 Influence of material composition and object's orientation

Nowadays, X-ray industrial CT is widely used for inspecting and measuring a large variety of materials; ranging from light plastics to dense metals. Material composition determines the object's X-ray attenuation property and influences the corresponding machine settings (X-ray voltage, current, filter material and thickness, beam hardening correction etc.). As a result, it is suspected that material composition would also be an important influence factor for CT dimensional metrology. Weckenmann A. et al. have investigated three major operator settings during the preparation of a CT scan and concluded that the orientation of the workpiece is vital for the quality of dimensional measurements *[Weckenmann A et al., 2009]*. Furthermore, Angel J. studied the influence of the object's density and orientation using three well calibrated step gauges; and he concluded that the material density affects the measurement results and a "vertical orientation" is not recommended due to high X-ray scattering noise on the planes that are parallel to the X-ray beams *[Angel J., 2014]*. Moreover, these observations mostly occur when scanning dense objects, such as aluminum, steel and zirconium dioxide. Thus, it is assumed that the influences of an object's (which contains flat surfaces) material composition and orientation are correlated. The following subsections try to verify these assumptions experimentally.

3.1.1 Workpiece description

As shown in Fig 3.1, four step gauges (manufactured at DTU, Danmarks Tekniske Universitet) have been selected to investigate the influences of an object's material composition and orientation on the accuracy of CT dimensional measurements. The step gauges' nominal dimensions are shown in Fig 3.2. Their corresponding materials, densities and thermal expansion coefficients are listed in Table 3.1.

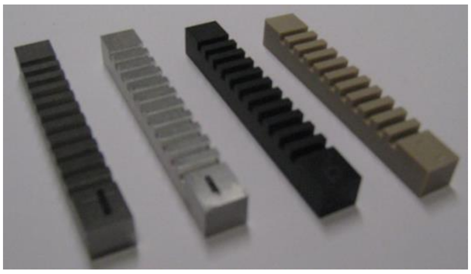

Figure 3.1 *Picture of step gauges. The corresponding materials are (from left to right): Steel, Aluminum, PPS (Polyphenylene sulfide) and PEEK(Polyether ether ketone)*

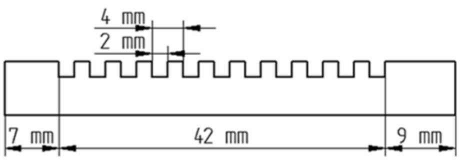

Figure 3.2 *Step gauge's nominal dimension [Angel J., 2014]*

Material	Supplier	Grade	Density (g/cm^3)	Thermal expansion coefficient (10^{-6} K^{-1})
Steel	Uddeholm A/S	UHB 11	7.8	11
Aluminum	Alumeco A/S	AW 2011	2.83	22.9
PPS	Röchling High Performance Plastics	PPS GF 40	1.65	30
PEEK	Nordisk Plast A/S	PEEK Natur	1.31	50

Table 3.1 *Materials, densities and thermal expansion coefficients of the step gauges [Angel J., 2014]*

The influence of thermal expansion is not studied seperately for three main reasons: first of all, both the X-ray source and the measuring space (closed cabinet) are temperature controlled and thus the raise of their temperature is largely reduced; second, even if there is certain temperature raise on the X-ray source, the scanned objects are placed far away from the X-ray source and their temperature won't raise as much as the X-ray source does; third, even if there is temperature induced dimensional variation, this will be largely compensated by the "voxel correction" process (this process is further explained in Section 3.1.6). CT dimensional metrology inherently involves edge offset errors which are caused by inaccurate thresholding, beam hardening effect and X-ray scattering etc.. Whereas a constant edge offset can easily be corrected, non-constant edge offset components originating from beam hardening and X-ray scatter are much harder to compensate for.

All step gauges contain two types of plane distances: unidirectional (Uni-) and bidirectional (Bi-) distances. Both terms are illustrated in Fig 3.3. "1" indicates the systematic edge offset error, "2" and "3" stand for unidirectional and bidirectional distances respectively. The chosen surfaces of distance "2" are offsetted to the same direction and thus the systematic edge offset error is naturally excluded. On the contrary, the systematic edge offset error is doubled for plane distance "3", resulting in larger dimensional measurement errors.

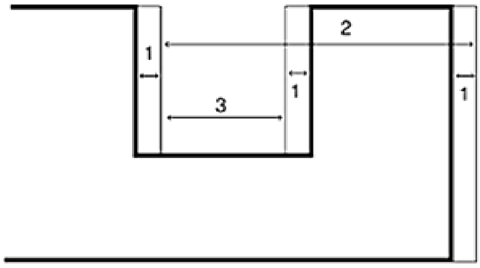

Figure 3.3 *Illustration of unidirectional and bidirectional plane distances: "1" refers to the systematic edge offset error; "2" refers to a unidirectional plane distance; "3" refers to a bidirectional plane distance.*

3.1.2 Alignment system

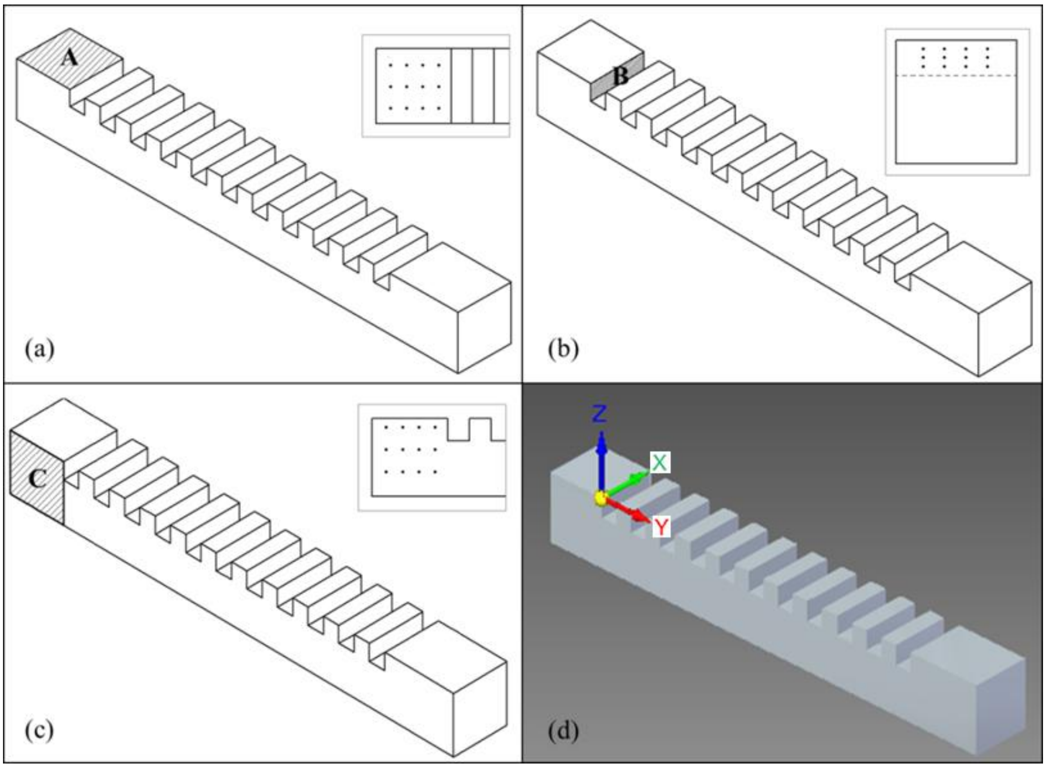

Figure 3.4 *The alignment system. (a) – (c): reference planes A, B and C defined by 12 points respectively (d) the origin is defined by the intersection point of these three reference planes.*

As demonstrated in Fig 3.4, the common 3-2-1 alignment method is chosen for aligning the workpiece for the following measurement tasks. The x-y plane is defined by 12 points (plane A); the x-axis is defined by the intersection between plane A and B; the origin is placed at the intersection point of the three reference planes (plane A, B and C).

3.1.3 Equipment for obtaining reference measurements

In order to obtain traceable and reliable reference measurement values, all step gauges are calibrated on a Mitutoyo FN905 tactile CMM (Fig 3.5). A Ø0.6 mm tactile probe was chosen for performing the corresponding measurement task. The applied software is COSMOS V2.2.

Figure 3.5 *Measurement equipment and clamping method for performing the reference measurement*

The CMM manufacturer specified a one-dimensional length measuring accuracy: $u_1 = (4.2 + L / 200)$ µm, with L in mm, for each axis. To verify the measurement accuracy of the tactile CMM, three end gauges have been measured five times; the measurement results are shown in Table 3.2.

Gauge block reference value (mm)	Average of five CMM measurements (mm)	Error (mm)	Standard deviation (mm)
10.000	10.000	0.000	0.0005
20.000	20.001	0.001	0.0006
30.000	29.999	-0.001	0.0005

Table 3.2 *Verification of tactile CMM measurement accuracy using Mitutoyo Grade 0 gauge blocks. The specified dimensional tolerances for 10mm, 20mm and 30mm gauge blocks are: ±0.12 µm, ±0.14 µm and ±0.20 µm.*

As shown in Table 3.2, the average CMM measurement values (five times repetition) are compared with the nominal dimensions of the end gauges. The maximum error is 1 µm on a 20 mm measurement length and the standard deviation of repeating the same measurement task five times is around 0.5 µm. All measurement results are within the declared accuracy range.

Moreover, an extended measurement repeatability test was also performed using the aluminum step gauge. Fig 3.6 indicates the definition of measurands on the step gauge. 11 planes are selected and each plane is defined by least square fitting of 12 equally spaced points. In total 10 plane distances (5 unidirectional and 5 bidirectional) are calculated using the x-y-z coordinates of the corresponding plane's center points.

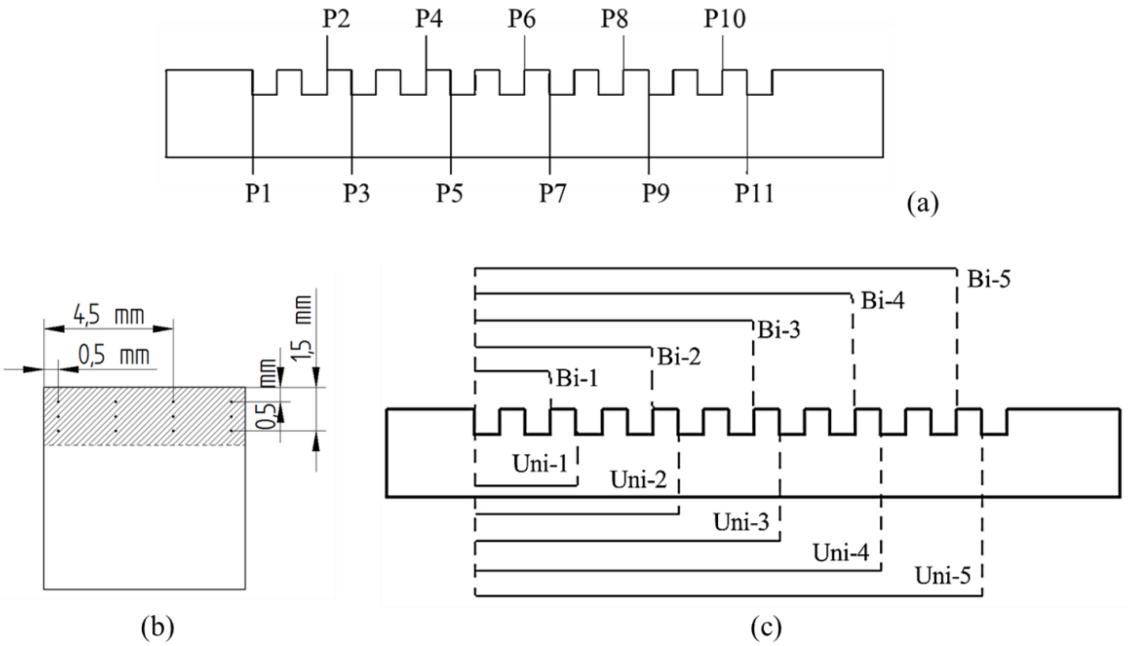

Figure 3.6 *measurand definition*

The aluminum step gauge is measured five times, the results are shown below:

Plane ID	Distance ID	Average distance (mm)	Distance measurement standard deviation (μm)	Fitting point standard deviation (μm)
P1				1.7
P2	Uni-1	8.0063	0.8	2.2
P3	Uni-2	16.0061	1.0	1.7
P4	Uni-3	24.0094	0.8	1.5
P5	Uni-4	32.0128	0.9	1.5
P6	Uni-5	40.0201	1.1	1.5
P7	Bi-1	6.0077	1.3	1.0
P8	Bi-2	14.0106	1.3	1.3
P9	Bi-3	22.0134	1.3	1.2
P10	Bi-4	30.0168	1.2	1.0
P11	Bi-5	38.0220	1.6	1.0

***Table 3.3** Repeatability test for the CMM reference measurement using the aluminum step gauge*

As seen in Table 3.3, the standard deviations of all distance measurements are within 2 μm. The fitting point standard deviations are also considerably low. Thus, the measurement results obtained on the Mitutoyo FN905 tactile CMM can be seen as the reference values for evaluating the corresponding CT measurements.

3.1.4 CT equipment and analysis software

The industrial CT system used for performing dimensional measurement tasks is a XT H 225 ST machine from Nikon Metrology, shown in Fig 3.7; more specifications of this device can be found in Table 3.5. The reconstruction software is CTPro (version XT 3.1.2 developed by Nikon Metrology) and the analysis software is VG Studio MAX 2.2 (developed by Volume Graphics).

Figure 3.7 *The used industrial CT system and workpiece fixation method*

Category	Specification
Accuracy (µm) (VDI/VDE 2630)	9+L/50 (L in mm)
Remark on the accuracy	Applies only to single material samples and on edge independent measurands with a maximum diameter of 250 mm and maximum height of 250 mm
Workpiece size (maximum)	Diameter 250 mm, Height 450 mm
Workpiece weight (maximum)	5 kg
Manipulator travel distance	X480 mm, Y450 mm, Z730 mm, R360 deg
Source to detector	1165 mm (nominal)
Detector	16 bit 4Mpixels (2000x2000 pixel)
Magnification	1.6x to 150x
Feature detectability (minimum)	2D radiography 2 µm
X-ray source	225 KV/225 W open tube
X-ray spot size	3 µm micro-focus
Radiation protection (DIN 54113-2, IRR99)	< 1 µSv/hr
Enclosure dimensions	W2214 mm x D1275 mm x H2205 mm

Table 3.5 *Specifications of the XT H 225 ST industrial CT system from Nikon Metrology*

As discussed earlier, the tactile CMM reference measurements use fitting planes through least square fitting of 12 well defined points; the plane distances are obtained by measuring the distances between center points of the corresponding planes. However, on the CT 3D model, the commonly applied plane fitting and plane distance measurement method follows a different approach. As illustrated in Fig 3.8, to define a plane, one can determine an area in which a large number (1000 as default) of points will be automatically fitted on the object's surface in a grid pattern. The final plane is obtained through least square fitting of these points. When measuring the distance between two planes, one plane is considered as finite while the other one is considered as infinitely extended. The mean value between minimum and maximum distances (orthogonal to the finite plane) will be the final plane distance. This approach has several advantages: first of all, using a large number of fitting points can eliminate the influence of surface noise and avoid making large errors caused by outliers. Secondly, defining fitting regions rather than particular points can avoid errors due to inaccurate alignment system. Thirdly, fitting plane by regions requires much less manual work than defining fitting points at specific positions.

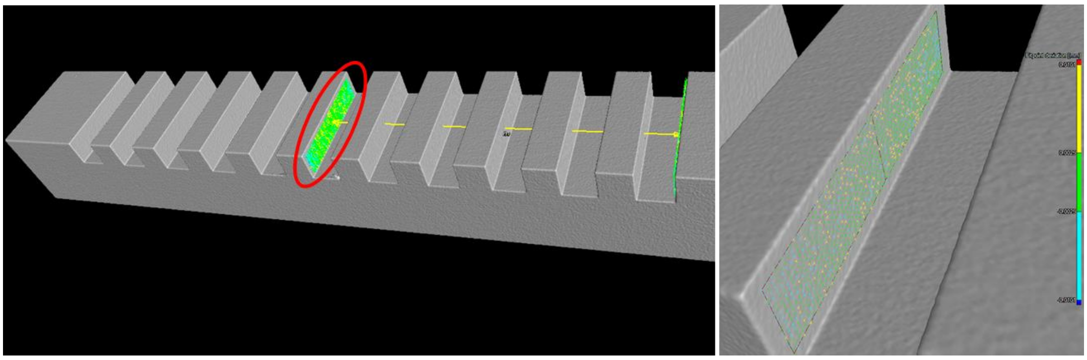

Figure 3.8 *Plane fitting and distance measurement in VG Studio MAX 2.2*

Three approaches are chosen to investigate the influence of different plane fitting and plane distance measuring methods:

<u>1. CT approach:</u> plane fitting using around 1000 points on a manually defined region. Plane distance is defined as the mean value between the minimum and maximum distances from one plane (finite) to the other (infinite).

<u>2. Combining CT and CMM approaches:</u> each plane is obtained by least square fitting through 12 pre-defined fitting points. Plane distance is defined as the mean between the minimum and maximum distances from one plane (finite) to the other (infinite).

<u>3. CMM approach:</u> each plane is obtained by least square fitting through 12 pre-defined fitting points. Plane distance is obtained by measuring the distance between the center points of two planes.

11 planes and 10 plane distances (as indicated in Fig 3.6 a and c) are measured using the above mentioned approaches on the CT 3D model of the aluminum step gauge. The measurement results are listed in Table 3.6:

Unit: mm	Approach Nr. 1	Approach Nr. 2	Approach Nr. 3
Uni-1	8.010	8.010	8.010
Uni-2	16.018	16.018	16.018
Uni-3	24.026	24.027	24.027
Uni-4	32.033	32.033	32.033
Uni-5	40.042	40.041	40.041
Bi-1	6.005	6.005	6.005
Bi-2	14.013	14.014	14.014
Bi-3	22.021	22.020	22.020
Bi-4	30.028	30.029	30.029
Bi-5	38.036	38.036	38.036

Table 3.6 *Comparing plane distance measurement results obtained by three different approaches*

As shown in Table 3.6, the plane distance measurements using different approaches coincide. The maximum deviation among 10 plane distance measurements is within 1 μm. Thus, there are no significant differences between the three approaches. Approach Nr.1 (CT approach) was chosen due to its high efficiency (less time consuming).

A measurement repeatability test was performed using the aluminum step gauge. It was scanned three times: one scan was performed on Oct 7th 2013 and two other scans were performed on Oct 8th 2013. The step gauge was taken out of the machine and re-clamped for each scan. The major machine settings are listed below:

Material	Voltage (kV)	Current (μA)	Filter	Nr. of projections	Voxel size (μm)	Orientation
Aluminum	205	225	1.5mm copper	3142	40	45 °inclined

Table 3.7 *Machine settings for the repeatability test*

To keep the processing procedure identical for all scans, beam hardening correction was excluded during reconstruction and local adaptive thresholding (using 50% isosurface as starting contour) was applied.

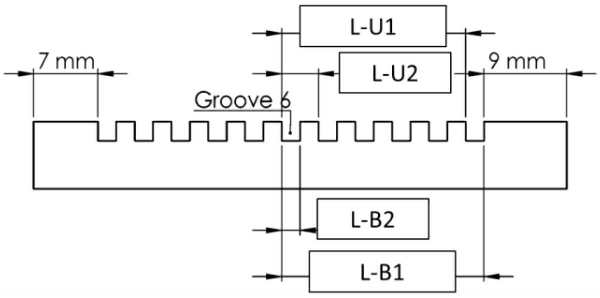

Figure 3.9 *The selected plane distances for the repeatability test [Angel J., 2014]*

As indicated in Fig 3.9, two unidirectional and two bidirectional plane distances were used to check the repeatability of CT dimensional measurements. Two terms were investigated: repeatability of measuring a certain feature several times in VG Studio MAX 2.2 (M1, 2 and 3) and repeatability of performing the same scan several times (Scan Nr.1, 2 and 3). The results are shown in Table 3.8:

Plane distance	Scan ID	Repeat measurements in VG Studio MAX 2.2				
		M1	M2	M3	Average (mm)	Stdev (mm)
L-U1	1	20.0193	20.0195	20.0197	20.0195	0.0002
	2	20.0197	20.0195	20.0197	20.0196	0.0001
	3	20.0196	20.0196	20.0196	20.0196	0.0000
Standard deviation of the average values of three CT scans						0.0001
L-U2	1	4.0035	4.0038	4.0036	4.0036	0.0002
	2	4.0034	4.0035	4.0037	4.0035	0.0002
	3	4.0038	4.0037	4.0037	4.0037	0.0001
Standard deviation of the average values of three CT scans						0.0001
L-B1	1	22.0175	22.0165	22.0179	22.0173	0.0007
	2	22.0171	22.0168	22.0173	22.0171	0.0003
	3	22.0175	22.017	22.0173	22.0173	0.0003
Standard deviation of the average values of three CT scans						0.0001
		M1	M2	M3	Average (mm)	Stdev (mm)
L-B2	1	1.9985	1.9978	1.9977	1.9980	0.0004
	2	1.9983	1.9982	1.9982	1.9982	0.0001
	3	1.9983	1.9978	1.9979	1.9980	0.0003
Standard deviation of the average values of three CT scans						0.0001

Table 3.8 *Measurement results for the repeatability test*

It can be seen that the CT measurements performed on the aluminum step gauge are highly repeatable; the standard deviations of repeating measurements in VG Studio MAX 2.2 and of different CT scans are both below 1 µm.

3.1.5 Raw measurement results

The CMM reference measurement results are listed in Table 3.9 and 3.10.

Fitting point standard deviation (µm)											
Plane ID	P1	P2	P3	P4	P5	P6	P7	P8	P9	P10	P11
Steel	1.7	1.7	1.7	1.7	1.7	1.4	1.4	1.4	2.2	1.4	1.4
Aluminum	1.7	1.7	1.7	1.5	1.5	1.5	1.0	1.4	1.2	1.0	1.0
PPS	1.4	1.7	2.0	2.0	2.0	1.4	2.0	2.0	2.0	1.4	3.2
PEEK	2.2	1.7	1.7	2.2	2.0	1.7	2.0	1.0	2.0	2.0	1.4

***Table 3.9** CMM reference measurements part one: fitting point standard deviation*

Plane distance (mm)										
Distance ID	Uni-1	Uni-2	Uni-3	Uni-4	Uni-5	Bi-1	Bi-2	Bi-3	Bi-4	Bi-5
Steel	7.999	16.007	23.993	31.999	40.001	6.003	14.003	22.008	30.002	38.002
Aluminum	8.006	16.006	24.009	32.013	40.020	6.008	14.011	22.013	30.017	38.022
PPS	8.002	16.004	24.003	32.005	40.020	6.015	14.015	22.016	30.016	38.024
PEEK	7.995	15.994	23.990	31.987	39.984	6.004	13.999	21.998	29.992	37.991

***Table 3.10** CMM reference measurements part two: plane distance*

In order to investigate the influences of object's material composition, orientation and their correlations, most of the step gauges were scanned at three different inclination angles (0 °, 90 °and 45 °as shown in Fig 3.10). Due to power limitation, it was only possible to scan the steel step gauge at two inclination angles: 90 °and 45 °. The detailed CT scan machine settings can be found in Table 3.11.

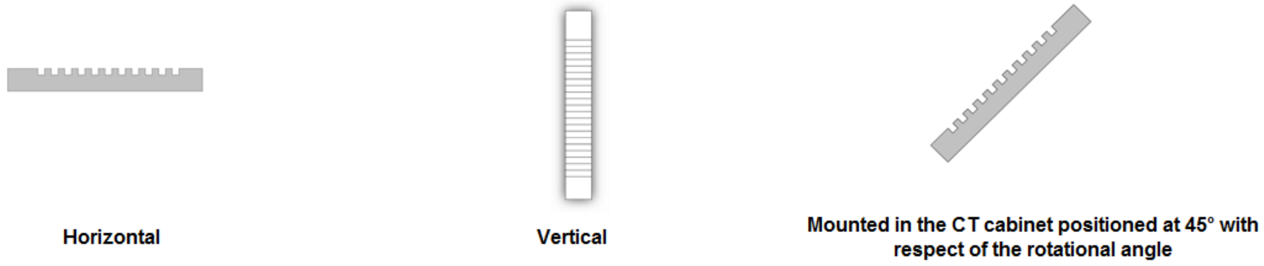

Horizontal

Vertical

Mounted in the CT cabinet positioned at 45° with respect of the rotational angle

***Figure 3.10** The tested orientations; from left to right: 0 °, 90 °and 45 °[Jais Angel, 2014]*

Material	Voltage (kV)	Current (µA)	Filter	Voxel size (µm)
Steel	220	300	2mm copper	40
Aluminum	205	225	1.5mm copper	40
PPS	100	170	none	40
PEEK	100	150	none	40

***Table 3.11** Main machine settings for scanning the step gauges*

The raw CT measurement results are listed in Table 3.12 and 3.13. Prior to the analysis, these data need to be treated with voxel size and edge offset correction (as described in the next section). Nevertheless, it can be noticed from Table 3.12 that the fitting point standard deviation of steel and aluminum gauge blocks scanned under 90 ° is significantly higher than them scanned under other angels.

Fitting point standard deviation (µm)											
Plane ID	P1	P2	P3	P4	P5	P6	P7	P8	P9	P10	P11
Steel – 90 °	**5.4**	4.1	2.4	2.8	4.2	4.4	3.5	3.7	2.2	2.2	2.2
Steel – 45 °	1.4	1.4	1.4	1.7	1.7	1.7	1.4	1.7	1.7	1.7	1.4
Aluminum – 90 °	**3.3**	2.4	1.7	2.0	2.2	2.2	2.6	2.2	2.4	1.7	2.2
Aluminum – 45 °	1.4	1.4	1.7	1.7	1.7	1.7	1.4	1.4	1.4	1.7	1.4
Aluminum – 0 °	1.4	1.7	1.7	1.7	1.7	1.4	1.4	1.4	1.4	1.7	1.4
PPS – 90 °	**2.6**	2.0	1.7	2.0	1.7	1.7	1.7	1.4	1.7	2.4	1.4
PPS – 45 °	1.7	2.0	2.0	2.0	2.0	2.0	1.7	1.7	1.7	1.7	1.4
PPS – 0 °	1.7	2.0	1.7	2.0	2.0	1.7	1.7	1.7	1.7	1.7	1.7
PEEK – 90 °	2.0	1.7	1.7	2.0	1.7	1.7	1.7	1.7	1.7	1.7	1.7
PEEK – 45 °	1.4	1.4	1.4	1.7	1.4	1.4	1.4	1.4	1.4	1.4	1.4
PEEK – 0 °	1.7	1.7	1.7	1.7	1.7	1.7	1.4	1.7	1.4	1.4	1.7

Table 3.12 *CT measurement result part one: fitting point standard deviation*

Plane distance (mm)										
Distance ID	Uni-1	Uni-2	Uni-3	Uni-4	Uni-5	Bi-1	Bi-2	Bi-3	Bi-4	Bi-5
Steel 90 °	7.972	15.972	23.983	31.991	39.998	5.917	13.947	21.977	29.978	37.970
Steel 45 °	8.006	16.012	24.017	32.022	40.028	5.996	14.002	22.007	30.011	38.017
Aluminum 90 °	7.998	16.016	24.043	32.049	40.027	5.989	14.002	22.029	30.043	38.022
Aluminum 45 °	8.010	16.018	24.026	32.033	40.042	6.005	14.013	22.021	30.028	38.036
Aluminum 0 °	8.010	16.018	24.025	32.032	40.042	6.004	14.013	22.020	30.027	38.035
PPS 90 °	8.005	16.018	24.029	32.040	40.050	5.998	14.007	22.016	30.024	38.034
PPS 45 °	8.005	16.008	24.010	32.014	40.019	5.994	13.997	22.000	30.003	38.008
PPS 0 °	8.004	16.006	24.008	32.010	40.016	5.993	13.995	21.998	30.000	38.006
PEEK 90 °	8.002	16.004	24.001	31.993	39.990	5.995	13.995	21.993	29.986	37.983
PEEK 45 °	8.004	16.004	24.001	31.997	39.994	5.997	13.996	21.993	29.990	37.987
PEEK 0 °	8.002	16.000	23.997	31.993	39.991	5.990	13.988	21.985	29.981	37.978

Table 3.13 *CT measurement result part two: plane distance*

3.1.6 Processing method for the raw CT measurement data

Before further analyzing the measurement results, the raw CT measurement data first need to be rescaled. This is a necessary step because the calculated voxel size often deviates from its real dimension due to potential errors involved in the X-ray source – rotation table – X-ray detector distance calibration. Most voxel size correction artefacts use calibrated center distances between spheres (Fig 3.11) because these distances are not affected by the thresholding errors.

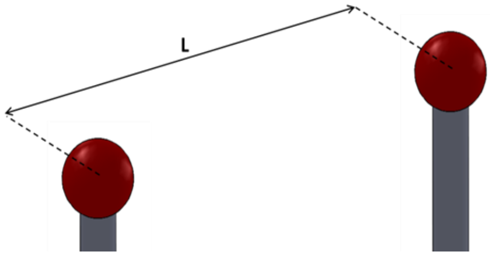

Figure 3.11 *Demonstration of sphere center distance to be used for voxel size correction [Jais Angel, 2014]*

Nevertheless, as discussed in Section 3.1.1, each step gauge contains many unidirectional distances. In this case, it is favorable to use these unidirectional features for self-calibration. The voxel size calibration will be repeated for scans of each material under each orientation. In this way, the potential errors due to differences in objects' scan conditions and material compositions can be avoided. In addition, it is also more efficient since no extra rescaling CT scan (scanning the calibration artefact) is required.

To minimize random influences, all five unidirectional distances are used to calculate the scaling factors for each CT scan. Under the assumption that there are no systematic errors present on the unidirectional distances, the CT and CMM measured values will fit with the formula:

$$\text{Value}_{\text{CT}} = \text{F} \times \text{Value}_{\text{CMM}} \qquad (1)$$

"F" is a constant factor (close to 1) and equals the inverse of the scaling factor. Fig 3.12 illustrates how the value "F" is obtained: the CT measured unidirectional distances (Y-axis) are plotted against their CMM reference values (X-axis). A linear regression going through the origin (0, 0) is performed. The first order coefficient will be taken as the inverse scaling factor "F". The new CT value is calculated following the formula:

$$\text{Value}_{\text{CT, new}} = \text{Value}_{\text{CT, old}} / \text{F} \qquad (2)$$

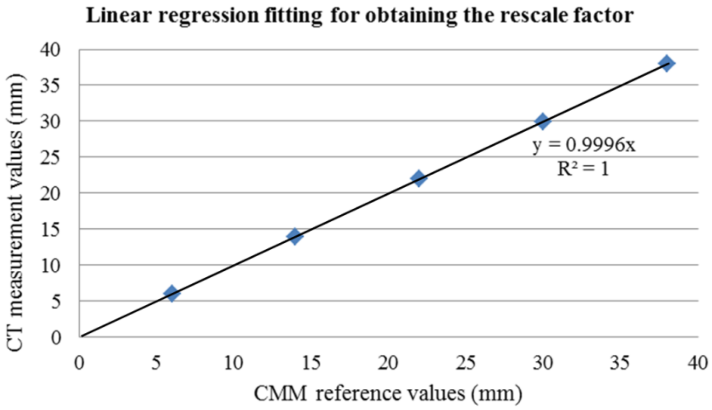

Figure 3.12 *Example of the linear regression fitting between CT and CMM measured values for calculating the inverse scaling factor "F"*

Since all unidirectional distances include plane Nr.1, this can be a potential risk of including systematic error in case plane Nr.1's fitting quality differs significantly from other planes. The Quartile (Fourth-Spread or 75% two-sided interval) method *[Devore J.L., 2000]* was used to quantitatively evaluate the fitting qualities (variation on fitting points) of all planes for both CT and CMM measurements; the detected outliers are marked in red in Table 3.9 and 3.12. If any of P3, P5, P7, P9 or P11 is detected as outlier due to bad fitting quality, the involved unidirectional distance will be excluded from the linear regression analysis. In case P1 is detected as an outlier, the linear regression analysis needs to be adapted because the potential error caused by P1's bad fitting quality will be included for all distance measurements. Thus, the linear regression analysis between CT measured unidirectional plane distances and their CMM reference values should also include a constant term which describe the error (it is seen as "systematic" because this error will be present for any plane distances involving P1) caused by P1's bad fitting quality:

$$\text{Value}_{\text{CT}} = \text{F} \times \text{Value}_{\text{CMM}} + \text{C} \qquad (3)$$

"F" still stands for the reverse scaling factor, meanwhile a constant term "C" is introduced to describe the "systematic" error caused by the bad fitting quality of P1. The new CT measurement value is calculated following the formula:

$$\text{Value}_{\text{CT, new}} = (\text{Value}_{\text{CT, old}} - \text{C}) / \text{F} \qquad (4)$$

After voxel size correction, a further data treatment was performed. As mentioned earlier, systematic edge offset errors are present on the bidirectional distance measurements. It can be calculated by taking the average of the differences between CT measured bidirectional distances and their CMM reference values. The next step is to subtract this edge offset term from the CT measured bidirectional distances. Similarly, if a plane is proven to be an outlier due to its bad fitting quality, the corresponding bidirectional distance will be excluded when calculating the edge offset term. The linear regression first order coefficients, constant terms (where applicable), and the bidirectional edge offset terms are listed in Table 3.14.

CT scan ID	Constant term for linear fitting (µm)	Linear coefficient	Bidirectional edge offset term (µm)
Steel - 90 °	-33.4	1.0008	-30.2
Steel - 45 °	---	1.0007	-12.5
Aluminum - 90 °	24.1	0.9999	-19.1
Aluminum - 45 °	---	1.0006	-7
Aluminum - 0 °	---	1.0006	-7.6
PPS - 90 °	-7.5	1.0013	-22.6
PPS - 45 °	---	1.0003	-23.6
PPS - 0 °	---	1.0002	-23.1
PEEK - 90 °	---	1.0003	-12.8
PEEK - 45 °	---	1.0004	-12.9
PEEK - 0 °	---	1.0002	-16.5

Table 3.14 *Rescaling and bidirectional edge offset term calculation results for all CT scans*

3.1.7 Data analysis

After voxel size and edge error correction, all CT dimensional measurements are compared with their corresponding CMM reference values. The results are arranged for revealing influences of object's material composition (Fig 3.13), orientation and planes' fitting quality (Fig 3.14).

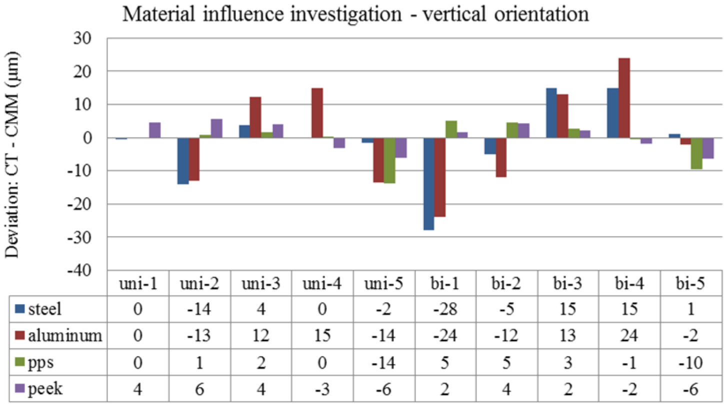

	uni-1	uni-2	uni-3	uni-4	uni-5	bi-1	bi-2	bi-3	bi-4	bi-5
■ steel	0	-14	4	0	-2	-28	-5	15	15	1
■ aluminum	0	-13	12	15	-14	-24	-12	13	24	-2
■ pps	0	1	2	0	-14	5	5	3	-1	-10
■ peek	4	6	4	-3	-6	2	4	2	-2	-6

(a)

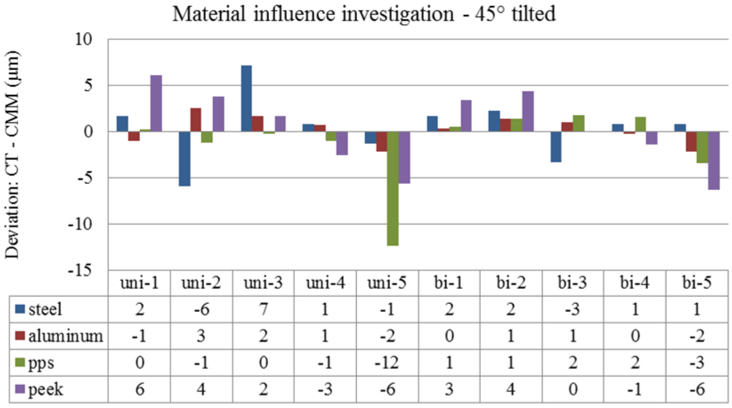

	uni-1	uni-2	uni-3	uni-4	uni-5	bi-1	bi-2	bi-3	bi-4	bi-5
■ steel	2	-6	7	1	-1	2	2	-3	1	1
■ aluminum	-1	3	2	1	-2	0	1	1	0	-2
■ pps	0	-1	0	-1	-12	1	1	2	2	-3
■ peek	6	4	2	-3	-6	3	4	0	-1	-6

(b)

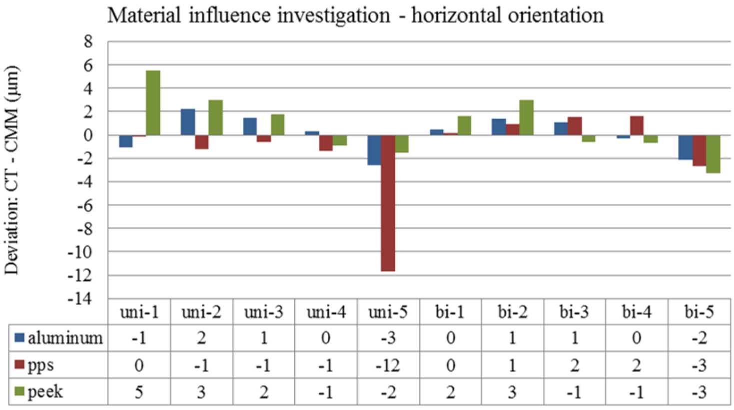

	uni-1	uni-2	uni-3	uni-4	uni-5	bi-1	bi-2	bi-3	bi-4	bi-5
🟦 aluminum	-1	2	1	0	-3	0	1	1	0	-2
🟥 pps	0	-1	-1	-1	-12	0	1	2	2	-3
🟩 peek	5	3	2	-1	-2	2	3	-1	-1	-3

(c)

Figure 3.13 *Influence of object's orientation: comparison between CT dimensional measurement results and tactile CMM measured reference values. Notice that the steel step gauge cannot be successfully scanned horizontally due to the power limitation of the CT scanner*

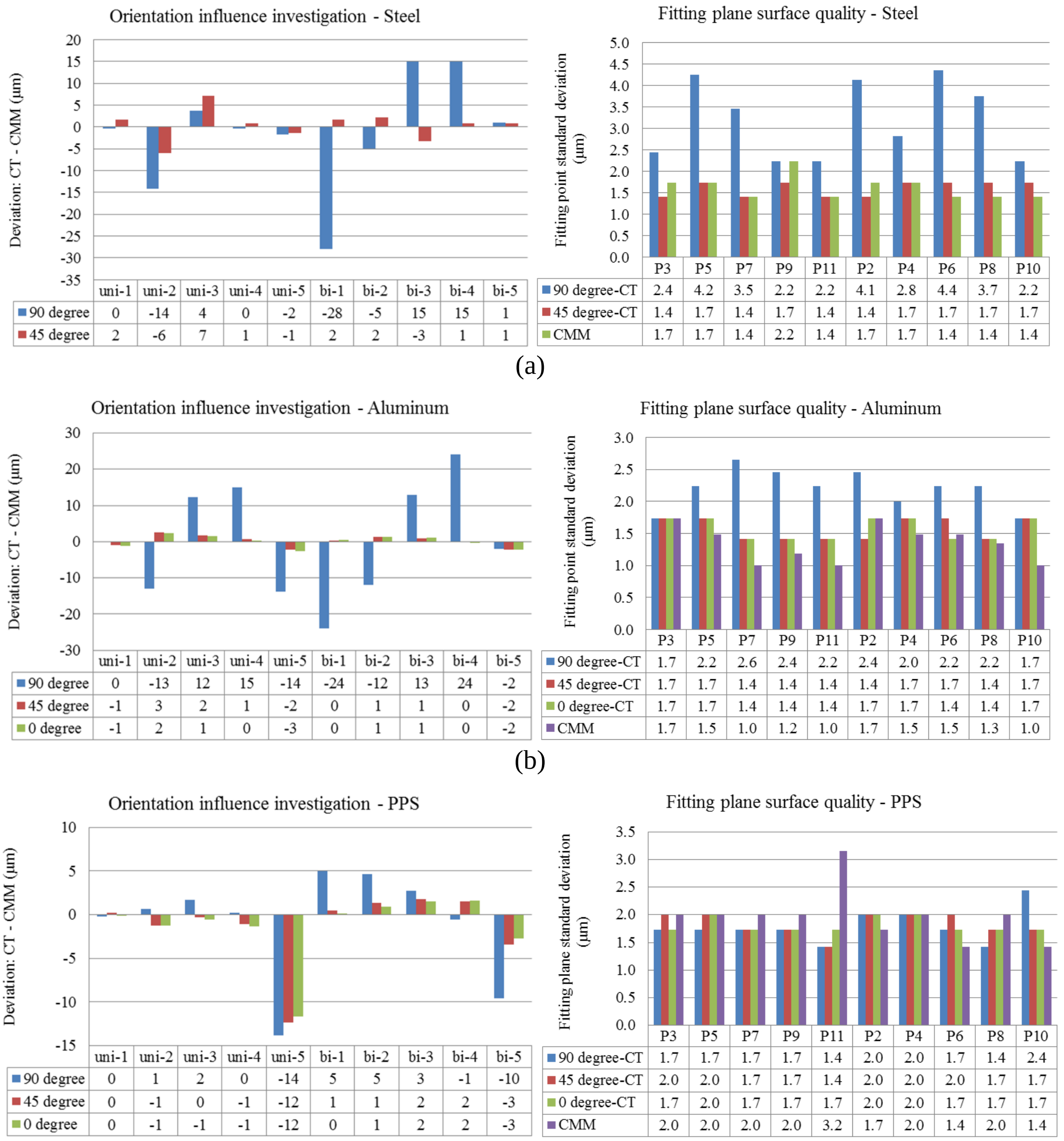

	uni-1	uni-2	uni-3	uni-4	uni-5	bi-1	bi-2	bi-3	bi-4	bi-5
🟦 90 degree	0	-14	4	0	-2	-28	-5	15	15	1
🟥 45 degree	2	-6	7	1	-1	2	2	-3	1	1

	P3	P5	P7	P9	P11	P2	P4	P6	P8	P10
🟦 90 degree-CT	2.4	4.2	3.5	2.2	2.2	4.1	2.8	4.4	3.7	2.2
🟥 45 degree-CT	1.4	1.7	1.4	1.7	1.4	1.4	1.7	1.7	1.7	1.7
🟩 CMM	1.7	1.7	1.4	2.2	1.4	1.7	1.7	1.4	1.4	1.4

(a)

	uni-1	uni-2	uni-3	uni-4	uni-5	bi-1	bi-2	bi-3	bi-4	bi-5
🟦 90 degree	0	-13	12	15	-14	-24	-12	13	24	-2
🟥 45 degree	-1	3	2	1	-2	0	1	1	0	-2
🟩 0 degree	-1	2	1	0	-3	0	1	1	0	-2

	P3	P5	P7	P9	P11	P2	P4	P6	P8	P10
🟦 90 degree-CT	1.7	2.2	2.6	2.4	2.2	2.4	2.0	2.2	2.2	1.7
🟥 45 degree-CT	1.7	1.7	1.4	1.4	1.4	1.4	1.7	1.7	1.4	1.7
🟩 0 degree-CT	1.7	1.7	1.4	1.4	1.4	1.7	1.7	1.4	1.4	1.7
🟪 CMM	1.7	1.5	1.0	1.2	1.0	1.7	1.5	1.5	1.3	1.0

(b)

	uni-1	uni-2	uni-3	uni-4	uni-5	bi-1	bi-2	bi-3	bi-4	bi-5
🟦 90 degree	0	1	2	0	-14	5	5	3	-1	-10
🟥 45 degree	0	-1	0	-1	-12	1	1	2	2	-3
🟩 0 degree	0	-1	-1	-1	-12	0	1	2	2	-3

	P3	P5	P7	P9	P11	P2	P4	P6	P8	P10
🟦 90 degree-CT	1.7	1.7	1.7	1.7	1.4	2.0	2.0	1.7	1.4	2.4
🟥 45 degree-CT	2.0	2.0	1.7	1.7	1.4	2.0	2.0	2.0	1.7	1.7
🟩 0 degree-CT	1.7	2.0	1.7	1.7	1.7	2.0	2.0	1.7	1.7	1.7
🟪 CMM	2.0	2.0	2.0	2.0	3.2	1.7	2.0	1.4	2.0	1.4

(c)

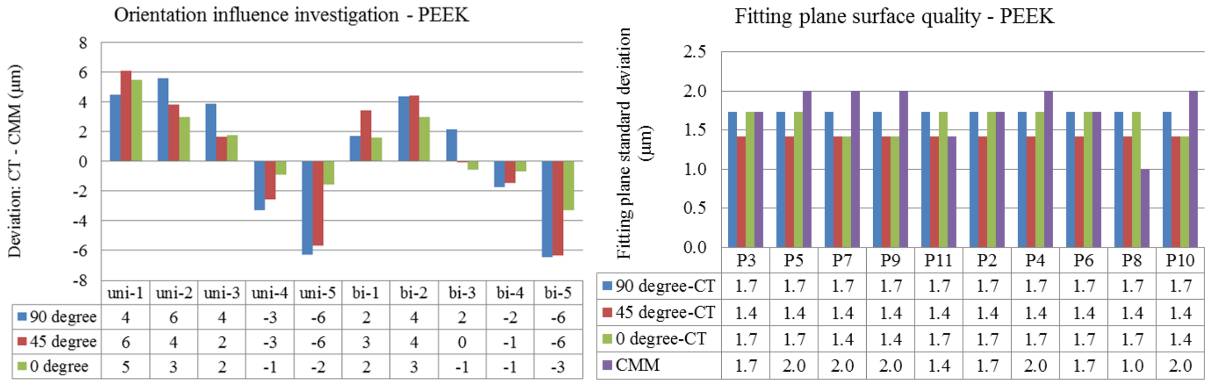

	uni-1	uni-2	uni-3	uni-4	uni-5	bi-1	bi-2	bi-3	bi-4	bi-5
🟦 90 degree	4	6	4	-3	-6	2	4	2	-2	-6
🟥 45 degree	6	4	2	-3	-6	3	4	0	-1	-6
🟩 0 degree	5	3	2	-1	-2	2	3	-1	-1	-3

	P3	P5	P7	P9	P11	P2	P4	P6	P8	P10
🟦 90 degree-CT	1.7	1.7	1.7	1.7	1.7	1.7	1.7	1.7	1.7	1.7
🟥 45 degree-CT	1.4	1.4	1.4	1.4	1.4	1.4	1.4	1.4	1.4	1.4
🟩 0 degree-CT	1.7	1.7	1.4	1.4	1.7	1.7	1.7	1.7	1.7	1.4
🟪 CMM	1.7	2.0	2.0	2.0	1.4	1.7	2.0	1.7	1.0	2.0

(d)

Figure 3.14 *Influence of object's material composition: comparison between CT dimensional measurement results, plane's fitting point standard deviation and the tactile CMM measured reference values. Notice that the steel step gauge cannot be successfully scanned horizontally due to the power limitation of the CT scanner*

Several effects related to object's material compositions and orientations can be observed from Table 3.14, Fig 3.13 and 3.14:

1. Table 3.14 shows that scanning the steel and aluminum step gauges vertically will result in much higher bidirectional edge errors than scanning them with other orientations. Such trend is not present when scanning the PPS and PEEK step gauges.

2. Fig 3.13 shows two aspects regarding the material influence. On one hand, Fig 3.13 (a) indicates that the measurement results of the steel and aluminum step gauges, when scanned vertically, are significantly worse than the results of PPS and PEEK step gauges. Thus, when scanning vertically, material composition is an important influence factor. On the other hand, no clear differences can be found between the measurement results of different step gauges from Fig 3.13 (b) – when scanned at 45 ° and (c) – when scanned horizontally.

3. As shown in Fig 3.14, except for the PEEK step gauge, scanning the other step gauges vertically all lead to much larger dimensional deviations than the other orientation. For example, the error range increased from 6 µm to nearly 30 µm for steel step gauge, from 5 µm to 25 µm for aluminum step gauge, and from 5 µm to 10 µm for PPS step gauge (except for the deviations of Uni-5 distance). More importantly, combining the information of planes' fitting quality, it is clearly shown that the magnitudes of dimensional deviations are closely related to planes' fitting quality. When a plane's fitting points have larger variations, the corresponding plane distance measurement also tends to deviate more from its reference value.

3.1.8 Conclusions

The conclusions from the above investigations can be summarized as follows:

- The orientation of the workpiece and of the measurands is important in CT metrology, especially for heavily absorbing workpiece materials. This relates, on the one hand, to the maximum penetration lengths, and, on the other hand, to the orientation of flat surfaces. The latter should not be positioned perpendicular to the rotational axis of the rotation stage, which would imply that they would be approximately parallel to the incident X-ray beam in all projections throughout the full 360 ° rotation (Fig 3.15).

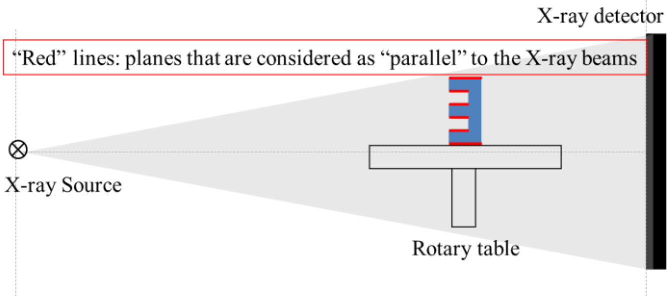

Figure 3.15 *Illustration of the planes that are "parallel" to the incident X-ray beams throughout the entire rotating process*

- A feature's fitting point deviation (on the 3D CT model) is a good indicator for the uncertainty of corresponding dimensional measurements
- The tested step gauges can be applied as reference objects for calibrating CT scans of other objects which have the same material compositions. Both the voxel size rescaling factor and thresholding edge offset terms can be easily obtained.

3.2 Influence of the surface roughness

3.2.1 Theoretical assumptions

Surface roughness is an important workpiece property which is quantified by the vertical deviations of a real surface from its ideal form *[Whitehouse D., 2012]*. It is typically considered to be the high-frequency, short-wavelength component of a measured surface (Fig. 3.16).

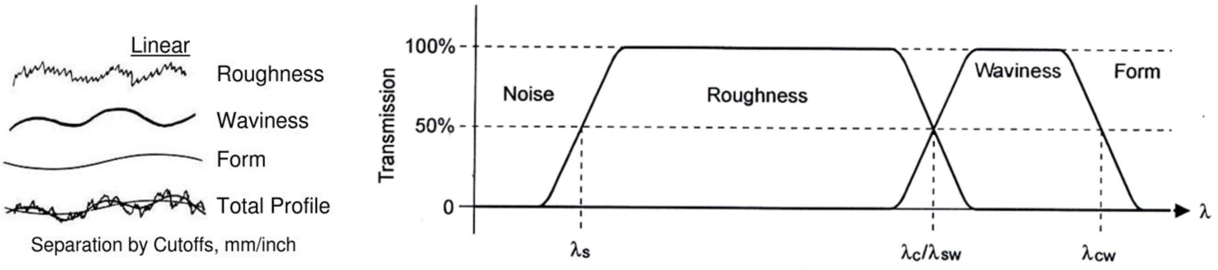

(a) (b)

Figure 3.16 *(a) Basic components & elements of surface topography; (b) surface components separated by their wavelength [http://www.metrologycenter.com/]*

In daily practice, tactile CMM is often taken as the reference method for evaluating the accuracy and traceability of CT dimensional measurements. However, there are fundamental differences between these two techniques regarding structural resolution, feature fitting and data filtration. On the one hand, the touching probes that are commonly available for tactile CMMs have diameters ranging from 10mm to 0.5mm, which also defines the available structural resolution. On the other hand, the structural resolution of nowadays industrial CT devices can reach up to micron or even nano level. Secondly, tactile CMM measurements usually use very limited number of fitting points (normally under 30 points) for defining standard features; on the contrary, defining features on the CT 3D model often takes around 1000 fitting points. As a result, the limited structural resolution and number of fitting points when measuring with tactile CMM serve as a natural filter which can filter out high frequency surface elements, such as roughness; meanwhile, micron level structural resolution and large number of fitting points allow industrial CT system to capture small details from the object's surface, inherent surface noise on the 3D CT model can as well influence the form error values. These often lead to an "underestimation" of the CMM measured form error when comparing with the corresponding CT measured value. Examples of this trend can be found by analyzing the measurement reports of two inter-laboratory comparison projects (information about these two projects can be found in Chapter 1, Section 1.2.3). Within these projects, when compared with the tactile CMM "reference values", larger form errors were reported by all participants for measuring various audit objects using industrial CT systems.

Furthermore, the differences in the physical principles between tactile CMM and CT can lead to significant differences in their dimensional measurement results when handling objects with rough surfaces. As shown in Fig 3.17, when measuring an object that is manufactured by turning process, due to the relatively large probe size, the surface captured by tactile CMM "neglects" many details. Thus, the material edge defined by tactile CMM is inherently offsetted towards the "peaks". However, similar to other optical sensors, industrial CT is capable of capturing finer details of rough surfaces and the material edge defined by CT is at the average level between the peaks and valleys.

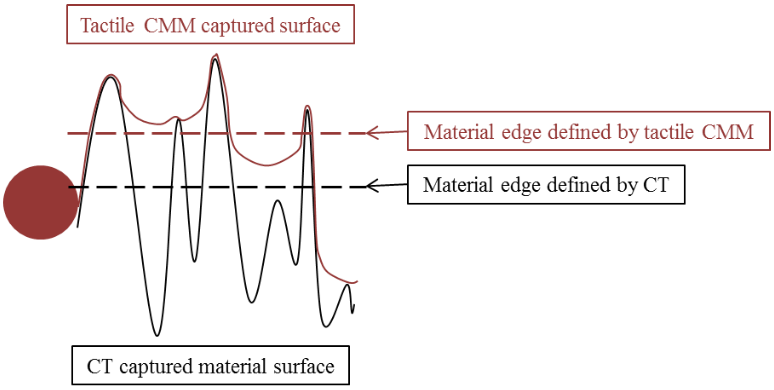

Figure 3.17 *Difference between tactile CMM and CT when measuring a rough surface. Notice that probe radius compensation has been applied to the CMM measurements*

3.2.2 Experimental verification of the influence of surface roughness

3.2.2.1 Workpiece description

Three aluminum cylinders are manufactured to experimentally investigate the influence of surface roughness on the differences between tactile CMM and CT dimensional measurements. As shown in Fig 3.18, each cylinder contains 5 sections with different surface roughness.

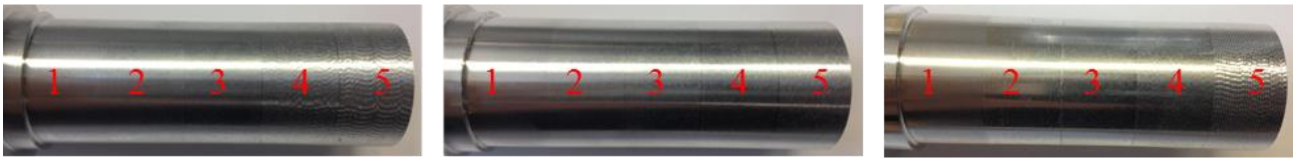

(a) (b) (c)

Figure 3.18 *Aluminum cylinders each contains 5 sections with different surface roughnesses.*

3.2.2.2 Initial data collection

The equipment used for measuring surface roughness is Taylor Hobson F47 (form talysurf series), which has a surface measuring resolution of 10 nanometers. On each cylinder, the surface roughness has been measured 3 times along 3 equal spacing lines, the angular space between two adjacent lines is 120 °. Three different surface roughness terms (R_a, R_z and R_p, illustrated in Fig 3.19) were measured, the cutoff length was set to be 0.8 mm. The measurement results are listed in Table 3.15.

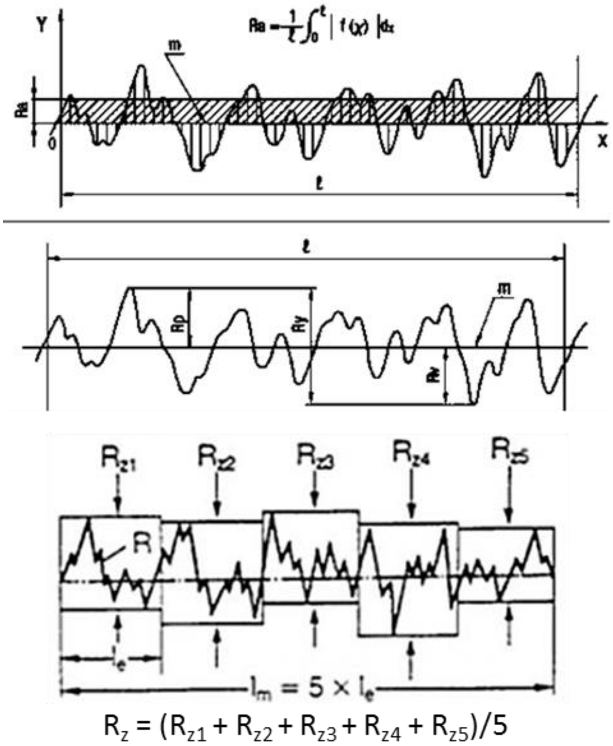

Figure 3.19 *Illustration of different surface roughness terms. R_a: Arithmetical mean of the sums of all profile values. R_z: Rz is the average between the "peak-to-valley" distances (Rzi) measured with 5 successive cut-off length(le). R_p: the peak value deviates from the mean profile line. [DIN EN ISO 4287:1998] [Nyembwe K. et al., 2012]*

Section ID	Cylinder a			Cylinder b			Cylinder c		
	R_a	R_z	R_p	R_a	R_z	R_p	R_a	R_z	R_p
	(µm)								
1	0.44	2.38	1.21	0.10	0.95	0.40	0.17	1.47	0.49
2	1.14	4.87	2.65	1.09	4.84	2.69	0.16	1.45	0.65
3	1.61	7.71	4.24	1.65	7.35	4.09	0.78	3.86	2.29
4	4.91	22.45	14.39	2.91	13.36	8.21	1.91	8.24	5.42
5	7.20	31.84	21.60	4.98	22.03	14.34	4.72	24.28	18.47

Table 3.15 *Surface roughness measurement results for each cylinder. The listed surface roughness are average values of three measurements performed along three equally spaced lines.*

Table 3.15 shows that, for each cylinder, the surface roughness increases while going from section 1 towards section 5. This trend holds true for all three surface roughness terms.

A Mitutoyo FN905 tactile CMM was used to measure these cylinders. Cylindrical features are repeatedly fitted (3 times) on each section of each cylinder using 20 fitting points per feature. The 20 points are equally distributed over 4 axial sections which cover the entire length of the cylinder with each section containing 5 fitted points (as indicated in Fig 3.20 (right)). In order to be comparable with CT measurements, the final features are refitted as cylinders using all 20 points. The diameters and form errors measured by tactile CMM are listed in the Appendix A, Table A1 – A3.

Subsequently, all three cylinders are scanned separately using the XT H 225 ST CT scanner from Nikon Metrology. More detailed information about the industrial CT system can be found in Section 3.1.4. The scanning conditions (Table 3.15) were kept identical in order to reduce the involved influence factors.

Voltage (kV)	Current (μA)	Filter	Voxel size	Target material
180	250	0.5mm copper	42.5	Tungsten

Table 3.15 *Main machine settings for scanning the aluminum cylinders*

The dimensional measurements on the CT 3D model was performed using VG Studio MAX 2.2. Cylindrical features are repeatedly fitted (5 times) on each section of each cylinder, their diameters and form errors are measured. Initially, 1000 points were used for each feature fitting (Fig 3.20 (left)), which was also the default setting provided by Volume Graphics (software provider). In order to study the influence of the number of fitting points, all feature fittings were repeated using only 20 points (Fig 3.20 (right), same number as the tactile CMM). The corresponding diameter and form error measurements can be found in Appendix A, Table A4 – A6.

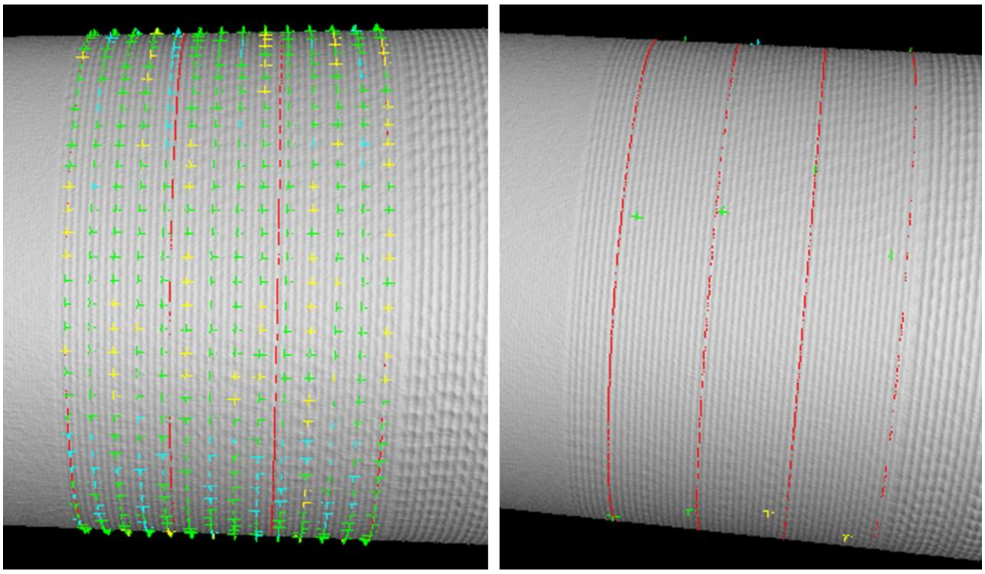

Figure 3.20 *cylindrical feature fitting at one section using 1000 points (a) and using 20 points*

It can be observed that the measured form errors follow a certain trend: CT measurements (1000 fitting points) > CT measurements (20 fitting points) > CMM measurements. As discussed earlier, this trend is primarily caused by the limited number of fitting points in the latter two cases. Meanwhile, part of the surface details are not detectable using tactile CMM due to its structural resolution which results in smaller measured form errors than CT even if they apply the same number of fitting points.

Furthermore, the standard deviation of repeating CT diameter measurements 5 times using 1000 fitting points is much lower than those using only 20 fitting points. Due to the noisy nature on the surfaces of the CT 3D model, there is a high chance of picking some “outlier” points while fitting a feature. The influence of these “outlier” points will be more significant when applying less fitting points.

3.2.2.3 Data analysis

A. Comparing edge profiles obtained by CT and Taylor Hobson F47

Fig 3.21 gives an example of cylinder a’s surface profile along one line, which sequentially passes through sections 1 to 5. Both the CT material edge and the surface raw profile measured by the Taylor Hobson F47 are shown.

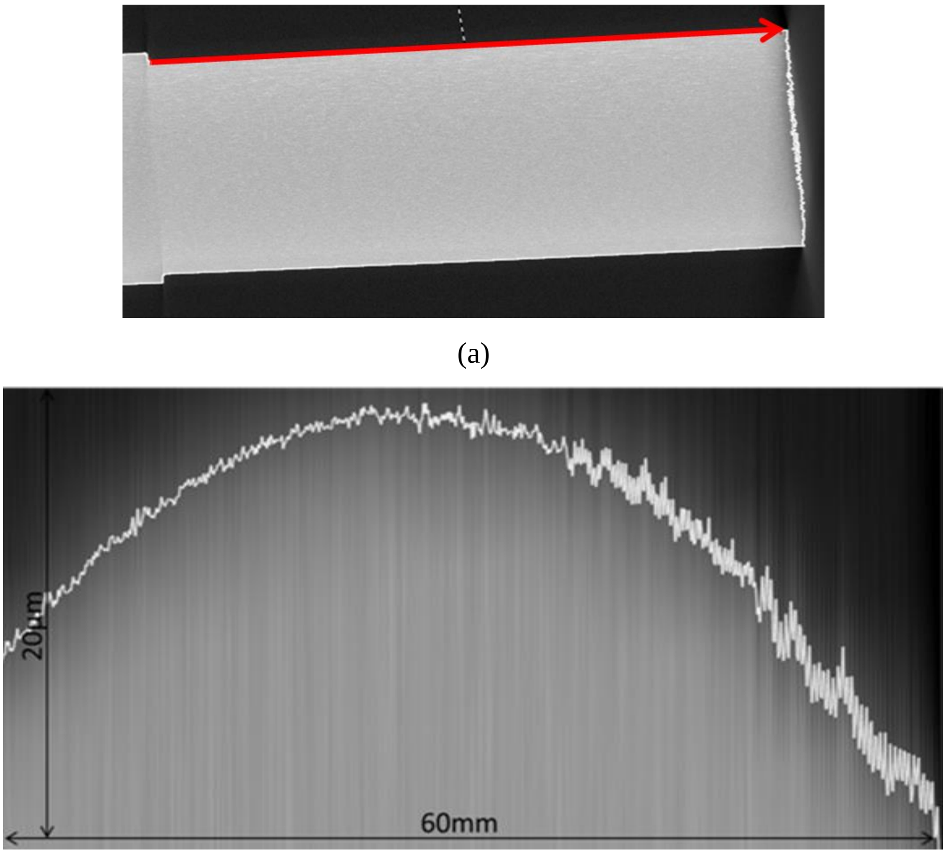

(a)

(b)

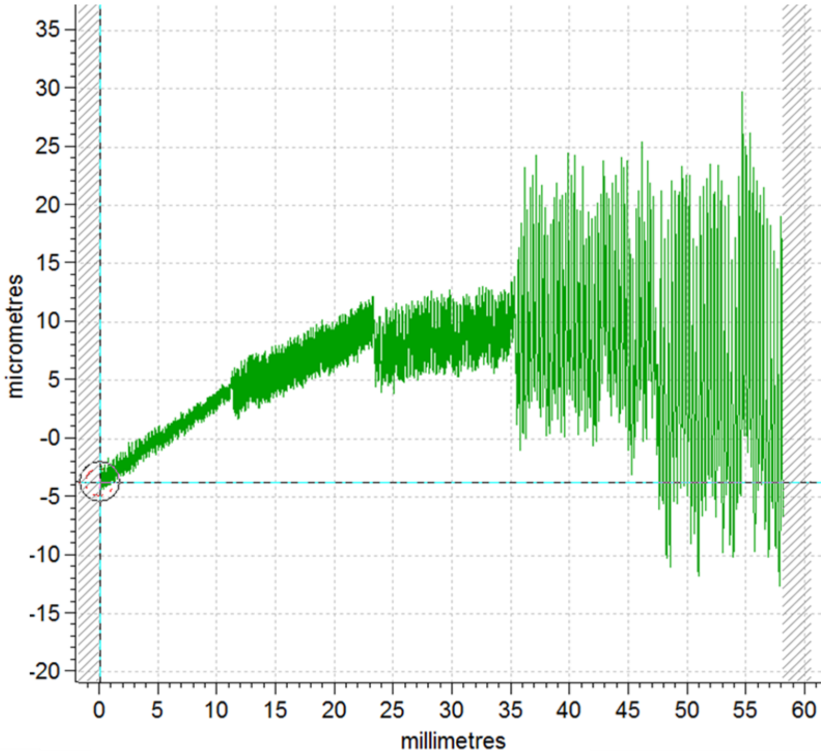

(c)

Figure 3.21 *Cylinder a's surface profile. (a) 2D CT reconstructed slice. The arrow line indicates the direction alone which the corresponding material edge/surface profiles are plotted; (b) Material edge of the CT 3D model along the "red line" in "a". Notice that, for the purpose of visualization, the figure has been enlarged in the vertical direction.(c) unfiltered profile obtained using the surface roughness measurement equipment (Taylor Hobson F47)*

Several conclusions can be drawn by comparing the surface profile plots in Fig 3.21:

1. The material edge of the CT 3D model and the surface profile obtained by Taylor Hobson F47 indicate similar trend. The surface roughness increases from section 1 towards section 5. This supports one of the previous assumptions: CT is capable of capturing small surface details (e.g. part of the surface roughness), which is fundamentally different from tactile CMM.
2. Comparing with Taylor Hobson F47's 10 nanometer resolution, the resolution of an industrial CT system is limited by many factors, such as the focal spot size, X-ray detector and the applied thresholding technique. Thus, due to the limitation of industrial CT's structural resolution, part of the high frequency surface components are naturally filtered out or reduced. For example, the differences between section 1, 2 and 3 are rather unclear in the CT gray value profile and the magnitude of surface variations on section 4 and 5 is also less when comparing with the profile obtained using Taylor Hobson F47. More importantly, the surface profile obtained by CT can be the result of both surface roughness and X-ray scattering noise. It is very difficult to clearly separate these effects and thus CT is not yet a reliable technique for measuring the surface roughness. Nevertheless, it has shown potential for evaluating the surface roughness qualitatively.

B. Comparing cylinder diameter and cylindricity measurements obtained by CT and tactile CMM

In order to investigate the influence of surface roughness and number of fitting points on the accuracy of CT dimensional measurements when compared with tactile CMM, the deviations of CT dimensional measurements (CT measured values minus tactile CMM measured values) are plotted against the corresponding surface roughness of each section on each cylinder. In addition, each feature was measured on the CT 3D model using both 1000 and 20 fitting points. Three different surface roughness terms (Ra, Rz and Rp) were used.

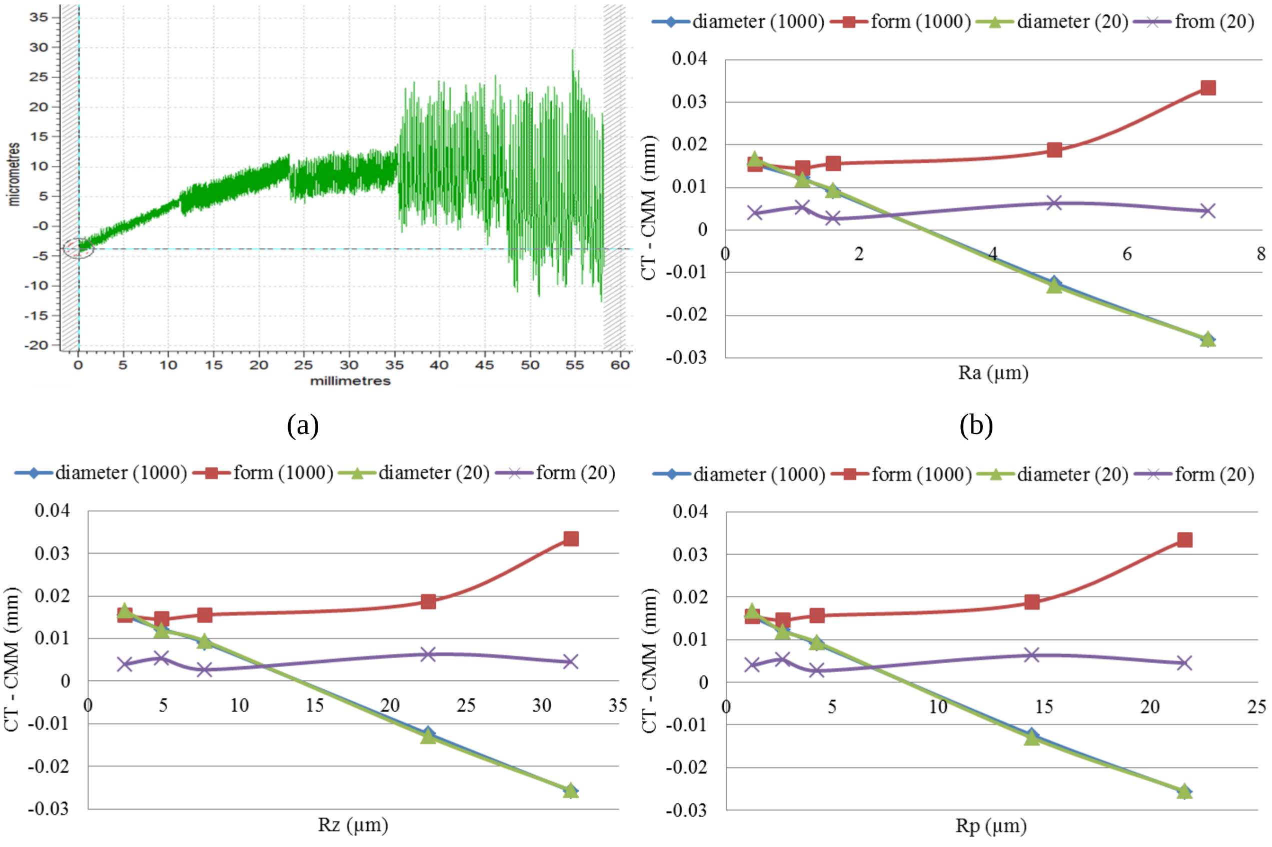

(a) (b)

(c) (d)

Figure 3.22 *Comparing cylinder a's diameter and form measurements obtained by CT and tactile CMM under different surface roughness conditions. Each CT measurements are repeated using both 1000 and 20 fitting points. (a) raw profile plot along a straight line on the surface of cylinder "a" (b) roughness term "Ra" is used for comparison (c) roughness term "Rz" is used for comparison (d) roughness term "Rp" is used for comparison*

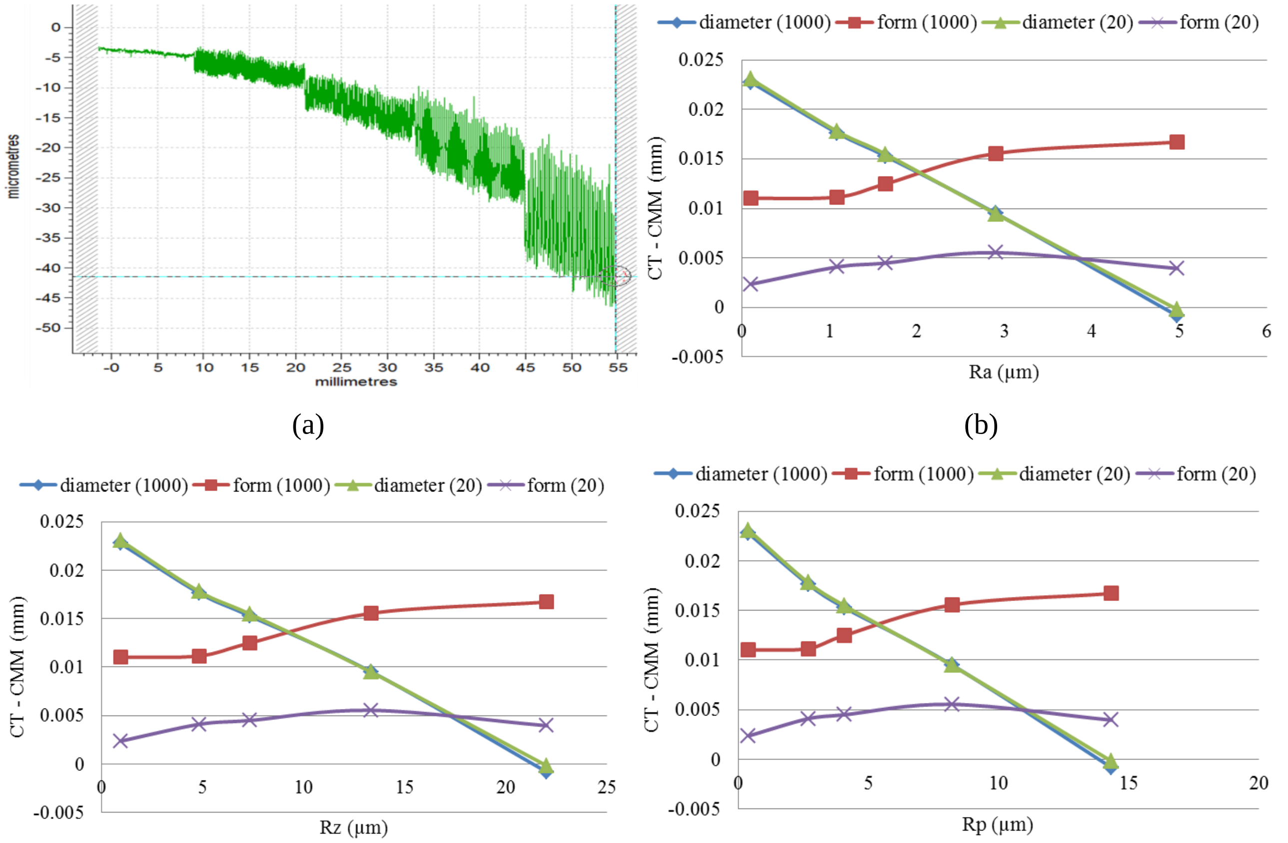

(a) (b)

(c) (d)

Figure 3.23 *Comparing cylinder b's diameter and form measurements obtained by CT and tactile CMM under different surface roughness conditions. Each CT measurements are repeated using both 1000 and 20 fitting points. (a) raw profile plot along a straight line on the surface of cylinder "b" (b) roughness term "Ra" is used for comparison (c) roughness term "Rz" is used for comparison (d) roughness term "Rp" is used for comparison*

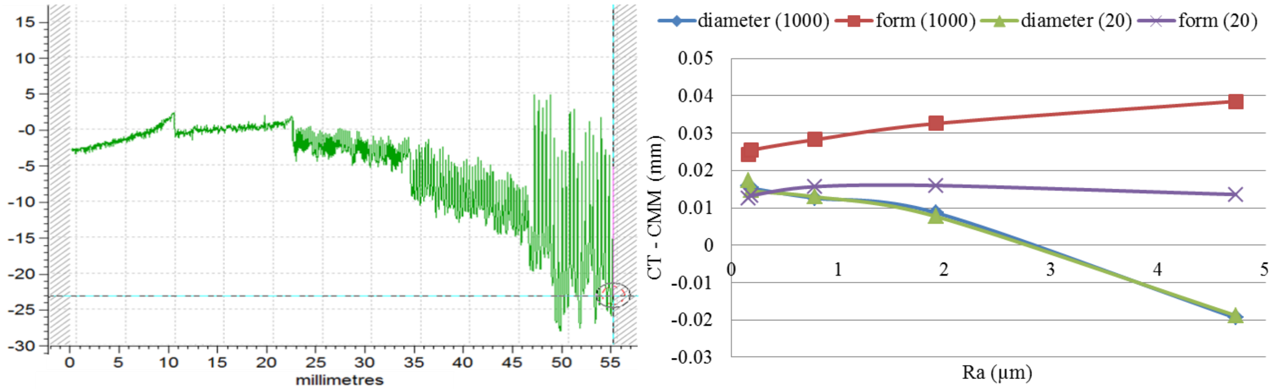

(a) (b)

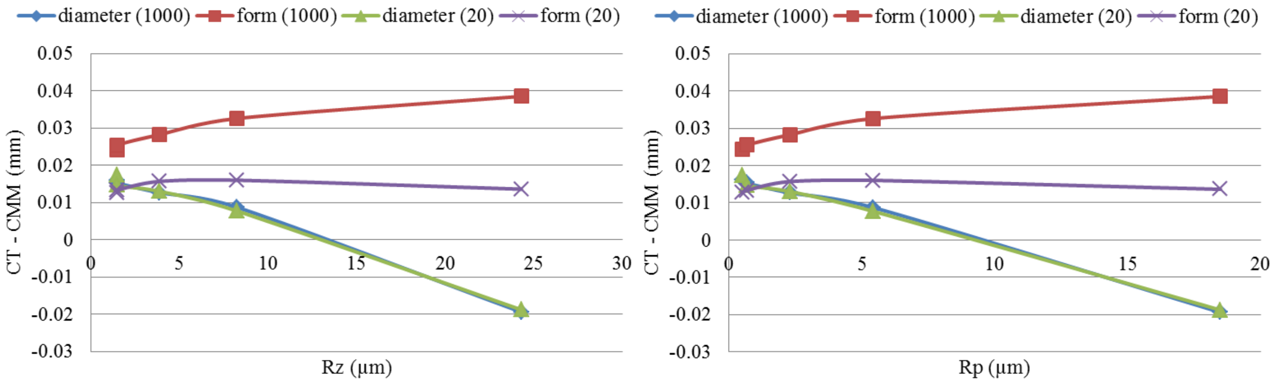

(c) (d)

Figure 3.24 *Comparing cylinder c's diameter and form measurements obtained by CT and tactile CMM under different surface roughness conditions.Each CT measurements are repeated using both 1000 and 20 fitting points. (a) raw profile plot along a straight line on the surface of cylinder "c" (b) roughness term "Ra" is used for comparison (c) roughness term "Rz" is used for comparison (d) roughness term "Rp" is used for comparison*

Several effects related to the surface roughness and number of fitting points can be observed from Fig 3.22, 3.23 and 3.24.

1. As shown in Fig 3.25, in theory, the differences between the CT and CMM defined edges will increase when the measured surfaces get rougher. Thus, in case of using tactile CMM as the reference for measuring outer cylinder diameters and without considering the thresholding edge offset error, the CT measured diameters will decrease while the surface roughness increases. This hypothesis is confirmed by all experimental results.

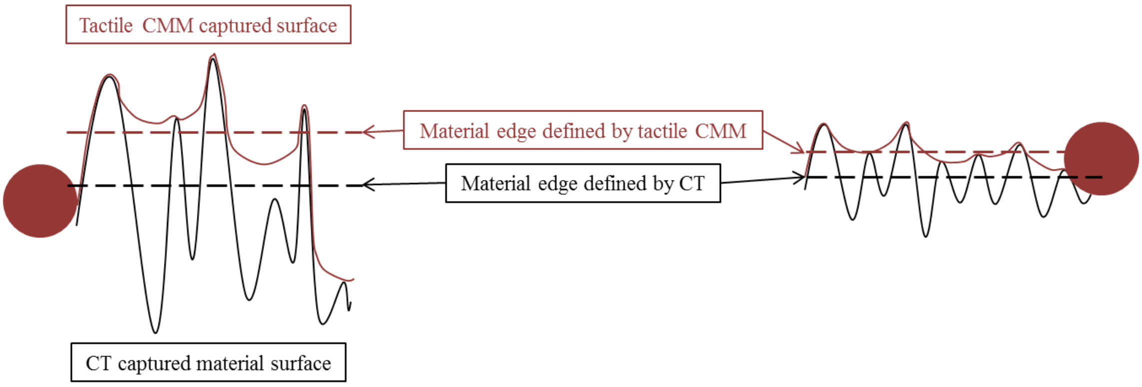

Figure 3.25 *Illustration of the influence of surface roughness on the difference between CT and tactile CMM defined material edges. Notice that probe radius compensation has been applied to the CMM measurements*

2. It can also be noticed that the "edge offset" (CT measured value minus tactile CMM measured value) between section 1 and section 5 differs a lot: 41.1 µm for cylinder a, 23.6 µm for cylinder b and 35.4 µm for cylinder c. The large magnitudes of the "edge offset" differences prove that surface roughness is an important influence factor.

3. As indicated in Fig 3.20, Rp is the peak value deviation from the mean profile line. Theoretically, tactile CMM tend to measure the peaks while CT is more likely measuring the mean profile line. Thus, it is assumed that certain correlation exists between the “edge offset” differences and the surface roughness (Rp) differences between sections. To investigate this correlation, for each cylinder, the “edge offset” differences and Rp differences are calculated taking the values of section 1 as reference. The results (absolute values regardless of the +/- sign) are listed in Table 3.23. Notice that cylinder diameter is an edge dependent feature, thus the diameter differences is divided by 2.

	Cylinder a		Cylinder b		Cylinder c	
	Diff – edge offset	Diff - Rp	Diff – edge offset	Diff - Rp	Diff – edge offset	Diff - Rp
	(µm)					
Section 2 - 1	2	1.4	3	2.3	0	0.2
Section 3 - 1	3	3.0	4	3.7	2	1.8
Section 4 - 1	14	13.2	7	7.8	4	4.9
Section 5 - 1	21	20.4	12	13.9	18	18.0

***Table 3.23** The “edge offset” differences and double Rp differences taking section 1 as reference*

It can be noticed from Table 3.23 that the two calculated terms have similar magnitudes. In addition, the “edge offset” differences versus the Rp differences for all three cylinders are plotted in Fig 3.26, a linear relationship between the “edge offset” differences and Rp differences is observed.

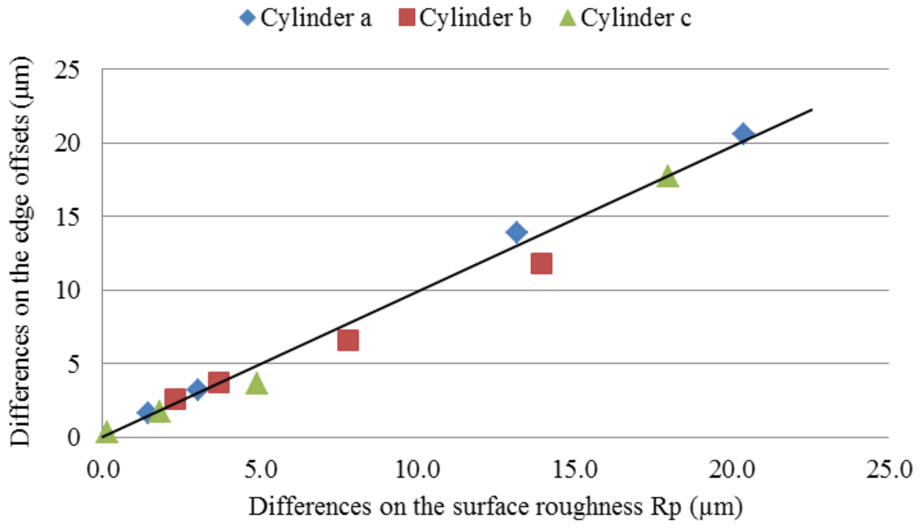

***Figure 3.26** The relationship between the “edge offset” differences and the Rp differences*

Thus, when comparing tactile CMM and CT dimensional measurements, the “edge offset” is closely related to the surface roughness Rp. Their relation follows a linear trend. This applies to objects that are manufactured by turning using the same tool.

4. Regarding the cylinder diameter measurements, using 1000 or 20 fitting points does not make big difference. Nevertheless, it can be seen from the raw CT measurement data (Table 3.19 – Table 3.21) that the standard deviations get much higher when we only apply 20 points for feature fitting, because the chance of picking outliers increases in case of using insufficient fitting points.

5. The number of fitting points becomes more influential when form error measurements are concerned. It is shown that when 20 points are applied for feature fitting, the CT measured form error stays more or less constant regardless of the varying surface roughness. The limited number of fitting points inherently filters out most of the high frequency surface components. As a result, the influence of the surface roughness on the measured form error will be largely reduced.

3.2.3 Conclusions

The influence of surface roughness and number of fitting points on CT dimensional measurements can be summarized as follows:

- Industrial CT is capable of capturing part of the small surface details, such as the surface roughness. However, it cannot be directly used for quantitative evaluation of the surface roughness. First of all, due to limited resolution, industrial CT cannot provide a complete evaluation of the surface roughness. Second, it is almost impossible to separate the effects between X-ray scattering noise and surface roughness.
- When evaluating CT dimensional measurements of rough surfaces, the “edge offsets” (when using tactile CMM as reference) are dependent on the surface roughness. For objects that are manufactured by turning using a single tool yet varying feeds, the edge offsets are linearly related to the surface roughness.
- In general, CT measured form errors are larger than the ones measured by using tactile CMM. Furthermore, the number of applied fitting points significantly influences the measured form error.

CHAPTER 4

Influence of Scan Setting Parameters

Various influence factors and their interactions make the parameter optimization rather complicated and result in high operator dependency for CT dimensional metrology. Several major machine settings are investigated in this chapter, including X-ray voltage, filter and voxel size. A 3×3 design of experiment was performed to study their influences on both global measurement accuracy and local dimensional variations. Furthermore, analysis of variances (ANOVA) was applied to statically analyze the significance of their individual influence and their interactions. In addition, the influence of X-ray target material is also studied.

4.1. Operator's decisions during the scanning process

As discussed in Chapter 2, the operator's decision for the scanning settings can be categorized based on the related hardware components (as shown in Fig 4.1):

- X-ray source – target material; X-ray voltage and current; filter material and thickness.
- Axes – magnification
- Turn table – number of projections
- Workpiece – workpiece orientation and clamping material
- X-ray detector – exposure time and amplification

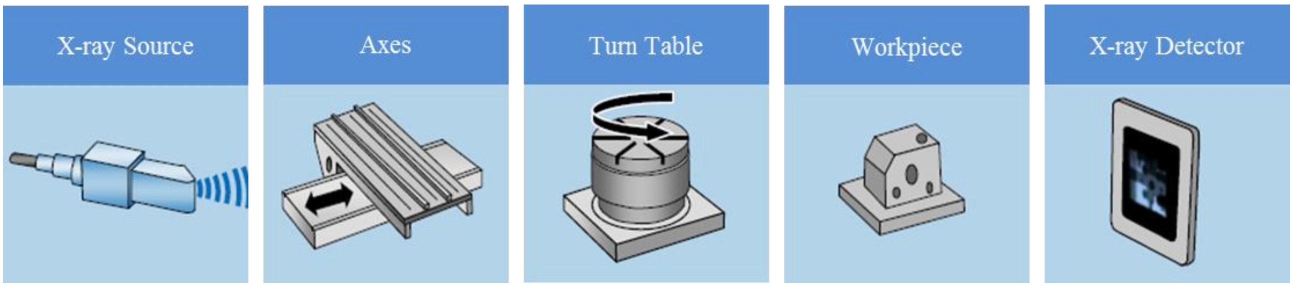

Figure 4.1 *Basic hardware components of an industrial CT system [Based on Schmitt R. et al., 2011]*

In this chapter, besides the influence of target material, the effects of several major machine settings (X-ray voltage, filter and magnification) and their interactions are also investigated.

4.2 Scanning settings and their influences

4.2.1 Target material

As shown in Fig 4.2, the "target" of an industrial X-ray source refers to the metal block onto which the accelerated electrons are focused. Due to the collision between these electrons and the target material, polychromatic X-ray beams are generated. Fig 4.2 shows a traditional "reflective" target; other types of target configuration exist, such as transmitting target (thin plate) and rotating (reflective or transmitting) target. The choice of target material is closely related to the generated X-ray intensity: the X-ray intensity is fundamentally limited by the maximum possible heat dissipation of the X-ray target; exceeding a critical material dependent power density will result in melting and evaporating the target. *[Bergmann R.B. et al., 2004]*. Thin transmitting targets are only used for low power CT sources, as they cannot resist high temperatures. High power CT sources are therefore generally equipped with water cooled massive reflective targets. In some cases high precision rotating targets are used to spread the heat input over a larger area. *[Kruth J.P. et al., 2011]*

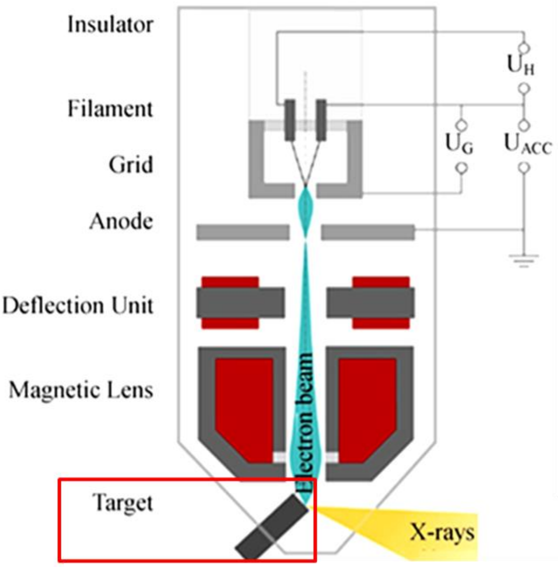

Figure 4.2 *Typical X-ray tube with reflection target*

Moreover, in order to allow easy multi-spectrum measurement, some sources can have a multi-material target where different target materials are fitted into an indexed head. The 225kV industrial CT scanner at the Department of Mechanical Engineering - KU Leuven is equipped with a target containing four different materials: copper, molybdenum, silver and tungsten. Fig 4.3 demonstrates the X-ray emission spectrum of these target materials at a tube voltage of 225 kV. The average X-ray energies and efficiency of X-ray generation increases with increasing the atomic number of the target material. Currently, as the rule of thumb, copper/molybdenum targets are mainly used for looking at biological materials, carbon fiber or light plastic parts; silver can be used for higher energy applications but is not as robust as tungsten, since it is more easily eroded. However, the above mentioned target material selection method is mainly based on the image quality of 2D projection images. Its influence on CT dimensional metrology applications remains unclear. Thus, several experimental setups have been designed to check how the CT measurements differ when the target material varies.

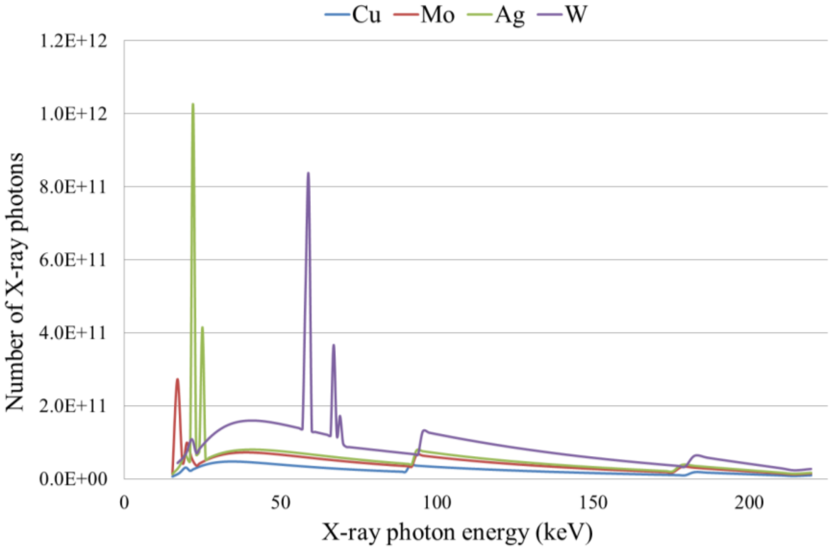

Figure 4.3 *X-ray emission spectra of 4 different target materials (copper, molybdenum, silver and tungsten) under 225kV tube voltage. The electron incident angle is 18°. [Bellon C. et al., 2012]*

The first group of experiments investigates the influence of the target material on porosity measurement. A plastic (polyamide 12) block (Fig 4.4 a) produced by selective laser sintering was scanned 4 times using the same machine settings (125kV tube voltage, 200 µA tube current, no filter and 15.6 µm voxel size) but with different target materials (copper, molybdenum, silver and tungsten). A region of interest (Fig 4.4 b, within the red rectangle) was selected on the middle slice (Fig 4.4 a, indicated by the red cutting line); porosity measurements were performed on a 2D level using ImageJ (open source image processing software). Fig 4.4 c, e, g and i demonstrate 2D images of the same region of interest acquired using copper, molybdenum, silver and tungsten targets. Correspondingly, these images were further binarized (Fig 4.4 d, f, h and j) for porosity analysis.

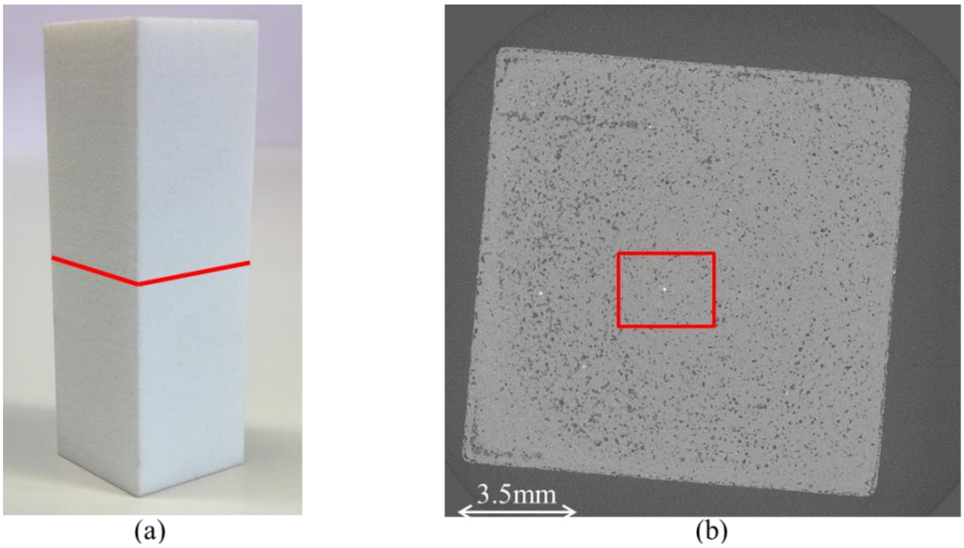

(a)
(b)

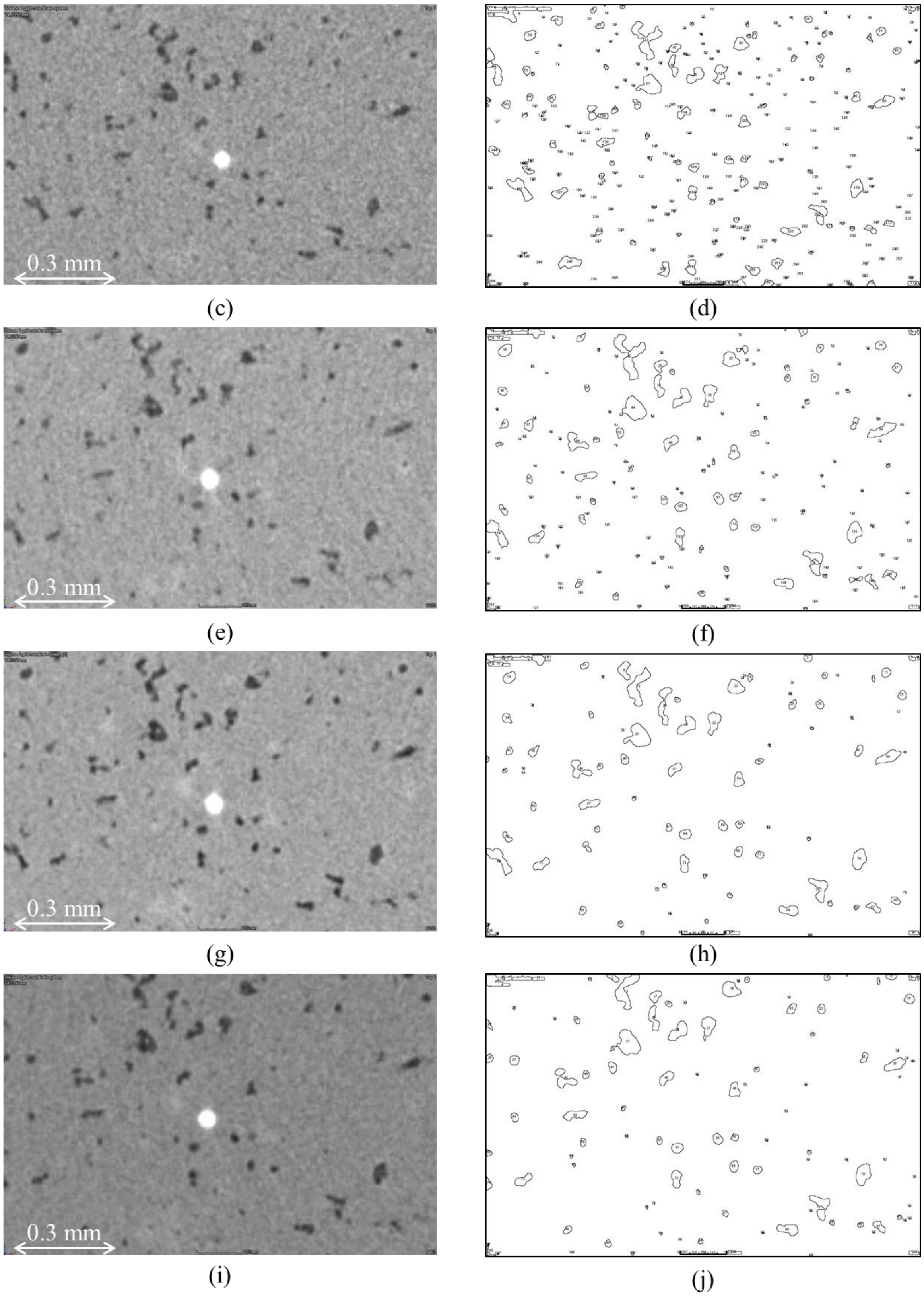

Figure 4.4 *Influence of the target material on image quality and porosity analysis. (a) plastic-Polyamide 12 block produced by selective laser sintering; (b) cross section image taken from the middle slice of the CT 3D model; (c, e, g and i) 2D images of the region of interest (marked in the red rectangle in "b") acquired using copper, molybdenum, silver and tungsten target materials; (d, f, h and j) the corresponding binarized images.*

As discussed previously, although the X-ray power settings are identical, the spectrum can differ a lot depending on the chosen target material. Through visual inspection, the image obtained using copper target shows the best contrast and the most details after binarization. Table 4.1 lists the porosity measurement results performed on the binarized images. Meanwhile, the porosity of this block sample was also measured using the method of Archimedes, which gives a reference porosity value of 5.6%.

Target Material	Copper	Molybdenum	Silver	Tungsten
Measured Porosity (%)	5.051	4.927	4.651	4.403

Table 4.1 *CT Porosity measurements using different target materials*

First of all, it is shown that all CT measured porosity values are smaller than the one obtained by the Archimedes method. There are two potential reasons: the limited structural resolution of the CT equipment (focal spot size > 5 µm, voxel size is 15.6 µm) makes part of the small pores not detectable; the porosity of the sample is not evenly distributed and the selected region of interest has smaller porosity than the average value.

Second, the measured porosity values decrease when shifting the target material from copper to tungsten. Theoretically, low energy X-ray beams are better for detecting small details; if the X-ray spectrum contains too much high energy X-ray, most of the X-ray beams will just penetrate the object without creating sufficient contrast. When all other scanning settings are kept identical, the measured porosity is higher when using a copper target than when using a tungsten target. This is because the average X-ray energy generated by the copper target is much lower and therefore can detect a larger range of pore sizes.

Third, there might be a large measurement uncertainty of the Archimedes method; particularly because gas bubbles might adhere to the surface of an SLS part.

The second group of experiments studies the influence of target material on dimensional measurements. Two test setups were designed: the first setup (Fig 4.5 a) consists of two ruby spheres and the second setup (Fig 4.5 b) consists of two ceramic (ZrO_2) spheres. Both setups were calibrated with a Mitutoyo FN905 tactile CMM, sphere diameter and center distance measurements were repeated 3 times (Table 4.2).

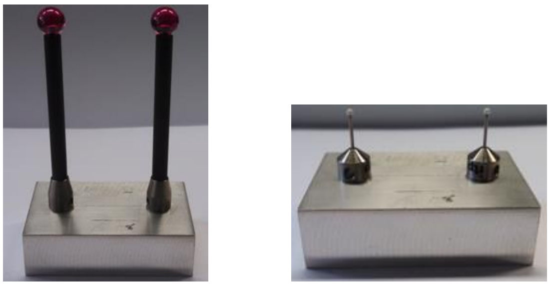

(a) (b)

Figure 4.5 *Two experimental setups designed for investigating the influence of target material on CT dimensional measurements; (a) calibrated ruby spheres (b) calibrated ceramic (ZrO_2) spheres.*

	Ruby sphere			Ceramic (ZrO_2) sphere		
	Diameter 1	Diameter 2	Center distance	Diameter 1	Diameter 2	Center distancec
M1 (mm)	9.9968	9.9984	39.5048	1.9970	1.9981	39.6362
M2 (mm)	9.9970	9.9981	39.5048	1.9970	1.9978	39.6361
M3 (mm)	9.9972	9.9987	39.5075	1.9969	1.9978	39.6360
Average (mm)	9.9970	9.9984	39.5057	1.9970	1.9978	39.6361
Stdev (µm)	0.2	0.3	1.5	0.0	0.0	0.0

Table 4.2 *CMM reference measurements for the two test setups (Fig 4.5)*

Furthermore, each test setup was scanned 4 times with the same machine settings (Table 4.3) but with different target materials (copper, molybdenum, silver and tungsten). Subsequently, sphere diameters and their center distance were measured 3 times for each scan. Moreover, the fitting point standard deviations were also recorded and seen as indications on the surface qualities. The CT measurement results are listed in Table 4.4

Test setup	Voltage (kV)	Current (µA)	Filter	Voxel size
Ruby sphere	120	150	none	30.3
Ceramic sphere	130	120	none	30.3

Table 4.3 *Main machine settings for scanning the rubi sphere and ceramic (ZrO_2) sphere test setups*

Target material		Ø 1 (mm)	Fitting point standard deviation (µm)	Ø2 (mm)	Fitting point standard deviation (µm)	Center distance (mm)
Copper	M1	10.020	2.0	10.020	2.0	39.553
	M2	10.020	2.0	10.020	2.0	39.553
	M3	10.020	2.0	10.020	2.0	39.553
	Average	10.020	2.0	10.020	2.0	39.553
Molybdenum	M1	10.026	2.2	10.027	2.1	39.553
	M2	10.026	2.2	10.027	2.1	39.553
	M3	10.026	2.2	10.027	2.1	39.553
	Average	10.026	2.2	10.027	2.1	39.553
Silver	M1	10.022	2.1	10.022	2.0	39.553
	M2	10.022	2.2	10.022	2.0	39.553
	M3	10.022	2.1	10.022	2.0	39.553
	Average	10.022	2.1	10.022	2.0	39.553
Tungsten	M1	10.014	1.8	10.014	1.8	39.554
	M2	10.014	1.8	10.014	1.8	39.554
	M3	10.014	1.8	10.014	1.8	39.554
	Average	10.014	1.8	10.014	1.8	39.554

(a)

Target material		Ø 1 (mm)	Fitting point standard deviation (µm)	Ø2 (mm)	Fitting point standard deviation (µm)	Center distance (mm)
Copper	M1	2.018	1.3	2.018	1.4	39.675
	M2	2.018	1.3	2.018	1.4	39.675
	M3	2.018	1.3	2.018	1.4	39.675
	Average	2.018	1.3	2.018	1.4	39.675
Molybdenum	M1	2.016	1.4	2.016	1.3	39.675
	M2	2.016	1.4	2.016	1.3	39.675
	M3	2.016	1.4	2.016	1.3	39.675
	Average	2.016	1.4	2.016	1.3	39.675
Silver	M1	2.016	1.3	2.016	1.3	39.674
	M2	2.016	1.3	2.016	1.3	39.674
	M3	2.016	1.3	2.016	1.3	39.674
	Average	2.016	1.3	2.016	1.3	39.674
Tungsten	M1	2.008	1.3	2.009	1.3	39.677
	M2	2.008	1.3	2.009	1.3	39.677
	M3	2.008	1.3	2.009	1.3	39.677
	Average	2.008	1.3	2.009	1.3	39.677

(b)

Table 4.4 *CT measurement results for (a) rubi sphere test setup and (b) ceramic (ZrO_2) sphere test setup.*

All CT diameter measurements were rescaled using the following formula:

$$\text{Diameter}_{\text{CT,new}} = \text{Diameter}_{\text{CT,old}} \times (\text{Center-Distance}_{\text{CMM}} / \text{Center-Distance}_{\text{CT}}) \qquad (1)$$

The comparison between CT and CMM diameter measurements are shown in Fig 4.6.

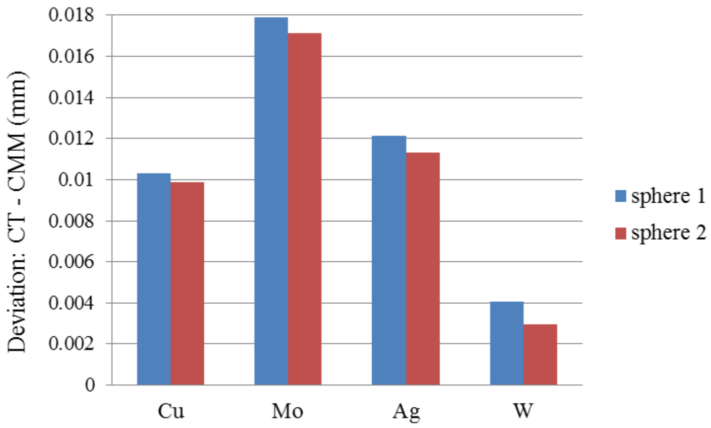

(a)

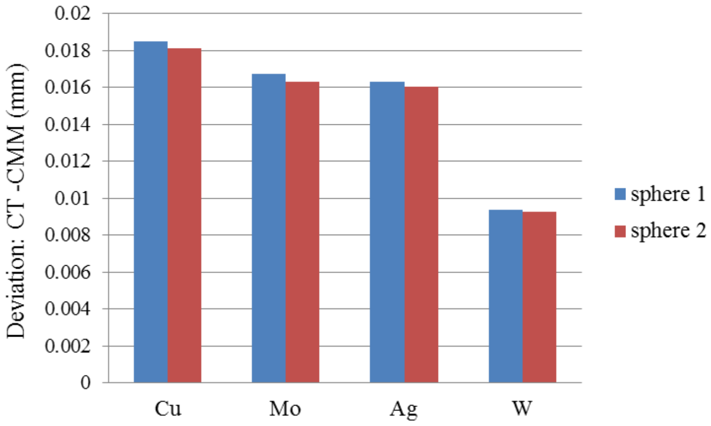

(b)

Figure 4.6 *Comparison between CT and CMM diameter measurements. (a) ruby sphere test setup (b) ceramic (ZrO_2) sphere test setup*

It can be concluded from Fig 4.6 that the choice of target material has an influence on the dimensional measurement results. For measuring the two test setups shown in Fig 4.5, the tungsten target appears to be more reliable than the others. However, the choice of target material is dependent on many other factors, such as: the material composition of the scanned object, the applied X-ray power and filter etc. Thus, further researches are required in order to draw solid conclusions.

4.2.2 Conclusions

The above experimental investigation reveals the following messages regarding the influences of target material for X-ray generation:

- When applying the same X-ray power, the measured porosity decreases when shifting the target material from copper to tungsten.
- The choice of target material has an influence on the dimensional measurement results.

4.2.3 X-ray voltage, filter and voxel size

4.2.3.1 X-ray voltage

X-ray voltage and current are important machine settings which can directly influence the quality of the 2D projection images.

The available X-ray voltage range determines the maximum penetration length for different materials. Table 4.5 lists the typical allowable thicknesses for common industrial materials depending on the applied X-ray voltage.

X-ray Voltage (kV)	130	150	190	225	450
Steel/Ceramic	< 5 mm	< 8 mm	< 25 mm	< 40 mm	< 70 mm
Aluminum	< 30 mm	< 50 mm	< 90 mm	< 150 mm	< 250 mm
Plastic	< 90 mm	< 130 mm	< 200 mm	< 250 mm	< 450 mm

Table 4.5 *Typical maximum penetrable material thicknesses for common industrial materials [Christophe R. et al., 2011]*

Note that the values in the above table are maximum thicknesses producing low signal-to-noise ratios; with smaller thicknesses the transmitted intensity increases. In order to have a good signal to noise ratio, a minimum X-ray transmission has to be ensured. For non-destructive testing applications, the recommended minimum transmission is around 14% *[ISO 15708:2002, Non-destructive testing - Radiation methods - Computed tomography; part 2 chapter 7.3.1]*. Figure 4.7 illustrates the relationship between material thickness and the relative transmission at 420kV X-ray voltage.

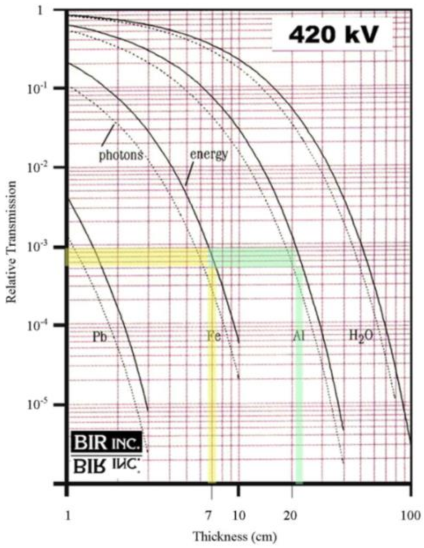

Figure 4.7 *Relationship between material thickness and the relative X-ray transmission at 420 kV [DTU (2010), 14th CMM Danish users' club conference on "Application of CT scanning in industry"].*

Moreover, it has to be mentioned that the average energy of the spectrum in keV is much less than the applied acceleration voltage of the electrons in kV. The reason is that the generated X-rays feature a continuous spectrum ranging from very low keV up to the full keV of the accelerated electrons. For example, with no filtering and an acceleration of 225 kV, the average X-ray energy from a tungsten target is around 77keV (Fig 4.3).

The applied current is less influential comparing with the X-ray voltage. Nevertheless, it also has important functions: on the one hand, the applied current should be high enough to make sure the number of transmitted X-ray photons is sufficient for creating an acceptable signal to noise ratio; on the other hand, the applied current should not be too high to avoid saturation and too large focal spot (due to heat concentration).

4.2.3.2 X-ray filter: material and thickness

Hardware filters are frequently applied for all kinds of CT scans. Common materials of X-ray filters include aluminum, copper, tin and silver etc. The thickness of X-ray filters varies from 0.1mm up to several millimeters depending on the application. A few examples of X-ray filters are shown in Fig 4.8. X-ray filters can be placed next to the X-ray source (Fig 4.8 a and b) or close to the X-ray detector (Fig 4.8 c).

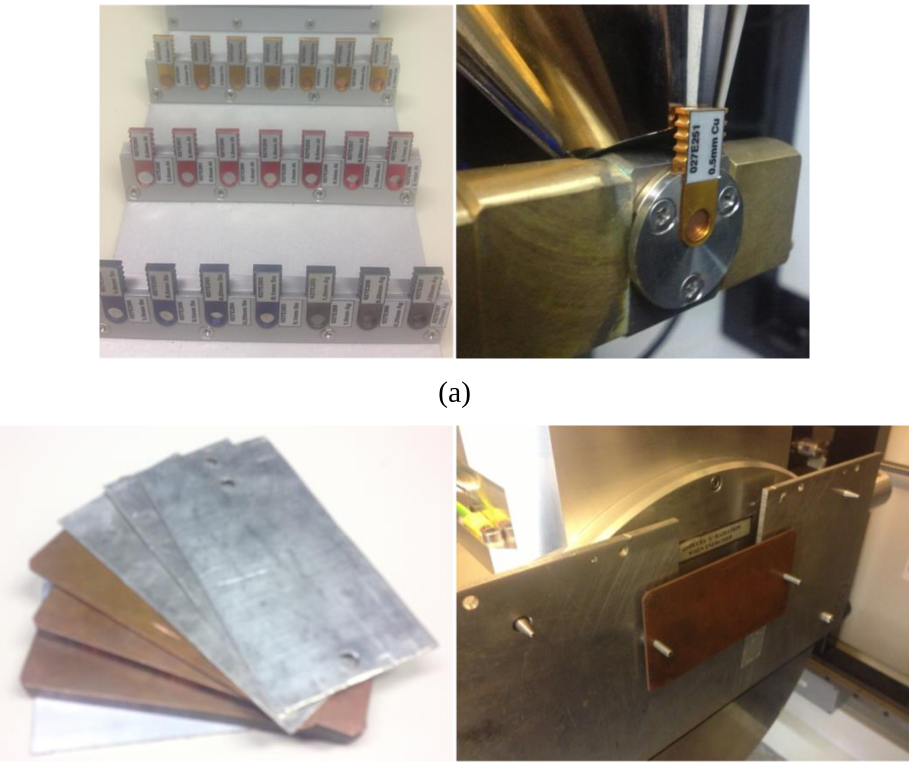

(a)

(b)

(c)

Figure 4.8 *Hardware filters for industrial CT systems. (a) Filter tool kit (including copper, aluminum, tin and silver filters) for 225kV industrial CT scanner; (b) aluminum, copper and tin filters for 450kV industrial CT scanner; (c) copper filter plate placed next to the X-ray detector.*

Hardware filters have two basic functions: reducing the beam hardening effect and adjusting the applicable X-ray power range. The function related to beam hardening correction will be discussed in Chapter 5. When talking about the applicable X-ray power range, it mainly refers to the range of X-ray voltage and current settings which can produce sufficient X-ray transmission without resulting in over-exposure on the X-ray detector.

4.2.3.3 Voxel size

Theoretically, the voxel size can be calculated by a simple formula as follows:

$$\textbf{Voxel size} = \textbf{detector pixel size} \times \textbf{FOD/FDD} \qquad (2)$$

Whereas FOD denotes the distance between X-ray focal spot and the scanned object, and FDD is the distance between X-ray focal spot and the X-ray detector.

However, the voxel’s quality is also influenced by the number of angular positions at which images are taken. Fig 4.9 demonstrates the result of the reconstruction of a slice when scanning three balls with different number of angular positions (from 2 to 128 projections over 360 degrees). With only 2 different angular positions the reconstructed slice image is very vague and resembles a grid of 3×3 square objects. As the number of angular position increases, the reconstruction becomes more precise, ending with an accurate slice picture of three balls.

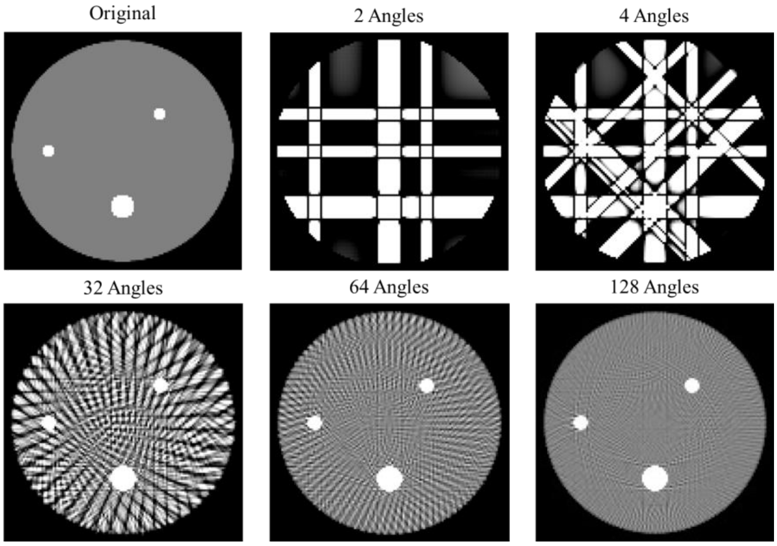

Figure 4.9 *Illustration of the effects of angular under-sampling on image quality for FBP reconstruction [Fessler J., 2009]*

On one hand, a sufficient number of angular positions should be guaranteed so that the voxel's quality will not be degraded due to the lack of 2D projection images; on the other hand, taking too many 2D projection images will result in over sampling which is of little use but will increase the scanning and reconstruction time.

As shown in Fig 4.10, a practical rule for avoiding under sampling due to lack of 2D projection images is: looking at the furthest moving point on the object; its moving distance between two adjacent projections (distance "S" in Fig 4.10) should be smaller than the theoretical voxel size which is calculated by the detector pixel size and the magnification.

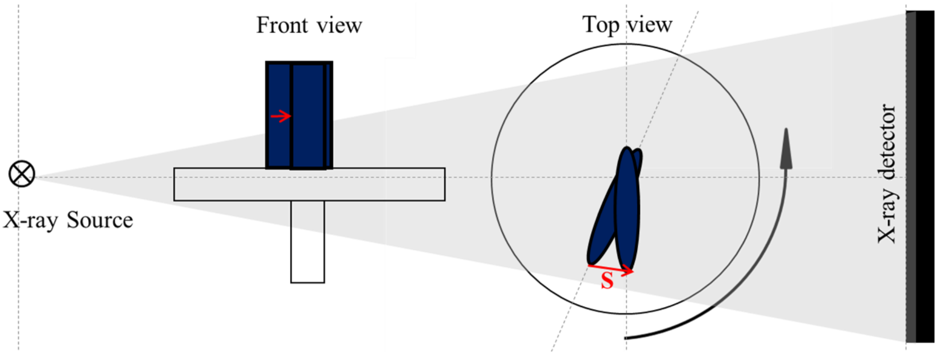

Figure 4.10 *Illustration of a single rotation step*

4.2.3.4 Experimental investigation

As discussed earlier, it was suspected that the X-ray voltage, filter and voxel size are all important influence factors for CT dimensional metrology applications. However, their individual effect and their correlations are yet unclear. In order to investigate the influence and interactions of X-ray voltage, filter and voxel size on the accuracy and uncertainty of CT dimensional measurements, a 3×3 design of experiment (DOE) was performed.

- **Experimental setup and reference measurements**

As shown in Fig 4.11, the experimental setup consists of two components:

Component Nr.1 - Ø4 mm stainless steel pin. Dimensional tolerance is ±1 µm.

Component Nr.2 - stainless steel hollow step cylinder; its nominal dimensions are shown in Fig 4.12 (b).

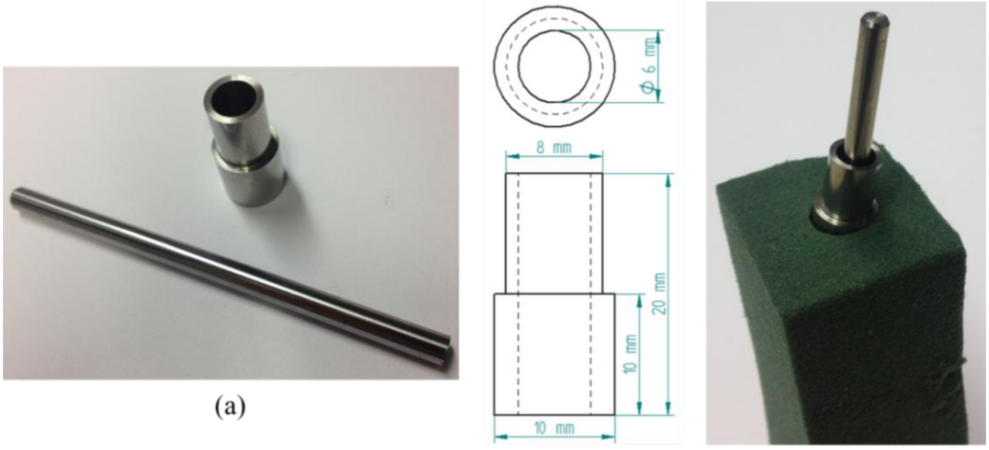

(a) (b) (c)

Figure 4.11 *Experimental setup for the DOE analysis. (a): a stainless steel hollow step cylinder and a Ø4 mm (dimensional tolerance ±1 µm) stainless steel pin; (b): nominal dimensions for the stainless steel hollow step cylinder; (c) fixation of the two workpieces using light weight foam material.*

As shown in Fig 4.12, the experimental setup comprises eight measurands: the middle pin contains four measurands depending on different locations; the hollow step cylinder includes two outer diameters and two inner diameters depending on their sizes and locations.

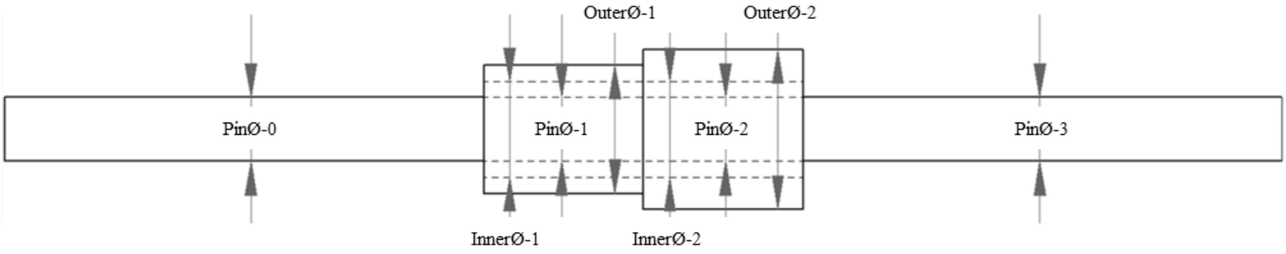

Figure 4.12 *Definition of the measurands on the experimental setup*

The design concepts of this experimental setup are as follows:

First of all, CT dimensional measurements on cylindrical features are highly repeatable; moreover, they are relatively easy to be machined up to good dimensional and geometrical accuracy.

Second, the middle pin is partly "covered" by the step cylinder. Thus, the difference between the "covered" and "uncovered" parts can be evaluated.

Third, the inner hole and outer diameters of the step cylinder can largely reveal the thresholding edge offsets. Meanwhile, the influence of wall thickness can also be studied.

All measurands on the hollow step cylinder were measured on a Mitutoyo FN904 tactile CMM using a Ø1 mm probe (the machine specifications are described in Section 3.1.3). All measurements were shown to be repeatable (standard deviations of 3 repetitions are all below 1 µm). The reference CMM measurement results are shown in Table 4.6.

Feature	M - 1 (mm)	M - 2 (mm)	M - 3 (mm)	Stdev (µm)	Average (mm)
Top outer cylinder	8.0055	8.0058	8.0052	0.0003	8.0055
Bottom outer cylinder	10.0027	10.0028	10.0028	5.77E-05	10.0028
Inner hole	5.9583	5.9582	5.9575	0.000436	5.9580

***Table 4.6** CMM reference measurement value for the stainless steel hollow step cylinder*

- **CT dimensional measurements**

All scans were performed with the XT H225 ST CT scanner developed by Nikon Metrology. Detailed machine specifications can be found in Section 3.1.4. The fixation method and an example of the 2D X-ray projection image are shown in Fig 4.13.

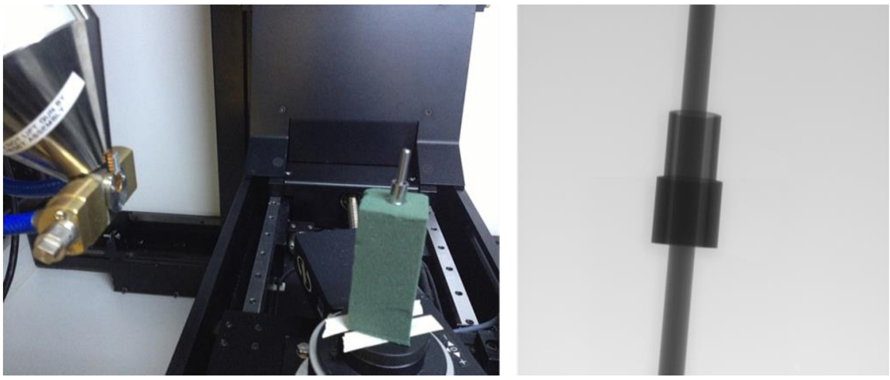

***Figure 4.13** Fixation method and an example of the 2D X-ray projection image*

As shown in Table 4.7, the investigation mainly focused on three major influence factors: X-ray voltage, filter and voxel size; three levels were chosen for each of these influence factors resulting in a total number of 27 CT scans (Table 4.8).

	1	**2**	**3**
A: Voltage (kV)	220	180	160
B: Filter	2 mm copper	1 mm copper	2 mm aluminum
C: Voxel size (μm)	15.5	25.9	52.1

Table 4.7 *The influence factors and levels for the 3×3 design of experiment*

Scan Nr.	voltage (kV)	Current (μA)	Filter		Magnification	Nr. of projections	Voxel size (μm)
			material	(mm)			
1	180	220	Copper	1	x3.84	1333	52.1
2	160	280	Copper	1	x3.84	1333	52.1
3	220	170	Copper	1	x3.84	1333	52.1
4	220	170	Copper	1	x12.9	3142	15.5
5	180	220	Copper	1	x12.9	3142	15.5
6	160	280	Copper	1	x12.9	3142	15.5
7	160	280	Copper	1	x7.71	2399	25.9
8	220	170	Copper	1	x7.71	2399	25.9
9	180	220	Copper	1	x7.71	2399	25.9
10	180	95	Aluminum	2	x7.71	2399	25.9
11	220	75	Aluminum	2	x7.71	2399	25.9
12	160	105	Aluminum	2	x7.71	2399	25.9
13	160	105	Aluminum	2	x3.84	1276	52.1
14	180	95	Aluminum	2	x3.84	1276	52.1
15	220	75	Aluminum	2	x3.84	1276	52.1
16	220	75	Aluminum	2	x12.9	3142	15.5
17	160	105	Aluminum	2	x12.9	3142	15.5
18	180	95	Aluminum	2	x12.9	3142	15.5
19	220	300	Copper	2	x7.71	2308	25.9
20	180	420	Copper	2	x7.71	2308	25.9
21	160	590	Copper	2	x7.71	2308	25.9
22	160	590	Copper	2	x12.9	3142	15.5
23	180	420	Copper	2	x12.9	3142	15.5
24	220	300	Copper	2	x12.9	3142	15.5
25	220	300	Copper	2	x3.84	1333	52.1
26	160	590	Copper	2	x3.84	1333	52.1
27	180	420	Copper	2	x3.84	1333	52.1

Table 4.8 *Design of experiments: list of CT scanning settings*

VG Studio MAX 2.2 was used for measuring the eight measurands (Fig 4.12). Local adaptive thresholding method (Fig 4.14) was used for determining material surfaces: the starting contour was placed in the middle between the last background peak (there were two “background” peaks: air and fixation foam) and the first material peak (multiple material peaks might appear due to the beam hardening effect, X-ray scattering etc.).

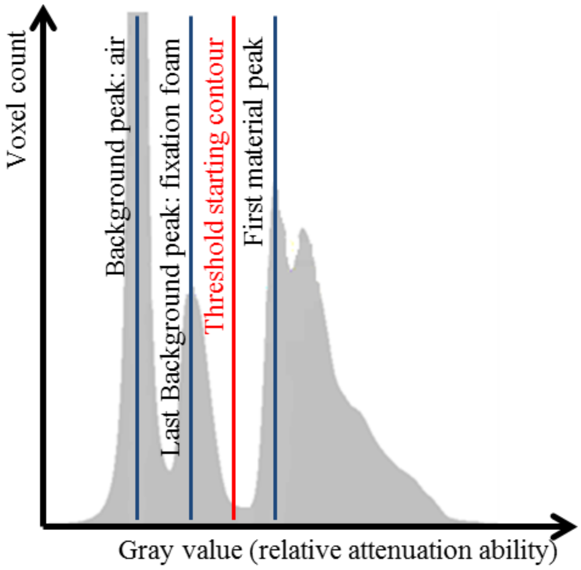

Figure 4.14 *Starting contour for local adaptive thresholding*

The applied cylinder fitting algorithm was least squares; a method that tries to minimize the sum of squared deviations of all fit points relative to the fitted cylinder. In addition, the fitting points’ standard deviations were also noted. The overall CT measurement results are listed in Appendix B.

- **Data analysis**

After voxel size correction, the dimensional measurement results of 27 CT scans have been compared with the tactile CMM reference values; the deviations are plotted in Fig 4.15. In addition, the corresponding fitting point standard deviations are shown in Fig 4.16.

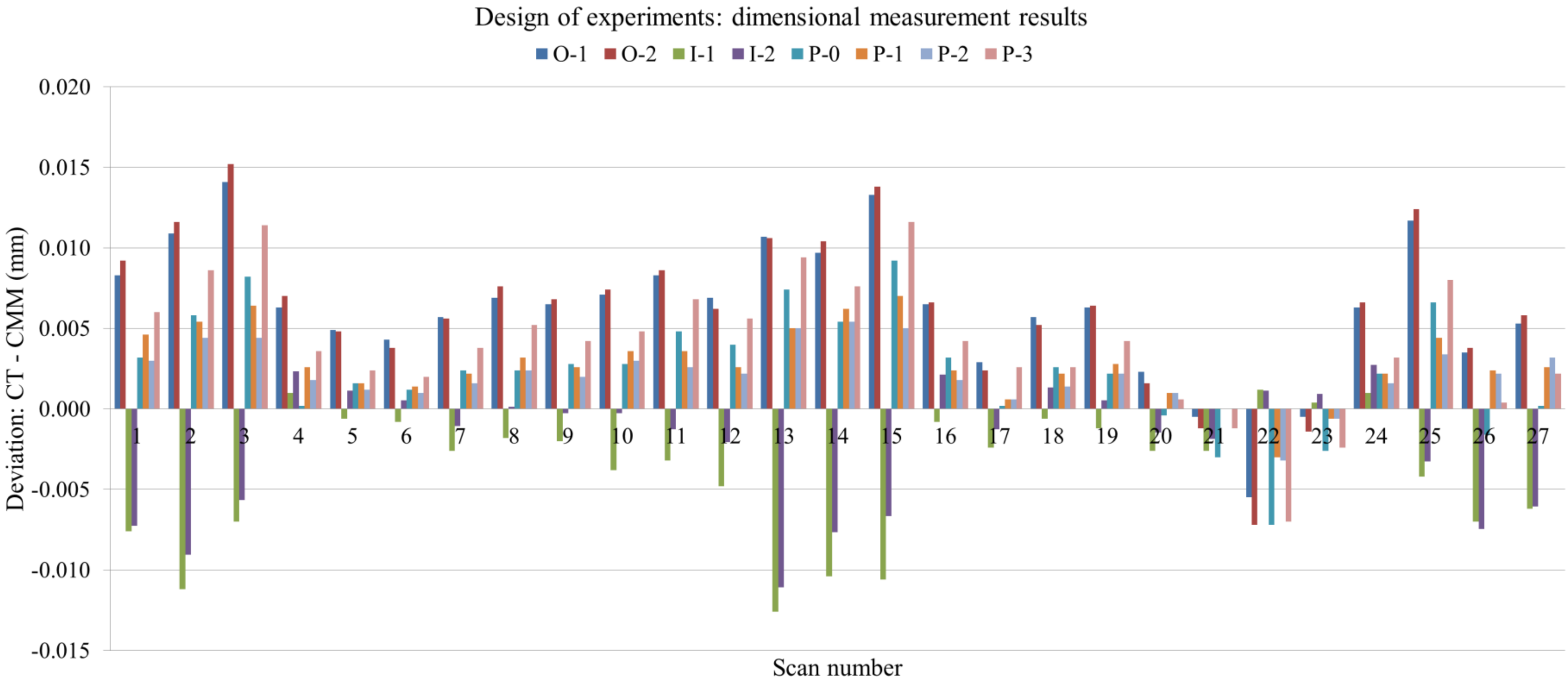

Figure 4.15 *Design of experiments: comparison between CT and tactile CMM dimensional measurement results. "O-1, O-2, I-1, I-2, P-0, P-1, P-2, P-3" are the 8 measurands defined in Fig 4.12. The list of machine settings of the 27 CT scans can be found in Table 4.7*

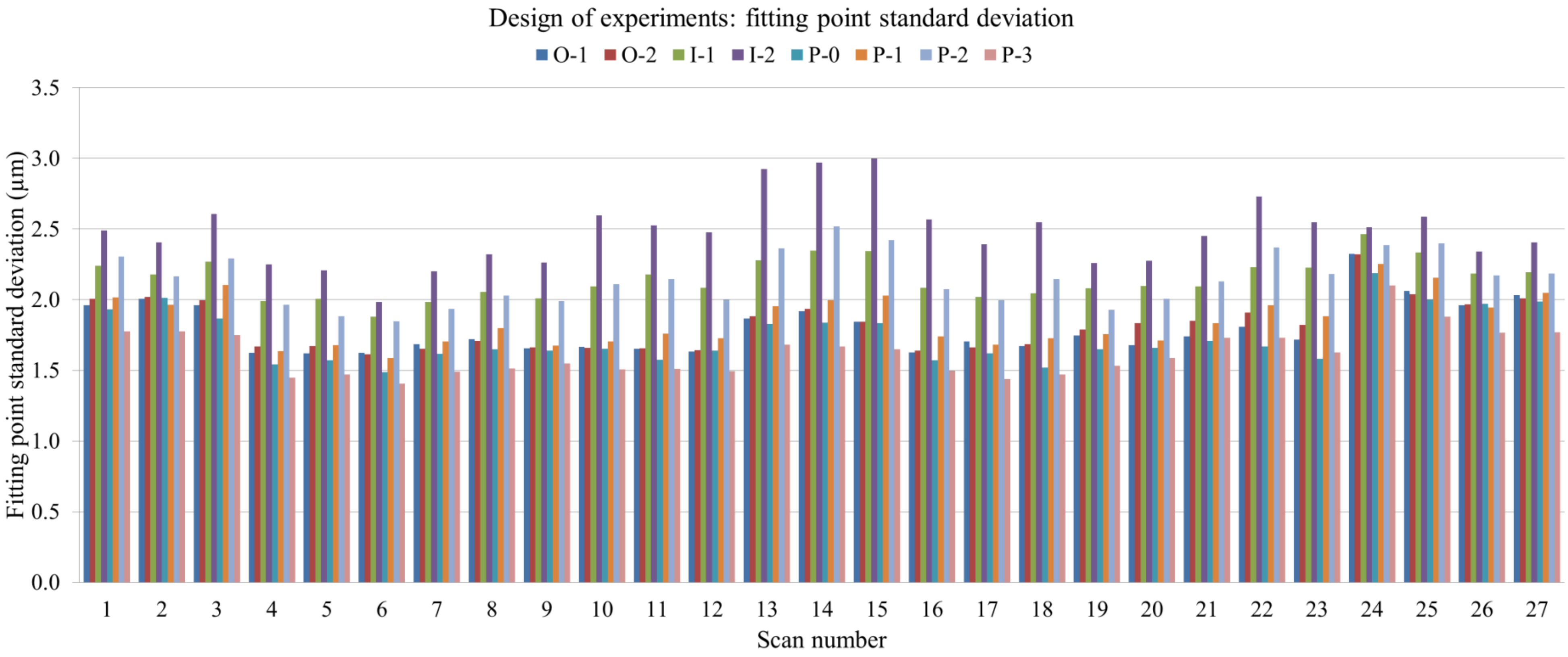

Figure 4.16 *Design of experiments: fitting point standard deviations different features. "O-1, O-2, I-1, I-2, P-0, P-1, P-2, P-3" are the 8 measurands defined in Fig 4.12. The list of machine settings of the 27 CT scans can be found in Table 4.7*

Several messages are revealed by observing the results in Fig 4.15 and 4.16:

1. Scan Nr.1, 2, 3, 13, 14, 15, 25, 26 and 27 have larger edge offsets than the other scans; and they all share one common property: largest voxel size (52.1 µm). Increasing the voxel size will increase the uncertainty of the thresholding process. Thus, the voxel size is an important influence factor for the thresholding edge offset errors.

2. The deviations of many CT dimensional measurements are within ±10 µm when compared to the CMM reference values. This yields an order of magnitude similar to the one axis accuracy of the tactile CMM stated by the manufacturer, which is +/- (4.2 +L/200) um with L in mm.

3. The features' fitting qualities (fitting point standard deviation) are influenced by the voxel size. When the voxel size increases, the fitting point standard deviations will also increase. Evidences can be found by comparing average fitting point standard deviations of scan Nr. 1, 2, 3, 13, 14, 15, 25, 26 and 27 to those of the other scans.

4. The fitting point standard deviations of inner features (inner hole and the covered part of the pin) are shown to be worse. As shown in Fig 4.17, it can be noticed that the gray values of "inner air" are relatively higher than those of "outer air". Thus, the inner surfaces' signal to noise ratio is also lower than that of outer surfaces'.

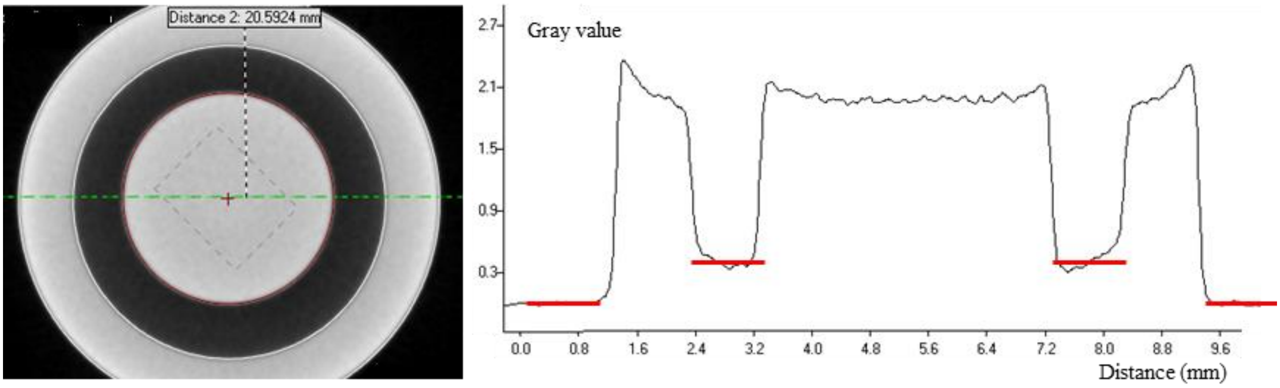

***Figure 4.17** The gray value profile along the "green line" through a reconstructed slice of the test setup. It shows that the gray value of air varies depending on the location*

To further analyze the large amount of measurement data, 5 indicators were defined to evaluate the overall quality of each CT scan.

<u>"O1, O2, I1, I2, P0, P1, P2, P3" stand for the edge offsets indicated in Fig 4.15.</u>

"Internal-external offset average deviation" – difference between internal and external features' average edge offsets.

$a = (O1 + O2 + P0 + P1 + P2 + P3)/6 + (I1 + I2)/2$ (3)

"Internal offset deviation" – difference between edge offsets of two inner holes.

$b = I1 - I2$ (4)

"Step cylinder external offset deviation" – difference between edge offsets of two outer cylinders.

$c = O1 - O2$ (5)

"Pin offset deviation range" – difference between edge offsets of the middle pin diameters at different locations.

d = MAX (P0, P1, P2, P3) – MIN (P0, P1, P2, P3) (6)

"CT-CMM offset range" – range of deviations from the CMM reference values.

e = MAX (O1, O2, I1, I2, P0, P1, P2, P3) – MIN (O1, O2, I1, I2, P0, P1, P2, P3) (7)

The first four quality indicators evaluate local dimensional deviations while the last quality indicator evaluates the global deviation range. These quality indicators were calculated for each CT scan and the results can be found in Table 4.9. In addition, they are also plotted and shown in Fig 4.18.

Unit: µm	B1			B2			B3		
	C1	C2	C3	C1	C2	C3	C1	C2	C3
Internal-external offset average deviation									
A1	5.5	3.7	4.0	5.2	3.8	3.6	4.8	3.5	1.3
A2	-0.7	-1.0	-2.9	3.0	3.0	-1.7	3.6	2.7	-1.6
A3	-4.4	-3.2	-5.5	2.1	1.7	-2.4	-0.3	1.1	-3.8
Internal offset deviation									
A1	-1.7	-1.7	-0.9	-1.3	-1.9	-1.3	-2.9	-1.9	-3.9
A2	-0.5	-1.1	-0.1	-1.7	-1.7	-0.3	-1.9	-3.5	-2.7
A3	0.1	-0.7	0.5	-1.3	-1.5	-2.1	-1.1	-2.7	-1.5
Step cylinder external offset deviation									
A1	-0.3	-0.1	-0.7	-0.7	-0.7	-1.1	-0.1	-0.3	-0.5
A2	0.9	0.7	-0.5	0.1	-0.3	-0.9	0.5	-0.3	-0.7
A3	1.7	0.7	-0.3	0.5	0.1	-0.7	0.5	0.7	0.1
Pin offset deviation range									
A1	1.6	2.0	4.6	3.4	2.8	7.0	2.4	4.2	6.6
A2	2.0	1.4	3.0	1.2	2.2	3.0	1.2	2.0	2.2
A3	4.2	3.0	4.0	1.0	2.2	4.2	2.4	3.4	4.4
CT-CMM offset range									
A1	5.6	7.6	16.6	6.8	9.4	22.2	7.4	11.8	24.4
A2	3.5	4.9	12.0	5.5	8.8	16.8	6.3	11.2	20.8
A3	8.4	3.0	11.3	5.1	8.3	22.8	5.3	11.7	23.3

Table 4.9 *The quality indicators' values for each CT scan. The terms "A, B and C" stand for the three influence factors (X-ray voltage, filter and voxel size). The terms "1, 2 and 3" stand for the three levels. More information can be found in Table 4.7.*

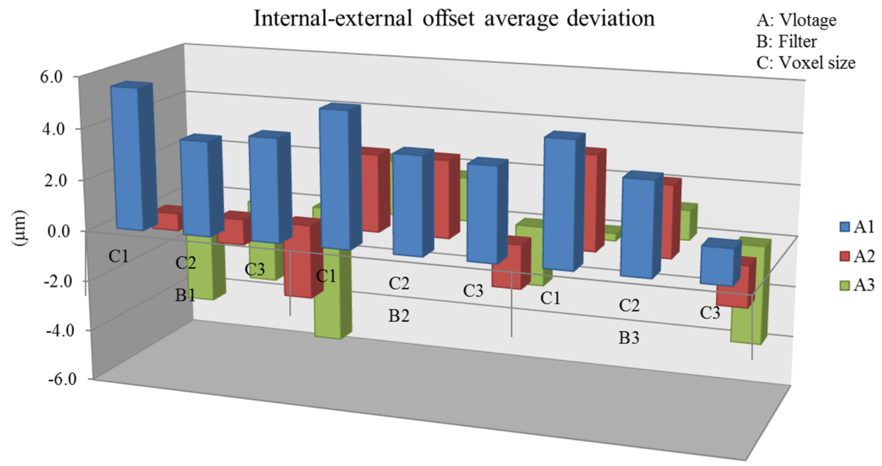
Internal-external offset average deviation
A: Vlotage
B: Filter
C: Voxel size
6.0
4.0
2.0
0.0
-2.0
-4.0
-6.0
(µm)
C1
C2
C3
B1
C1
C2
C3
B2
C1
C2
C3
B3
A1
A2
A3

(a)

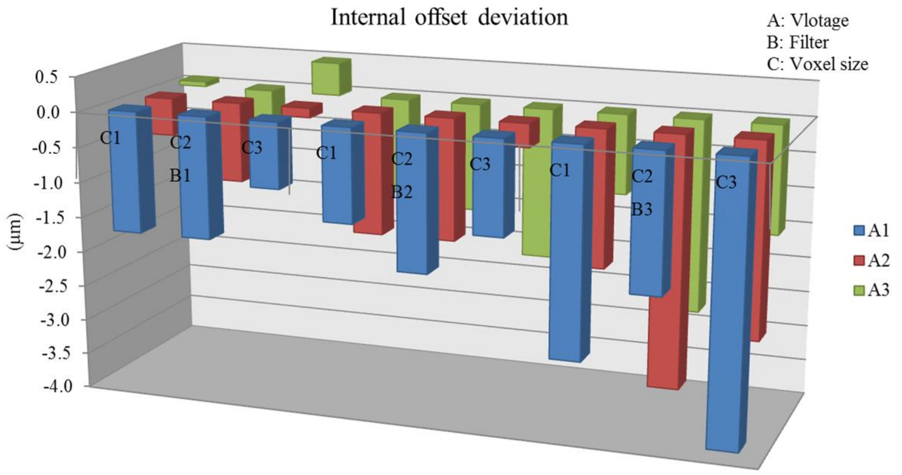
Internal offset deviation
A: Vlotage
B: Filter
C: Voxel size
0.5
0.0
-0.5
-1.0
-1.5
-2.0
-2.5
-3.0
-3.5
-4.0
(µm)
C1
C2
C3
B1
C1
C2
C3
B2
C1
C2
C3
B3
A1
A2
A3

(b)

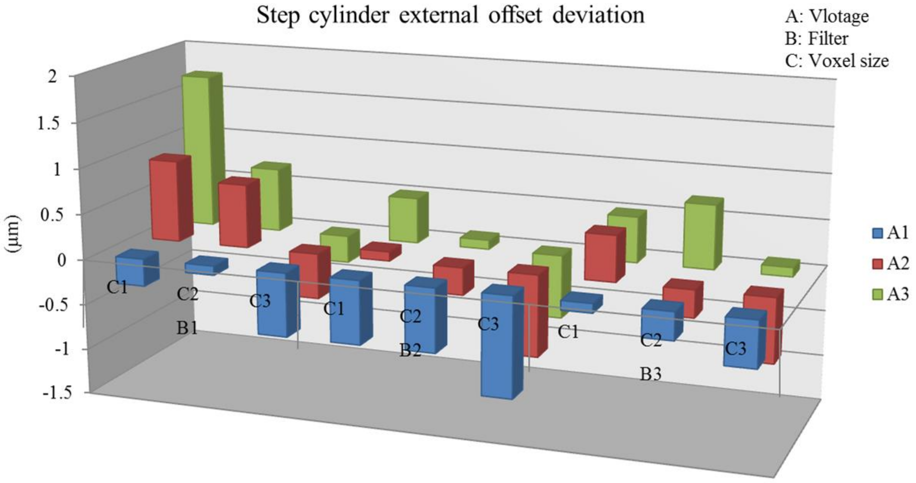
Step cylinder external offset deviation
A: Vlotage
B: Filter
C: Voxel size
2
1.5
1
0.5
0
-0.5
-1
-1.5
(µm)
C1
C2
C3
B1
C1
C2
C3
B2
C1
C2
C3
B3
A1
A2
A3

(c)

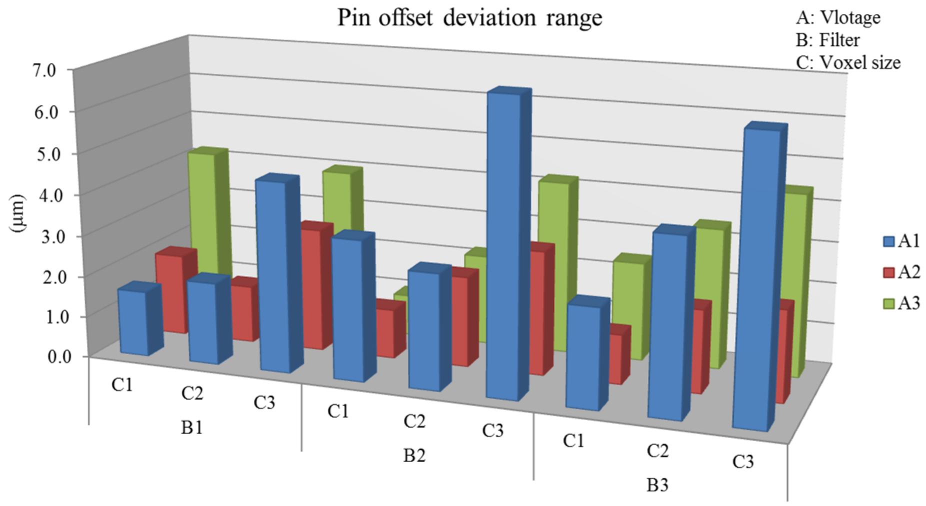

(d)

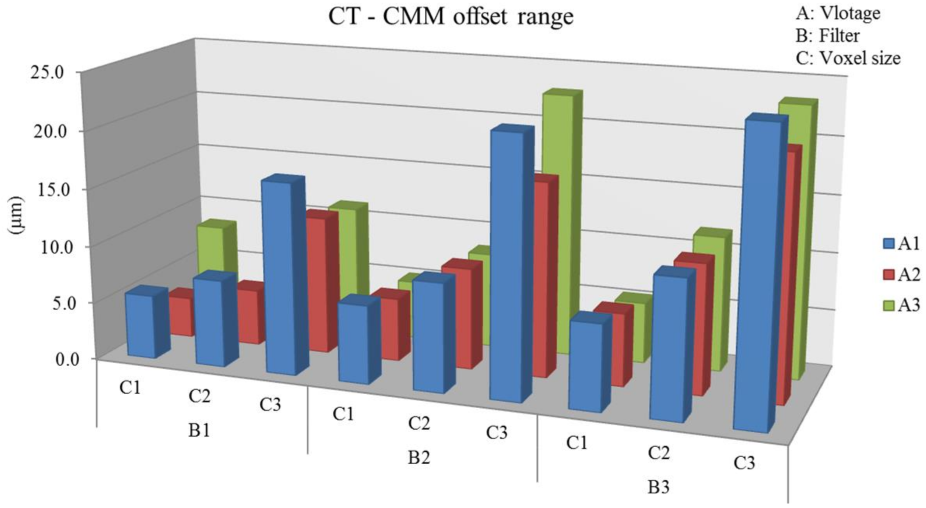

(e)

Figure 4.18 *Design of experiments: the values of different quality indicators for each CT scan. The terms "A, B and C" stand for the three influence factors (X-ray voltage, filter and voxel size). The terms "1, 2 and 3" stand for the three levels. More information can be found in Table 4.7.*

In order to have a clear view of the significances of each influence factor and their interactions, analysis of variances (ANOVA) has been performed for each quality indicator. The significance level "α" was set to be 0.05. The resulting p-values of the three influence factors and their interactions for different quality indicators are listed in Table 4.10. The complete collection of results of these ANOVA can be found in Appendix C.

	A	B	C	AB	AC	BC
Internal-external offset average deviation	1E-07	4E-05	5E-06	2E-04	0.007	0.021
Internal offset deviation	0.101	0.002	0.273	0.328	0.529	0.564
Step cylinder external offset deviation	0.001	0.003	3E-04	0.487	0.173	0.425
Pin offset deviation range	0.001	0.516	1E-04	0.019	0.042	0.134
CT-CMM offset range	0.072	0.001	1E-06	0.925	0.491	0.026

Table 4.10 *The p-values of the three influence factors and their interactions for different quality indicators. "A, B, C, AB, AC and BC" stand for the influence factors and their interactions. The red marked values are smaller than the significance level (0.05) and thus the corresponding influence factors are proven to be significant.*

Several conclusions can be drawn from the above analysis regarding each quality indicator:

"Internal-external offset average deviation"

The ANOVA proves that all three influence factors and their interactions have significant impact on the "internal-external offset average deviation". As shown in Fig 4.18 (a), decreasing the X-ray voltage or increasing the voxel size will both result in a relatively smaller value. Generally speaking, there are two major causes for this offset deviation: the beam hardening effect on the external surfaces and the signal to noise ratio around the internal surfaces. To reduce this offset deviation, one should try to limit the beam hardening level on the external surfaces and to improve the internal surfaces' signal to noise ratio. Thus, one has to keep good balance between these two effects when selecting the scanning parameters. For instance, in this DOE, small internal-external offset variations (in their absolute values) are achieved when applying medium X-ray voltage – heavy filter – small voxel size (A2B1C1) and low X-ray voltage – less filtration – small voxel size (A3B3C1).

"Internal offset deviation"

The ANOVA indicates the filtration to be the most important factor regarding the internal offset deviation. Fig 4.18 (b) shows that the magnitude of internal offset deviation is smaller when using heavier filters (2 mm copper filter). These surfaces suffer from X-ray scattering noise which can be largely reduced by pre-filtration. Thus, to reduce the internal offset deviation, one should apply sufficient pre-filtration.

"Step cylinder external offset deviation"

All three influence factors are proven to be significant regarding the external offset deviation. Generally speaking, decreasing the X-ray voltage and decreasing the voxel size can both increase the value of the offset deviation. Due to the beam hardening effect which enhances the contrast of external surfaces, the magnitude of this offset deviation is relatively small. Except for setting combination A3B1C1 (low X-ray voltage – heavy filtration – small voxel size), the offset deviation of all other setting combinations are within the repeatability range of the measuring software (VGStudio Max v2.2): ±1 µm.

“Pin offset deviation range”

This quality indicator describes the difference in the edge offsets with/without surrounding materials. Similar to the “internal-external offset deviation”, this quality indicator is also influenced by the differences in the level of beam hardening effect and in the signal to noise ratio at different locations. The only difference is that the measurements performed on the pin are still considered as “outer” dimensions (convex feature) even for the two sections that are surrounded by the outer step cylinder. Due to the beam hardening effect, these surfaces still possess relatively high edge contrast and are less affected by the X-ray scattering noise than the surfaces of the internal holes. The X-ray voltage and its interaction with the other two influence factors are all proven to be influential. In addition, the voxel size also plays an important role. Fig 4.18 (d) shows that the combination of small voxel size and medium X-ray voltage can generate relatively good results.

“CT-CMM offset range”

This quality indicator gives an overview of the possible offset range when taking tactile CMM as reference. The ANOVA indicates significant influence from filter, voxel size and their combination; this can also be noticed from Fig 4.18 (e): the offset range increases when reducing the filtration level, and decreases when decreasing the voxel size. The filtration can reduce the internal X-ray scattering noise and thus limit the edge offset of inner features. Generally speaking, using smaller voxel size can reduce the uncertainty of the thresholding process and thus reduce the edge offset range.

Thus, taking all quality indicators into consideration, we can see that the “optimal” setting combination would be: medium X-ray voltage – heavy filtration – small voxel size (A2B1C1).

Due to the limited sample size and the lack of replicates, the results of these ANOVA tests might vary to certain extent. Nevertheless, these analyses give good indications on the relative significance level of different influence factors and their interactions regarding different offset terms.

- **Minimum transmission ratio (MTR)**

It was proven that the influences of X-ray voltage, filter and voxel size are often correlated. The “minimum transmission ratio” (MTR) can indicate the combined effects of all three influence factors; thus, its influence was further investigated. MTR is defined as the ratio of X-ray transmission along the longest penetration path of an object and is frequently used in non-destructive testing (NDT) applications. For example, the EN 16016-2 standard proposes a minimal transmission of about 10 to 20% for best SNR and measurement results *[EN 16016-2, ÖNORM EN 16016:2011-08 Non-destructive testing - Radiation methods – Computed tomography];* ISO 15708-2 suggests 14% minimal transmission for optimal contrast sensitivities *[ISO 15708:2002, Non-destructive testing - Radiation methods - Computed tomography]*. However, the influence of MTR on CT dimensional metrology is yet unknown.

Within this DOE analysis, the minimum transmission ratio was calculated from two 2D X-ray projection images. The calculation procedure is described below.

Rotate the workpiece so that the longest penetration length of the workpiece is perpendicular to the X-ray detector; start the CT scan from this angular position. The minimum transmission ratio can be calculated using the following formula

$$\mathbf{MTR = (D_1 + D_2) / (B_1 + B_2)} \qquad (8)$$

MTR – minimum transmission ratio

D_1 *– lowest pixel gray value on the first 2D projection image (2D projection image at 0°)*

D_2 *– lowest pixel value on the last 2D projection image (2D projection image at 360°)*

B_1 *– average pixel gray value of a fixed sampling region on the first 2D projection image*

B_2 *- average pixel gray value of a fixed sampling region on the last 2D projection image*

Remark: theoretically, D_1 *and* D_2*,* B_1 *and* B_2 *are equal. However, due to the dynamic behavior of the X-ray source and the X-ray detector, there will be differences between their values.*

Following the above mentioned procedure, the MTR was calculated for each CT scan, shown in Table 4.11.

Unit: %	B1			B2			B3		
	C1	C2	C3	C1	C2	C3	C1	C2	C3
A1	18	19	21	13	14	15	7	7	8
A2	14	15	16	9	10	11	5	5	6
A3	11	12	14	7	8	9	4	4	5

Table 4.11 *The calculated MTR for each CT scan. The terms “A, B and C” stand for the three influence factors (X-ray voltage, filter and voxel size). The terms “1, 2 and 3” stand for the three levels. More information can be found in Table 4.7*

Table 4.11 shows that the MTR increases when increasing the X-ray voltage, filtration level and voxel size. Moreover, the influences of changing X-ray voltage and filtration levels appear to be more significant than the influence of varying the voxel size. The MTR and the 5 quality indicators are plotted together in Fig 4.20.

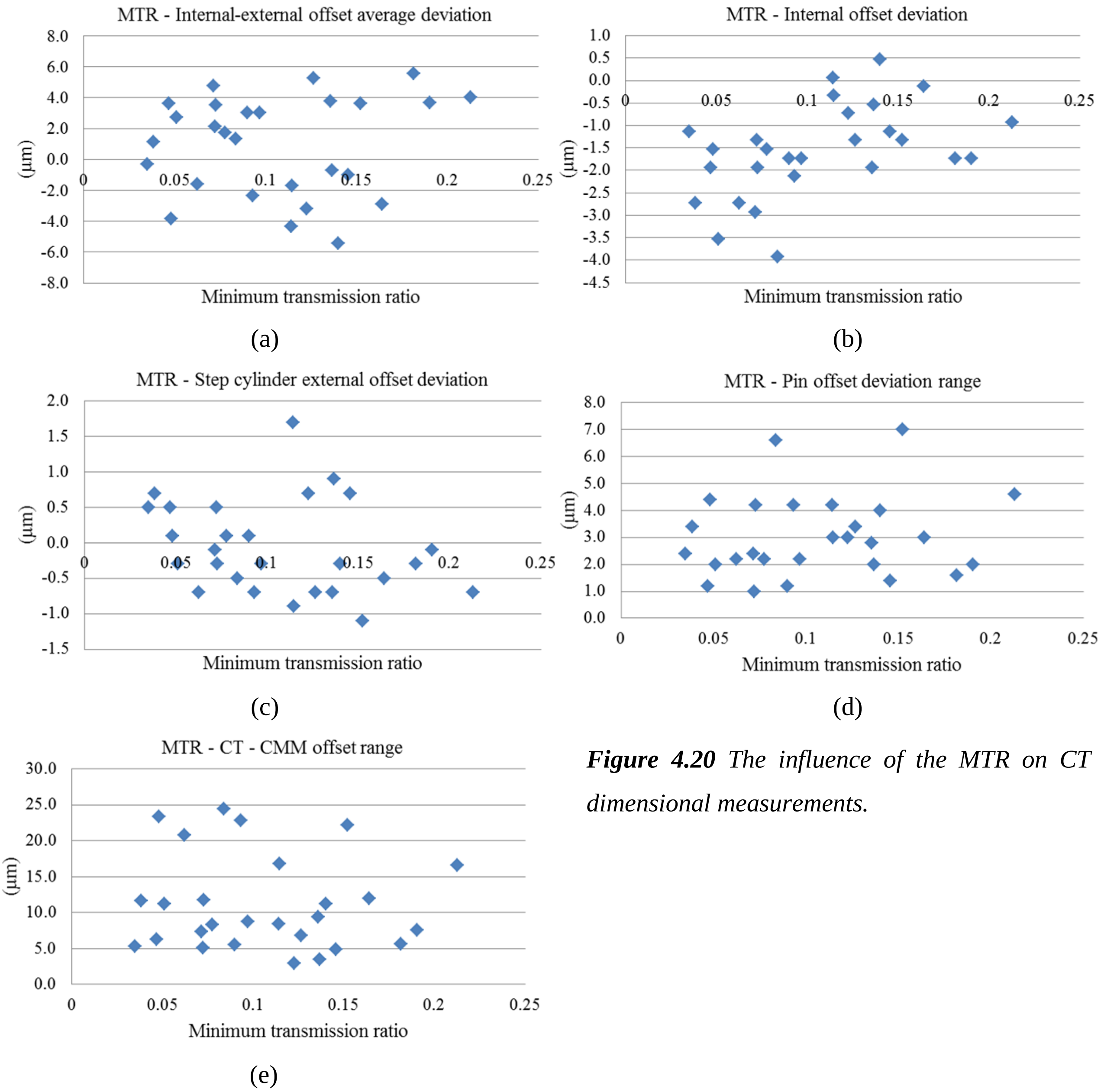

(a) (b)

(c) (d)

(e)

Figure 4.20 *The influence of the MTR on CT dimensional measurements.*

Fig 4.20 (b) indicates that higher MTR leads to smaller (in absolute value) internal offset deviation. However, no particular trend or correlation can be found between the MTR and the other four quality indicators. CT scans sharing the same MTR can generate totally different dimensional measurement results. Although the general guidelines for CT NDT applications have suggested to set the MTR to around 14%, or between 10 and 20%, this cannot be directly transferred to CT dimensional metrology applications. First of all, MTR does not indicate the relative importance between different influence factors. For example, the combination of A1B2C3 and A2B1C2 can both lead to 15% MTR (Table 4.11); however, the dimensional measurement results of the latter are much better than the former. Second, MTR only reflects the transmission through the maximum penetration length, image regions with higher transmissions may be acquired with suboptimal image quality.

4.2.4 Conclusions

Several conclusions can be drawn regarding the influence and relationship between X-ray voltage, filter and voxel size:

- The design of experiments proves that the X-ray voltage, the filter usage and the voxel size are closely related scanning parameters.
- The “ANOVA” gives a good indication of the relative importance of the X-ray voltage, the filter usage and the voxel size and their interactions when evaluating different quality terms of dimensional measurements.
- The “optimal” scanning parameters differ from case to case. For the tested setup (the combination of a steel pin and a steel hollow step cylinder), it is suggested to use: medium level X-ray voltage + heavy filtration + small voxel size.
- MTR (minimum transmission ratio) cannot be applied as a standalone indicator when setting up CT scans for dimensional metrology applications.

CHAPTER 5

Influence of Post-processing Parameters

Similar to many other measuring techniques, data post-processing is an essential step for CT dimensional metrology applications. This first part of this chapter elaborates the pros and cons of two commonly applied thresholding techniques; while the second part of this chapter looks at the influence of beam hardening effect on dimensional measurements. In addition, two commonly applied beam hardening correction methods are evaluated.

5.1 Thresholding techniques – advantages and disadvantages

Thresholding is an essential step for CT dimensional metrology. It determines the material's surface, hence directly influences the accuracy of dimensional measurements. Currently, there are two commonly applied thresholding methods: global thresholding and local adaptive thresholding, as shown in Fig 5.1.

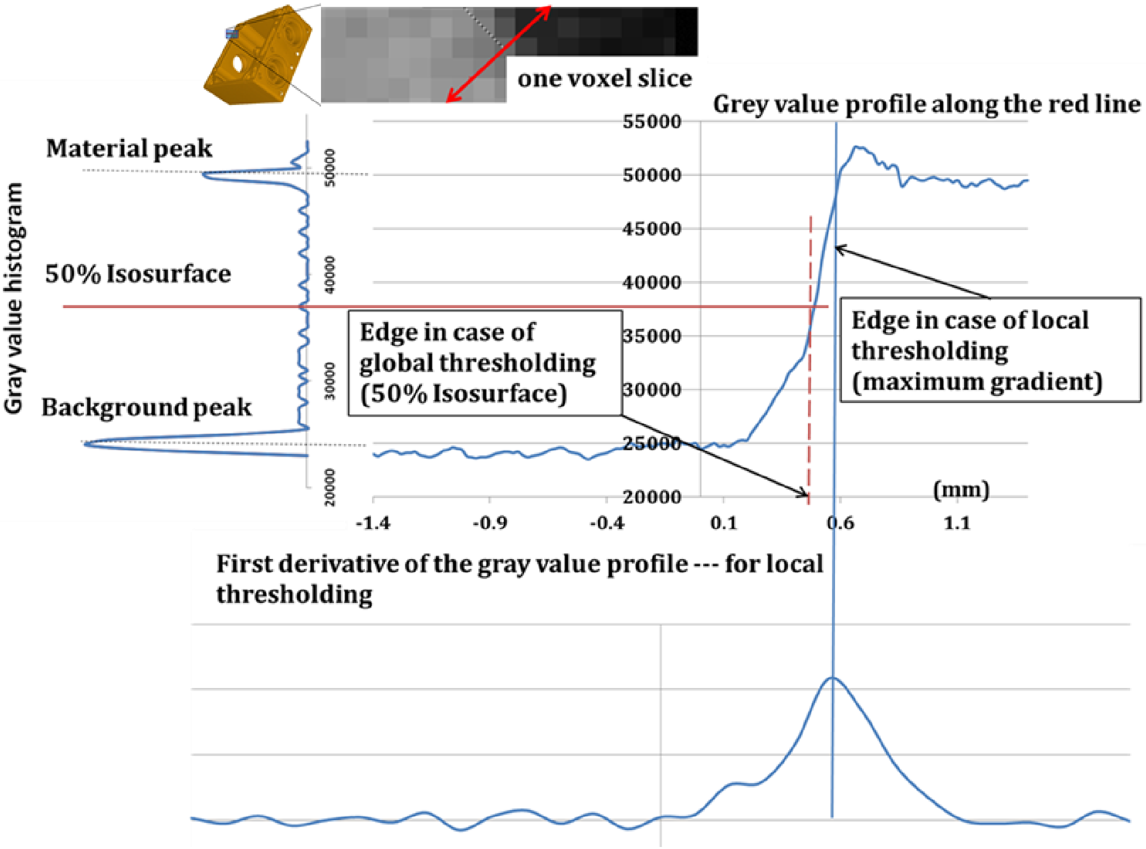

Figure 5.1 *Illustration of two thresholding methods: 50% isosurface global thresholding and local adaptive thresholding [Tan Y. et al., 2011]*

The global thresholding method defines the material surface with one single gray value. The local adaptive thresholding method starts from a preliminary surface determined by the global thresholding algorithm, also known as starting contour. Subsequently, polynomial functions (e.g. 5th grade polynomial) are fitted within a predefined region (also known as search distance) along the normal direction of the starting contour. This is followed by calculating the largest gradient of this function (first derivative) which will be seen as the new material edge *[Schmitt R. et al., 2011]*.

These two thresholding methods are compared in three aspects: surface quality of the 3D model, accuracy of dimensional measurements and behavior when shifting the starting contour in the histogram.

5.1.1 Surface quality of the 3D model

As shown in Fig 5.2, the surface of a steel step gauge's (Fig 3.1) CT 3D model was determined using both global and local thresholding methods. 11 planes were fitted onto each model and the fitting point standard deviations were recorded (Table 5.1).

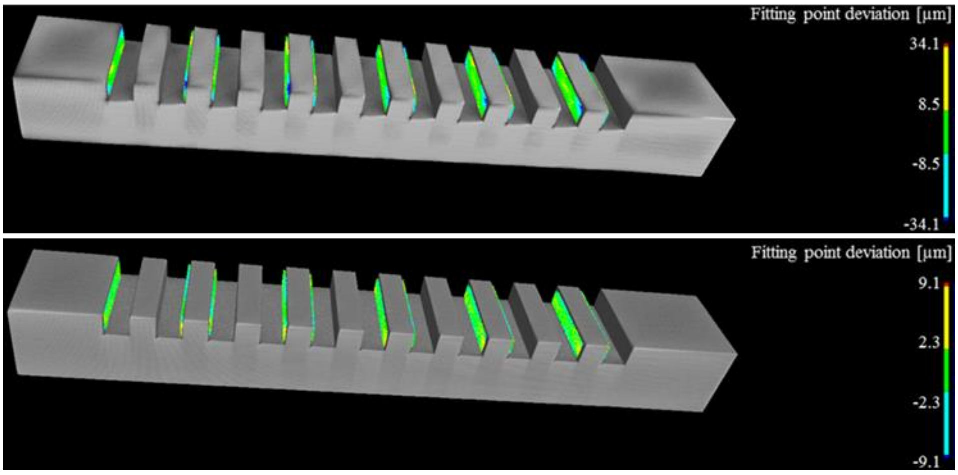

Figure 5.2 *CT 3D models of a steel step gauge generated using both global (top) and local (bottom) thresholding methods.*

Plane Nr.	Global thresholding	Local thresholding
	fitting point standard deviation (µm)	
1	3.5	1.9
2	3.2	1.9
3	3.3	1.9
4	3.5	2.0
5	3.6	2.1
6	3.6	2.0
7	3.5	2.0
8	3.8	2.1
9	3.4	2.0
10	3.6	2.0
11	3.6	2.0

Table 5.1 *The fitting point standard deviations of the 11 planes shown in Fig 5.2*

Table 5.1 shows that the fitting qualities of the planes are much better when using local thresholding than using global thresholding. Generally speaking, there are many factors (X-ray scattering, beam hardening effect etc.) that can cause surface noises and local gray value variations. Due to the nature of using one single gray value for surface determination, the global thresholding method is not robust against these surface noise and local variations. On the contrary, the local thresholding method defines the material edge using local gray value gradient; in this way, surface noise and local variations can be accounted for. Thus, the local thresholding method often outperforms the global thresholding method in the aspect of surface quality.

However, due to the X-ray power limitation, it is often difficult to obtain a sufficient signal to noise ratio when scanning large metallic objects. Under these circumstances, the global thresholding method might be a better choice. An example is shown in Fig 5.3, in which the 3D CT model generated with local adaptive thresholding presents a very “noisy” surface.

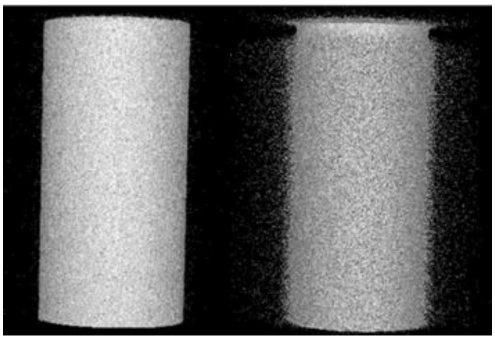

Figure 5.3 *CT 3D model of an Aluminum cylinder (Ø35mm). Left: global thresholding, Right: local thresholding*

5.1.2 Accuracy of dimensional measurements

The CT scans from the design of experiments in Chapter 4 are reused in this section to investigate the influence of thresholding methods on dimensional measurements

Five measurement quality indicators that describe both global measurement error range and local dimensional deviations have been used for the following comparison.

“Internal-external offset average deviation” – difference between internal and external features’ average edge offsets.

“Internal offset deviation” – difference between edge offsets of two inner holes.

“Step cylinder external offset deviation” – difference between edge offsets of two outer cylinders.

“Pin offset deviation range” – difference between edge offsets of the middle pin diameters at different locations.

“CT-CMM offset range” – range of deviations from the CMM reference values.

More detailed explanations on these quality indicators can be found in Chapter 4, Section 4.2.2.4.

The values for each quality indicator when using global and local thresholding methods are shown in Table 5.2. In addition, these values are also plotted in Fig 5.4.

Unit (µm)	Internal-external offset variation		Internal offset variation		Step cylinder external offset variation		Pin offset variation		CT-CMM offset range	
Scan Nr.	global	local	global	local	global	local	global	local	global	local
1	0	-2	-12	0	2	-1	31	3	57	17
2	1	-2	-11	-2	2	-1	31	4	59	23
3	8	4	-25	-1	2	-1	44	7	70	22
4	-19	5	-2	-1	1	-1	6	3	85	7
5	-26	3	13	-2	2	0	2	1	91	6
6	-26	2	19	-1	1	1	2	1	87	5
7	-44	2	32	-2	1	0	2	2	135	8
8	-35	4	8	-2	1	-1	4	3	125	9
9	-39	3	20	-2	1	0	2	2	129	9
10	-197	3	85	-4	2	0	8	2	350	11
11	-81	4	-6	-2	3	0	8	4	207	12
12	-56	1	-172	-3	2	1	7	3	248	12
13	4	-4	-39	-2	4	0	58	4	89	23
14	5	-2	-44	-3	4	-1	60	2	91	21
15	10	1	-56	-4	4	0	71	7	103	24
16	-71	5	-44	-3	2	0	2	2	180	7
17	-7	0	-182	-1	1	1	3	2	182	5
18	-92	4	-28	-2	2	1	3	1	183	6
19	-17	4	12	-2	1	0	2	2	86	8
20	-29	-1	25	-1	1	1	10	1	112	5
21	-35	-3	29	-1	1	1	14	3	126	3
22	-29	-4	28	0	1	2	12	4	107	8
23	-21	-1	20	-1	1	1	6	2	91	4
24	-7	6	5	-2	1	0	2	2	59	6
25	3	4	-4	-1	1	-1	23	5	54	17
26	-13	-5	-10	0	0	0	7	4	53	11
27	-9	-3	7	0	0	0	8	3	48	12

Table 5.2 *Design of experiments: the values for each quality indicator when using global and local thresholding methods.*

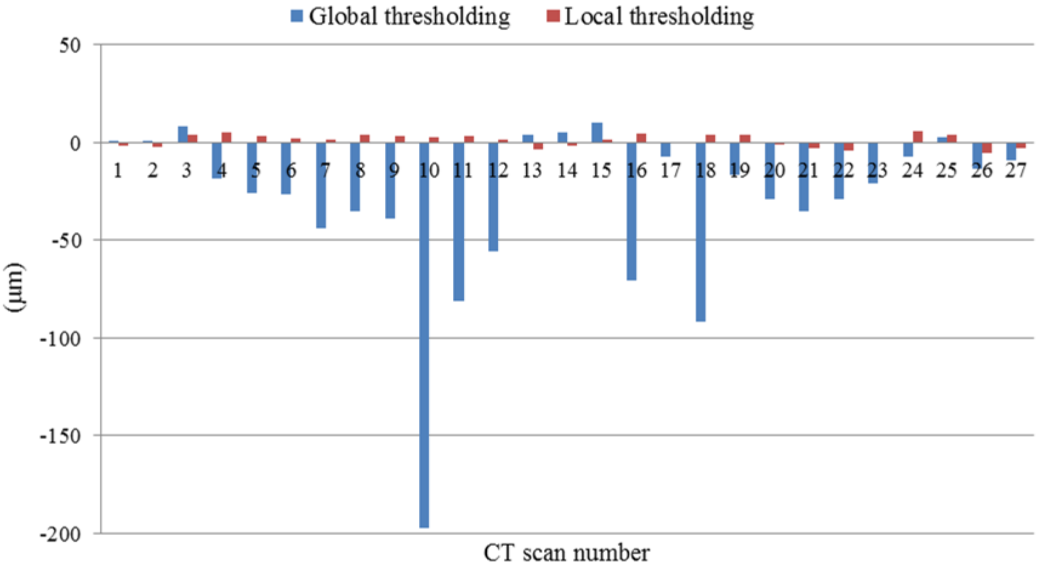

(a) Internal-external offset average deviation

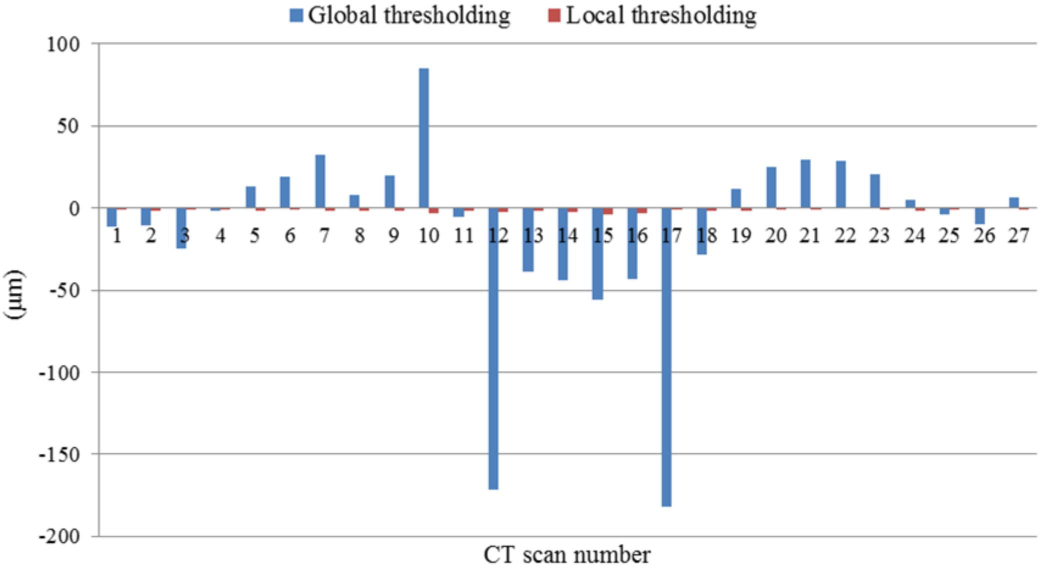

(b) Internal offset deviation

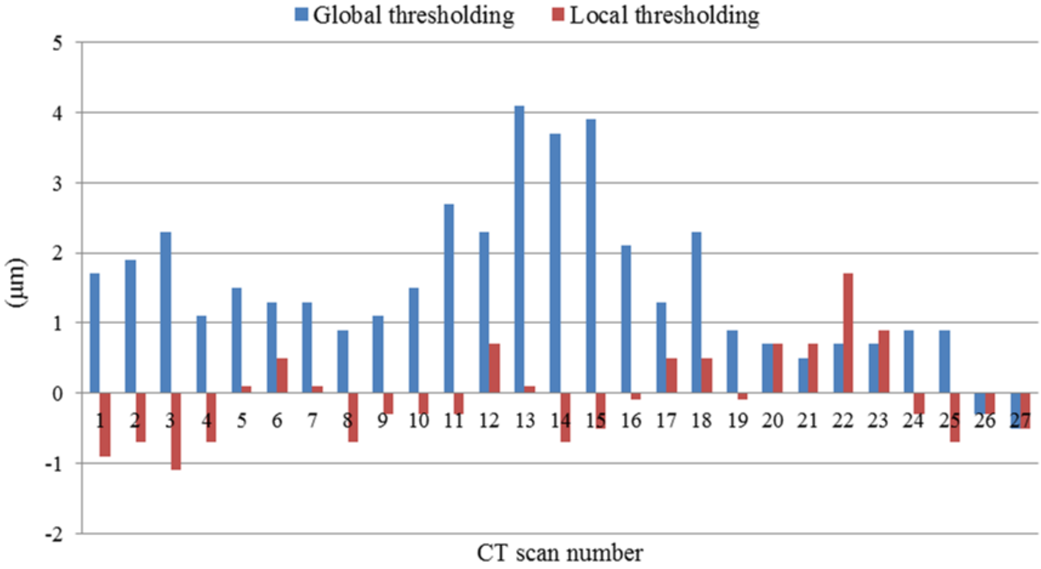

(c) Step cylinder external offset deviation

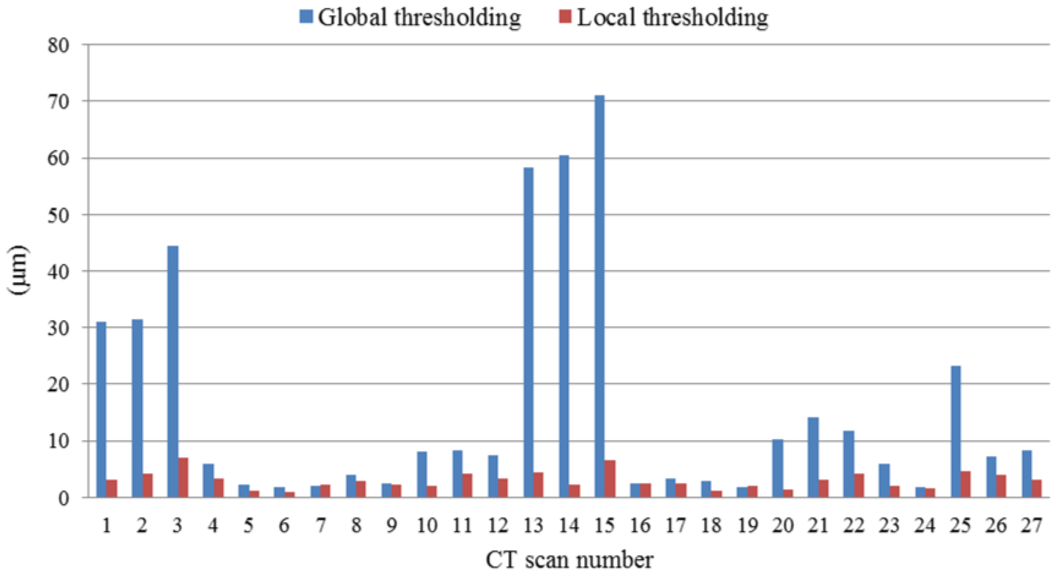

(d) Pin offset deviation range

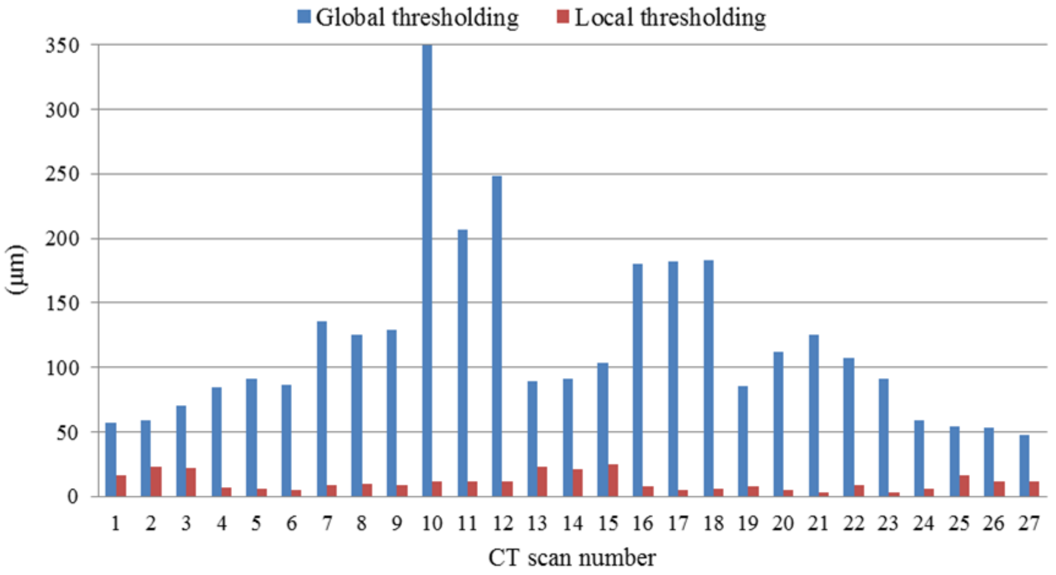

(e) CT-CMM offset range

Figure 5.4 *Comparison between global and local thresholding methods regarding the accuracy of dimensional measurements.*

Fig 5.4 clearly indicates that the local thresholding method outperforms the global thresholding method regarding the accuracy of dimensional measurements.

5.1.3 Behavior when shifting the isosurface/starting contour in the histogram

The isosurface (global thresholding)/starting contour (local thresholding) are usually put in the middle between the largest background (air) and material peaks. However, as shown in Fig 5.5, it is often necessary to manually shift the isosurface/starting contour for avoiding minor peaks (peaks caused by the fixation material, X-ray scattering noise or beam hardening etc.). Since this shifting process is entirely operator dependent, it is important to know how it influences the dimensional measurement results.

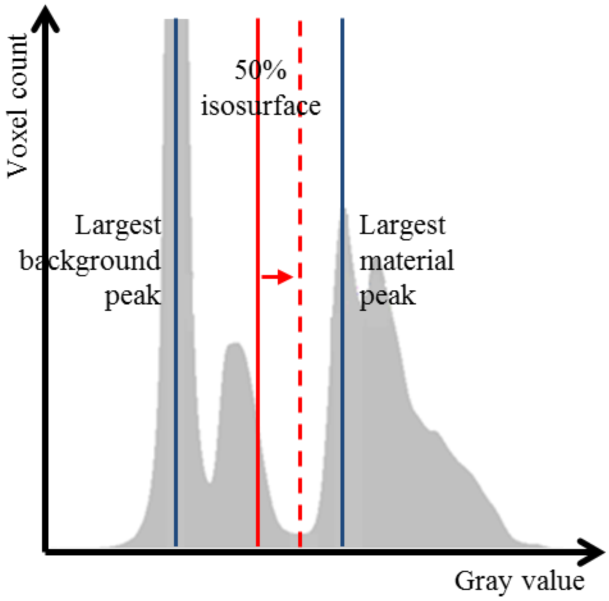

Figure 5.5 *Shifting the isosurface/starting contour (the red line) in the histogram to avoid minor peaks*

When global thresholding method is applied, changing the isosurface will also change the material's edge globally *[Tan Y. et al., 2011] [Kiekens K. et al., 2011]*. For instance, shifting the isosurface towards the background peak will result in increasing dimensions of convex features (e.g. shaft,...) and decreasing dimensions of concave features (e.g. hole,...).

A reference example *[Kiekens K. et al., 2011]* is adopted as depicted in Fig 5.6: 2 unidirectional and 2 bidirectional plane distances on an aluminum artefact have been measured. The material's surface has been determined using 50% isosurface. Significant edge offset errors have been noticed on the bidirectional distances which indicated a possibility for improvement by shifting the isosurface towards the background peak. Starting from the 50% isosurface, the initial edge offset on the bidirectional distances was around 45 µm. While shifting the isosurface towards the background peak, the edge offset decreased continuously and was reduced to ±5 µm, which was the same accuracy level as for the unidirectional distances. Thus, when applying a global thresholding method with known reference values, shifting the isosurface can be an effective way for improving the overall accuracy of the CT 3D model.

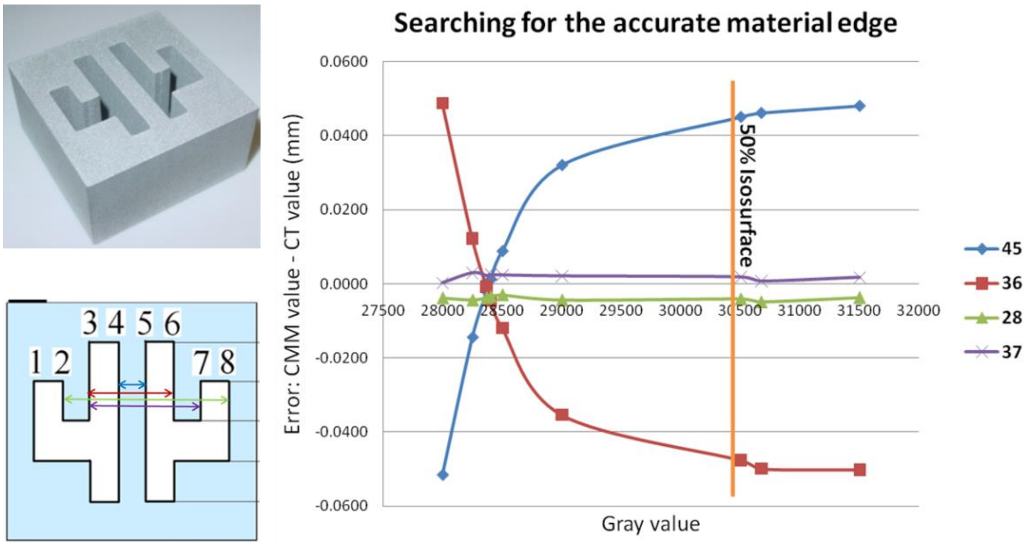

Figure 5.6 *Effect of shifting the thresholding starting contour on the dimensional measurement results [Kiekens Kim et al., 2011]*

Similarly, scan Nr.3 and Nr.20 from the design of experiment in Chapter 4 were selected to study the effects of changing starting contours when applying local thresholding method. Scan Nr.3 ranks in the lower half among 27 CT scans while scan Nr.20 outperforms most of the other scans. As shown in Fig 5.7, assuming the largest background peak is 0% and the largest material peak is 100%, 3 equally spaced starting contours were investigated (25%, 50% and 75%). Except for the starting contour, the influence of search distance was also studied. As discussed earlier, the search distance defines the region of interest for polynomial fitting along the gray value profile in the normal direction of the starting contour. As shown in Fig 5.8, the transition from air to material typically covers a few voxels and the ideal material edge is assumed to be within this region. In daily practice, the search distance is often set to be “2 voxel sizes”; this means that the local searching region is 2 voxel sizes for each side along the normal direction of the starting contour. In the following study, search distances “0.5” and “3” were also tested. Thus, 9 tests (3 starting contours × 3 search distances) were performed for each CT scan.

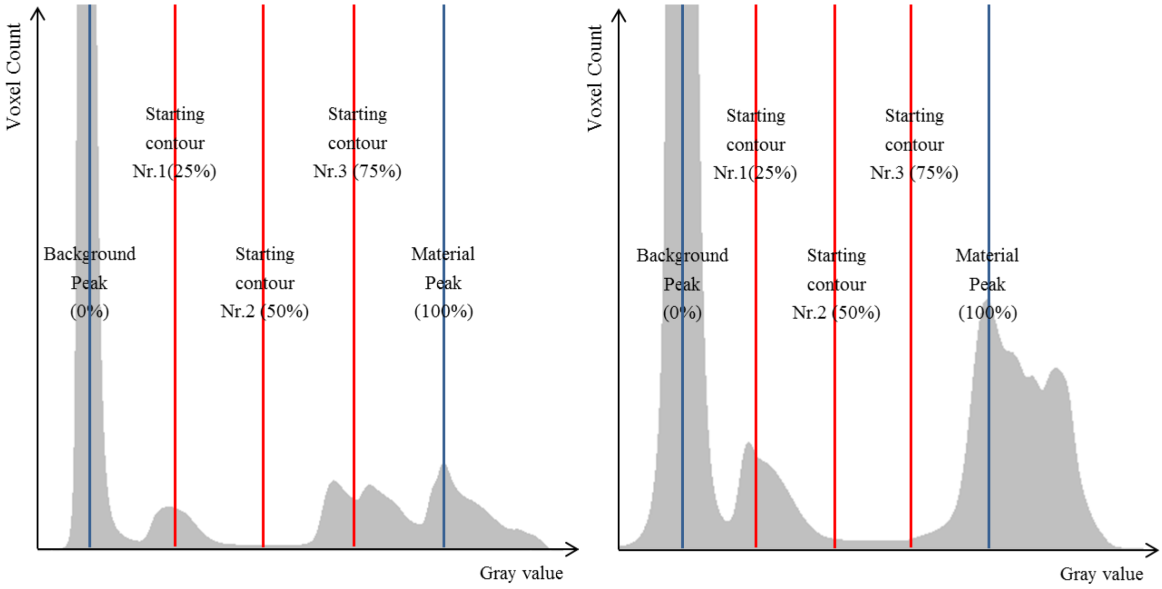

Figure 5.7 *Illustration of different starting contours. Left: histogram of scan Nr.3; Right: histogram of scan Nr.20. Scan Nr. 3 and Nr. 20 refer to two CT scans from the design of experiment on the test setup (Fig 4.11) discussed in Chpater 4*

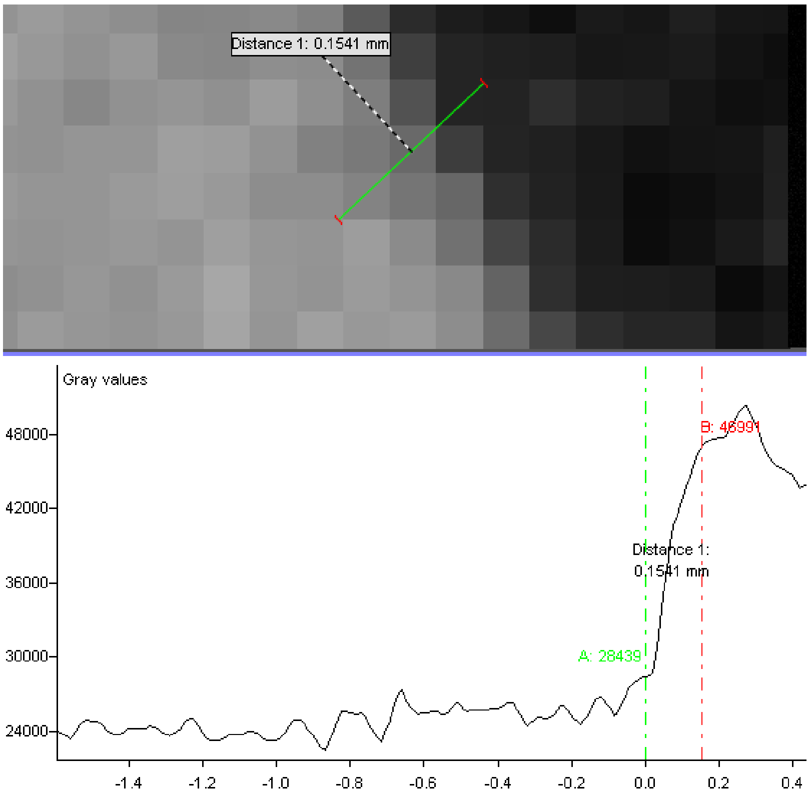

Figure 5.8 *Illustration of the transition region between material (left) and air (right) on a slice level.*

Five quality indicators (internal-external offset deviation range, internal offset deviation, step cylinder external offset deviation, pin offset deviation and CT-CMM offset range, detailed explanation can be found in Chapter 4, Section 4.2.2.4) were used to evaluate the measurement accuracy and local dimensional variations under each thresholding condition. The results are plotted in Fig 5.9 while the exact numbers can be found in Appendix D.

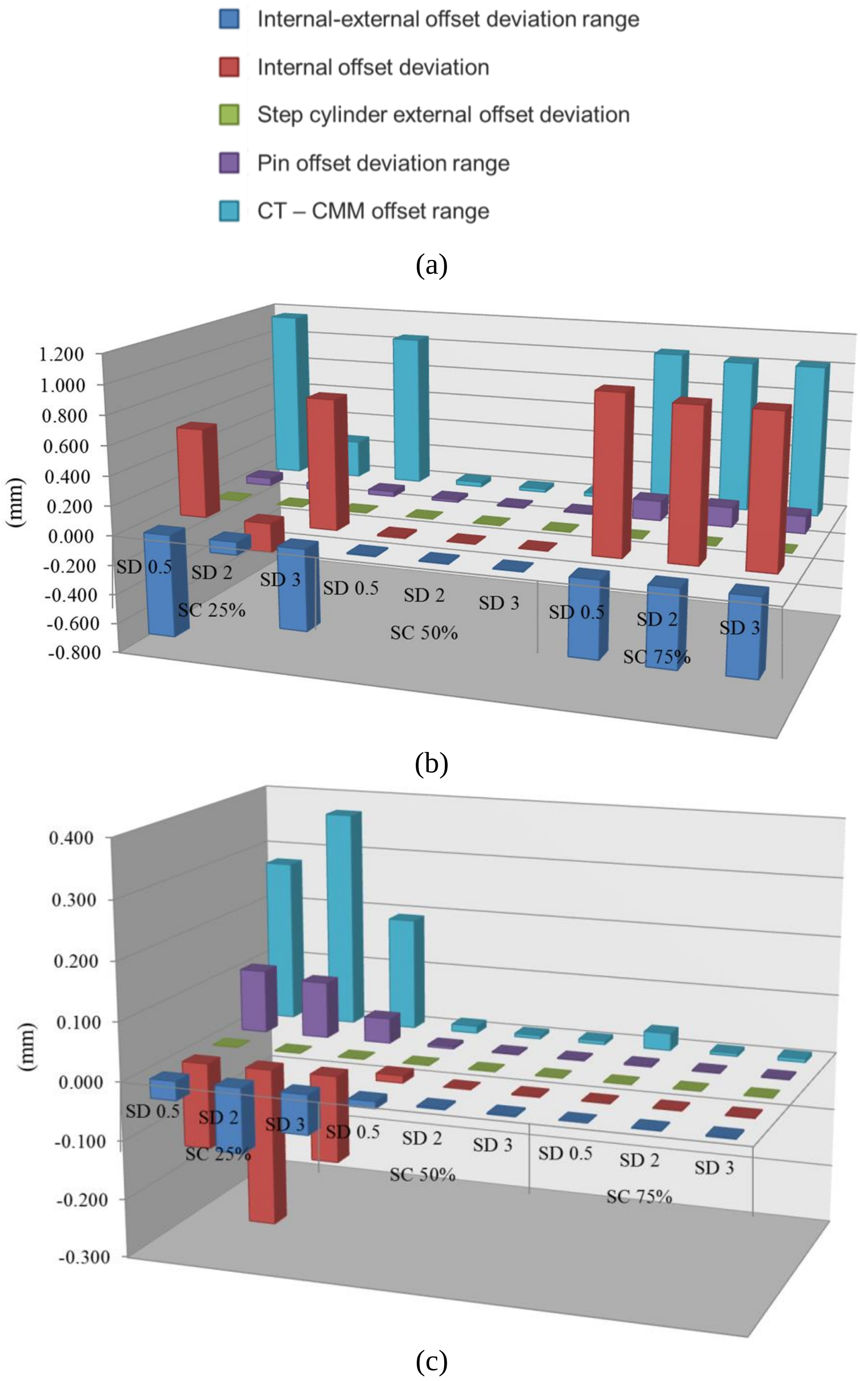

Figure 5.9 *Dimensional measurement results of two CT scans under different thresholding conditions.“SC” stands for starting contour, “SD” stands for search distance. (a) legend for different quality indicators (b) scan Nr.3 from the DOE analysis (c) scan Nr.20 from the DOE analysis*

As seen in Fig 5.9, the dimensional measurement results are significantly worse for both scans when using 25% starting contour; in addition, using 75% starting contour also produces bad results for scan Nr.3. Combining these observations with Fig 5.7, it can be noticed that these “bad” starting contours all cross large peaks in the histograms, hence result in relatively noisy surroundings around the starting contour and hinders the local edge searching process.

Furthermore, the measurement results were replotted after removing data of “bad” starting contours, shown in Fig 5.10.

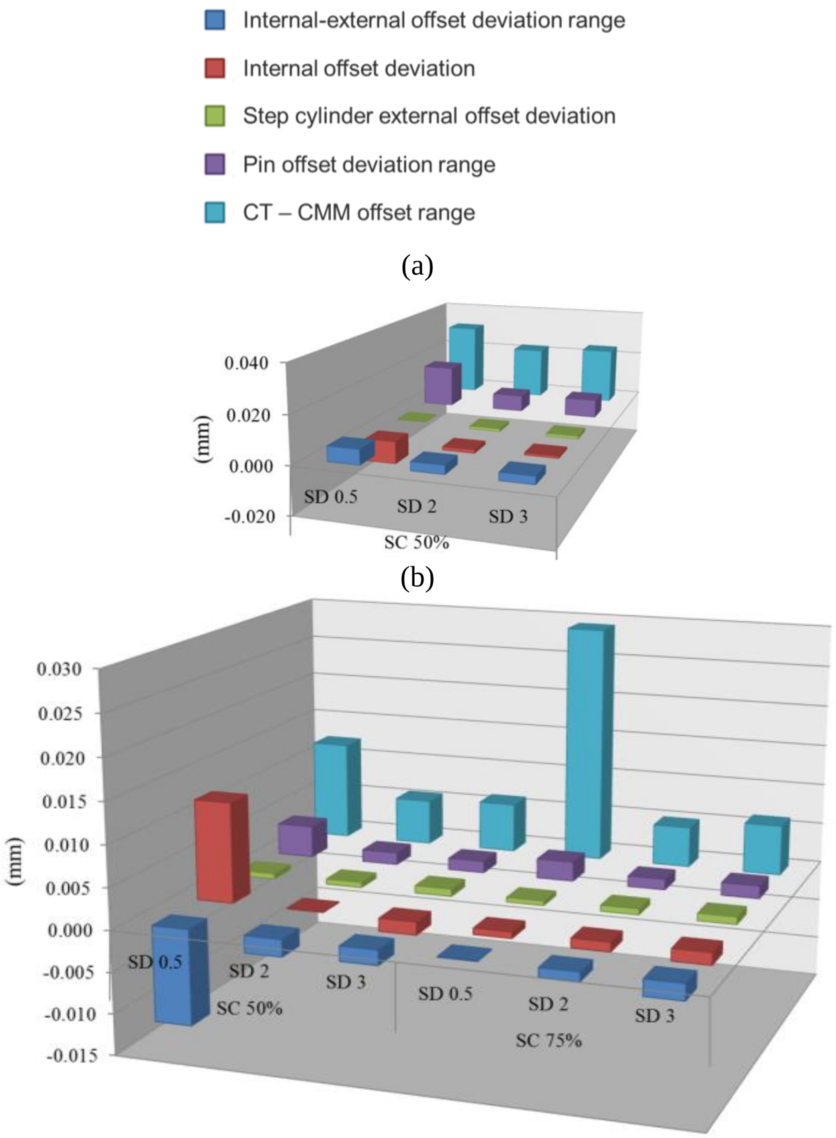

(a)

(b)

(c)

Figure 5.10 *Dimensional measurement results of two CT scans under different thresholding conditions. “a, b, c, d, and e” are five quality indicators (Chapter 4 – Section 5.2.2.4). “SC” stands for starting contour, “SD” stands for search distance. (a) legend for different quality indicators (b) scan Nr.3 from the DOE analysis (c) scan Nr.20 from the DOE analysis*

It can be seen from Fig 5.10 that using 0.5 voxel search distance produces the worse results while using 2 and 3 voxel search distances yields similar results.

As shown in Fig 5.11, to further analyze the influence of different search distances, a reconstructed slice was taken from scan Nr.3; the evolutions of material edges were observed at 3 locations: outer cylinder, inner hole and middle pin. The edge points were noted on the gray value profile and are shown in Fig 5.11.

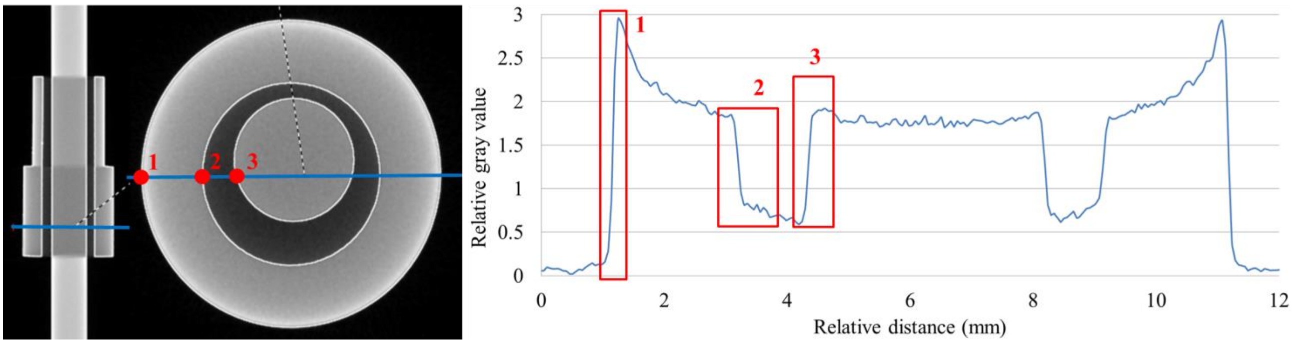

(a)

● Starting edge point ● Edge of SD0.5 ● Edge of SD2 ● Edge of SD3

▨ Range of SD0.5 ▨ Range of SD2 ▨ Range of SD3

(b)

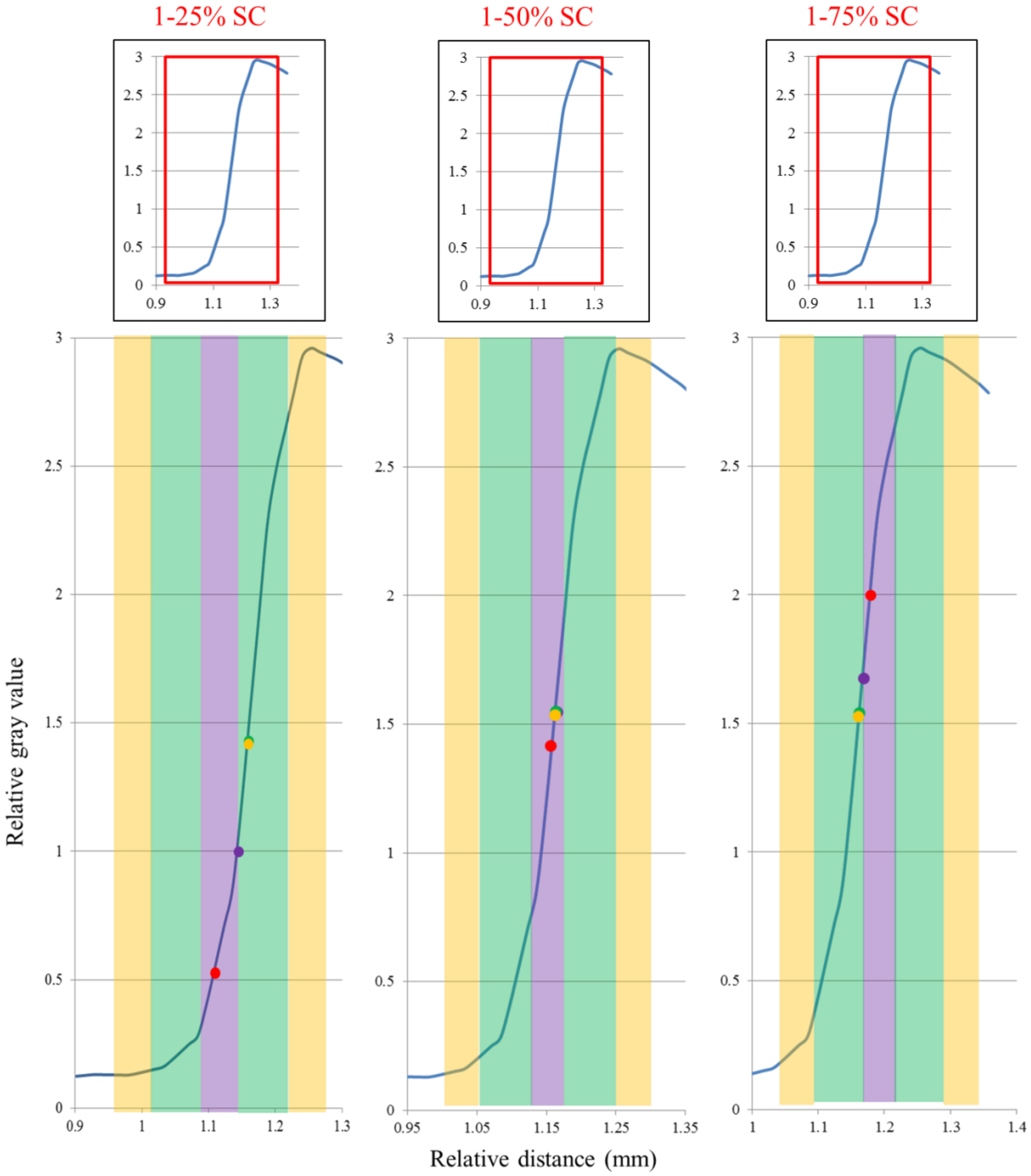

(c)

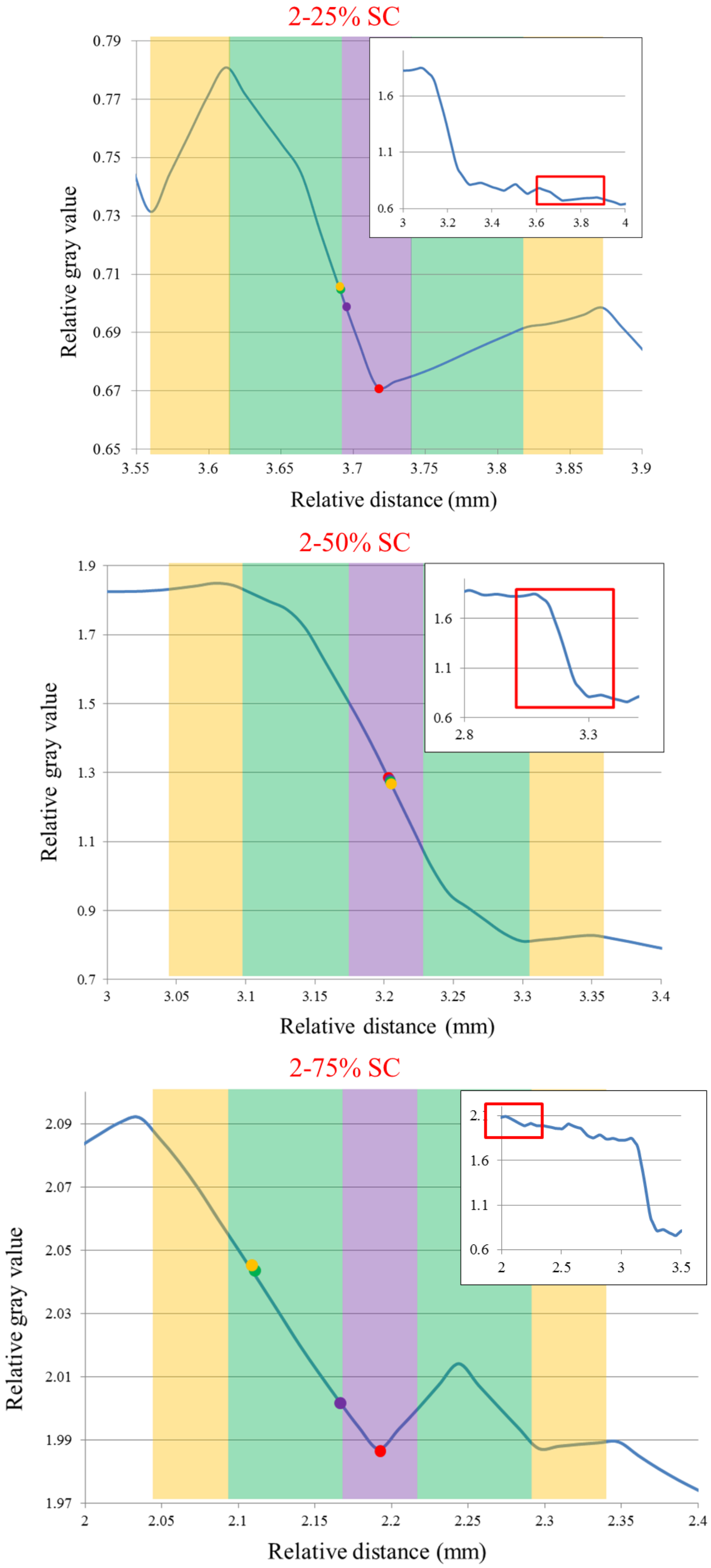
2-25% SC
0.79
0.77
0.75
0.73
0.71
0.69
0.67
0.65
Relative gray value
3.55
3.6
3.65
3.7
3.75
3.8
3.85
3.9
Relative distance (mm)
1.6
1.1
0.6
3
3.2
3.4
3.6
3.8
4
2-50% SC
1.9
1.7
1.5
1.3
1.1
0.9
0.7
Relative gray value
3
3.05
3.1
3.15
3.2
3.25
3.3
3.35
3.4
Relative distance (mm)
1.6
1.1
0.6
2.8
3.3
2-75% SC
2.09
2.07
2.05
2.03
2.01
1.99
1.97
Relative gray value
2
2.05
2.1
2.15
2.2
2.25
2.3
2.35
2.4
Relative distance (mm)
2.
1.6
1.1
0.6
2
2.5
3
3.5

(d)

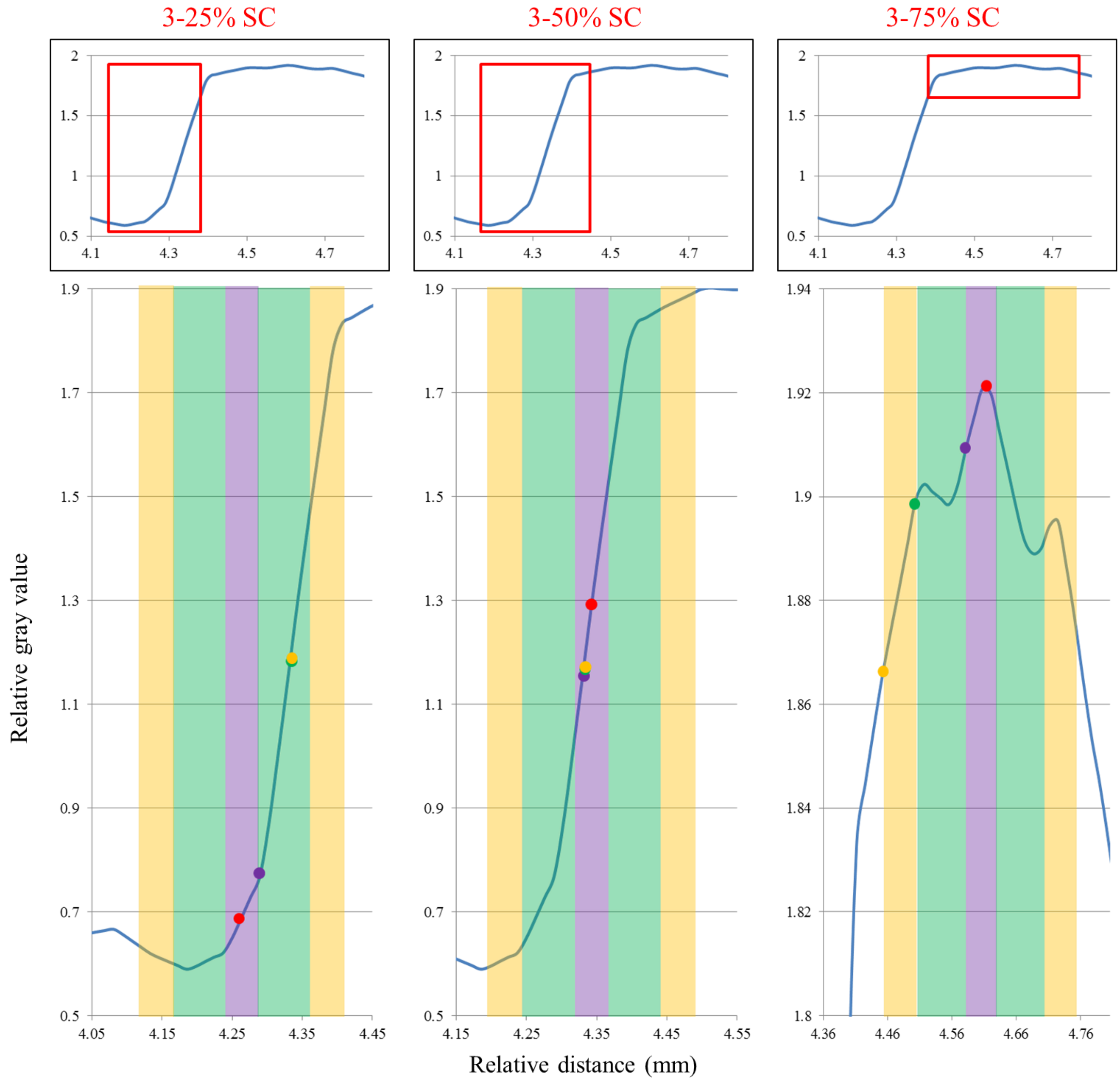

(e)

Figure 5.11 *The evolution of edge points along the gray value profile under different thresholding conditions. (a) a 2D reconstructed slice taken from the region of longest penetration path. The gray value profile along the "blue line" is drawn. Material edges were observed at 3 locations: outer cylinder, inner hole and middle pin. (b) signs denoting different edge points and search distance regions. (c) the evolution of material edge points at location Nr.1. (d) the evolution of material edge points at location Nr.2. (e) the evolution of material edge points at location Nr.3.*

Several conclusions can be drawn from the above analysis:

1. When applying local thresholding method, it is important to avoid using a starting contour which "cut through" large peaks in the histogram.

2. Using too small search distance usually cannot cover the entire transition region from air to material, resulting in high risk of locating wrong material edges.

3. Using 2 voxel size as the search distance is a good estimation of the transition and can in general provide good dimensional measurement results.

4. The influences of shifting the starting contour and varying the search distance are combined. Using an inappropriate starting contour or using too small search distance can both result in large edge errors.

5.1.4 Conclusions

This section compares two major thresholding methods: global thresholding and local thresholding. The results of the comparison can be summarized as follows:

- Local thresholding outperforms global thresholding in the following aspects
    - Image quality (in case of low signal to noise ratio, global thresholding might be a better choice)
    - Accuracy and local deviations of dimensional measurements
- When shifting the thresholding starting contour, the material edge will also shift accordingly. When global thresholding is applied, the material edge will shift continuously; when local thresholding is applied, the material edge will shift discontinuously which is determined by the gray value gradient and the “search distance”).

5.2 Beam hardening effect and its correction

5.2.1 The nature of the beam hardening effect and its influences

The origin of beam hardening effect lies in the reconstruction method. As shown in Fig 5.12, many algorithms were developed for image reconstruction, among which the filtered back projection (FBP) method has been widely used by most industrial and academic users.

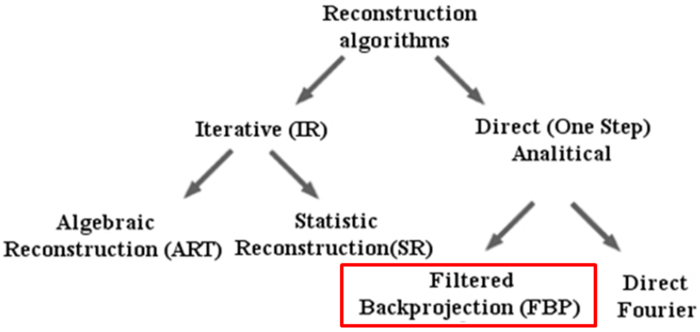

Figure 5.12 *different algorithms developed for 3D image reconstruction*

The FBP reconstruction is based on the inverse Radon transformation which requires the X-ray attenuation to be a linear function of the material thickness, which is also known as the Beer’s law:

$I = I_0 \times e^{-\mu x}$ or Attenuation $= \ln(I_0/I) = \mu x$ (1)

Where "I" is the intensity of the X-ray beam that passes through the object; 'I_0" is the intensity detected when no attenuating object is present; "μ" is the linear attenuation coefficient; "x" is the penetration length through the material. For monochromatic X-ray beams, the linear attenuation coefficient μ is a constant number, determined by the material properties (chemical composition of the absorber (Z), and physical density of the absorber (ρ)) and the energy of the X-ray beams *[Herman G. T., 2009]*. Few examples demonstrating the relationships between X-ray attenuation and material thickness are shown in Fig 5.13.

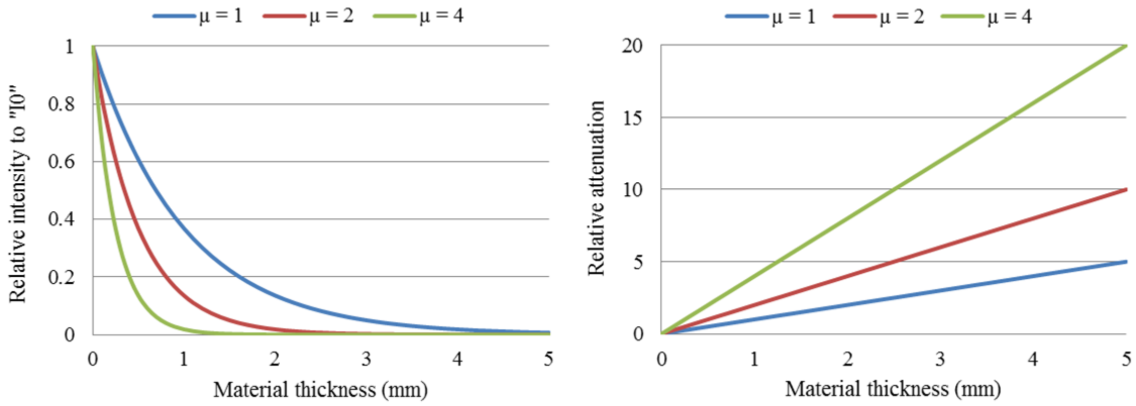

Figure 5.13 *examples demonstrating the relationships between X-ray attenuation and material thickness*

However, most industrial X-ray sources generate polychromatic X-ray beams which are characterized by a continuous energy spectrum within a certain bandwidth. During the scanning process, the X-ray beam will be attenuated depending on its own energy, the object's material and geometry. Due to the energy dependent attenuation, low energy (soft) photons are more easily absorbed than high energy (hard) photons. Thus, the average X-ray energy increases while passing through the material; this is referred to as "hardening" of the X-ray beam.

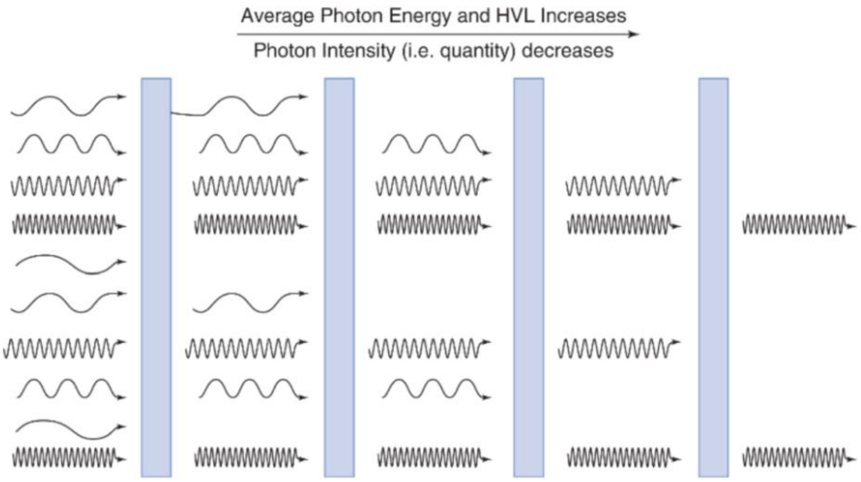

Figure 5.14 *"Hardening" of the X-ray beams throughout the penetration process. "HVL" (half value layer): the thickness of the material at which the intensity of the entered radiation is reduced by 50%. [Jerrold T. B. et al., 2011]*

As shown in Fig 5.15, due to the beam hardening effect, the linear relationship between the penetrated material thickness and the X-ray attenuation is distorted.

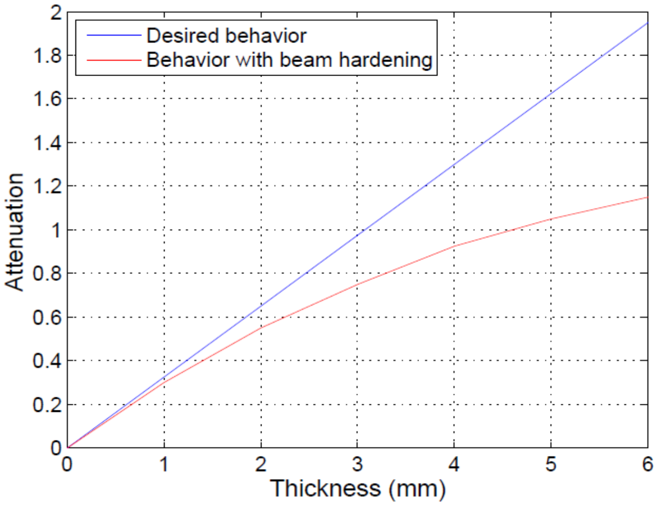

Figure 5.15 *The relation between the X-ray attenuation and the penetrated material thickness with (red line) and without (blue line) beam hardening effect.*

The combination of polychromatic attenuation and FBP reconstruction leads to various image artifacts in the reconstructed data. As demonstrated in Fig 5.16 – 5.18, beam hardening typically manifests itself as false density gradients in the reconstructed CT images of homogeneous materials, known as cupping effect; and as streaks between highly attenuating structures.

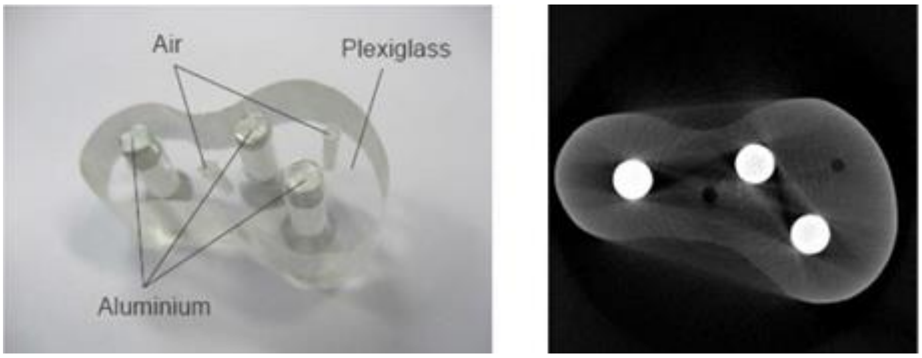

Figure 5.16 *A multi-material object and a reconstructed slice from its CT scan. Dark bands are visible between the aluminum pins and while lighter zones appear at the outer border of the plexiglass body. [Van Aarle W. et al., 2008]*

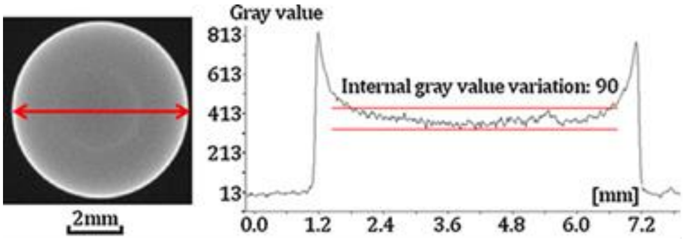

Figure 5.17 *Reconstructed slice of a steel cylinder (left) and the corresponding gray value profile along the red arrow line (right). The high absorption of soft X-rays at the edge of the part gives a false impression that the skin of the part was made of more attenuating material. [Dewulf W. et al., 2012]*

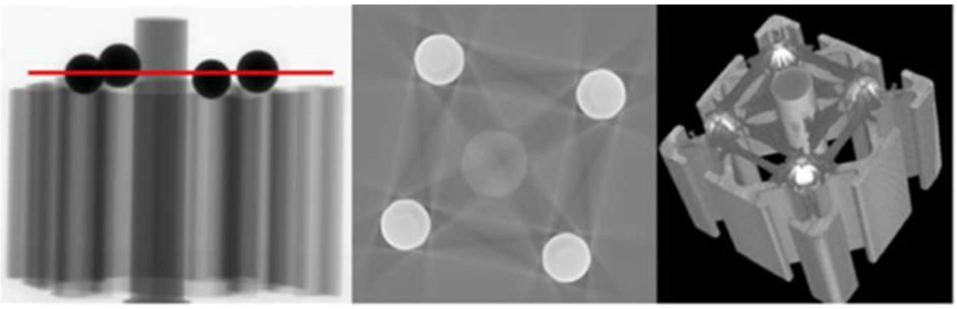

Figure 5.18 (a) 2D X-ray projection image of an aluminum profile with four steel spheres; (b) streak artifacts visible in a reconstructed slice of the line section in (a); (c) 3D voxel model of the objects. [Dewulf W. et al., 2012]

Beam hardening artifacts strongly degrade the surface quality of the reconstructed 3D model and hinder accurate material analysis and non-destructive testing. Furthermore, they affect the gray value distribution and therefore influence dimensional measurements.

- **Initial experimental investigations**

An experimental setup (Fig 5.19) was developed to investigate the influence of the beam hardening effect on the accuracy and local variations of dimensional measurements. This setup consists of two components: a steel hollow step cylinder and a steel pin. The hollow step cylinder was calibrated with a Mitutoyo FN905 tactile CMM, the reference values can be found in Appendix E. The steel pin's diameter is Ø3mm ± 1 µm as stated by the manufacturer. The main machine settings for scanning this setup and the related software are listed in Table 5.3. The raw scan data were reconstructed without any beam hardening correction; a local thresholding method was applied for creating the 3D model and the voxel size was corrected using a calibration artefact (a vertical row of adjacent spheres). As shown in Fig 5.20, the diameters of the middle pin were measured as circles at equidistant slices from top to bottom; the dimensional deviations between CT measured values and the CMM reference values are plotted against the slice number from top to bottom. Moreover, 17 measurands (Fig 5.19 a) on the entire setup were measured as cylinders and the comparison between CT and CMM measurement values are shown in Fig 5.21

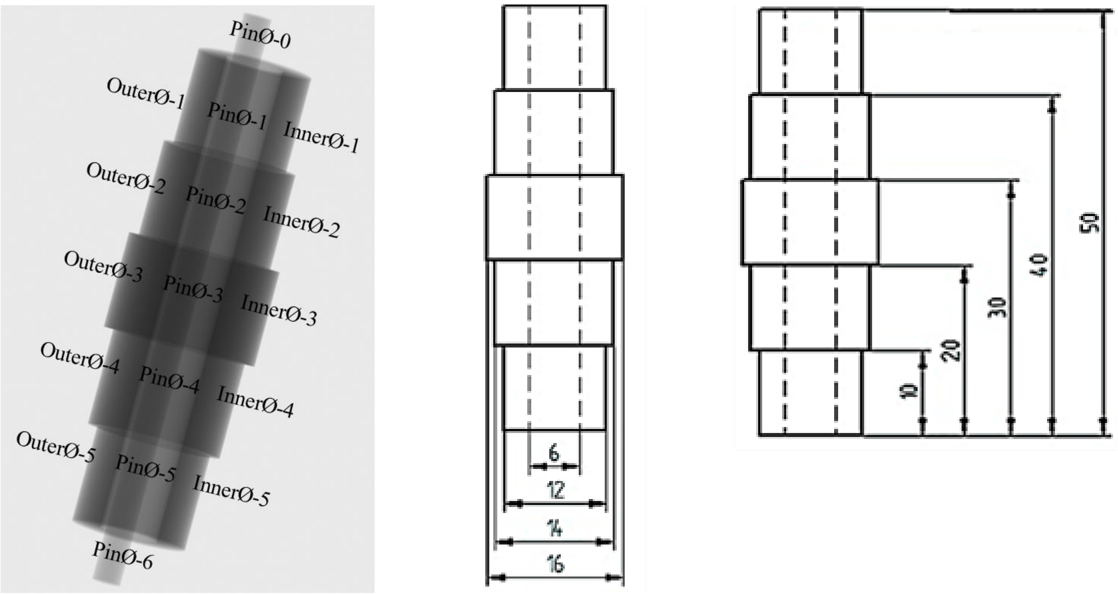

(a) (b)

Figure 5.19 *(a) 2D projection image of the test object: a steel hollow step cylinder and a steel pin (Ø3mm, dimensional tolerance is ±1 µm) placed in the middle; in total 17 measurands were defined and measured. On the hollow step cylinder: 5 outer cylinder diameters and 5 inner hole diameters; on the middle pin: 7 cylinder diameters at different locations. (b) The nominal dimensions of the hollow step cylinder.*

Voltage (KV)	Voxel Size (µm)	Current (µA)	Copper filter (mm)	Reconstruction	Segmentation
210	39	195	2	FBP by CTPro XT 3.1.2	Local thresholding by VGStudio MAX 2.2

Table 5.3 *Main X-ray CT scanning settings and the involved software*

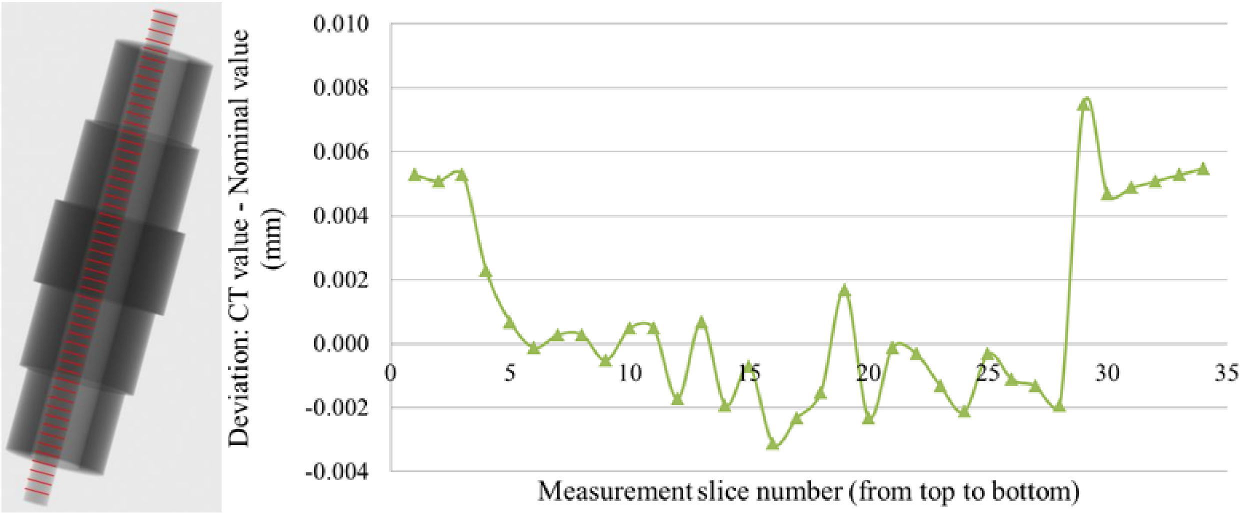

Figure 5.20 *Local dimensional deviations on the middle pin: measured as "circle diameters" at equidistant slices from top to bottom*

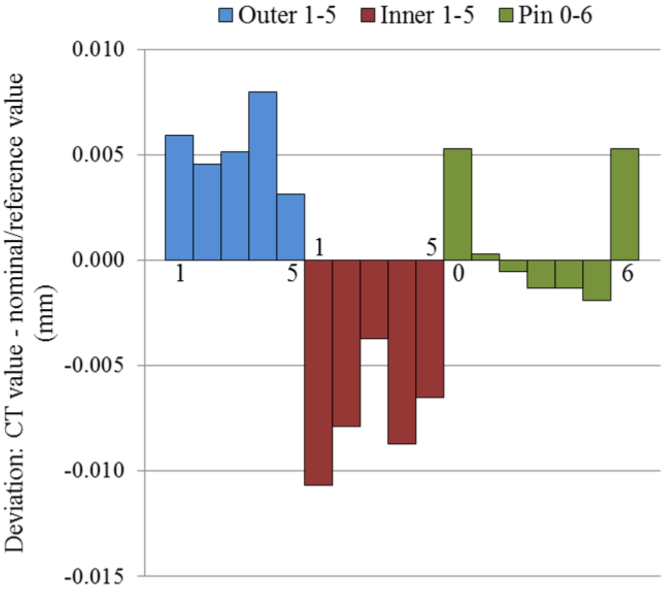

Figure 5.21 *Dimensional measurement results of the 17 measurands indicated in Fig 5.19 (a). The CT measurements were compared to the nominal value stated by the manufacturer (for the middle pin) or to the reference values obtained from tactile CMM measurements (for the dimensions related to the step hollow cylinder).*

In the above figures, local dimensional variations (up to 8 µm) are observed when the middle pin enters or leaves the surrounding step cylinder. It is suspected that these dimensional discontinuities are caused by the combined effect of beam hardening and thresholding method. The hypothesis is as follows: the surfaces of the "uncovered" part of the middle pin will have higher edge contrast due to the beam hardening effect while the surfaces of the "covered part" of the middle pin have much lower edge contrast due to the surrounding material. The difference in the edge contrasts complicates the thresholding process and can cause the dimensional discontinuity seen in Fig 5.20 and 5.21.

- **Investigations using X-ray CT simulations**

In order to verify the above hypothesis and to identify the influence of the beam hardening effect on dimensional measurements, it is important to eliminate other influence factors (e.g. machine axes misalignment, focal spot drift, X-ray scattering etc.). These conditions can be easily realized by X-ray CT simulation. Thus, the simulation software developed by Welkenhuyzen et al. *[Welkenhuyzen F. et al., 2012]* was applied for this purpose.

Two simulations of the test setup (shown in Fig 5.19) were performed: the first simulation applies a monochromatic spectrum (210 keV), to serve as a benchmark; the second simulation uses a polychromatic spectrum with photon energies up to 210 keV. Similarly, after local thresholding, the middle pin's diameters were measured as circles at equidistant slices; meanwhile, the 17 measurands (Fig 5.19 a) were measured as cylinders. The measurement results are shown in Fig 5.22 and 5.23.

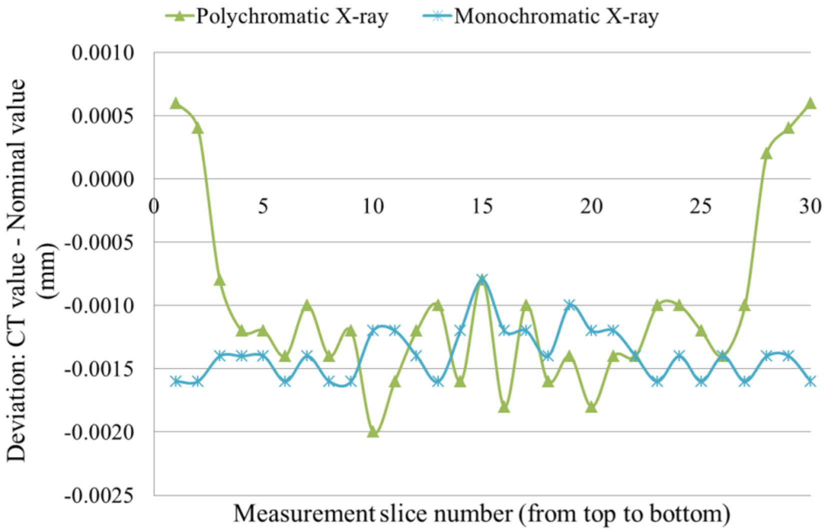

Figure 5.22 *The middle pin's diameters were measured as circles at equidistant slices. CT scans were simulated using both monochromatic and polychromatic X-ray beams*

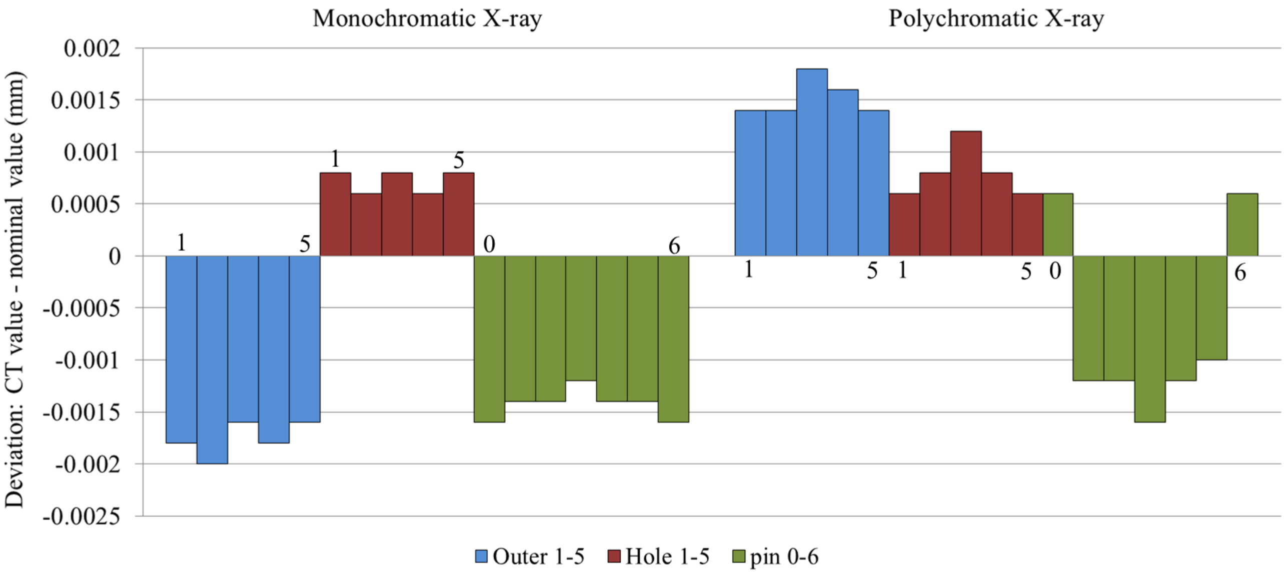

Figure 5.23 *Comparison between the CT measured values and the nominal values of the 17 measurands (as defined in Fig 5.19). CT scans were simulated using both monochromatic and polychromatic X-ray beams.*

In general, the simulated measurement results coincide with the previous findings. Local dimensional variations are observed when the pin enters and leaves the surrounding step cylinder in case of polychromatic X-ray source. More importantly, when a monochromatic X-ray source is applied, the dimensional discontinuity disappears. Thus, the previous hypothesis about the cause of these dimensional discontinuities holds true. Figure 5.23 shows the dimensional measurement results for the outer step cylinders, inner hole and middle pin measured at different sections. These results also coincide with the previous findings.

Thus, both experimental and simulation results prove that the beam hardening effect is a major cause for local dimensional variations.

5.2.2 Beam hardening correction

5.2.2.1 State of the art for beam hardening correction

Beam hardening correction has been a major research challenge for decades. An overview of different beam hardening correction methods is shown below:

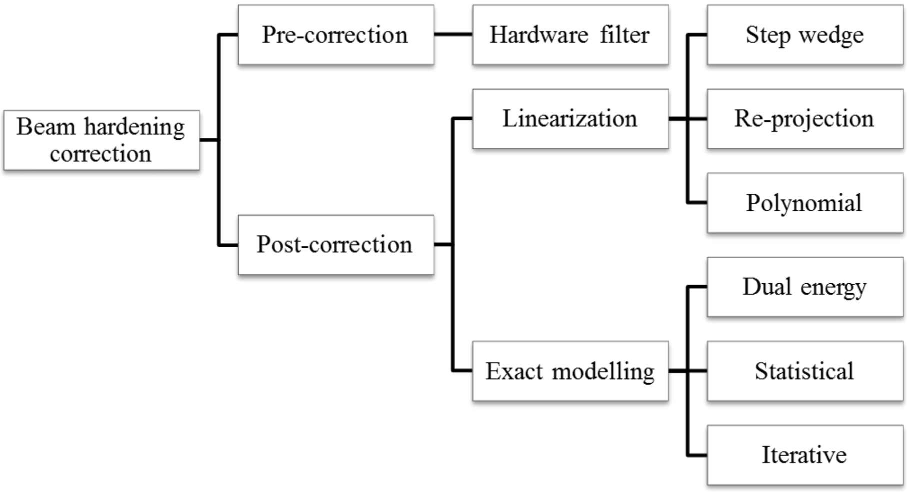

Figure 5.24 *Overview of beam hardening correction methods*

Hardware filtration: until now, using metal filter plates (Fig 5.25) to reduce low energy content from the incident X-ray beams is seen as one of the most efficient and effective way of beam hardening reduction. However, hardware filters are not capable of fully eliminating beam hardening artifacts. Thus, it is primarily applied as an initial beam hardening reduction step, which is often followed by more dedicated beam hardening correction methods *[Tan Y. et al., 2013]*.

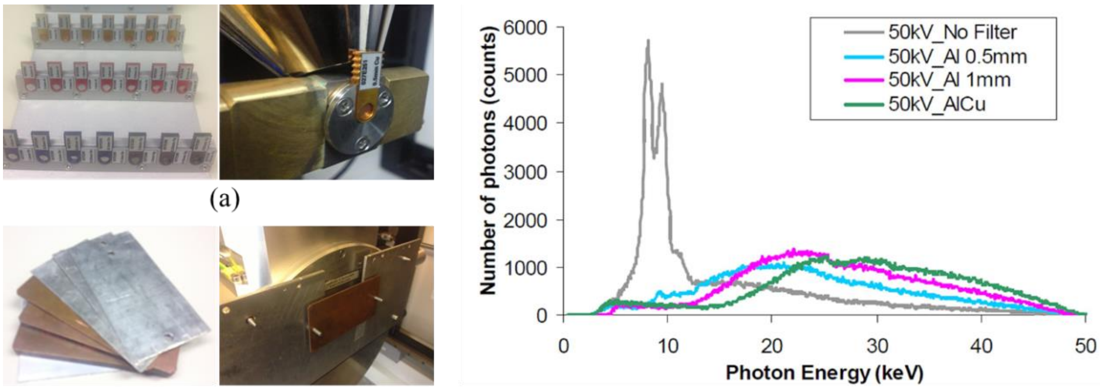

(a)

(b)

(c)

Figure 5.25 *(a) example of metal filters for a 225kV CT scanner; (b) example of metal filters for a 450kV CT scanner; (c) Spectrum of a 50 kV X-ray source before and after passing various filters (larger count time when using filters). It can be noticed that the number of low energy photons is significantly reduced when filters are applied. [Kerckhofs G. et al., 2008]*

Linearization: as shown in Fig 5.26, the basic concept of all types of linearization methods is to adapt the measured attenuation values to the ideal linear curve.

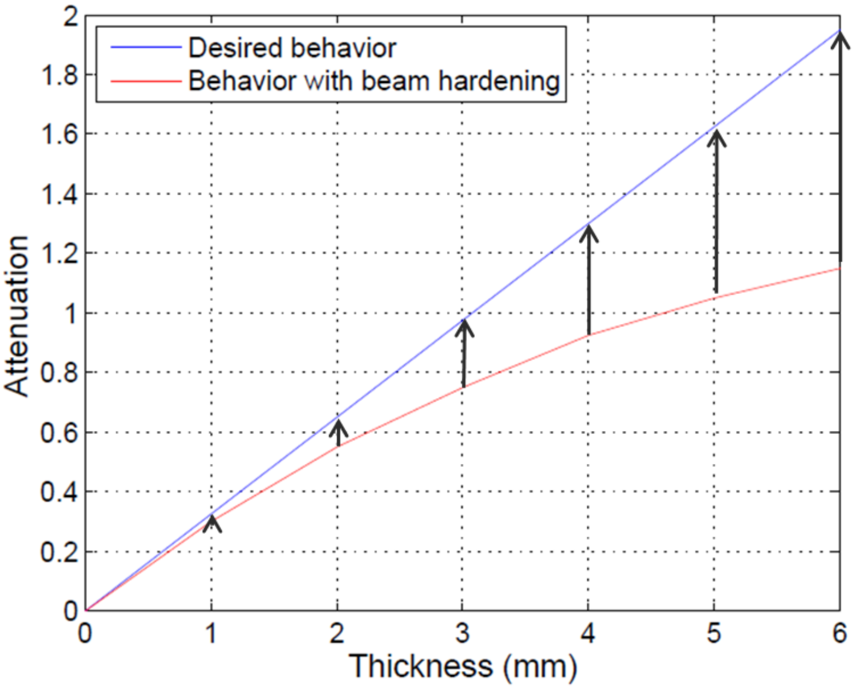

Figure 5.26 *The basic concept of linearization methods for beam hardening correction*

<u>*Step wedge*</u>***:*** in the medical field, step wedge (Fig 5.27) transmission measurements were often used for reducing beam hardening artifacts. However, to meet the requirements for accurate dimensional metrology, pre-knowledge of the object's material composition is required. In addition, case specific step wedges need to be produced and calibrated. When taking transmission measurements, the step wedge should be positioned perpendicular to the incident X-ray beams. These constraints make it less attractive than many other beam hardening correction methods.

Figure 5.27 *Step wedges for beam hardening correction [Davisa G. et al., 2008]*

<u>*Reprojection*</u>*:* reference-based reprojection method has been around for over 30 years as one of the major beam hardening correction methods. The differences between monochromatic and polychromatic reprojection are calculated which indicate the necessary corrections to be applied to the original X-ray images. The major drawback of this method is the need for large amount of

reference data such as the X-ray beam energy distribution as well as attenuation characteristics of all workpiece materials. More recently, two methods using the concept of "forward projection" or "referenceless reprojection" (next to the X-ray images no additional reference data is needed) have been proposed *[Amirkhanov A. et al., 2011] [Krumm M. et al., 2008]*. As shown in Fig 5.28, both methods relay on an initial reconstruction and thresholding; useful information is extracted from this initial 3D model thus avoiding the needs for pre-knowledge of the object's material composition, geometry and the X-ray spectrum. These methods have shown strength in reducing beam hardening image artifacts. However, the accuracy of these methods is dependent on the initial reconstruction and thresholding step. These initial steps are often far from accurate and thus influence the accuracy of the final 3D model.

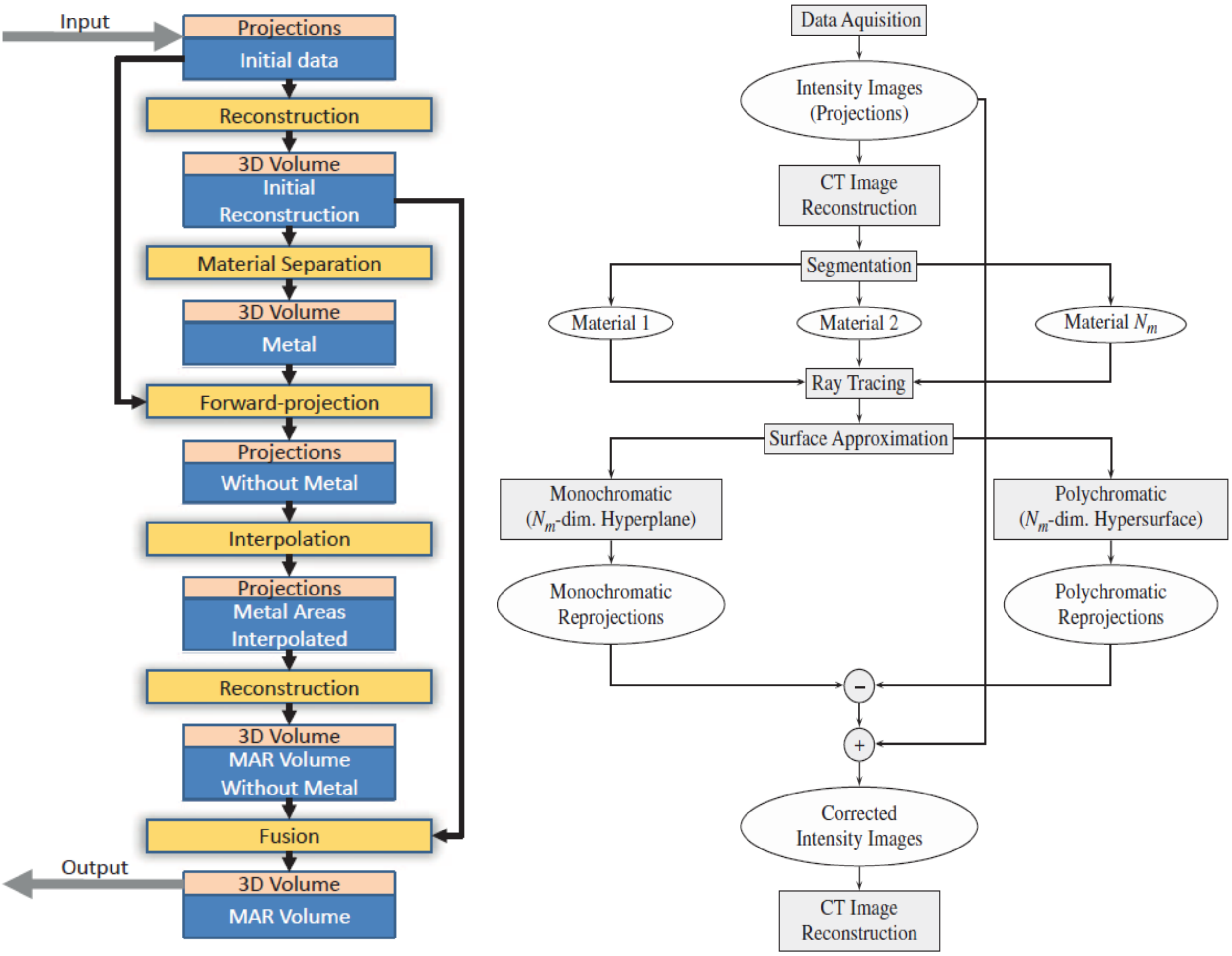

(a) (b)

***Figure 5.28** (a): Working flow chart of the forward-projection beam hardening correction method [Amirkhanov A. et al., 2011] (b) Working flow chart of the referenceless beam hardening correction method. [Krumm M. et al., 2008]*

<u>Polynomial</u>: polynomial functions are often used to adjust the attenuation values during the reconstruction process. At the moment, it is the most widely used beam hardening correction method. The polynomial functions are often determined empirically, based on experience and on

dedicated calibration procedures *[Kachelrieß M. et al., 2006]*. In addition, an algorithm has been developed which calculates the polynomial functions based on the central slice. The basic idea is that the penetrated material thickness on the central slice for each 2D projection image remains constant over 360 degrees *[Nishihata T., 2012]*. However, this method requires the object's longest penetration path to be projected onto the central slice which is not very practical.

Exact modelling*:* this type of beam hardening correction method focuses on modelling the X-ray attenuation process.

Dual energy: the energy-dependence of the attenuation coefficients is modeled as a linear combination of two basic functions representing the separate contributions of the photo-electric effect and of the X-ray scattering. To obtain reliable results, it is important to cover an as wide as possible energy range with dual CT scans. Due to the power limitation of industrial CT scanners, this is not always possible. Moreover, applying dual energy CT scan also significantly increases the scanning and processing time, thus the overall efficiency is rather low *[Stonestrom J. et al., 1981] [Alvarez R. et al., 1976] [Kelcz F. et al., 1979]*.

Statistical: a statistical beam hardening correction method was proposed by Raphaël Thierry et al. This method relies on the histogram analysis of a first uncorrected reconstruction. At each voxel, the mass attenuation is re-expressed as the weighted sum of the mass attenuation of a given set of reference materials. However, the method requires a pre-knowledge of the X-ray spectrum, detector response and a set of calibration curves, which is often inaccessible *[Thierry R. et al., 2006]*.

Iterative: an iterative beam hardening correction method was developed by Van.de.Casteele E. et al. It is assumed that the object can be segmented into a few materials with different attenuation coefficients, and the X-ray spectrum can be parameterized using a small number of energy bins. The corresponding unknown spectrum parameters and material attenuation values are estimated by minimizing the difference between the measured sinogram and a simulated polychromatic sinogram *[Van de Casteele E. et al., 2004]*.

5.2.2.2 Further investigation on two beam hardening correction methods

Within this PhD thesis, two linearization based beam hardening correction methods were thoroughly investigated: the look up table method and the predefined polynomial correction curves.

- **Look up table method**
  - **Initial concept**

The look up table method tries to transform the measured non-linear X-ray attenuation values to the ideal attenuation values. Usually, the look-up table is generated through prior measurements performed on a step wedge (with known dimensions) that has the same material composition as the target object. The look up table method was chosen to be investigated due to its potential for multi-material beam hardening correction.

Due to the multi-material composition, an additional parameter is introduced: the thickness combination of different materials. For example, the combination of 1mm material “A” and 3mm material “B” can result in the same attenuation as 1.5mm material “A” combined with 2mm material “B”. This problem can be solved by applying dual energy CT scan. The working concept of using look up table for dual-material beam hardening correction is demonstrated in Fig 5.29:

As shown in Fig 5.29 (a), suppose X-ray projection images of a step wedge consisting of two materials are acquired at a certain X-ray energy level, a surface map which describes the relationship between material thickness combination and the relative attenuation values can be drawn. When the target object is scanned under the same condition, a certain pixel’s attenuation value can be the result of many possible material thickness combinations. All these possibilities are included in a curve which is the intersection between the surface map (created by the step wedge) and the flat surface denoting the pixel’s attenuation value. Another similar curve can be obtained by scanning both the step wedge and the target object at another X-ray energy level (Fig 5.29 b). Thus, the exact material combination for that particular pixel can be obtained by looking at the intersecting point of the two curves (Fig 5.29 c). Once the exact material combination is known, the pixel’s attenuation value can be easily adjusted.

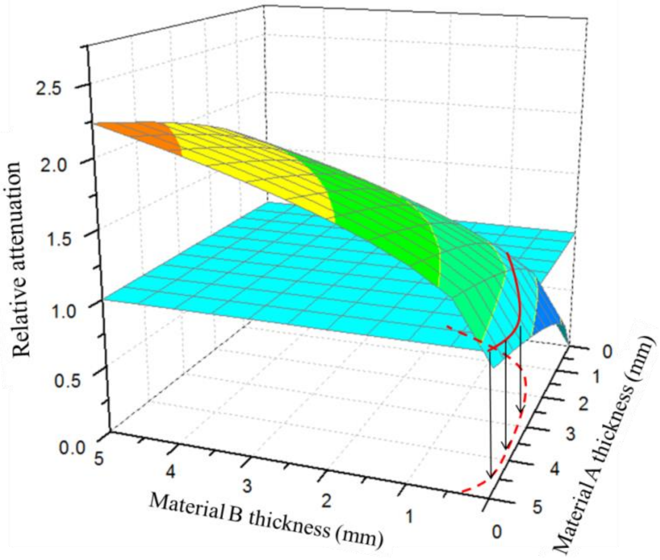

Scan the step wedge using the 1st energy level:

Due to the known dimensions of the step wedge, a "rough" curved surface representing the relationship between attenuation (calculated from the gray value) and the penetrated material lengths (material A and B) can be generated.

However, for a particular pixel on the 2D projection image of the object (scanned using the 1st energy level) which has attenuation equal to 1, there might be many possible material thickness combinations

(a)

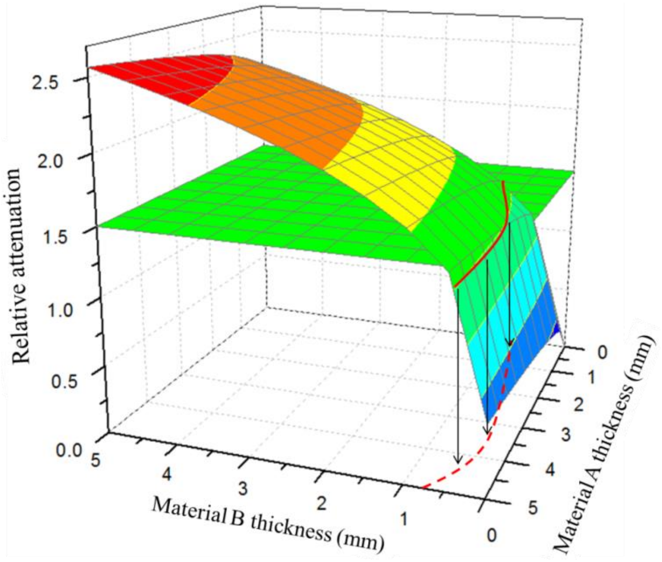

Scan the step wedge using the 2nd energy level:

Similarly, a "rough" curved surface representing the relationship between attenuation (calculated from the gray value) and the penetrated material lengths (material A and B) can be generated.

For the same pixel on the 2D projection image of the object (scanned under the 2nd energy level) its attenuation value changes to 1.5. There might be many possible material thickness combinations yielding this value. These combinations are included in the red

(b)

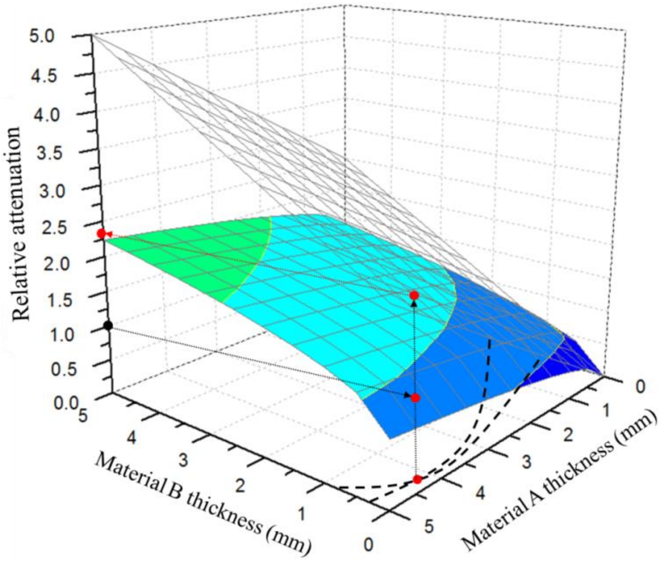

Creating the final "look-up" table:

By combining the two "red" curves from the above graphs, it is possible to deduce the actual material combination for each individual pixel (intersecting point)

Once the material combination is known, it is possible to linearize any of the two scans from the curved surface into the ideal flat surface.

(c)

***Figure 5.29** The working concept of using look up table for dual-material beam hardening correction*

The above described beam hardening correction concept looks promising but requires large amount of data processing. Thus, the look up table method was first tested on a single material object to see whether it can improve the quality of CT dimensional measurements.

A Matlab program (Appendix F) was developed to test the look up table method for single material beam hardening correction; its basic framework (Fig 5.30) mainly involves 3 steps:

1. Acquire X-ray projection images of the step wedge.
2. Create the look up table
3. Correct the object's 2D X-ray projection images

In addition, the following constraints should be met:

1. The step wedge should have the same material composition as the target object. The thickness of each step should be well calibrated.
2. The 2D projection image of the step wedge should be acquired when the step wedge is perpendicular to the incident X-ray beams.
3. The object should be scanned under the same condition as the step wedge.

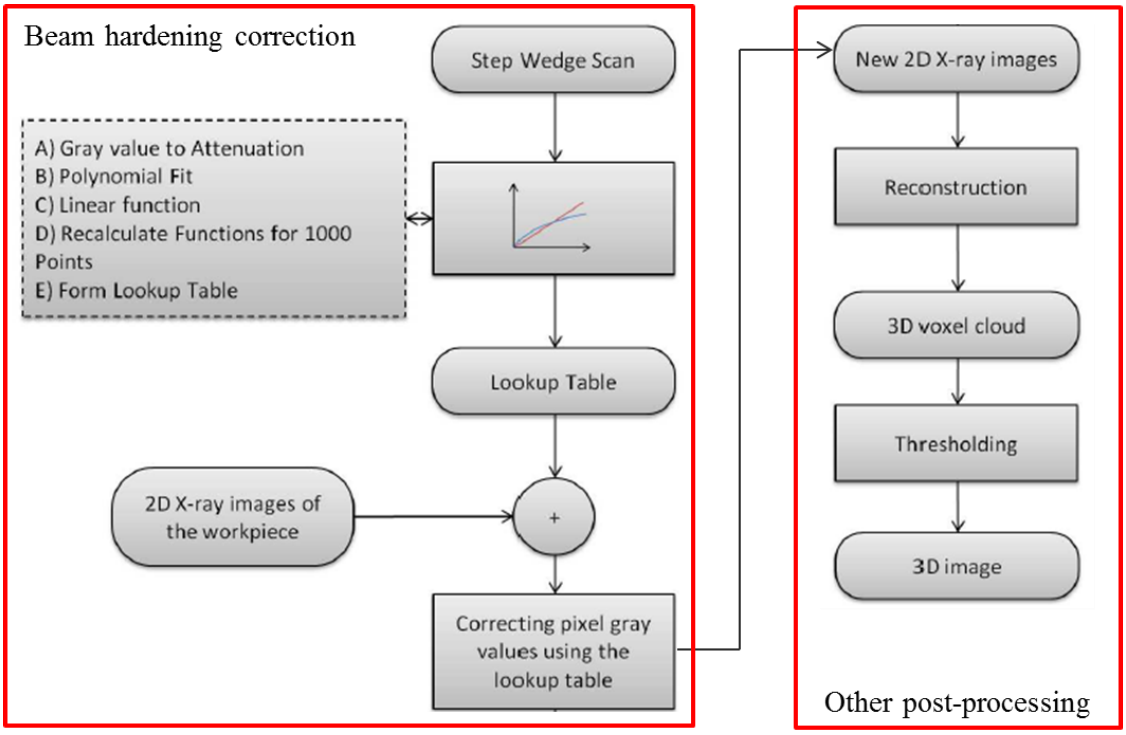

Figure 5.30 *Basic framework of the look up table beam hardening correction method*

- **Refinement of the correcting algorithm**

Initial tests were performed using X-ray CT simulation; the simulation software "aRTist" developed by BAM (Federal institute for materials research and testing, Germany) was used.

As shown in Fig 5.31, X-ray projection images of a steel wedge containing ten steps (from 1mm to 10mm) were simulated. The major machine settings are: 200kV X-ray voltage (polychromatic spectrum) and a 2mm copper filter. On each step, a region of interest (ROI) was defined and the average attenuation values within each ROI were calculated. These attenuation values were plotted against the material thickness, forming a non-linear curve. A straight line was drawn through the first (minimum) and last (maximum) point denoting the ideal attenuation – thickness relationship. Subsequently, the attenuation graph was converted to gray value graph; forming a look up table which describes 1 to 1 relationship between the old (red curve) and new (green curve) gray values.

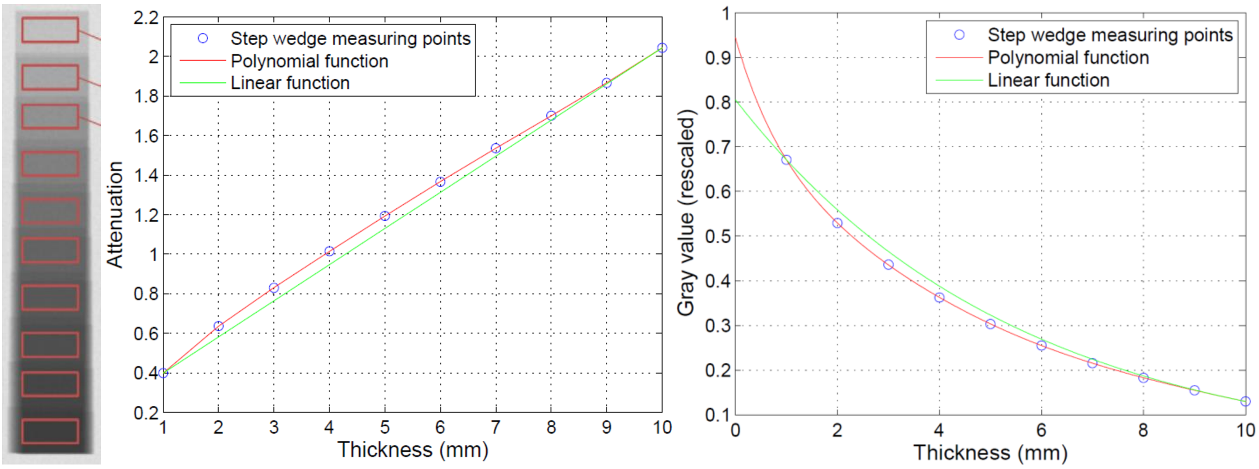

(a) (b) (c)

Figure 5.31 *Left: the simulated step wedge consists of 10 sections. The sampling regions for calculating the average attenuation values are also indicated. The polynomial function represents the original attenuation-thickness relationship. The linear function represents the ideal attenuation-thickness relationship*

Similarly, a 2D projection image of a steel cone (Fig 5.32 a. maximum diameter; 10mm) was simulated as the target object. Each of its pixel gray value was "corrected" using the look up table generated by the step wedge. A "corrected" image is shown in Fig 5.32 (b).

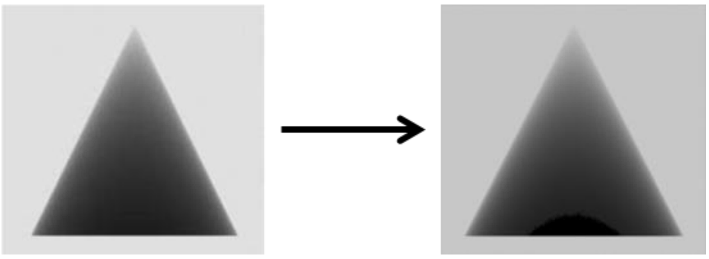

(a) *(b)*

Figure 5.32 *2D projection image of the simulated steel cone, before (a) and after (b) correction*

Two effects can be noticed on the "corrected" image: a black region inside the cone emerges and the background becomes darker.

The black region is caused by the limited thickness range of the step wedge. The bottom diameter of the cone is 10 mm, which equals to the thickest step of the wedge. However, due to the conical shape of the X-ray beam, the actual penetration lengths of the center-bottom region of the cone exceed the range defined by the step wedge image. These points became black because a default value “0” was set for points lying out of the range.

The surrounding air becoming darker is caused by the lack of information between 0 and 1mm thickness. The steps of the simulated wedge are between 1 and 10mm, thus the fitting curves have to be extrapolated for thicknesses less than 1mm. As shown in Fig 5.31 (c), the linear function (new gray values) is below the polynomial function (old gray values) within the 0 to 1mm interval. Thus, the gray values within this interval are reduced.

To eliminate these effects, the thickness of the step wedge was increased and an artificial point (0, 0) was added when creating the look up table assuming 0 attenuation at 0 thickness. The new result is shown in Fig 5.33.

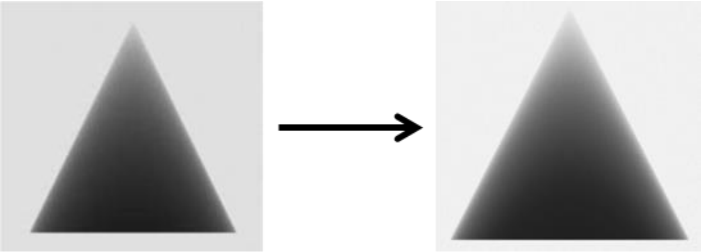

(a) *(b)*

Figure 5.33 *2D projection images of the simulated steel cone. (a): original image; (b): “corrected” image*

Linear regression analyses on the 2D images were performed to evaluate the result of the beam hardening correction. As indicated in Fig 5.34 (a) and (b), a line was drawn from the top of the cone straight down to the base. Because of the cone shape, the material penetration length increases linearly alone the line. The attenuation values of each pixel along the line are plotted as a function of the pixel’s relative position (Fig 5.34 c and d); ideally, they should form a straight line. Linear regression analyses were performed to assess the linearity before and after correction.

(a) (b)

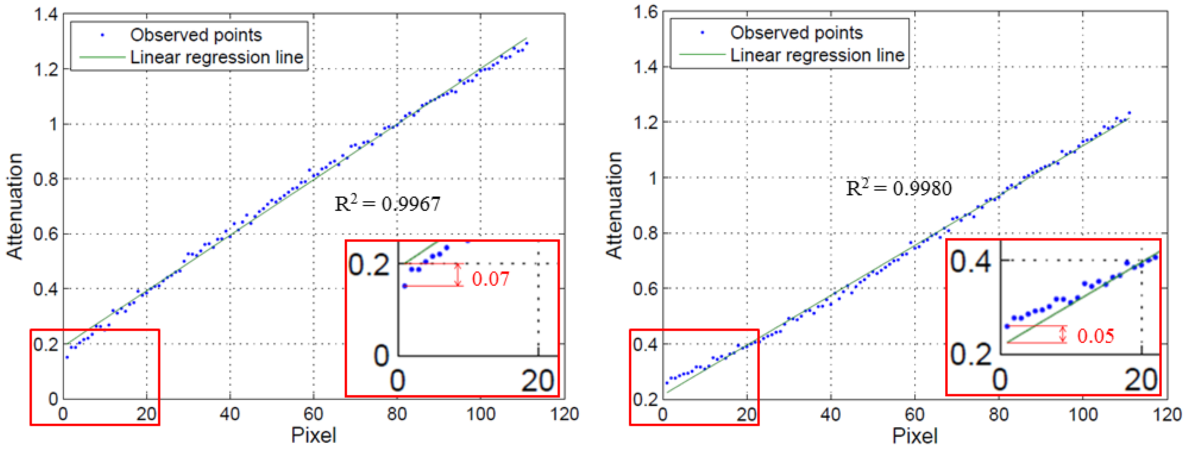

(c) (d)

Figure 5.34 *(a) original X-ray projection image of a steel cone (b) X-ray projection image of the steel cone after beam hardening correction (c) along the blue line in "a", the pixels' attenuation values are plotted against their relative position (d) along the blue line in "b", the pixels' attenuation values are plotted against their relative position*

As shown in Fig 5.34 (c) and (d), the linearity of one single 2D projection image is slightly improved: from 0.9967 to 0.9980. However, "over correction" can be noticed: the attenuation values of the first pixel increases from 0.07 below the regression line to 0.05 above the regression line. There are two reasons for this "over correction":

1. Inserting (0, 0) point arbitrarily when creating the look up table;
2. The difference in the background's attenuation value between the step wedge image and the cone image, which introduces an additional offset.

In order to tackle the above mentioned issues, the investigation was shifted to projection images of real test setup for the following reasons:

1. The dynamics of both X-ray source and X-ray detector can be included.
2. The X-ray scattering noise can be accounted for. Due to different geometry between the step wedge and the object, the associated X-ray scattering noise will also be different. This difference can add additional offset between two projection images.

As shown in Fig 5.35, the test setup consists of 3 parts: a steel step wedge containing 8 larger steps and 7 smaller steps, a steel pin and a steel ring. Moreover, a white reference image was taken prior to other projection images.

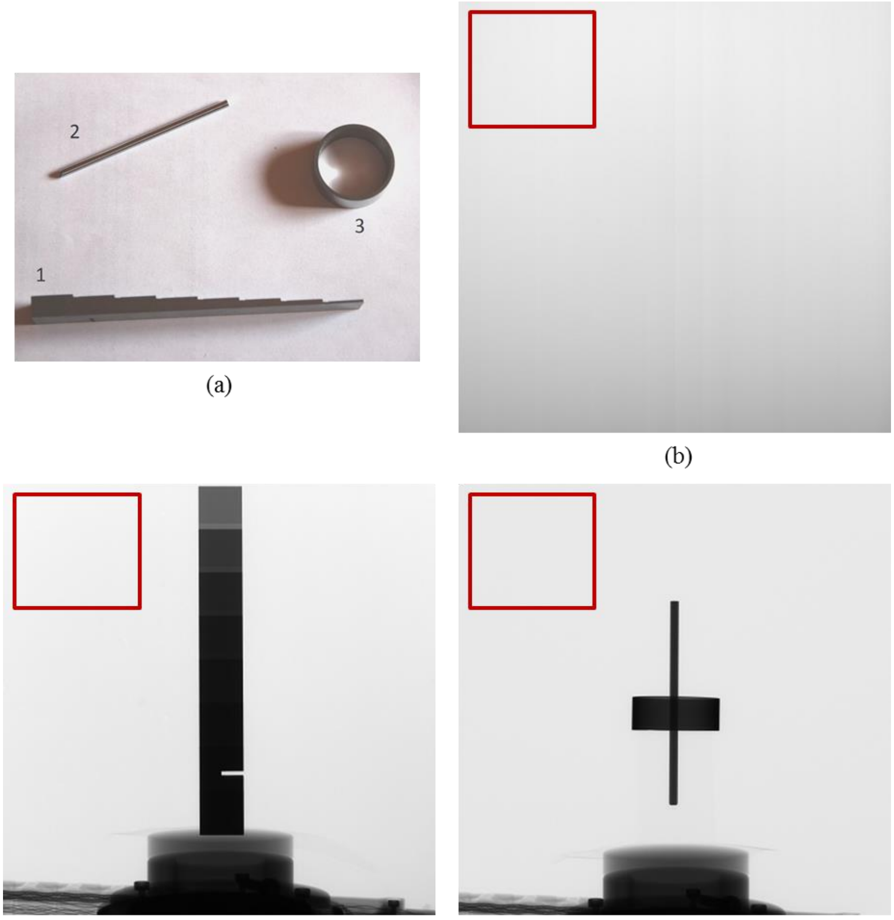

(a)

(b)

(c)

(d)

Figure 5.35 *(a) Test setup for investigating the improvement strategies for the look up table beam hardening correction method. The setup consists of 3 parts. 1: steel step wedge containing 8 larger steps and 7 smaller steps. 2: a steel pin. 3: a steel ring (b) white reference projection image (c) X-ray projection image of the step wedge (d) X-ray projection image of the test object. The "red square" indicates the selected ROI.*

Several improvement strategies were designed for refining the look up table. The basic concept is to calculate an average background attenuation value within a ROI to replace the arbitrary inserted (0, 0) point, and to construct the ideal linear curve using different approaches. Fig 5.36 gives an overview of these strategies.

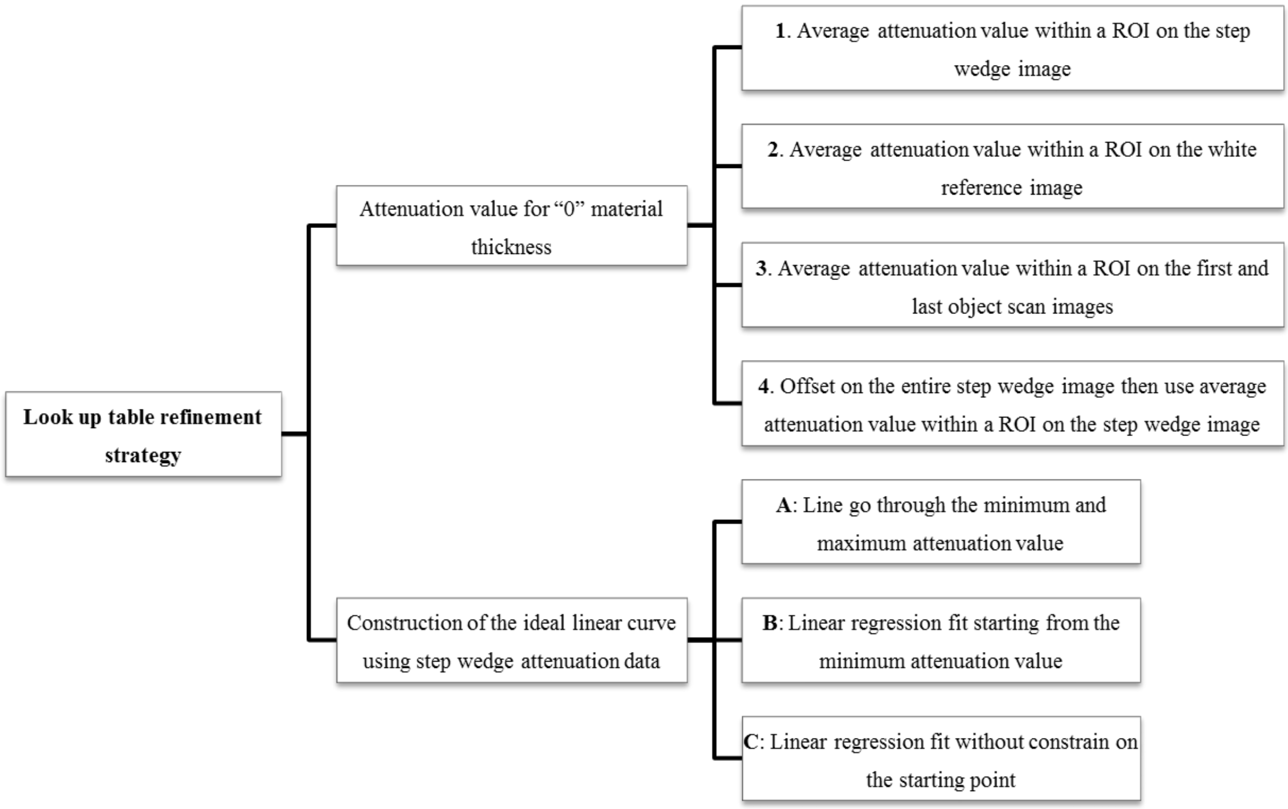

Figure 5.36 *strategies for improving the look up table beam hardening correction method. Notice the "additional offset" mentioned in "4" refers to the difference of average attenuation value within the same ROI on the object and on the step wedge's projection images: Offset value = (average attenuation* $_{\text{first object image ROI}}$ *+ average attenuation* $_{\text{last object image ROI}}$*)/2 - average attenuation* $_{\text{step wedge ROI}}$*. This offset value is added to the attenuation value of every pixel of the step wedge image before creating the look up table.*

Four approaches were tested for estimating the attenuation value at "0" material thickness.

1. Use the average attenuation value within a ROI on the step wedge image as the value for "0" material thickness and insert this additional data point into the look up table

2. Use the average attenuation value within a ROI on the white reference image as the value for "0" material thickness and insert this additional data point into the look up table

3. Use the average attenuation value within a ROI on the first and last projection images of the object as the value for "0" material thickness and insert this additional data point into the look up table. Theoretically, the first and last projection images of the object are taken at the same rotation angle but over a certain time period, thus the variation of X-ray intensity due to the dynamics of the X-ray source and X-ray detector can be accounted for.

4. Calculate the difference of the ROI's average attenuation value between the step wedge image and the object's first and last projection images using the following formula:

Offset value = (average attenuation $_{\text{first object image ROI}}$ + average attenuation $_{\text{last object image ROI}}$)/2 - average attenuation $_{\text{step wedge ROI}}$ (2)

Subsequently, the step wedge image is offset using this value and the look up table is generated from the "new" step wedge image. The average attenuation value within a ROI on this "new" step wedge image is set as the value for "0" material thickness. This approach takes into account both the dynamics of the X-ray intensity and the difference between step wedge and object's projection images due to their differences in X-ray scattering etc.

Moreover, three fitting methods for generating the "ideal" linear curve were tested:

A. Drawing a line that goes through the minimum (0 material thickness) and maximum attenuation values.

B. Linear regression fit starting from the minimum (0 material thickness) attenuation value.

C. Linear regression fit without constraints.

In total 12 ways of generating the look up table were tested, resulting in 12 "corrected" 2D projection images of the test setup. Two factors were selected as the criteria for evaluating these images: linearity and the "over correction value". As shown in Fig 5.37, the attenuation values are interpolated (linearly) between pixels. After an initial thresholding using the edge detection algorithm in the 2D image processing software ImageJ, the attenuation values of 15 sampling points (with the first point starting at the left material edge) along the "red arrow" were recorded. Subsequently, the penetrated material thicknesses were calculated for each sampling point using the following formula:

$$L = 2\sqrt{r^2 - (r - x)^2} \tag{3}$$

"L" stands for the penetrated material thickness

"r" is the steel pin's nominal radius, which is 1.5mm

x = measured length on the 2D image × source to detector distance / source to object distance (4)

Subsequently, the attenuation values were plotted against the material thickness and linear regression analysis was applied. The linearity is indicated by the R^2 value and the "over correction value" is defined as the difference between measured "0 thickness" attenuation value and the value indicated by the linear regression line. The R^2 value and "over correction value" of the original projection image together with 12 "corrected" projection images are listed in Table 5.4. Correction strategy A4 is shown to be the best, as it has the highest linearity and generates minimum "over correction". Thus, strategy A4 was selected and implemented in the final version of the correction algorithm (Appendix F).

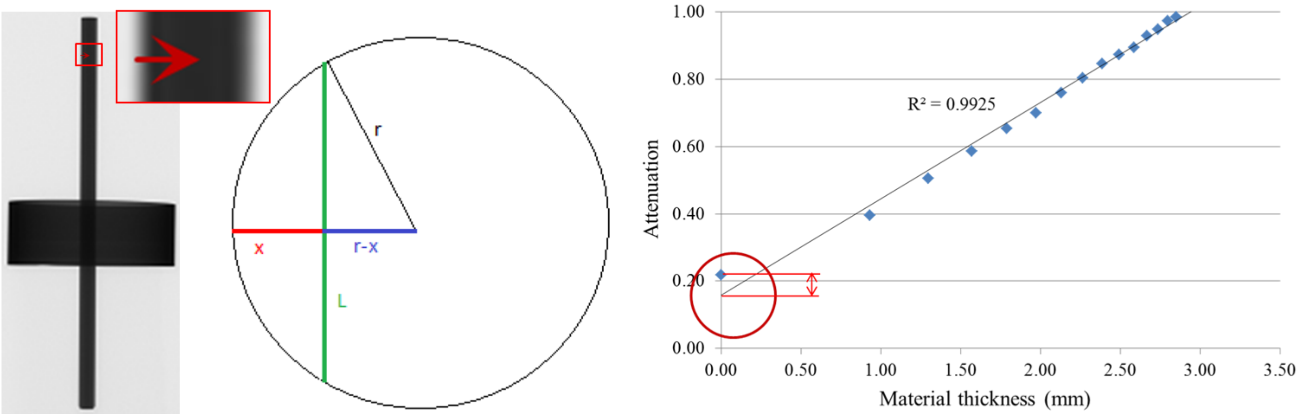

(a) (b) (c)

Figure 5.37 *(a) one of the 12 "corrected" projection images, the attenuation values of every pixel along the "red arrow" are calculated (b) illustration of the different terms for calculating the penetrated material thickness (c) the attenuation value plotted against the penetrated material thickness, linear regression analysis is performed.*

Correction strategy	**R^2 value**	**Over correction value**
Original	0.9583	-0.0846
A1	0.9925	0.0606
A2	0.9891	0.0649
A3	0.9927	0.0646
A4	**0.9962**	**0.0441**
B1	0.9926	0.0601
B2	0.9871	0.0645
B3	0.9927	0.0549
B4	0.9913	0.0656
C1	0.9901	0.0574
C2	0.9887	0.0678
C3	0.9929	0.0551
C4	0.9927	0.0549

Table 5.4 *R^2 value and "over correction value" of the original projection image and of 12 "corrected" projection images. "A, B and C" stand for how the linear line is fitted; "1, 2, 3 and 4" stand for different ways of estimating the attenuation value of "0 material thickness". Their detailed definition can be found in Fig 5.36.*

- **Influence of the look up table beam hardening correction on the 3D model**

The analysis on 2D projection images is important for fine tuning the correction algorithm. However, it does not provide information of its influences on dimensional measurements. For this reason, the investigation continued with analysis on the 3D model with the help of X-ray CT simulation.

As shown in Fig 5.38, the simulated setup consists of a steel pin (Ø4mm) and a steel hollow cylinder. The X-ray voltage was set at 185 kV (polychromatic) and no filter was applied, such that the beam hardening effect will be more severe and the difference before and after beam hardening correction can be better revealed. 1800 2D projection images of the workpiece were simulated over 360 degrees. Each image has a dimension of 1024x1024 pixels and a bit depth of 16. The reconstructed software was CTPro (developed by Nikon Metrology); the 3D visualization and dimensional measurements were performed with VG Studio Max 2.2 (developed by Volume Graphics). Steel step wedge projection image was also simulated for creating the look up table. The reconstructed 3D models, their histograms, 2D reconstructed slices, gray value profiles and dimensional measurements on the middle pin are shown in Fig 5.39 –5.42.

Figure 5.38 *X-ray projection image of the simulated test setup: (1) Ø3mm steel pin (2) hollow steel cylinder*

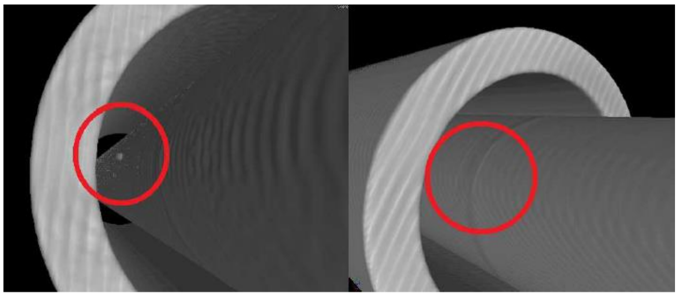

(a)

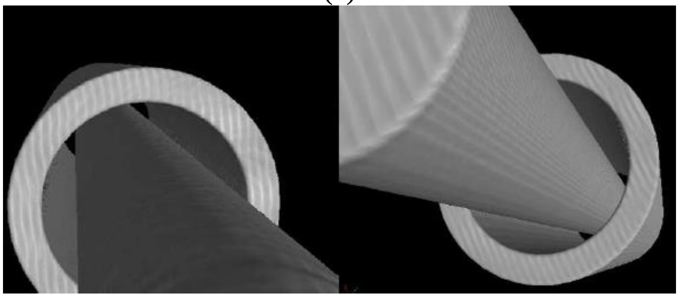

(b)

Figure 5.39 *(a) 3D model reconstructed using the original 2D projection images. False floating materials and surface discontinuities are visible. (b) 3D model reconstructed using the corrected 2D projection images. The surface quality is improved, floating material particles and surface discontinuities are eliminated.*

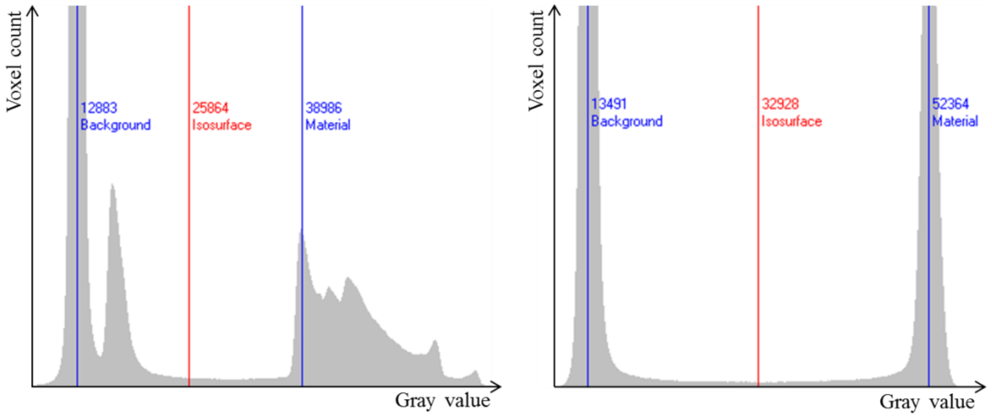

Figure 5.40 *Histogram of the reconstructed voxel cloud. Left: before correction; Right; after correction*

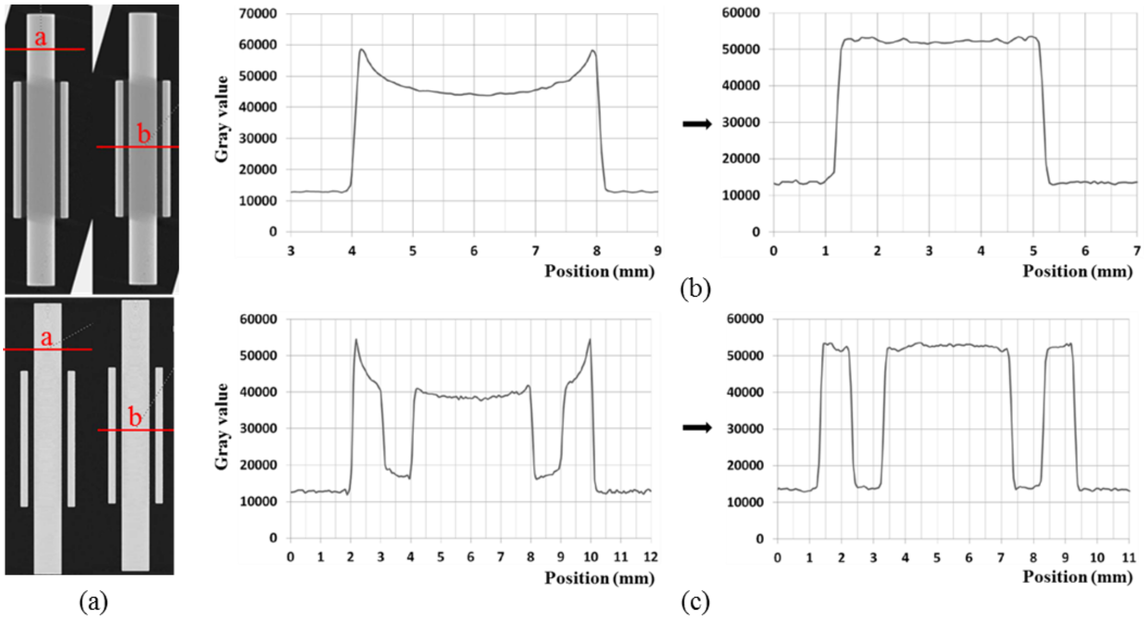

(a)

(b)

(c)

Figure 5.41 *(a) Reconstructed 2D slices. Top: uncorrected; bottom: corrected. (b) Gray value profiles along the red line "a" in (a). Left: uncorrected; right: corrected. (c) Gray value profiles along the red line "b" in (a). Left: uncorrected; right: corrected*

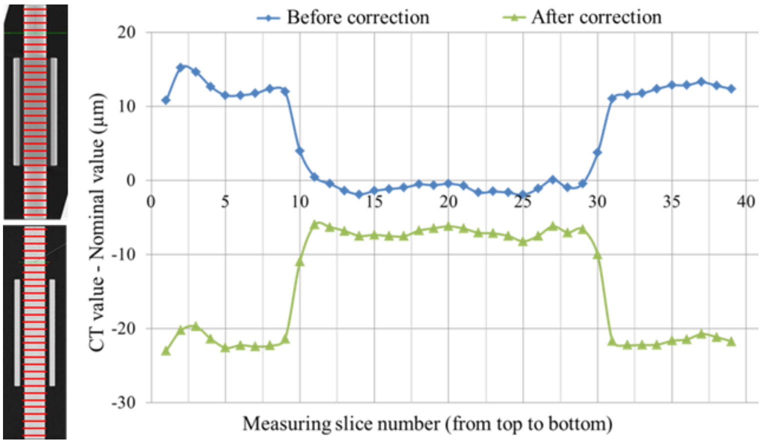

Figure 5.42 *The middle pin's diameters measured as circles at equidistant slices before and after beam hardening correction.*

Several messages are revealed from the comparisons shown in Fig 5.39 - 5.42:

1. Fig 5.39: without beam hardening correction, bumps appear at the transition between the uncovered and covered part of the middle pin. In addition, floating material particles are also observed. These image artifacts are eliminated after the look up table beam hardening correction.
2. Fig 5.40: the original histogram is distorted (multiple peaks) due to the beam hardening effect. After correction, the histogram becomes nice and clean, with one peak for air and one peak for steel.
3. Fig 5.41: severe cupping effects can be noticed on the uncorrected gray value profile plots, which are no longer visible after look up table beam hardening correction.

The developed beam hardening correction algorithm is effective for reducing various image artifacts. However, it does not improve the dimensional measurement results (Fig 5.42). This is mainly due to the lack of reference values between 0 and 1mm attenuating steps, which results in an “over-correction”.

Beam hardening effect is most severe at the outer layers of the object’s surface, whose range is typically around few millimeters or even micrometers. Thus, reference data within this range are crucial for constructing an accurate look up table. Although wedges with micron steps can be simulated, they are in practice very costly or even impossible to be manufactured. Because of its potential for multi-material beam hardening correction, the look up table method was selected and investigated. However, it was discovered throughout the investigation process that this method is highly sensitive to the reference values from micron level attenuating steps. This is a fundamental drawback for practical applications. Thus, although showing good potential in reducing image artifacts, the look up table method cannot meet the requirements of CT dimensional metrology.

- **Pre-defined polynomial correction curve**

At the moment, beam hardening correction using pre-defined polynomial correction curves is favored by most industrial and academic users. Thus, this method was also selected and investigated.

- **Basic concept**

Many reconstruction software programs offer pre-defined/user-defined polynomials for beam hardening correction. Despite of minor variations, the general format representing the polynomial is as follows:

$$Y = r\,(A_0 + A_1X + A_2X^2 + A_3X^3 + ...) \qquad (5)$$

The polynomial represents the estimated relationship between the ideal attenuation values without beam hardening - Y and the measured attenuation values - X. "r" is the scaling factor, which is set to 1 by default; A_0 is the offset value, which is also set to 0 by default. "A_1" through "A_3" represent coefficients that can be fine-tuned depending on the severity of the beam hardening effect. A number of polynomial presets for beam hardening correction (BHC) are available in CTPro, as listed in Table 5.5.

Parameters	**presets**					
	1	**2**	**3**	**4**	**5**	**6**
r	1	1	1	1	1	1
A_0	0	0	0	0	0	0
A_1	1	0.75	0.5	0.2	0.1	0
A_2	0	0.25	0.5	0.8	0.9	0.2
A_3	0	0	0	0	0	0.8

Table 5.5 *6 presets integrated in CTPro (reconstruction software developed by Nikon Metrology) for beam hardening correction. The higher the preset number is, the higher the amount of correction will be. Notice that BHC preset Nr.1 preserves the original values.*

- **Initial investigation on the BHC presets**

The experimental setup discussed earlier (Fig 5.20, described in Section 5.2.1) was used to investigate the influences of 6 BHC presets (Table 5.5). The 2D projection images (both experimental and simulation) were reconstructed several times using different BHC presets. A qualitative comparison between different BHC presets is shown in Fig 5.43.

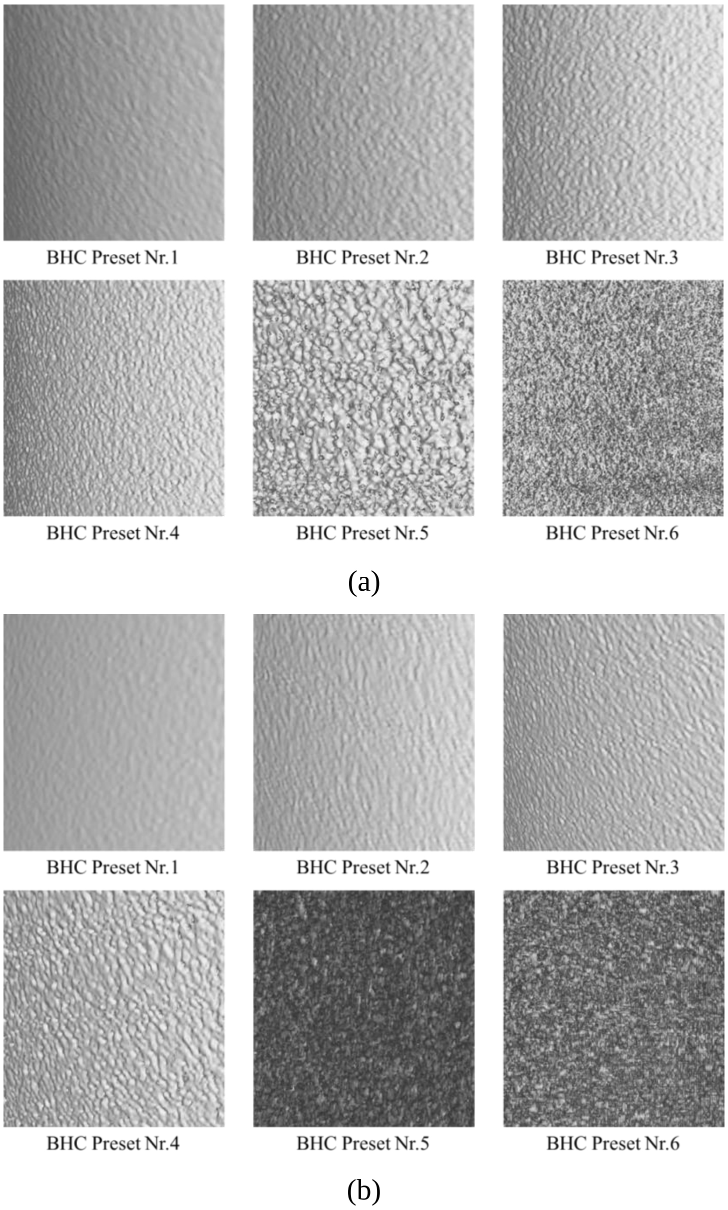

Figure 5.43 *Comparison of the 3D models' surface quality when using different BHC presets (a) experimental data (b) simulated data*

The above figure shows a clear trend that the surface noise increases while increasing the level of beam hardening correction. The polynomials applied for BHC are high pass filters which will enhance high frequency noise. Thus, regarding image quality, using polynomial functions for BHC is a compromise made for reducing image artefacts at the cost of increasing surface noise level. Moreover, as shown in Fig 5.44, the relative distance between background and material peaks decreases while increasing the BHC level; this becomes troublesome when the two peaks start merging with each other (BHC preset Nr.5 and 6).

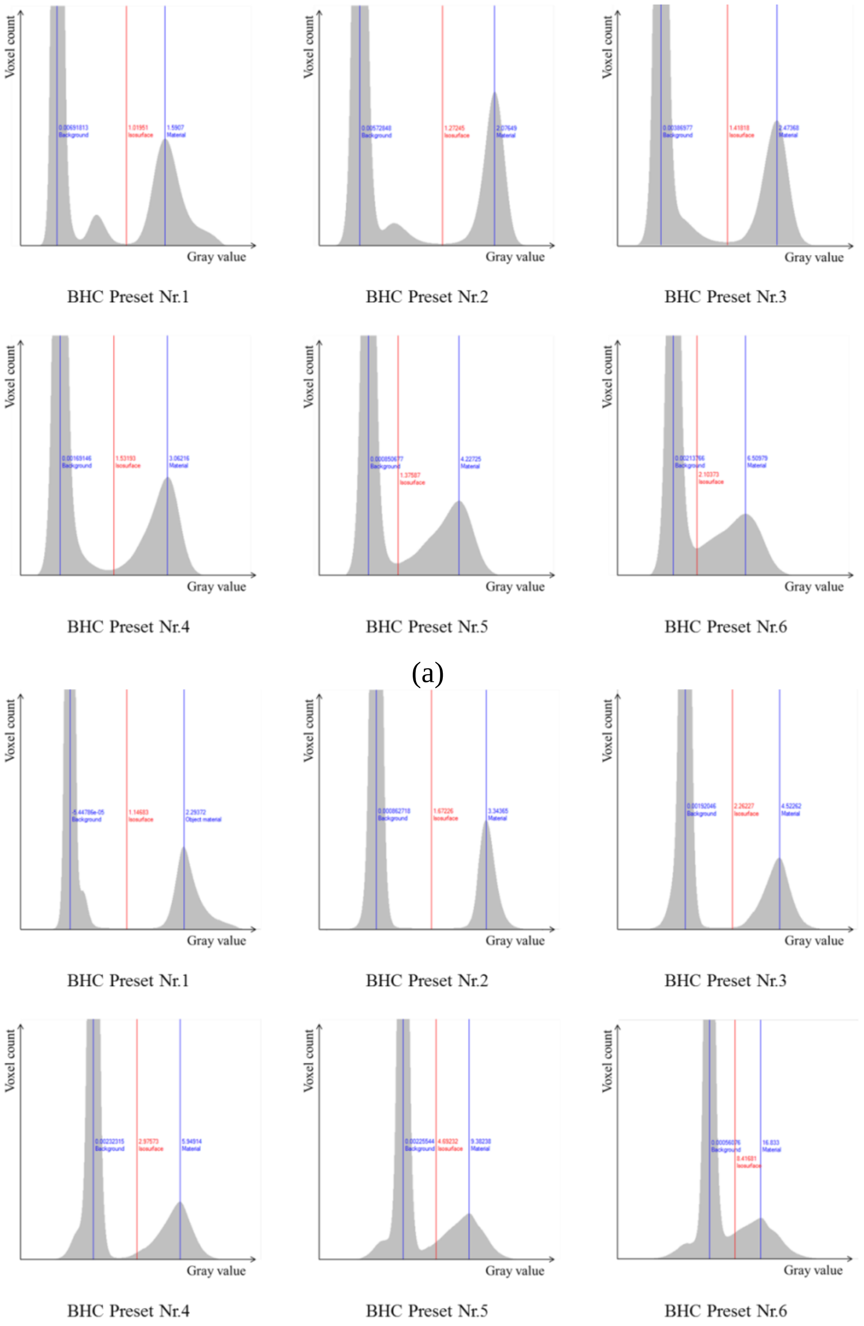

(a)

(b)

***Figure 5.44** Histograms when applying different BHC presets. (a) Experimental data (b) simulated data*

To quantitatively evaluate the influence of different BHC presets on dimensional measurements, 5 quality indicators are defined as follows:

O1-O5, I1-I5, P0-P6 stands for the edge offsets calculated by subtracting the CMM reference values (in case of experimental data)/nominal values (in case of simulation data) from the CT measured values for the 17 measurands shown in Fig 5.19.

"Internal-external offset deviation range" – difference between internal and external features' average edge offsets.

$$a = (O1 + O2 + O3 + O4 + O5 + P0 + P1 + P2 + P3 + P4 + P5 + P6)/10 + (I1 + I2 + I3 + I4 + I5)/5 \qquad (6)$$

“Internal offset deviation” – largest difference between edge offsets of the inner hole diameters at 5 different sections

b = MAX (I1, I2, I3, I4, I5) – MIN (I1, I2, I3, I4, I5) (7)

“Step cylinder external offset deviation” – largest difference between edge offsets of 5 outer cylinders

c = MAX (O1, O2, O3, O4, O5) – MIN (O1, O2, O3, O4, O5) (8)

“Pin offset deviation range” – largest difference between edge offsets of the middle pin diameters at 7 different sections

d = MAX (P0, P1, P2, P3, P4, P5, P6) – MIN (P0, P1, P2, P3, P4, P5, P6) (9)

“CT-CMM offset range” – range of deviations from the CMM reference values

e = MAX (O1, O2, O3, O4, O5, I1, I2, I3, I4, I5, P0, P1, P2, P3, P4, P5, P6) – MIN (O1, O2, O3, O4, O5, I1, I2, I3, I4, I5, P0, P1, P2, P3, P4, P5, P6) (10)

The first four quality indicators evaluate the magnitude of local dimensional deviations and the last quality indicator reveals the total offset range.

Due to large amount of surface noise, BHC preset Nr.5 and 6 were excluded from the following quantitative analyses. The values of the above quality indicators were calculated for the remaining BHC presets; the results are shown in Fig 5.45.

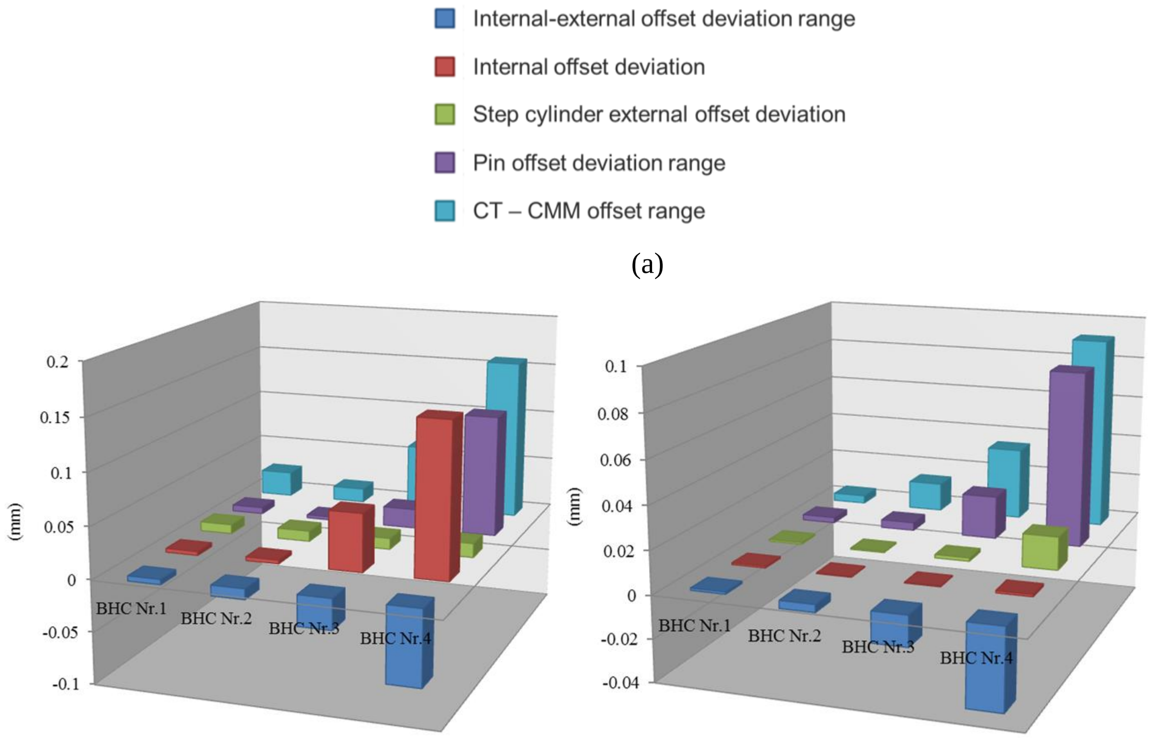

(a)

(b) (c)

__Figure 5.45__ The values of different quality indicators when using different BHC presets (a) legend for different quality indicators (b) experimental results (c) simulation results

Fig 5.45 shows that the dimensional measurement results of BHC preset Nr.3 and 4 are significantly worse than the results of BHC preset Nr.1 and 2.

- **Investigation on the effects of the polynomial's coefficients**

The previous results prove that using high order polynomials can significantly degrade both the image quality and the dimensional measurement results. It can also be concluded that BHC preset Nr.3 and above should be avoided for this test setup. Thus, BHC preset Nr.1 (no correction) and 2 (moderate correction) were chosen for further investigation.

While observing the dimensional variations on the middle pin (Fig 5.46), it was noticed that the direction of the dimensional discontinuities changed between BHC preset Nr.1 and BHC preset Nr.2. It was suspected that an "optimal" BHC polynomial could be found by fine tuning its coefficients. Thus, based on BHC preset Nr.1 and 2, the relative portion of the polynomial's coefficients (A_1, A_2 and A_3) were adjusted, generating 16 coefficient combinations (Table 5.6). Similarly, the previously defined quality indicators were calculated for each coefficient combination. The overall results are shown in Fig 5.47.

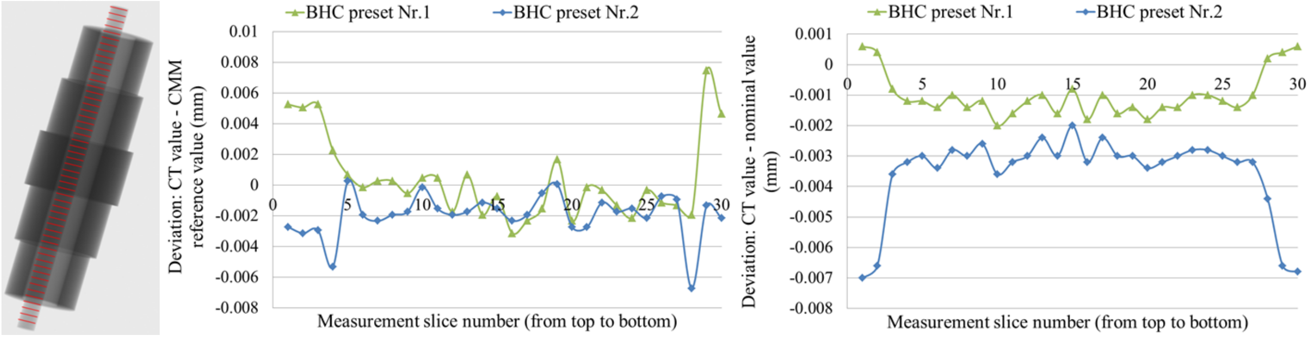

(a) (b) (c)

Figure 5.46 *Local dimensional deviations on the middle pin, its diameters were measured as circles at equidistant slices from top to bottom (a) 2D projection image of the test setup (b) measurement results from experiment (c) measurement results from simulation*

Test Nr.	A_1	A_2	A_3	Remark
1	1	0	0	BHC preset Nr.1
2	0.95	0.05	0	
3	0.95	0	0.05	
4	0.95	0.025	0.025	
5	0.9	0.1	0	
6	0.9	0	0.1	
7	0.9	0.05	0.05	
8	0.85	0.15	0	
9	0.85	0	0.15	
10	0.85	0.075	0.075	
11	0.8	0.2	0	
12	0.8	0	0.2	
13	0.8	0.1	0.1	
14	0.75	0.25	0	BHC preset Nr.2
15	0.75	0	0.25	
16	0.75	0.125	0.125	

Table 5.6 *16 BHC polynomials with different coefficient combinations. "A_1, A_2, and A_3" stand for the coefficients of the "1st, 2nd, and 3rd" order components (see formula 5). Notice that test Nr.1 is the same as BHC preset Nr.1; test Nr.14 is the same as BHC preset Nr.2*

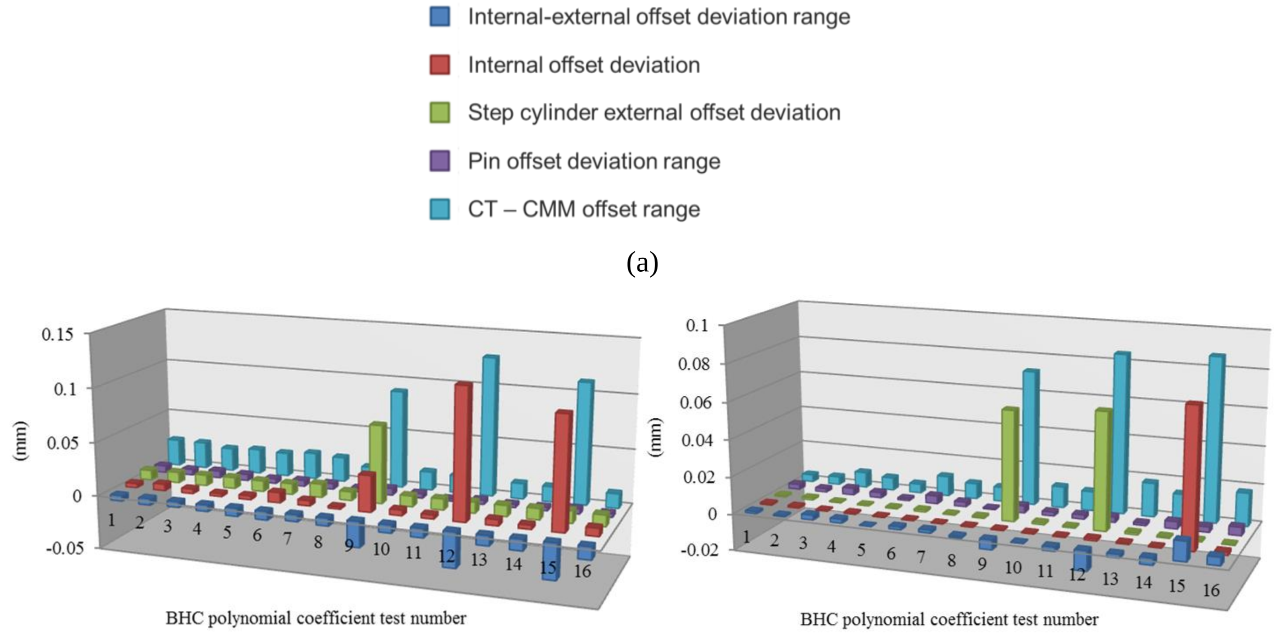

(a)

(b) (c)

Figure 5.47 *The overall dimensional measurement results on the 16 3D models generated by applying different BHC polynomials (Table 5.6) (a) legend for different quality indicators (b) experimental results (c) simulation results*

As shown in Fig 5.47, the overall dimensional measurement quality of test Nr.9, 12 and 15 are significantly worse than the others. These tests share a common feature: the coefficient of the 3rd order component (A_3) is relatively large. Combining this observation with the previous tests using the 6 BHC presets, it can be concluded that assigning large 3rd order coefficient for the BHC polynomial is not recommended for this test setup.

Subsequently, the results of test Nr.9, 12 and 15 are removed and the remaining tests were compared and shown in Fig 5.48.

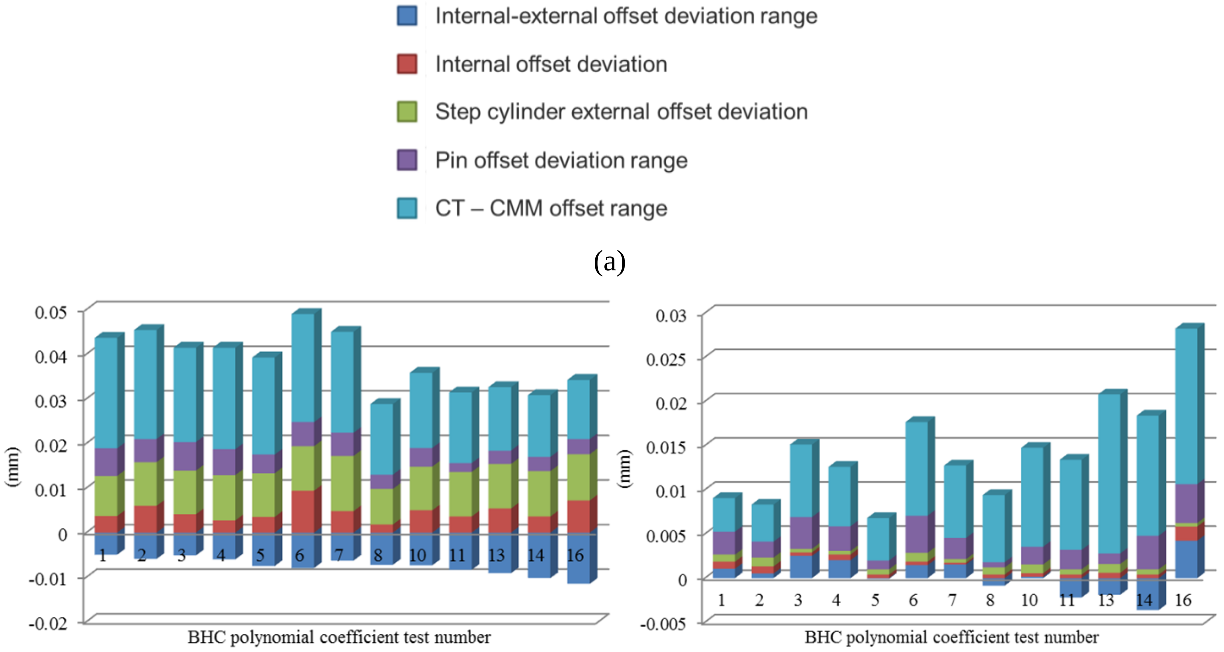

(a)

(b) (c)

Figure 5.48 *The overall dimensional measurement quality of different CT 3D models generated by applying different BHC polynomials (Table 5.6); outliers are excluded (a) legend for different quality indicators (b) experimental results (c) simulation results*

The information obtained from Fig 5.48 can be summarized as follows:

- Fig 5.48 (b)

1. The differences between these test results are rather small.
2. The overall dimensional measurement result of test Nr.8 is shown to be the best.

- Fig 5.48 (c)

1. The dimensional measurement results of different tests vary a lot.
2. The overall dimensional measurement result of test Nr.5 outperforms all the rest.

- Combining Fig 5.48 (b) and (c)

1. Generally speaking, the errors of the real scan are much larger than the ones of the simulation. This is due to various error sources (e.g. X-ray scattering, machine axes misalignment, uncertainty of the tactile CMM reference values etc.) that were excluded from the simulation.

2. Varying the coefficients of BHC polynomial mainly affects the magnitude of internal-external offset deviation range, internal offset deviation and pin offset deviation range, since they are more sensitive to the changing SNR

3. Varying the coefficients of BHC polynomial has very limited effect on the step cylinder external offset deviation. This term tends to be stable due to the enhanced external edge contrast by the beam hardening effect.

4. By comparing Fig.5.48 (b) and (c), the relatively large magnitude of "step cylinder external offset deviation" in Fig 5.48 (b) is most likely due to the uncertainty of the tactile CMM reference measurements.

5. The CT-CMM offset range is inherently larger than the others because it includes both local dimensional deviations and global thresholding errors.

6. When keeping the linear coefficient (A_1) constant and varying the 2nd and 3rd order coefficients (A_2 and A_3), a general trend can be observed: the larger the 3rd order coefficient is, the worse the dimensional measurement results will be.

7. The test setup was made from dense metal and was scanned at 210kV, which is close to the maximum X-ray voltage of the CT scanner. The BH level seen from this setup can roughly represent the most severe BH level one would encounter when using this CT scanner. Nevertheless, it was shown that applying 2nd order polynomial could offer sufficient BHC for this setup. Thus, for the tested 225kV CT scanner, it is recommended to limit the BHC polynomial within the 2nd order to avoid over correction.

8. Fig 5.49 plots the dimensional measurement results for tests whose 3rd order coefficients are 0. Both experimental and simulation results indicate that the overall quality of dimensional measurements can be improved by adjusting the relative proportion between the 1st (A_1) and the 2nd (A_2) coefficients. It can also be noticed that the overall dimensional measurement quality improves along with increasing A_2 until it reaches a certain point from where further increasing A_2 will degrade the quality; in most cases, BHC preset Nr.2 (test Nr.14) will already exceed this point.

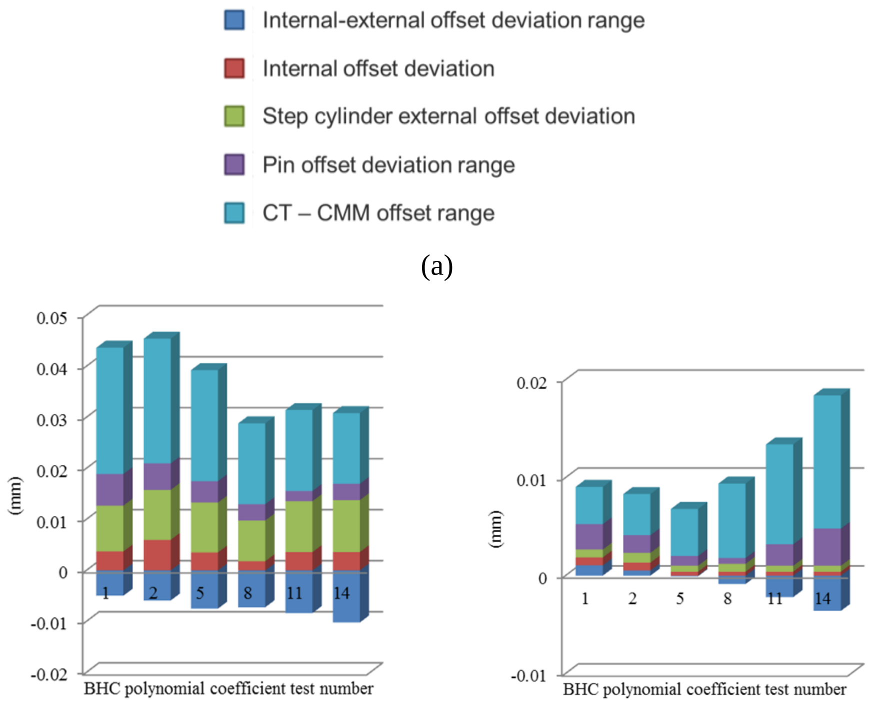

(a)

(b) (c)

Figure 5.49 *Dimensional measurement results for tests whose 3rd order coefficients are 0 (a) legend for different quality indicators (b) experimental results (c) simulation results*

5.2.2.3 Conclusions

This section investigated the influence of beam hardening effect on CT dimensional measurements. Furthermore, two beam hardening correction techniques were tested. Several conclusions can be drawn as follows:

- The Beam hardening effect not only causes various image artifacts but also induces local dimensional deviations
- The developed look-up table beam hardening correction method has a positive impact on various image artifacts. However, local dimensional deviations are not reduced. More importantly, to achieve micron level improvements on dimensional measurements, this method will require micron level attenuating steps which are in practice very difficult to be accurately manufactured.
- It is possible to improve the overall quality of dimensional measurements using the pre-defined polynomial beam hardening correction method. Regarding CT scans performed on the 225kv industrial CT system, 2nd order polynomial is sufficient. In addition, the "optimal" coefficients are case dependent and the tested setup (hollow cylinder + middle pin) can serve as a calibration object.

CHAPTER 6

Case Study – Verification of Industrial CT for Dimensional Metrology

Although the achievable accuracy of industrial CT can be improved up to micron level when measuring regular features and academic workpieces, its applicability as a measuring tool for dimensional quality control of industrial objects still needs to be justified.

This chapter presents an in-depth investigation on the accuracy and repeatability of a 225kV industrial CT scanner when performing complex dimensional measurement tasks on a multi-material industrial part: an ABS brake module (anti-lock brake system) from the automotive industry. Except for the previously discussed influence factors, two additional factors – the alignment system and operator dependency – are also investigated.

6.1 Background and workpiece description

Ever since industrial CT was introduced into the dimensional metrology application field, a number of attempts have been made to quantify the achievable accuracy of CT measurements. Clark suggests a simple but general rule for calculating the accuracy of an industrial micro-focus CT system, which is approximately 1/3 of the voxel size *[Clark J., 2010]*. Carmignato et al. have developed a test specimen with shaft and hole structures to determine the thresholding value and they have reported the dimensional deviations to be within $\pm 4\,\mu m$ for a voxel size of $9\,\mu m$ *[Carmignato S. et al., 2009]*. Suppes and Neuser claim that proper beam hardening correction and surface extraction methods reduce the deviations on diameters to less than 10% of the voxel size, whereas distance deviations can be lower than 1/50 of the voxel size *[Suppes A. et al., 2008]*. All the above results indicate a promising future for CT in the metrology field. However, most tests are done using workpieces with certain "easy" features, such as parallel planes, cylindrical shafts and holes, and spheres. Due to the large number of influence factors (such as workpiece material characteristics, changing penetration length, scattering noise, beam hardening artifacts, filter usage, resolution and X-ray power limitations, etc.), the measurement accuracy when measuring laboratory testing objects often deviates from the measurement accuracy when handling real industrial objects. In order to get a clearer view on the achievable accuracy of industrial CT systems when dealing with complex industrial components, an ABS electronic wiring module (Fig 6.1) from the automotive industry is scanned multiple times and various features are measured on the CT 3D models. The measurement accuracy (compared to the tactile CMM reference values) and repeatability of different CT scans are investigated.

As shown in Fig 6.1, the ABS brake module is a multi-material assembly which consists of three types of materials: PBT (polybutylene terephthalate) plastic, aluminum and copper. Its general dimensions are around 120mm × 90mm × 40mm, which can be considered as a medium size object among typical industrial CT measurement tasks.

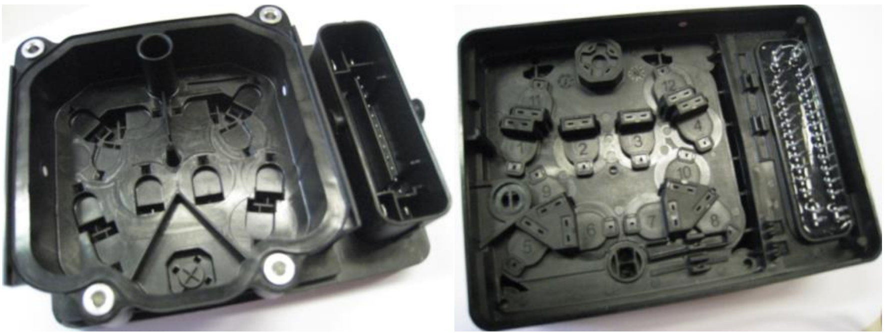

(a)

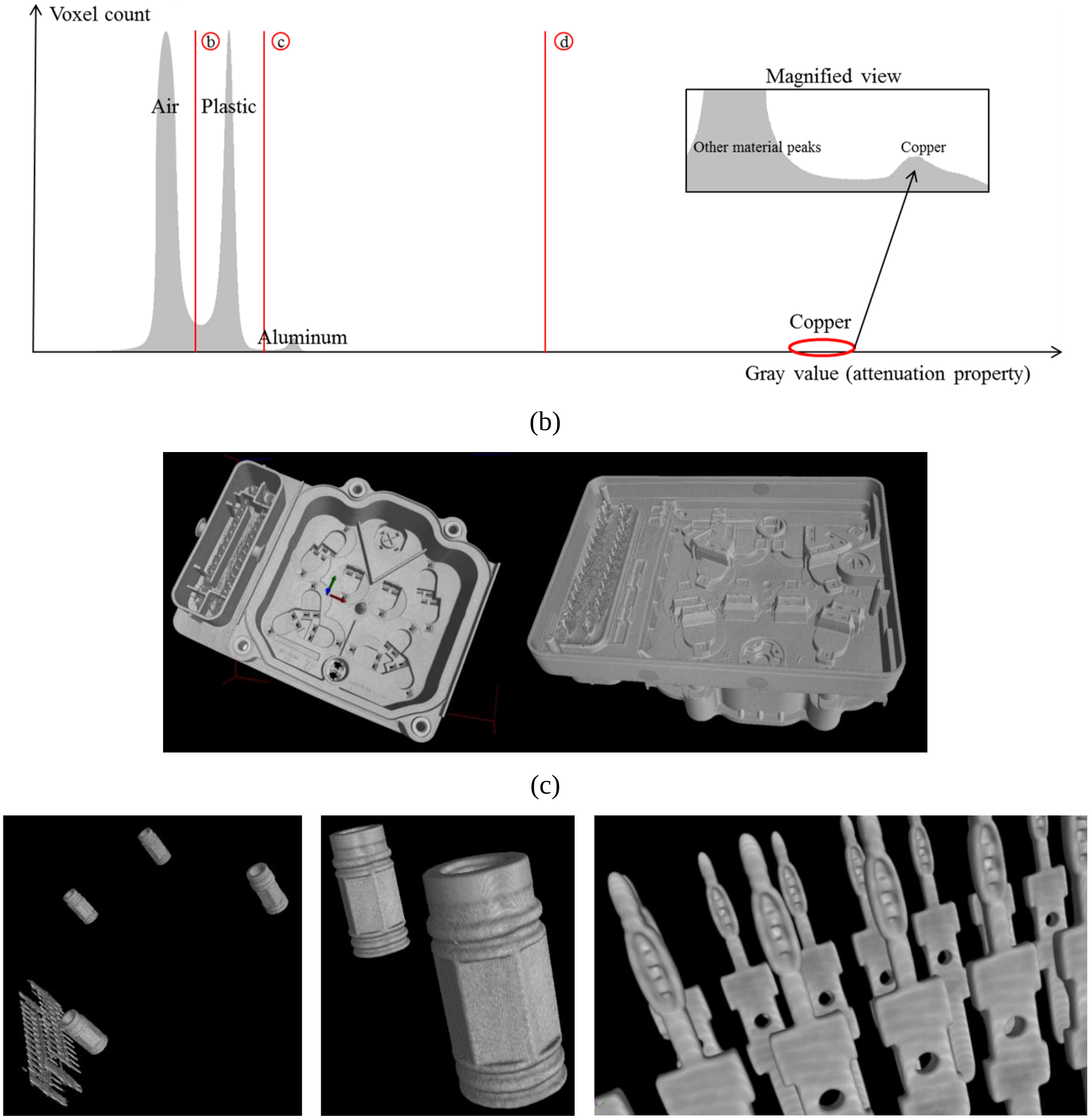

(b)

(c)

(d)

Figure 6.1 *(a): photo of the multi-material assembly – ABS wiring connector module containing three types of materials: PBT plastic, aluminum and copper. (b): the overall histogram of the 3D voxel model. The three red lines stand for the selected gray values as the starting contours for local adaptive thresholding which are 'optimized' for different materials. (c): 'optimized' 3D model for the plastic component. (d): 'optimized' 3D model for the aluminum components – cylindrical bushing inserts and copper components – pin wiring connectors respectively.*

6.2 CT scanning conditions and data processing strategy

The ABS module is scanned six times using different machine settings and by different operators; such that the operator influences can also be studied. The major machine settings for different CT scans are listed in Table 6.1.

Scan Nr.	Voltage (kV)	Current (μA)	Copper filter	Voxel size (μm)	Operator Nr.	Scan date
1.1	225	180	1.5mm	89.3	1	2013-10-30
1.2	225	180	1.5mm	89.3	1	2013-10-30
1.3	225	180	1.5mm	89.3	1	2013-10-30
2.1	205	270	1.5mm	87.9	2	2014-03-18
2.2	205	270	1.5mm	87.9	2	2014-03-20
2.3	205	270	1.5mm	87.9	2	2014-03-21

Table 6.1 *Major machine settings for six CT scans*

Two experienced operators have scanned the ABS module independently. They both followed similar scan setting optimization strategies but due to their different interpretations, the resulting machine settings were slightly different from each other. As shown in Table 6.1, the first three scans were performed by operator Nr.1 on the same day, one after another. The ABS module stayed on the rotary table in the CT scanner during the entire process and was not moved between different scans. This resembles the 'repeatability' test, because the scanning process was repeated three times with identical conditions. The last three scans were performed by operator Nr.2 on three different days and the ABS module was removed from the rotary table in the CT scanner and repositioned for each scan. This resembles the 'reproducibility' test, which describes the ability of an entire experiment to be reproduced according to the same reproducible experimental description and procedure.

Due to the applied 1.5mm copper filter and the large amount of light PBT material, no post beam hardening correction was needed. In order to compare the CT dimensional measurements with their tactile CMM reference values, the CT 3D model needs to be properly aligned. The workpiece coordinate system is defined using the aluminum bushing inserts, as indicated in Fig 6.2.

X-Y plane: The X-Y plane is defined using the top surface of bushing Nr.1, 2 and 4. It was mentioned by the manufacturer that bushing Nr.3 is relatively lower than the others and thus was not used for determining the coordinate system.

X-axis: two circles are fitted on bushing Nr.1 and Nr.2, 1mm below the X-Y plane. Their center points are then projected onto the X-Y plane. The line connecting the two projected points is the X-axis, its positive direction is pointing from bushing Nr.1 to bushing Nr.2.

Origin: the projected circle center point of bushing Nr.1 is chosen as the origin.

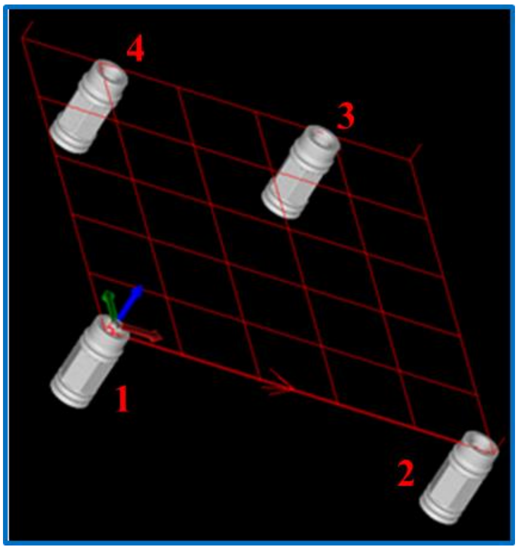

Figure 6.2 *The workpiece alignment system*

Due to its multi-material composition and the fact that the determination of the entire alignment system is based on the aluminum bushings, the procedures for measuring different features on the ABS module are rather complex. As shown in Fig 6.3, there are 8 major steps throughout the entire measuring process:

1. Local adaptive thresholding is performed with the starting contour optimized for the aluminum bushings (the thresholding starting contour is placed between the peaks for plastic and aluminum, see Fig 6.1b). Hence, a 3D model is generated which contains the aluminum bushings and copper connector pins, see Fig 6.1d.
2. The features needed for the alignment system are fitted on the bushing surfaces. The workpiece coordinate system is created.
3. The X-Y coordinates of different bushing center points are measured and compared with the reference values obtained using tactile CMM. This allows calculating the average rescaling factor.
4. The voxel size of the CT 3D model is corrected using the average rescaling factor.
5. The features needed for the alignment system are re-fitted and the workpiece coordinate system is recreated.
6. The required dimensional measurements on the aluminum components are performed.
7. A new local adaptive thresholding is performed with the starting contour optimized for the plastic parts (the thresholding starting contour is placed between the peaks for air and plastic, see Fig 6.1b). A new 3D model is created which contains plastic components, aluminum bushing and copper connector pins: see Fig 6.1c.
8. The required dimensional measurements on the plastic components are performed.

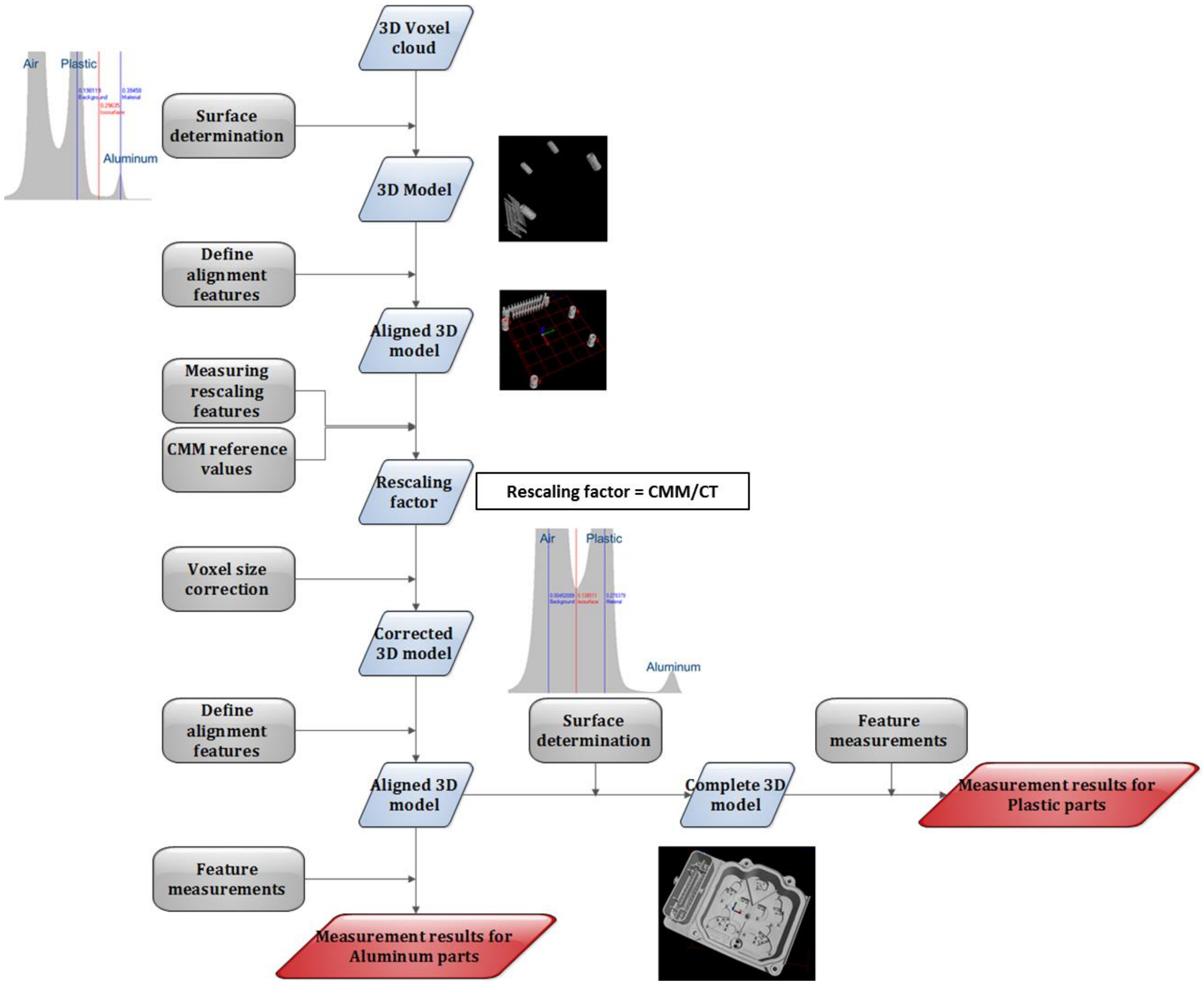

Figure 6.3 *Working flow chart for measuring the ABS wiring connector module.*

6.3 Description of the measured features

6.3.1 Dimensional measurements on the aluminum bushings

There are three types of features (Fig 6.4) measured on the aluminum bushings, as listed below:

A1. Circle diameters (Fig 6.4 a): inner circles are fitted on each bushing at a level that is 1mm below the X-Y plane. Their diameters are measured.

A2. Circle center point coordinates (Fig 6.4 b): the center points of the previously fitted circles are projected onto the X-Y plane. The x and y coordinates of the projected points are recorded.

A3. Flatness of the X-Y plane.

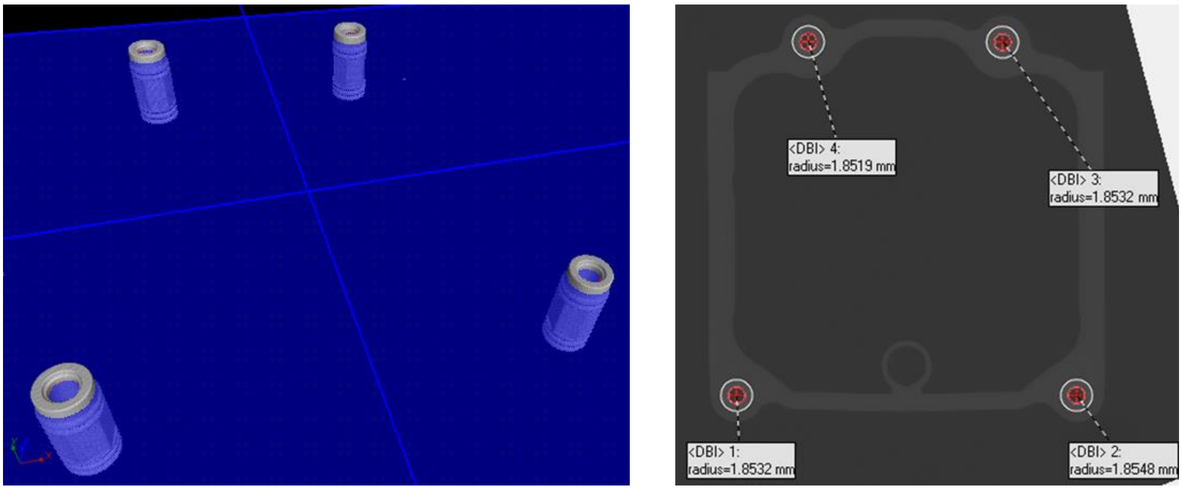

(a) (b)

Figure 6.4 *Features measured on the aluminum bushings. (a) inner circles are fitted on each bushing at a level that is 1mm below the X-Y plane. Their diameters are measured. (b) the center points of the previously fitted circles are projected onto the X-Y plane. The x and y coordinates of the projected points are recorded.*

6.3.2 Dimensional measurements on the plastic components

Similarly, three types of features (Fig 6.5) are measured on the plastic part, as listed below:

P1. Circle diameter (Fig 6.5 a): an inner circle is fitted on the middle cylinder at a level that is 1mm below the X-Y plane. Its diameter is measured.

P2. Circle center point x-y position (Fig 6.5 a): the center point of the above fitted circle is projected onto the X-Y plane; the x-y coordinates of the projected point are recorded.

P3. Point distances (Fig 6.5 c): four distances connecting pre-defined points are measured.

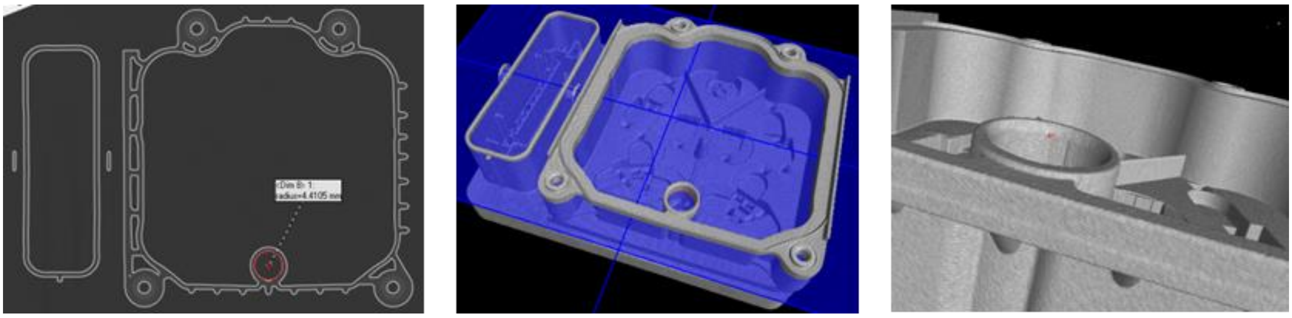

(a)

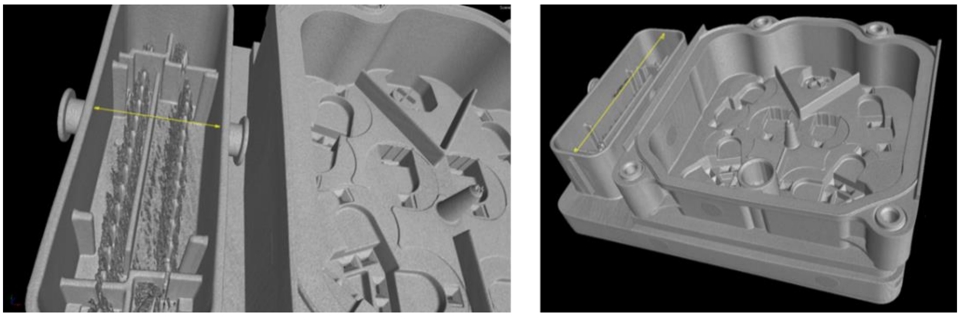

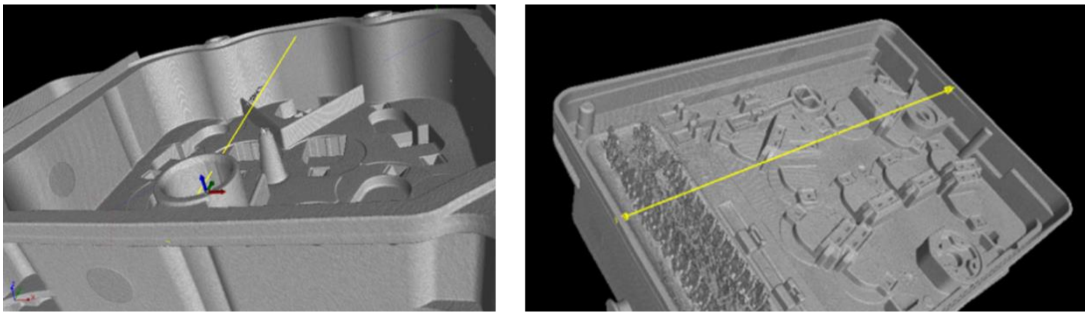

(b)

Figure 6.5 *Features measured on the ABS components. (a) circle diameter and its center point x-y coordinates (b) four distance measurements.*

6.4 Decision on the alignment system

Initially, there were two methods for defining the X-Y plane:

1. Three local coordinates are created respectively for bushing Nr.1, 2 and 4. Four points with pre-defined radius at 45°, 135°, 225° and 315° are fitted on each bushing's top surface. The global X-Y plane is fitted using the 12 points on the top surfaces of bushing Nr. 1, 2 and 4.

2. The X-Y plane is fitted through the top surfaces of bushing Nr.1, 2 and 4 using maximum 1000 fitting points.

Method Nr.1 resembles the procedure of tactile CMM measurements while method Nr.2 takes advantage of the large amount of available points on the CT 3D model. In order to decide which method should be applied, the 3D model of scan Nr.1.1 (Table 6.1) is aligned using both methods; feature A1 and A2 (Section 6.3) are measured under both alignment systems and compared. The results are shown in Fig 6.6.

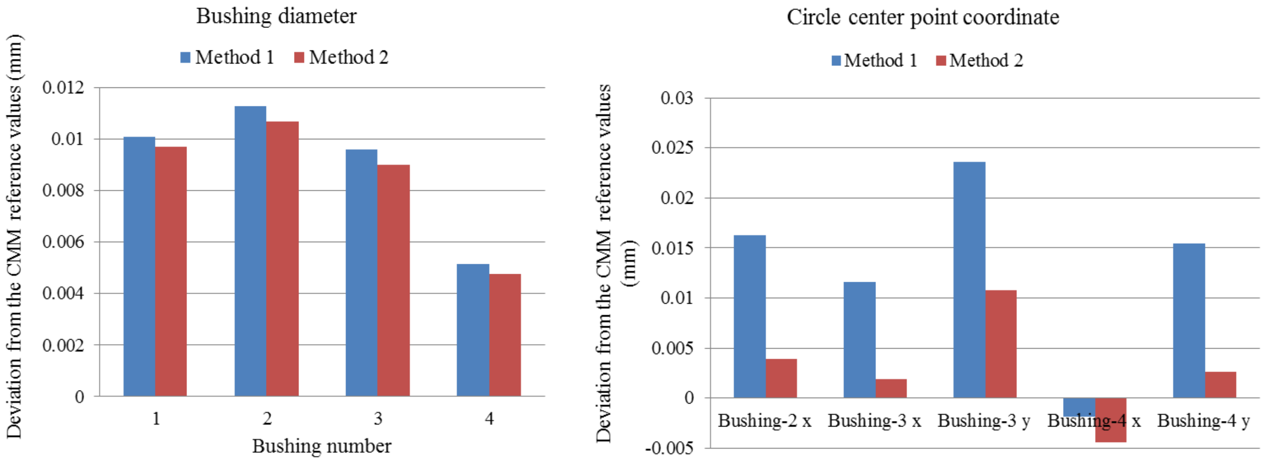

(a) (b)

Figure 6.6 *Comparison of measurement results using different methods for defining the X-Y plane. (a) measurement result of four circle diameters (b) measurement result of the x-y coordinates of different circle center points.*

The measurement accuracy of circle diameters are mainly influenced by the thresholding error, while the circle center point coordinates are affected by the accuracy of the alignment system. As indicated in Fig 6.6, although the measurement results of circle diameters are indifferent between the two methods, the circle center point coordinates are significantly better when method Nr.2 is applied. This reveals that defining the X-Y plane with more points tends to reduce the error made on the alignment system despite its differing from the procedure applied for the CMM reference measurements. CT 3D model inherently suffers from surface noise and various image artifacts. Thus, defining the X-Y plane with only 12 points has a high risk of picking outliers on the surface; hence, the entire alignment process might be hindered. On the other hand, defining features using a large amount of fitting points can easily be achieved on the CT 3D model, which can largely eliminate the high risk of picking outliers. Thus, for defining the X-Y plane, method Nr.2 is selected for aligning the 3D models of all the other scans.

6.5 Data analysis and conclusions

The dimensional measurement results for the previously described features are shown below:

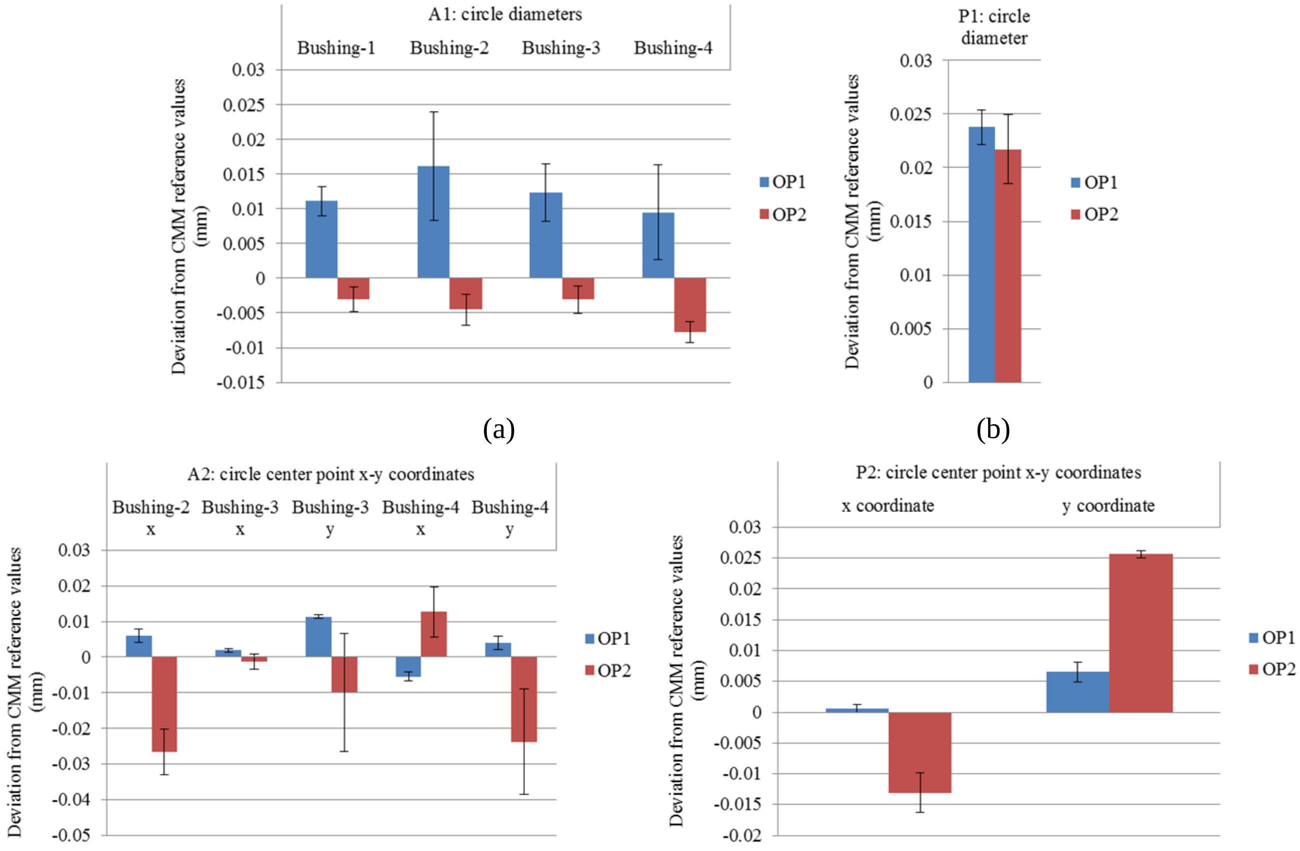

(a)

(b)

(c)

(d)

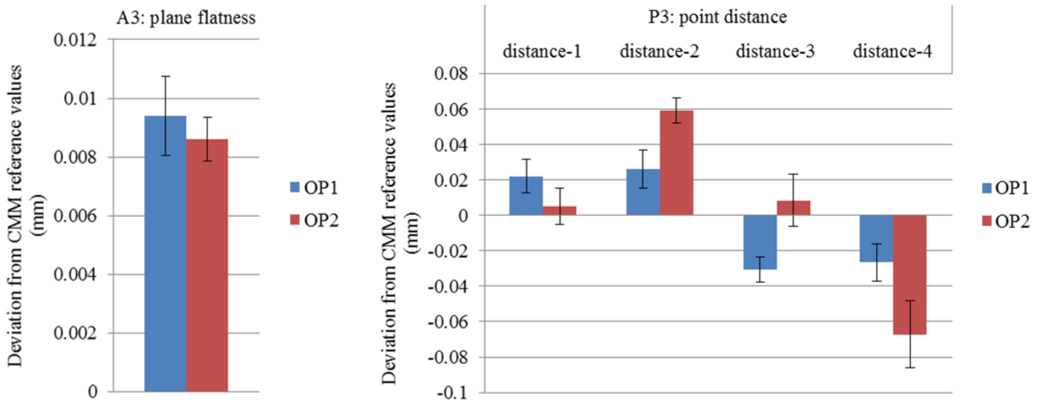

(e) (f)

Figure 6.7 *Overall dimensional measurement results. "OP1" stands for operator 1; "OP2" stands for operator 2. The detailed scan settings can be found in Table 6.1. The definition of different feature measurements can be found in Section 6.3. The average deviations of feature measurements by each operator are plotted in the graphs; the error bar indicates the standard deviation of 3 scans performed by the same operator.*

Fig 6.7 reveals the following facts:

Fig 6.7 (a): the average edge offset errors for the aluminum parts are 12 µm and -5 µm for the scans performed by operator 1 and 2 respectively; meanwhile, the standard deviation of measurements performed by operator 1 is significantly higher than the ones performed by operator 2.

Fig 6.7 (b): the average edge offset errors for the plastic parts are similar for all scans, which are in the range of 20 to 25 µm. The measurement results produced by two operators are indifferent when measuring circle diameters on the plastic part.

Fig 6.7 (c) and (d): regarding the x-y coordinates of the circles' center points, the measurement results produced by operator 1 are significantly better than the ones produced by operator 2, in the aspects of both accuracy and repeatability.

Fig 6.7 (e): the measurement results produced by both operators are similar. Generally speaking, the plane flatness measured by CT is around 9 µm larger than measured by tactile CMM.

Fig 6.7 (f): although the standard deviations of measurements performed by both operators are comparable, the 'error' range of the measurements from operator 2 is much larger.

Several conclusions can be drawn based on the above observations:

1. The accuracy of circle diameter measurements is mainly influenced by the thresholding process. From the measurement results on 'A1' and 'P1', we see that two operators' performances are very similar when measuring dimensions on the plastic part, but differ when measuring on the aluminum part. Both operators applied 1.5mm copper filter and similar voxel size for their scans; however, operator 2 used a lower X-ray voltage. This voltage difference induces differences in the beam hardening level and thus influences the thresholding process. It is shown that measurements on 'A1'

are more accurately performed by operator 2, which matches the suggestions proposed in Chapter 4: using a relatively lower X-ray voltage whenever possible.

2. When measuring the coordinates of a certain point (such as 'A2' and 'P2') or measuring distances between points (such as 'P3'), there is one additional influence factor: the alignment system. The definitions of these points are dependent on the alignment system and thus any inaccuracy of the alignment system will also affect the measurement results related to these points. Fig 6.7 (c), (d) and (f) indicate potential alignment errors for the scans performed by operator 2; it was later discovered that the workpiece was sprayed with white powder after the scans of operator 1 in order to be scanned with a fringe projection system. Although a cleaning process was performed and most of the powder was removed before operator 2 scanned the part, there was still some white powder attached to the inner surface of the aluminum bushings; thus inducing large alignment errors. Nevertheless, these measurement results are strong evidences which reveal the large impact of the alignment system. Many artefacts used for academic research have simple geometry and do not require sophisticated alignment procedures. However, a workpiece coordinate system is an essential part when measuring industrial components. More importantly, inaccuracies of the alignment system can directly influence the corresponding dimensional measurements. Thus, when dealing with complex industrial components, one should try to develop reliable alignment strategies and test its influences before conducting any dimensional measurements.

3. The measurements on 'P3' performed by operator 1, showed a clear edge offset error, which is around 25 µm; this reinforces the observation from 'P1'. When the alignment errors are insignificant, the thresholding edge offset errors can be clearly detected. This error can be further compensated by manually offsetting the measurement results or by varying the thresholding starting contour (discussed in Chapter 5).

4. Fig 6.7 (e) shows that the flatness measured by CT is higher than measured by tactile CMM; this is not a coincidence. A similar trend can also be found when analyzing the measurement report of two inter-laboratory comparison projects (a brief introduction on these two international projects can be found in Chapter 1, Section 1.2.3). A clear 'overestimation' (when comparing with the reference tactile CMM measurements) of form error values measured by all participants for both inter-laboratory comparison projects can be observed. This trend is primarily caused by the inherent differences between industrial CT and tactile CMM measurements. First of all, the surface quality of the CT 3D model is largely influenced by beam hardening and X-ray scattering artifacts, which tend to increase the measured form error. Secondly, tactile CMM measurement usually uses very limited fitting points (around or even below 20 points); on the contrary, the corresponding CT form measurement includes large amount of fitting points (around 1000 points). Thus, CT is more capable of capturing high frequency surface texture, such as: waviness and roughness (as discussed

in Chapter 3, Section 3.2). This can also make the CT measured form error larger than the one measured using tactile CMM.

5. The measurement repeatability is dependent on several factors:

- The selected scan settings: as shown in Fig 6.7 (a), the repeatability of the scans performed by operator 2 when measuring feature 'A1' is significantly better than the scans performed by operator 1. The thresholding process can benefit from a proper selection of scan settings, which in return makes the measurements more repeatable.
- The accuracy of alignment system: when measuring features which are closely linked with the alignment system, the measurement repeatability will also depend on the repeatability of the alignment process.
- Feature type: the repeatability of measuring standard features (e.g. circle, cylinder and sphere diameters) is usually better than measuring user defined features (plane distance, point coordinates. When the scanning settings are 'optimized' and the alignment system is well repeatable, one can expect the standard deviation to be within 5 µm when measuring a standard feature.

CHAPTER 7

General Conclusions: Industrial CT for Dimensional Metrology

This PhD thesis describes a small part of the wonderful CT dimensional metrology world. In this final chapter, the general conclusions and main contributions of the research conducted are summarized. In addition, perspectives for future research are suggested.

7.1 Context of the research

Industrial CT is increasingly favoured by the manufacturing industry due to its capabilities to provide geometric information of inner and hidden structures of complex or assembled parts. However, due to the large amount of influence factors and various image artifacts, micron-level accuracy and traceability to the unit of length remains a challenge for CT dimensional metrology.

Within this PhD research, different influence factors throughout the measuring process of CT dimensional metrology are investigated.

7.2 Main contributions

7.2.1 Influence of workpiece properties

The influences of two major workpiece properties are investigated: material and surface roughness. It was found that the workpiece material is not a standalone influence factor, but is closely related to the orientation of the object during the scanning process and the type of features it contains. When dealing with different materials, the accuracies of CT dimensional measurements are similar as long as the objects are scanned under proper machine settings. In case a workpiece is highly attenuating and contains a lot of flat surfaces, it is important to avoid positioning the flat surfaces parallel to the incident X-ray beams. In addition, it was discovered that the accuracy of plane distance measurements is closely related to the planes' fitting qualities. The distances between planes that have small fitting point standard deviations also tend to have smaller errors.

As tactile CMM is still considered to be a more accurate dimensional measuring technique and often set as reference for evaluating CT measurements, it is important to also understand the inherent differences between these two technologies. Surface roughness has proven to be an important factor which differentiates them. Due to the limited structural resolution, tactile CMM tends to 'measure' the peak points of a rough surface profile while CT, similar like many other optical measuring techniques, is measuring the middle profile between peaks and valleys. When measuring parts that are manufactured with turning process, the edge offsets of CT dimensional measurements (when taking tactile CMM measurements as reference) are linearly related to the R_p value.

7.2.2 Influence of scanning parameters

High operator dependency is remaining a major limitation for CT dimensional metrology. A large part of this PhD research focuses on investigating the influences of different machine settings and their correlations.

The influences of target material for different applications are studied. It is noticed that copper target has certain advantage when analyzing micron features (e.g. porosity analysis); its X-ray emission spectrum is more suitable for detecting small details and therefore can cover a wider range of pore sizes. In addition, it was proved that when measuring larger features (millimeter or centimeter range), the choice of target material also have an influence on the dimensional measurement results.

A 3×3 full design of experiment was conducted to investigate the influences and correlations between X-ray voltage, filter and voxel size. It was revealed that all three factors can be influential on various edge offset terms. Moreover, their influences are often interlinked. Generally speaking, the "optimal" scanning setting combination should be: medium X-ray voltage – heavy filtration – small voxel size. In addition, it was proven that the general guideline for CT NDT applications (setting the MTR to around 14%, or between 10 and 20%) cannot be directly transferred to CT dimensional metrology applications; as a general image quality indicator, MTR cannot distinguish the effects of different influence factors.

7.2.3 Influence of post processing parameters

There are two major post processing steps which generate a 3D model from the obtained 2D X-ray projection images: reconstruction and thresholding.

Two commonly applied thresholding methods – global thresholding and local adaptive thresholding are compared in three aspects: surface quality of the 3D model, accuracy of dimensional measurement, and behavior when shifting the starting contour in the histogram. Generally speaking, local adaptive thresholding method outperforms global thresholding method in all aspects. However, in case of low signal to noise ratio, global thresholding might be more favorable. Local adaptive thresholding looks at the gray value changing gradient and requires good edge contrast, thus it is more vulnerable to surrounding noises when they are inevitable. In addition, the effects of 'shifting starting contour' and 'search region' are studied in depth for the local adaptive thresholding method. Two general conclusions can be drawn from this study: when applying the local thresholding method, it is important to avoid putting the starting contour cross major peaks in the histogram. Using a too small search distance is not recommended, because they usually don't cover the entire transition from air to material and thus the risk of defining wrong material edges increases.

Beam hardening correction has long been a major research challenge for the CT society. Within this PhD study, the influence of the beam hardening effect and its correction on the accuracy and local dimensional variations are investigated using both experimental and simulation approaches.

It is revealed that the beam hardening effect can create differences in edge contrast between external and internal features, thus resulting in local dimensional variations which are difficult to be compensated. Two linearization techniques have been investigated and explored: the step wedge based look-up table method and the pre-defined polynomial correction method.

The look-up table method was investigated due to its potential for multi-material beam hardening correction. However, severe drawbacks were soon discovered while testing it for single material beam hardening correction. The demand for micron level attenuating steps makes it extremely costly for practical implementation. Nevertheless, with the help of CT simulation, the developed algorithm has been proven to be effective for eliminating various image artefacts.

The pre-defined polynomials are shown to be effective for reducing various dimensional measurement errors. Both simulation and experimental results show that polynomial up to the 2nd order is sufficient for beam hardening correction. Using higher order polynomials has a high risk of degrading the dimensional measurement results. Moreover, it is shown that an 'optimal' polynomial can be reached by adjusting the relative portion between 1st and 2nd order coefficients.

7.2.4 From academic research to industrial applications

Although the achievable accuracy of industrial CT can be improved up to micron level when measuring regular features and academic workpieces, its applicability as a measuring tool for dimensional quality control of industrial objects still needs to be justified. As the last part of this PhD research, a case study was performed on a multi-material assembly from the automotive industry. Generally speaking, the measurement accuracy is within 25 µm for most measurands which is below 1/3 of the voxel size. In addition, the impact of the alignment system is studied, which proves that the process for defining an alignment system can have large impact on the final results when comparing dimensional measurements obtained by CT and tactile CMM.

7.3 Suggestions for future research

Although CT technology already exists for over 40 years, its application as a tool for dimensional quality control only started a few years ago. The conducted PhD research tries to investigate various influence factors using both simulation and experimental approaches, aiming to optimize the scanning and post-processing parameters for CT dimensional metrology.

The knowledge acquired through these studies can form a solid base for in-depth investigation on specific topics and for developing more advanced optimization algorithms. The author believes that further research on the following topics will generate meaningful insights for CT dimensional metrology applications:

1. It was discovered, by using several turned aluminum cylinders, that the surface roughness has significant influence on CT dimensional metrology when taking traditional tactile CMM as the reference technique. The research can be further extended by investigating workpiece manufactured by other techniques which contains different types of surface textures.
2. The investigation on the influence of various scanning parameters (X-ray voltage, filter and voxel size) was performed using a steel setup. It might be interesting to perform similar research on other types of materials, such as aluminum alloys and plastics.
3. Initial investigation reveals interesting effects of the target material. Further research is necessary for obtaining a deeper understanding of the influence of various target materials on CT dimensional metrology applications.
4. Beam hardening correction using pre-defined polynomials can reduce local dimensional variations. However, the choice of its coefficients is shown to be crucial. It is necessary to apply similar approach on other types of materials, such as aluminum alloys and plastics, so that the "proper range" of different coefficients can be determined.

References

[1] Aaron G. F., 2009, The history, development, and impact of computed imaging in neurological diagnosis and neurosurgery: CT, MRI, DTI: Nature Proceedings doi:10.1038/npre.2009.3267.5

[2] Abutaleb A.S., 1989, Automatic thresholding of grey-level pictures using two-dimensional entropies. Pattern Recognition 47, p. 22-32

[3] Alvarez R., Macowski A., 1976 Energy-selective Reconstructions in X-ray Computerized Tomography, Physics in Medicine and Biology, 21, 733–744

[4] Angel J., De Chiffre L., 2013, Final report: Inter-laboratory comparison on Industrial Computed Tomography

[5] Angel J., 2014, Quality assurance of CT scanning for industrial applications, PhD Thesis, Department of Mechanical Engineering, Technical University of Denmark

[6] Amirkhanov A., Heinzl C., Reiter M., Kastner J., Groller M.E., 2011, "Projection-Based Metal-Artifact Reduction for Industrial 3D X-ray Computed Tomography" IEEE transactions on visualization and computer graphics, Vol. 17, No.12

[7] Bartscher M., Neukamm M., Hilpert U., Neuschaefer-Rube U., Härtig F., Kniel K., Ehrig K., Staube A., Goebbels J., 2010, Achieving traceability of inudstrial computed tomography, Key Engineering Materials, Volume 437, p. 79-83

[8] Batenburg K.J., Sijbers J., 2011, DART: A practical reconstruction algorithm for discrete tomography, IEEE Transactions on Image Processing, Vol. 20 Issue 9, pp. 2542-2553

[9] Bellon C., Deresch A., Gollwitzer C., Jaenisch G-R., 2012, "Radiographic Simulator aRTist: Version 2," 18th World Conf. on Non-destructive Testing, Durban, South Africa

[10] Bergmann R.B., Bessler F.T., Bauer W., 2004, Computer tomography for nondestructive testing in the automotive industry, Proceedings of SPIE 5535 (1) 464–472.

[11] Brink A.D., 1992, Thresholding of digital images using two-dimensional entropies. Pattern Recognition 25, p. 803-808

[12] Campbell-Kelly M. et al., 2003, the History of Mathematical Tables From Sumer to Spreadsheets

[13] Carmignato S., Dreossi D., Mancini L., Marinello F., Tromba G., Savio E., 2009, Testing of X-raymicro tomography systems using a traceable geometrical standard. Meas.Sci.Technol. 20 084021

[14] Carmignato S., 2012, Accuracy of industrial computed tomography measurements: Experimental results from an international comparison, CIRP Annals - Manufacturing Technology, Volume 61 (1)P491-494

[15] Carmignato S., Pierobon A., Savio E., 2011, Final report (draft): Inter-laboratory Comparison of Computed Tomography Systems for Dimensional Metrology

[16] Chotas H.G., Dobbins J.T., Ravin C.E., 1999, Principles of digital radiography with large-area, electronically readable detectors: a review of the basics. Radiology, 210:595e9

[17] Christoph R., Neumann H.J., 2011, X-ray Tomography in Industrial Metrology. Süddeutscher Verlag onpact GmbH, 81677 Munich. ISBN 978-3-86236-020-8

[18] Clark J., 2010, Computed tomography goes mainstream, Quality Global Edition, p. 16-20

[19] Connie L.D., 2006, Fundamentals of Dimensional Metrology, 5th edition, ISBN-13: 978-1418020620

[20] Davisa G., Jainb N., Elliotta J., 2008, A modelling approach to beam hardening correction, Proc. of SPIE Vol. 7078 70781E-1

[21] Devore J.L., 2000, Probability and statistics for engineering and the sciences. 5th ed. Duxbury, Pacific Grove, CA

[22] Dewulf W., Tan Y., Kiekens K., 2012, “Sense and non-sense of beam hardening correction in CT metrology,” Annals of the CIRP, Manufacturing Technology, Vol.61 (1): 495-498

[23] Dewulf W. et al., 2013, Uncertainty Determination and Quantification for Dimensional Measurements with Industrial Computed Tomography, CIRP Annals. Manufacturing Technology vol:62 issue:1 pages:535-538

[24] Doris M., 2001, Radiation-induced defects in CoO-and NiO-doped fluoride- phosphate glasses, Glass Science and Technology, 74(2001):65-73

[25] DTU (Danmarks Tekniske Universitet). 2010, 14th CMM Danish users’ club conference on “Application of CT scanning in industry”.

[26] Encyclopaedia Britannica Online Academic Edition. Encyclopædia Britannica Inc., 2014

[27] Feldkamp L.A., Davis L.C., Kress J.W., 1984, Practical cone-beam algorithm, J. Opt. Soc. Am. A/Vol.1, No.6

[28] Fessler J., 2009, Analytical Tomographic Image Reconstruction Methods, PhD thesis

[29] Gargaud M. et al., 2011, Encyclopedia of Astrobiology – volume 1, Springer

[30] Geoff C., 2012, Understanding The New Statistics: Effect Sizes, Confidence Intervals, and Meta-Analysis. New York, USA: Routledge. pp. 27–28

[31] Gonzalez R.C., Woods R.E., 2002, Thresholding. In Digital Image Processing

[32] Goodman S.N., 1999, "Toward Evidence-Based Medical Statistics. 1: The P Value Fallacy.". Annals of Internal Medicine 130: 995–1004

[33] Herman G.T., 2009, Fundamentals of computerized tomography: Image reconstruction from projection, 2nd edition, Springer

[34] Hsieh J., 2003, computed tomography: Principles, design, artifacts, and recent advances. SPIE, Bellingham, WA.

[35] Hoffman E.J., Huang S.-C., Helps M.E., 1979, "Quantitation in positron emission computed tomography: 1. Effect of object size". J. Comput. Assist. Tomogr. 3 (3): 299–308. doi:10.1097/00004728-197906000-00001. PMID 438372

[36] International Committee F42 for Additive Manufacturing Technologies, ASTM

[37] International vocabulary of basic and general terms in metrology, second edition, 1993, International Organization for Standardization (Geneva, Switzerland)

[38] International vocabulary of metrology – Basic and general concepts and associated terms (VIM), 3rd edition, 2008

[39] Jerrold T.B., Seibert J.A., Leidholdt E.M., Boone J.M., 2011, The Essential Physics of Medical Imaging, 3rd edition

[40] Joseph P.M., Ruth C., 1997, A method for simultaneous correction of spectrum hardening artefacts in CT images containing both bone and iodine, Med. Phys., 24/10:1629–1634

[41] Kachelrieß M., Sourbelle K., Kalender W.A., 2006, Empirical cupping correction: A first-order raw data pre-correction for cone-beam computed tomography', Med. Phys., Vol 33, No 5, pp 1269–1274

[42] Kak A. C., Malcolm S., 2001, Principles of Computerized Tomographic Imaging, Society of Industrial and Applied Mathematics

[43] Kelcz F., Joseph P., Hilal S., 1979, Noise considerations in dual energy CT scanning, Medical Physics, 6, 418–425

[44] Kerckhofs G., Schrooten J., Van Cleynenbreugel T., Lomov S.V., Wevers M., 2008, Validation of X-ray Micro-CT as an Imaging Tool for Porous Structures, Review of Scientific Instruments, 79(1), Article number 013711 p. 1-9

[45] Kiekens K., et al., 2011, A test object with parallel grooves for calibration and accuracy assessment of industrial CT metrology, Measurement Science & Technology vol:22 pages:1-7

[46] Kiekens K., et al., 2012, Uncertainty Determination for Dimensional Measurements with Computed Tomography, Conference on Industrial Computed Tomography, Wels

[47] Kiekens K., Tan Y., Kruth J.P., Voet A., Dewulf W., 2011, Parameter dependent thresholding for dimensional X-ray computed tomography. Proceedings of the International Symposium on Digital Industrial Radiology and Computed Tomography

[48] Krämer Ph., Weckenmann A., 2010, Multi-energy image stack fusion in computed Tomography, Meas.Sci.Technol. 21:045105

[49] Kroll J., Effenberger I., Verl A., 2012, Adaptive Preprocessing and Segmentation for a Region-based Surface Extraction Method, ICT conference proceedings, Wels

[50] Krumm M., Kasperl S., Franz M., 2008, Referenceless Beam Hardening Correction in 3D Computed Tomography Images of Multi-Material Objects. 17th World Conference on Non-destructive Testing, Shanghai, China, 25–28 October

[51] Kruth J.P., Bartscher M., Carmignato S., Schmitt R., De Chiffre L., Weckenmann A., 2011, Computed Tomography for Dimensional Metrology, Annals of the CIRP, Manufacturing Technology Vol.60(2):821–842

[52] Kyriakou Y., Kalender W., 2007, A "X-ray scatter data for flat-panel detector CT," Physica Medica, Vol. 23 (1): 3-15

[53] Linn W. H., Clinard W.F., Zinkle S.J., Ewing R.C., 1994, Radiation effects in ceramics, Journal of Nuclear Materials 216, 291-321

[54] Luís L., Augusto S., 2009, Digital radiography detectors – A technical overview: Part 1, Radiography, Volume 15, Issue 1, Pages 58-62

[55] Moore D., McCabe G., 2003, Introduction to the Practice of Statistics (4 ed.). New York: W.H. Freeman and Co. p. 438

[56] Müller P., Hiller J., Cantatore A., De Chiffre L., 2011, Investigation of measuring strategies in computed tomography, New technologies in manufacturing, ISBN 978-80-214-4267-2

[57] Nyembwe K., de Beer D.J., van der Walt J.G., Bhero S., 2012, Assessment of surface finish and dimensional accuracy of tools manufactured by metal casting in rapid prototyping sand moulds, S. Afr. J. Ind. Eng. vol.23 no.3 Pretoria

[58] Oxford English Dictionary (3rd ed.). Oxford University Press. September 2005

[59] Ramakrishna K., Muralidhar K., Munshi P., 2006, Beam-hardening in simulated X-ray tomography, NDT&E International, 39/6:449-457

[60] Raphaël T., Alexander F., Alice M., Jürgen H., 2006, Statistical Beam-Hardening Correction for Industrial X-ray Computed Tomography, ECNDT - We.3.7.2

[61] Reimers P., Goebbels J., 1983, New possibilities of non-destructive evaluation by X-ray computed tomography, Mater. Eval, 41:732-737

[62] Schmitt R., Niggemann Christian., 2011, improving the Production using X-ray Computed Tomography - Potentials and Challenges, National conference on CT scanning - Application of CT Scanning in Industry, Danish Technological Institute Taastrup, May 31st

[63] Schmitt, R., Niggemann, C., 2010, Uncertainty in measurement for -ray-computed tomography using calibrated work pieces, Meas. Sci. Technol. 21

[64] Shammaa M.H., Ohtake Y., Suzuki H., 2010, Segmentation of multi-material CT data of mechanical parts for extracting boundary surfaces. Computer-Aided Design, 42, pp.118-128

[65] Stonestrom J., Alvarez R.E., Mackowski A., 1981, A framework for spectral artifact corrections in X-ray CT, IEEE Transactions on Biomedical Engineering, 28, 128–141

[66] Suppes A., Neuser E., 2008, Metrology with CT: precision challenge. Proc. SPIE 7078 70791G

[67] Takahiro N., 2012, “A Non-iterative Data-driven Beam-harding Correction for Single-material Object, Conference on Industrial Computed Tomography，Wels, Austria

[68] Tan Y., Kiekens K., Kruth J.P., Voet A., Dewulf W., 2011, Material Dependent Thresholding for Dimensional X-ray Computed Tomography. Intern Symp on Digital Industrial Radiology and Computed Tomography, Berlin, Germany, 20–22 June

[69] Tan Y., Kiekens K., Welkenhuyzen F., Kruth J.P., Dewulf W., 2013, “Defining the Optimal Beam Hardening Correction Parameters for CT Dimensional Metrology Applications” International Conference on Competitive Manufacturing，Stellenbosch South Africa

[70] Van Aarle W., Batenburg K.J., Sijbers J., 2008, Threshold Selection for Segmentation of Dense Objects in Tomograms, in: G. Bebis et al. (Eds.), ISVC 2008, Part I, LNCS 5358, pp.700-709

[71] Van de Casteele E., 2004, “Model-based Approach for Beam Hardening Correction and Resolution Measurements in Microtomography”, PhD Thesis, University of Antwerp

[72] Vogeler F., Verheecke W., Voet A., Kruth J.P., Dewulf W., 2011, Positional stability of 2D x-ray images for computer tomography Proc. Int. Symp. on Digital Industrial Radiology and Computed Tomography

[73] Weckenmann A. et al, 2009, Assessment of measurement uncertainty caused in the preparation of measurements using computed tomography, XIX IMEKO World Congress – Fundamental and Applied Metrology

[74] Weckenmann A., Kramer P., 2013, Computed tomography in quality control: chances and challenges, Proceedings of the Institution of Mechanical Engineers, Part B: Journal of Engineering Manufacture, 227: 634, DOI: 10.1177/0954405413479849

[75] Weckenmann A., Jiang X., Sommer K.-D., Neuschaefer-Rube U., Seewig J., Shaw L., Estler T., 2009, Multisensor data fusion in dimensional Metrology, CIRP Annals, 58/2:701-721

[76] Weckenmann A., Krämer P., 2009, Application of Computed Tomography in Manufacturing Metrology, Anwendung der CoWeckenmann, mputer-Tomographie in der Fertigungsmesstechnik, Technisches Messen, 76/7-8:340-346

[77] Weckenmann A., Krämer P., 2009, Computed Tomography for Application in Manufacturing Metrology, In: D.S. Rozhdestvensky Optical Society (Publ.): Proceedings 9th Int. Symp. On Measurement and Intelligent Instruments - ISMTII 2009, 1:11-26

[78] Weckenmann A., Krämer Ph., 2009, Assessment of measurement uncertainty caused in the preparation of measurements using computed tomography, XIX IMEKO World Congress Fundamental and Applied Metrology, Lisbon, Portugal, September 6-11

[79] Welkenhuyzen F., Boeckmans B., Kruth J.P., Dewulf W., Voet A., 2012, “Simulation of X-ray projection images for dimensional CT metrology,” 5th international conference on optical measurement techniques for structures and systems, p.477-487, Antwerp

[80] Welkenhuyzen F., Boeckmans B., Tan Y., Kiekens K., Dewulf W., Kruth J-P., 2014, Investigation of the kinematic system of a 450 kV CT scanner and its influence on dimensional CT metrology applications, ICT conference, Conference on Industrial Computed Tomography, Non-destructive Testing, 3D Materials Characterization and Dimensional Measurement

[81] Wenig P., Kasperl S., 2006, Examination of the measurement uncertainty on dimensional measurements by X-ray computed tomography, ECNDT, We.3.3.1

[82] Whitehouse D., 2012, Surfaces and their Measurement. Boston: Butterworth-Heinemann. ISBN 978-0080972015

[83] White J.M., Rohrer G.D., 1983, Image thresholding for optical character recognition and other applications requiring character image extraction. IBM Journal of Research and Development 27 (4), p. 400-411

[84] DIN EN ISO 4287:1998

[85] EN 16016-2, ÖNORM EN 16016:2011-08 Non-destructive testing - Radiation methods – Computed tomography; part 2 chapter 5.1 and 8.2; part 3 chapter 4.1.1, 4.1.3, 5.1.3 and 5.1.4

[86] ISO 12232: 1997 Photography

[87] ISO 15708:2002, Non-destructive testing - Radiation methods - Computed tomography; part 2 chapter 7.3.1

[88] ISO 3534-1

[89] ISO/TC XXX/SC N, 2010-09-17

[90] ISO/TS 15530-3 2004 Geometrical Product Specifications (GPS) — Coordinate measuring machines (CMM): Technique for determining the uncertainty of measurement — Part 3: Use of calibrated workpieces or standards

[91] VDI/VDE 2630–1.3/VDI/VDE 2617-13:2009. Computed tomography in dimensional measurement – guideline for the application of DIN EN ISO 10360 for coordinate measuring machines with CT-sensors

[92] VIM:1993, definition 3.7

[93] http://pmcnamee.net

[94] http://www.cmog.org/article/solarized-glass

[95] http://www.e-radiography.net

[96] http://www.fda.gov

[97] http://www.metrologycenter.com/

[98] http://www.ndted.org

[99] http://www.scanco.ch

[100] https://www.wordnik.com/words/thresholding

APPENDIX

A. Chapter 3: diameter and cylindricity measurements obtained using tactile CMM and CT

Measurement Nr.	M1	M2	M3	Average	Standard deviation
Section Nr.	(mm)				(µm)
S1	20.021	20.018	20.021	20.020	1.7
S2	20.021	20.020	20.022	20.021	1.0
S3	20.023	20.019	20.021	20.021	2.0
S4	20.043	20.044	20.043	20.043	0.6
S5	20.058	20.057	20.055	20.057	1.5

(a)

Measurement Nr.	M1	M2	M3	Average	Standard deviation
Section Nr.	(µm)				
S1	7	7	6	7	0.6
S2	6	6	6	6	0.0
S3	7	8	7	7	0.6
S4	12	11	12	12	0.6
S5	21	21	22	21	0.6

(b)

Table A1 *CMM measurements on cylinder "a". (a) diameter measurements (b) cylindricity measurements*

Measurement Nr.	M1	M2	M3	Average	Standard deviation
Section Nr.	(mm)				(µm)
S1	25.025	25.026	25.024	25.025	1.0
S2	25.028	25.028	25.028	25.028	0.0
S3	25.028	25.029	25.028	25.028	0.6
S4	25.035	25.036	25.036	25.036	0.6
S5	25.042	25.042	25.042	25.042	0.0

(a)

Measurement Nr.	M1	M2	M3	Average	Standard deviation
Section Nr.	(μm)				
S1	7	5	6	6	1.0
S2	7	6	7	7	0.6
S3	6	7	7	7	0.6
S4	6	8	7	7	1.0
S5	8	10	10	9	1.2

(b)

Table A2 *CMM measurements on cylinder "b". (a) diameter measurements (b) cylindricity measurements*

Measurement Nr.	M1	M2	M3	Average	Standard deviation
Section Nr.	(mm)				(μm)
S1	19.892	19.891	19.892	19.892	0.6
S2	19.892	19.893	19.892	19.892	0.6
S3	19.893	19.893	19.893	19.893	0.0
S4	19.896	19.895	19.895	19.895	0.6
S5	19.924	19.924	19.923	19.924	0.5

(a)

Measurement Nr.	M1	M2	M3	Average	Standard deviation
Section Nr.	(μm)				
S1	6	6	6	6	0.0
S2	8	7	6	7	1.0
S3	8	6	6	7	1.2
S4	9	7	7	8	1.2
S5	21	20	21	21	0.5

(b)

Table A3 *CMM measurements on cylinder "c". (a) diameter measurements (b) cylindricity measurements*

Measurement Nr.	M1	M2	M3	M4	M5	Average	Standard deviation (μm)
Section Nr.	(mm)						
S1(1000)	20.035	20.035	20.035	20.036	20.035	20.035	0.1
S1(20)	20.037	20.037	20.036	20.035	20.039	20.037	1.4
S2(1000)	20.033	20.033	20.033	20.033	20.033	20.033	0.1
S2(20)	20.034	20.033	20.033	20.032	20.032	20.033	0.9
S3(1000)	20.030	20.030	20.030	20.030	20.030	20.030	0.1
S3(20)	20.031	20.029	20.029	20.033	20.031	20.030	1.6
S4(1000)	20.031	20.031	20.031	20.030	20.031	20.031	0.4
S4(20)	20.029	20.032	20.030	20.030	20.030	20.030	1.0

S5(1000)	20.032	20.030	20.031	20.031	20.031	20.031	0.5
S5(20)	20.030	20.037	20.028	20.032	20.029	20.031	3.6

(a)

Measurement Nr.	M1	M2	M3	M4	M5	Average	Standard deviation (µm)
Section Nr.	(µm)						
S1(1000)	22	20	23	24	23	22	1.4
S1(20)	11	10	13	8	11	11	1.6
S2(1000)	20	20	19	22	22	21	1.4
S2(20)	10	14	10	12	10	11	1.7
S3(1000)	24	21	20	24	26	23	2.2
S3(20)	9	11	9	11	10	10	1.1
S4(1000)	34	35	24	28	31	30	4.4
S4(20)	16	19	18	21	16	18	2.4
S5(1000)	54	53	58	52	58	55	2.7
S5(20)	23	29	26	30	21	26	3.8

(b)

***Table A4** CT measurements on cylinder "a". Each feature (cylinder) has been fitted using both 1000 and 20 fitting points. (a) diameter measurements (b) cylindricity measurements*

Measurement Nr.	M1	M2	M3	M4	M5	Average	Standard deviation (µm)
Section Nr.	(mm)						
S1(1000)	25.048	25.048	25.048	25.048	25.048	25.048	0.2
S1(20)	25.049	25.047	25.048	25.048	25.048	25.048	0.6
S2(1000)	25.046	25.045	25.046	25.046	25.046	25.046	0.2
S2(20)	25.047	25.046	25.044	25.045	25.046	25.046	1.2
S3(1000)	25.044	25.044	25.043	25.044	25.043	25.044	0.2
S3(20)	25.043	25.043	25.044	25.044	25.045	25.044	0.8
S4(1000)	25.045	25.045	25.045	25.045	25.045	25.045	0.3
S4(20)	25.047	25.0456	25.044	25.043	25.046	25.045	1.5
S5(1000)	25.041	25.041	25.041	25.042	25.041	25.041	0.3
S5(20)	25.042	25.039	25.046	25.042	25.041	25.042	2.6

(a)

Measurement Nr.	M1	M2	M3	M4	M5	Average	Standard deviation (µm)
Section Nr.	(µm)						
S1(1000)	16	18	17	18	16	17	1.2
S1(20)	7	10	8	10	8	8	1.3
S2(1000)	16	18	19	19	16	18	1.4
S2(20)	13	9	9	10	12	11	2.0

S3(1000)	19	20	18	18	21	19	1.3
S3(20)	12	12	12	10	10	11	1.2
S4(1000)	23	22	21	24	22	23	1.4
S4(20)	12	16	13	9	13	13	2.6
S5(1000)	27	27	25	27	25	26	1.0
S5(20)	19	13	14	11	9	13	4.0

(b)

Table A5 *CT measurements on cylinder "b". Each feature (cylinder) has been fitted using both 1000 and 20 fitting points. (a) diameter measurements (b) cylindricity measurements*

Measurement Nr.	M1	M2	M3	M4	M5	Average	Standard deviation (µm)
Section Nr.	(mm)						
S1(1000)	19.907	19.908	19.908	19.908	19.908	19.908	0.2
S1(20)	19.909	19.910	19.910	19.906	19.911	19.909	2.0
S2(1000)	19.908	19.908	19.908	19.907	19.908	19.908	0.2
S2(20)	19.906	19.907	19.907	19.907	19.909	19.907	1.2
S3(1000)	19.906	19.906	19.906	19.905	19.906	19.906	0.4
S3(20)	19.905	19.906	19.907	19.906	19.905	19.906	0.8
S4(1000)	19.904	19.904	19.904	19.904	19.904	19.904	0.2
S4(20)	19.902	19.903	19.902	19.904	19.904	19.903	1.1
S5(1000)	19.905	19.904	19.905	19.903	19.904	19.904	1.0
S5(20)	19.904	19.906	19.909	19.898	19.907	19.905	4.0

(a)

Measurement Nr.	M1	M2	M3	M4	M5	Average	Standard deviation (µm)
Section Nr.	(µm)						
S1(1000)	29	30	30	31	32	30	1.2
S1(20)	21	18	16	18	21	19	1.9
S2(1000)	31	32	33	31	35	32	1.6
S2(20)	17	19	19	25	22	20	3.2
S3(1000)	34	36	34	35	36	35	1.3
S3(20)	21	25	16	23	27	22	4.1
S4(1000)	42	41	39	41	39	40	1.3
S4(20)	27	23	25	22	21	24	2.2
S5(1000)	55	61	58	55	66	59	4.4
S5(20)	32	31	31	43	34	34	5.1

(b)

Table A6 *CT measurements on cylinder "c". Each feature (cylinder) has been fitted using both 1000 and 20 fitting points. (a) diameter measurements (b) cylindricity measurements*

B. Chapter 4: CT dimensional measurement results for the 3 × 3 design of experiment

Scan Nr.	O-1	O-2	I-1	I-2	P-0	P-1	P-2	P-3
1 (mm)	8.0138	10.012	5.9504	5.9508	4.0032	4.0046	4.003	4.006
fitting point standard deviation(μm)	2.0	2.0	2.2	2.5	1.9	2.0	2.3	1.8
2 (mm)	8.0164	10.0144	5.9468	5.949	4.0058	4.0054	4.0044	4.0086
fitting point standard deviation(μm)	2.0	2.0	2.2	2.4	2.0	2.0	2.2	1.8
3 (mm)	8.0196	10.018	5.951	5.9524	4.0082	4.0064	4.0044	4.0114
fitting point standard deviation(μm)	2.0	2.0	2.3	2.6	1.9	2.1	2.3	1.7
4 (mm)	8.0118	10.0098	5.959	5.9604	4.0002	4.0026	4.0018	4.0036
fitting point standard deviation(μm)	1.6	1.7	2.0	2.2	1.5	1.6	2.0	1.4
5 (mm)	8.0104	10.0076	5.9574	5.9592	4.0016	4.0016	4.0012	4.0024
fitting point standard deviation(μm)	1.6	1.7	2.0	2.2	1.6	1.7	1.9	1.5
6 (mm)	8.0098	10.0066	5.9572	5.9586	4.0012	4.0014	4.001	4.002
fitting point standard deviation(μm)	1.6	1.6	1.9	2.0	1.5	1.6	1.8	1.4
7 (mm)	8.0112	10.0084	5.9554	5.957	4.0024	4.0022	4.0016	4.0038
fitting point standard deviation(μm)	1.7	1.7	2.0	2.2	1.6	1.7	1.9	1.5
8 (mm)	8.0124	10.0104	5.9562	5.9582	4.0024	4.0032	4.0024	4.0052
fitting point standard deviation(μm)	1.7	1.7	2.1	2.3	1.6	1.8	2.0	1.5
9 (mm)	8.012	10.0096	5.956	5.9578	4.0028	4.0026	4.002	4.0042
fitting point standard deviation(μm)	1.7	1.7	2.0	2.3	1.6	1.7	2.0	1.5
10 (mm)	8.0126	10.0102	5.9542	5.9578	4.0028	4.0036	4.003	4.0048
fitting point standard deviation(μm)	1.7	1.7	2.1	2.6	1.7	1.7	2.1	1.5
11 (mm)	8.0138	10.0114	5.9548	5.9568	4.0048	4.0036	4.0026	4.0068
fitting point standard deviation(μm)	1.7	1.7	2.2	2.5	1.6	1.8	2.1	1.5
12 (mm)	8.0124	10.009	5.9532	5.956	4.004	4.0026	4.0022	4.0056
fitting point standard deviation(μm)	1.6	1.6	2.1	2.5	1.6	1.7	2.0	1.5
13 (mm)	8.0162	10.0134	5.9454	5.947	4.0074	4.005	4.005	4.0094
fitting point standard deviation(μm)	1.9	1.9	2.3	2.9	1.8	2.0	2.4	1.7
14 (mm)	8.0152	10.0132	5.9476	5.9504	4.0054	4.0062	4.0054	4.0076
fitting point standard deviation(μm)	1.9	1.9	2.3	3.0	1.8	2.0	2.5	1.7
15 (mm)	8.0188	10.0166	5.9474	5.9514	4.0092	4.007	4.005	4.0116
fitting point standard deviation(μm)	1.8	1.8	2.3	3.0	1.8	2.0	2.4	1.6
16 (mm)	8.012	10.0094	5.9572	5.9602	4.0032	4.0024	4.0018	4.0042
fitting point standard deviation(μm)	1.6	1.6	2.1	2.6	1.6	1.7	2.1	1.5
17 (mm)	8.0084	10.0052	5.9556	5.9568	4.0002	4.0006	4.0006	4.0026
fitting point standard deviation(μm)	1.7	1.7	2.0	2.4	1.6	1.7	2.0	1.4

Scan Nr.	O-1	O-2	I-1	I-2	P-0	P-1	P-2	P-3
18 (mm)	8.0112	10.008	5.9574	5.9594	4.0026	4.0022	4.0014	4.0026
fitting point standard deviation(µm)	1.7	1.7	2.0	2.5	1.5	1.7	2.1	1.5
19 (mm)	8.0118	10.0092	5.9568	5.9586	4.0022	4.0028	4.0022	4.0042
fitting point standard deviation(µm)	1.7	1.8	2.1	2.3	1.6	1.8	1.9	1.5
20 (mm)	8.0078	10.0044	5.9554	5.9566	3.9996	4.001	4.001	4.0006
fitting point standard deviation(µm)	1.7	1.8	2.1	2.3	1.7	1.7	2.0	1.6
21 (mm)	8.005	10.0016	5.9554	5.9562	3.997	4	4	3.9988
fitting point standard deviation(µm)	1.7	1.9	2.1	2.5	1.7	1.8	2.1	1.7
22 (mm)	8	9.9956	5.9592	5.9592	3.9928	3.997	3.9968	3.993
fitting point standard deviation(µm)	1.8	1.9	2.2	2.7	1.7	2.0	2.4	1.7
23 (mm)	8.005	10.0014	5.9584	5.959	3.9974	3.9994	3.9994	3.9976
fitting point standard deviation(µm)	1.7	1.8	2.2	2.5	1.6	1.9	2.2	1.6
24 (mm)	8.0118	10.0094	5.959	5.9608	4.0022	4.0022	4.0016	4.0032
fitting point standard deviation(µm)	2.3	2.3	2.5	2.5	2.2	2.3	2.4	2.1
25 (mm)	8.0172	10.0152	5.9538	5.9548	4.0066	4.0044	4.0034	4.008
fitting point standard deviation(µm)	2.1	2.0	2.3	2.6	2.0	2.2	2.4	1.9
26 (mm)	8.009	10.0066	5.951	5.9506	3.9984	4.0024	4.0022	4.0004
fitting point standard deviation(µm)	2.0	2.0	2.2	2.3	2.0	1.9	2.2	1.8
27 (mm)	8.0108	10.0086	5.9518	5.952	4.0002	4.0026	4.0032	4.0022
fitting point standard deviation(µm)	2.0	2.0	2.2	2.4	2.0	2.0	2.2	1.8

Table A7 *Design of experiments: CT dimensional measurement results. "O-1, O-2, I-1, I-2, P-0, P-1, P-2, P-3" are the 8 measurands defined in Fig 4.12.*

C. Chapter 4: data of ANOVA for the DOE

		SS	df	MS	F	P
Internal-external offset variation	A	141.7854321	2	70.89271605	220.582349	0.0000001
	B	30.5491358	2	15.2745679	47.52674541	0.00003639
	C	51.20691358	2	25.60345679	79.66503409	0.00000522
	AB	27.60987654	4	6.902469136	21.4769999	0.0002454
	AC	10.35802469	4	2.589506173	8.057236147	0.00657546
	BC	6.897283951	4	1.724320988	5.365216556	0.02122894
	Error	2.571111111	8	0.321388889		
Internal offset variation	A	2.891851852	2	1.445926	3.095956	0.10097126
	B	14.2962963	2	7.148148	15.30531	0.00184304
	C	1.434074074	2	0.717037	1.535289	0.27269777
	AB	2.548148148	4	0.637037	1.363997	0.32757641
	AC	1.597037037	4	0.399259	0.854877	0.52936721
	BC	1.472592593	4	0.368148	0.788263	0.56407275
	Error	3.736296296	8	0.467037		
Step cylinder external offset variation	A	3.380740741	2	1.69037037	21.94230769	0.00056521
	B	1.905185185	2	0.952592593	12.36538462	0.00356898
	C	4.10962963	2	2.054814815	26.67307692	0.00028921
	AB	0.29037037	4	0.072592593	0.942307692	0.48697293
	AC	0.645925926	4	0.161481481	2.096153846	0.17317349
	BC	0.334814815	4	0.083703704	1.086538462	0.4245327
	Error	0.616296296	8	0.077037037		
Pin offset variation	A	15.36888889	2	7.684444444	21.8170347	0.00057626
	B	0.506666667	2	0.253333333	0.719242902	0.51612121
	C	24.00888889	2	12.00444444	34.08201893	0.00012172
	AB	7.857777778	4	1.964444444	5.577287066	0.01914375
	AC	5.822222222	4	1.455555556	4.132492114	0.04180638
	BC	3.404444444	4	0.851111111	2.416403785	0.13410418
	Error	2.817777778	8	0.352222222		
CT-CMM offset range	A	27.00982719	2	13.50491359	3.727949814	0.07177695
	B	139.9474074	2	69.9737037	19.3158182	0.00086624
	C	843.1392272	2	421.5696136	116.3717451	0.00000122
	AB	3.071409926	4	0.767852481	0.211961039	0.92454207
	AC	13.51732348	4	3.37933087	0.932843872	0.49138981
	BC	71.98647659	4	17.99661915	4.967857999	0.02614547
	Error	28.98089141	8	3.622611426		

Table A8 *The calculation results of the ANOVA for three influence factors and their interactions for 5 different quality indicators. "A, B, C, AB, AC and BC" stand for the influence factors and their interactions;*

D. Chapter 5: dimensional measurement results of two CT scans using different starting contours and search distances for local adaptive thresholding

SC: starting contour. 0% stands for the largest background peak in the histogram, 100% stands for the largest material peak in the histogram.

SD: search distance, which determines the region for local function fitting and calculating the material's edge. Search distances equal to 1, 4 and 6 voxel size are tested.

DOE: design of experiment discussed in Chapter 4, including 27 CT scans of the same object using different machine settings.

Unit: mm		Internal-external offset variation	Internal offset variation	Step cylinder external offset variation	Pin offset variation	CT-CMM offset range
SC 25%	SD 1	0.697	0.606	0.001	0.051	1.055
	SD 4	0.086	0.199	0.001	0.044	0.204
	SD 6	0.548	0.874	0.002	0.034	1.002
SC 50%	SD 1	0.006	0.009	0.000	0.018	0.020
	SD 4	0.004	0.001	0.001	0.007	0.015
	SD 6	0.003	0.001	0.001	0.008	0.016
SC 75%	SD 1	0.450	1.047	0.000	0.133	1.002
	SD 4	0.489	1.003	0.001	0.132	1.002
	SD 6	0.494	1.002	0.001	0.116	1.002

(a)

Unit: mm		Internal-external offset variation	Internal offset variation	Step cylinder external offset variation	Pin offset variation	CT-CMM offset range
SC 25%	SD 1	0.032	0.147	0.001	0.108	0.127
	SD 4	0.111	0.266	0.001	0.096	0.269
	SD 6	0.067	0.147	0.001	0.043	0.149
SC 50%	SD 1	0.001	0.012	0.001	0.004	0.013
	SD 4	0.002	0.000	0.001	0.001	0.003
	SD 6	0.002	0.002	0.001	0.001	0.004
SC 75%	SD 1	0.000	0.001	0.001	0.002	0.015
	SD 4	0.001	0.001	0.001	0.001	0.003
	SD 6	0.002	0.001	0.001	0.002	0.004

(b)

Table A9 *Dimensional measurement results of two CT scans using different starting contours and search distances for local adaptive thresholding. (a): measurement results of DOE scan Nr.3; (b) measurement results of DOE scan Nr.20.*

E. Chapter 5: reference CMM measurement results for the test setup

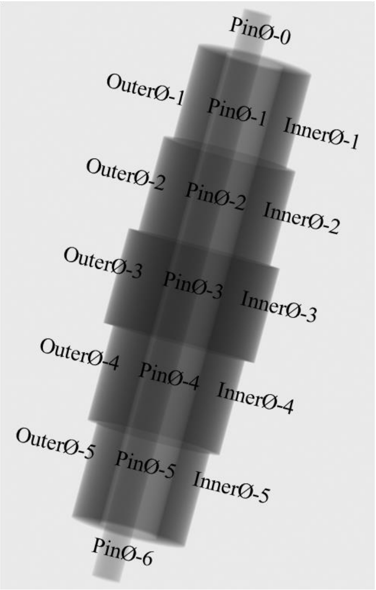

Figure A1 *Test setup used in Chapter 5 – Section 5.2 to investigate the influence of beam hardening effect and its correction methods on the accuracy and local deviations of dimensional measurements*

Unit: mm	Outer-1	Outer-2	Outer-3	Outer-4	Outer-5	Inner
Measurement 1	12.0907	14.0370	16.0263	14.0798	12.0580	5.9540
Measurement 2	12.0921	14.0365	16.0265	14.0807	12.0569	5.9547
Measurement 3	19.0917	14.0378	16.0273	14.0813	12.0564	5.9548
Average	12.0915	14.0371	16.0267	14.0806	12.0571	5.9545

Table A11 *Dimensional measurement results of two CT scans using different starting contours and search distances for local*

F. Chapter 5: matlab program for the look up table beam hardening correction

a. Creating the look up table

```
% -----------------------------------------------------------------------
% creating the look up table using the step wedge
%
% version: 2013-04-19
% -----------------------------------------------------------------------
clear all;
close all;
clc;
% -----------------------------------------------------------------------
% Creating Offset
myCTScan = sprintf('BH test_0001.tif');
scan = im2single(importdata(myCTScan));
scanROI = scan(50:300,50:300);
scanSetAvg = mean2(scanROI);
scanSetMin = min(scanROI(:));
scan(50:300,50:300) = 0;
myWedgeScan = sprintf('step wedge.tif');
wedge = im2single(importdata(myWedgeScan));
wedgeROI = wedge(50:300,50:300);
wedgeSetAvg = mean2(wedgeROI);
wedgeSetMin = min(wedgeROI(:));
wedge(50:300,50:300) = 0;
% offset Flag: necessary to determine whether to increase or decrease the gray value:
if scanSetAvg > wedgeSetAvg
offsetAvgFlag = 1;
% this means the final corrected gray value on the scan image = step wedge gray value + offset
else
offsetAvgFlag = 0;
% this means the final corrected gray value on the scan image = step wedge gray value - offset
end
if scanSetMin > wedgeSetMin
offsetMinFlag = 1;
```

```
% this means the final corrected gray value on the scan image = step wedge gray value + offset
else
offsetMinFlag = 0;
% this means the final corrected gray value on the scan image = step wedge gray value - offset
end
% calculating the offset:
offsetAvg = abs(scanSetAvg - wedgeSetAvg);
offsetMin = abs(scanSetMin - wedgeSetMin);
% choose which you would like to calculate with:
offset = offsetAvg;
offsetFlag = offsetAvgFlag;
% offset = offsetMin;
% offsetFlag = offsetMinFlag;
% -----------------------------------------------------------------------
% step wedge:
I = im2single(importdata('step wedge.tif'));
GV = zeros(20,1);
GV(1) = mean2(I(50:400,50:400)); % Average air gray value
for i = 2:20
p = 200 + 24*(i-2) + 6*(i-2);
q = 200 + 24*(i-1) + 6*(i-2);
GV(i) = mean2(I(p:q,440:583));
end
% -----------------------------------------------------------------------
% offsetting step wedge:
% and adding threshold value to first element of wedge
GVs = ones(20,1);
for i = 1:20
if offsetFlag == 0
GVs(i) = GV(i) - offset;
elseif offsetFlag == 1
GVs(i) = GV(i) + offset;
end
end
% -----------------------------------------------------------------------
```

```
% Create step wedge table
A = zeros(numel(GVs),1);
for i = 1:numel(GVs)
A(i) = log(1/GVs(i));
end
X = importdata('thickness.txt');
W(:,1) = X;
W(:,2) = GVs;
W(:,3) = A;
save wedge table-ASCII
% ------------------------------------------------------------------------
% Creating a lookup table
X = W(:,1); % mm thickness
Y = W(:,3); % corresponding attenuation value
k = 6; % k-order of polynomial fitting
% Creating a finer range of the thickness
Z = linspace(0,max(X),1000);
% -------------------------------------------------------------
% Fitting Curves on measurements
R = polynomFitZ(X,Y,Z,k);
[a,b] = linearFit(X,Y);
U = a*Z+b;
% Convert linear function and polynom function from
% Attenuation to Intensity (GV)
% oGVl = old GV linear
% oGVp = old GV polynom
% Preallocating
oGVl = zeros(size(Z));
oGVp = zeros(size(Z));
for i = 1:max(size(Z))
oGVl(i) = 1/exp(U(i));
oGVp(i) = 1/exp(R(i));
end
% Lookup table:
oGV = oGVp;
```

```
nGV = oGVl;
L(:,1) = oGV;
L(:,2) = nGV;
save Look up table-ASCII
```

b. Correction algorithm

```
% ----------------------------------------------------------------------
% look up table beam hardening correction on 1000 2D projection images
%
% version: 2013-04-13
% ----------------------------------------------------------------------
clear all
close all
clc
t = cputime;
% ----------------------------------------------------------------------
% input
L = load ('Look up table');
oGV = L(:,1);
nGV = L(:,2);
% ----------------------------------------------------------------------
% importing 2D projections, correcting and exporting
k4 = 0; % 1000
k3 = 0; % 0100
k2 = 0; % 0010
k1 = 1; % 0001
numfiles = 1800;
for k = 1:numfiles
myScan = sprintf('BH test_%d%d%d%d.tif',k4,k3,k2,k1);
view = im2single(importdata(myScan));
newView = interpolator(view,oGV,nGV); % correction happens here
newView16 = im2uint16(newView);
myNewScan = sprintf('BH test_%d%d%d%d.tif',k4,k3,k2,k1);
imwrite(newView16,myNewScan,'Compression','none','Resolution',127);
k1 = k1 + 1;
```

```
if k1/10 == 1
k1 = 0;
k2 = k2 + 1;
end
if k2/10 == 1 && k2 ~= 0
k2 = 0;
k3 = k3 + 1;
end
if k3/10 == 1 && k3 ~= 0
k3 = 0;
k4 = k4 + 1;
end
end
```

c. Search algorithm.

```
function [newView] = interpolator(view,oGV,nGV)
newView = zeros(size(view)); % pre-allocating
for i = 1:numel(view)
% adding more priority to the first 8 points of the lookup table -> Priority in speed
% this is because roughly 75% of the 2D projection images is filled with air. The first 8 points
% of our lookup table are Gray Values for air.
if view(i) > oGV(1)
newView(i) = view(i);
elseif view(i) <= oGV(1) && view(i) > oGV(2)
j = 1;
if view(i) >= oGV(j+1) && view(i) <= oGV(j)
newView(i)=nGV(j)+(nGV(j+1)-nGV(j))*((view(i)-oGV(j))/(oGV(j+1)-oGV(j)));
end
elseif view(i) <= oGV(2) && view(i) > oGV(3)
j = 2;
if view(i) >= oGV(j+1) && view(i) <= oGV(j)
newView(i)=nGV(j)+(nGV(j+1)-nGV(j))*((view(i)-oGV(j))/(oGV(j+1)-oGV(j)));
end
elseif view(i) <= oGV(3) && view(i) > oGV(4)
j = 3;
```

```
if view(i) >= oGV(j+1) && view(i) <= oGV(j)
newView(i)=nGV(j)+(nGV(j+1)-nGV(j))*((view(i)-oGV(j))/(oGV(j+1)-oGV(j)));
end
elseif view(i) <= oGV(4) && view(i) > oGV(5)
j = 4;
if view(i) >= oGV(j+1) && view(i) <= oGV(j)
newView(i)=nGV(j)+(nGV(j+1)-nGV(j))*((view(i)-oGV(j))/(oGV(j+1)-oGV(j)));
end
elseif view(i) <= oGV(5) && view(i) > oGV(6)
j = 5;
if view(i) >= oGV(j+1) && view(i) <= oGV(j)
newView(i)=nGV(j)+(nGV(j+1)-nGV(j))*((view(i)-oGV(j))/(oGV(j+1)-oGV(j)));
end
elseif view(i) <= oGV(6) && view(i) > oGV(7)
j = 6;
if view(i) >= oGV(j+1) && view(i) <= oGV(j)
newView(i)=nGV(j)+(nGV(j+1)-nGV(j))*((view(i)-oGV(j))/(oGV(j+1)-oGV(j)));
end
elseif view(i) <= oGV(7) && view(i) > oGV(8)
j = 7;
if view(i) >= oGV(j+1) && view(i) <= oGV(j)
newView(i)=nGV(j)+(nGV(j+1)-nGV(j))*((view(i)-oGV(j))/(oGV(j+1)-oGV(j)));
end
% ---
elseif view(i) <= oGV(8) && view(i) > oGV(50)
for j = 8:50;
if view(i) >= oGV(j+1) && view(i) <= oGV(j)
newView(i)=nGV(j)+(nGV(j+1)-nGV(j))*((view(i)-oGV(j))/(oGV(j+1)-oGV(j)));
end
end
elseif view(i) < oGV(50) && view(i) > oGV(100)
for j = 50:100
if view(i) >= oGV(j+1) && view(i) <= oGV(j)
newView(i)=nGV(j)+(nGV(j+1)-nGV(j))*((view(i)-oGV(j))/(oGV(j+1)-oGV(j)));
end
```

```
end
elseif view(i) < oGV(100) && view(i) > oGV(150)
for j = 100:150
if view(i) >= oGV(j+1) && view(i) <= oGV(j)
newView(i)=nGV(j)+(nGV(j+1)-nGV(j))*((view(i)-oGV(j))/(oGV(j+1)-oGV(j)));
end
end
elseif view(i) < oGV(150) && view(i) > oGV(200)
for j = 150:200
if view(i) >= oGV(j+1) && view(i) <= oGV(j)
newView(i)=nGV(j)+(nGV(j+1)-nGV(j))*((view(i)-oGV(j))/(oGV(j+1)-oGV(j)));
end
end
elseif view(i) < oGV(200) && view(i) > oGV(250)
for j = 200:250
if view(i) >= oGV(j+1) && view(i) <= oGV(j)
newView(i)=nGV(j)+(nGV(j+1)-nGV(j))*((view(i)-oGV(j))/(oGV(j+1)-oGV(j)));
end
end
elseif view(i) < oGV(250) && view(i) > oGV(300)
for j = 250:300
if view(i) >= oGV(j+1) && view(i) <= oGV(j)
newView(i)=nGV(j)+(nGV(j+1)-nGV(j))*((view(i)-oGV(j))/(oGV(j+1)-oGV(j)));
end
end
elseif view(i) < oGV(300) && view(i) > oGV(350)
for j = 300:350
if view(i) >= oGV(j+1) && view(i) <= oGV(j)
newView(i)=nGV(j)+(nGV(j+1)-nGV(j))*((view(i)-oGV(j))/(oGV(j+1)-oGV(j)));
end
end
elseif view(i) < oGV(350) && view(i) > oGV(400)
for j = 350:400
if view(i) >= oGV(j+1) && view(i) <= oGV(j)
newView(i)=nGV(j)+(nGV(j+1)-nGV(j))*((view(i)-oGV(j))/(oGV(j+1)-oGV(j)));
```

```
end
end
elseif view(i) < oGV(400) && view(i) > oGV(450)
for j = 400:450
if view(i) >= oGV(j+1) && view(i) <= oGV(j)
newView(i)=nGV(j)+(nGV(j+1)-nGV(j))*((view(i)-oGV(j))/(oGV(j+1)-oGV(j)));
end
end
elseif view(i) < oGV(450) && view(i) > oGV(500)
for j = 450:500
if view(i) >= oGV(j+1) && view(i) <= oGV(j)
newView(i)=nGV(j)+(nGV(j+1)-nGV(j))*((view(i)-oGV(j))/(oGV(j+1)-oGV(j)));
end
end
elseif view(i) < oGV(500) && view(i) > oGV(550)
for j = 500:550
if view(i) >= oGV(j+1) && view(i) <= oGV(j)
newView(i)=nGV(j)+(nGV(j+1)-nGV(j))*((view(i)-oGV(j))/(oGV(j+1)-oGV(j)));
end
end
elseif view(i) < oGV(550) && view(i) > oGV(600)
for j = 550:600
if view(i) >= oGV(j+1) && view(i) <= oGV(j)
newView(i)=nGV(j)+(nGV(j+1)-nGV(j))*((view(i)-oGV(j))/(oGV(j+1)-oGV(j)));
end
end
elseif view(i) < oGV(600) && view(i) > oGV(650)
for j = 600:650
if view(i) >= oGV(j+1) && view(i) <= oGV(j)
newView(i)=nGV(j)+(nGV(j+1)-nGV(j))*((view(i)-oGV(j))/(oGV(j+1)-oGV(j)));
end
end
elseif view(i) < oGV(650) && view(i) > oGV(700)
for j = 650:700
if view(i) >= oGV(j+1) && view(i) <= oGV(j)
```

```
newView(i)=nGV(j)+(nGV(j+1)-nGV(j))*((view(i)-oGV(j))/(oGV(j+1)-oGV(j)));
end
end
elseif view(i) < oGV(700) && view(i) > oGV(750)
for j = 700:750
if view(i) >= oGV(j+1) && view(i) <= oGV(j)
newView(i)=nGV(j)+(nGV(j+1)-nGV(j))*((view(i)-oGV(j))/(oGV(j+1)-oGV(j)));
end
end
elseif view(i) < oGV(750) && view(i) > oGV(800)
for j = 750:800
if view(i) >= oGV(j+1) && view(i) <= oGV(j)
newView(i)=nGV(j)+(nGV(j+1)-nGV(j))*((view(i)-oGV(j))/(oGV(j+1)-oGV(j)));
end
end
elseif view(i) < oGV(800) && view(i) > oGV(850)
for j = 800:850
if view(i) >= oGV(j+1) && view(i) <= oGV(j)
newView(i)=nGV(j)+(nGV(j+1)-nGV(j))*((view(i)-oGV(j))/(oGV(j+1)-oGV(j)));
end
end
elseif view(i) < oGV(850) && view(i) > oGV(900)
for j = 850:900
if view(i) >= oGV(j+1) && view(i) <= oGV(j)
newView(i)=nGV(j)+(nGV(j+1)-nGV(j))*((view(i)-oGV(j))/(oGV(j+1)-oGV(j)));
end
end
elseif view(i) < oGV(900) && view(i) > oGV(950)
for j = 900:950
if view(i) >= oGV(j+1) && view(i) <= oGV(j)
newView(i)=nGV(j)+(nGV(j+1)-nGV(j))*((view(i)-oGV(j))/(oGV(j+1)-oGV(j)));
end
end
elseif view(i) < oGV(950)
for j = 950:numel(oGV)-1
```

```
if view(i) >= oGV(j+1) && view(i) <= oGV(j)
newView(i)=nGV(j)+(nGV(j+1)-nGV(j))*((view(i)-oGV(j))/(oGV(j+1)-oGV(j)));
end
end
end
end
end
```

d. Function: PolynomFitZ

```
function [R] = polynomFitZ(X,Y,Z,k)
% -------------------------------------------------------
% version: 2012-11-08, this function creates a polynomial fitting curve
%
% input:
% X: x-axis values
% Y: y-axis values
% Z: new x-axis values
% k: order of polynomial
%
% output:
% R: calculated points of the polynomial equation
% -------------------------------------------------------
p=polyfit(X,Y,k);
% pre-allocating
K=zeros(1,k+1);
for i=1:k+1
K(i)=k+1-i;
end
% pre-allocating
R=zeros(1,numel(Z));
% for every value of X repeat equation p(1..k+1)*X.^(k..0)
for j=1:numel(Z)
R(j)=p*Z(j).^K';
end
end
```

Function: LinearFit

```
function [a,b] = linearFit(X,Y)
% -----------------------------------------------------
% a vector V of Nx2 (table) is inserted
% min and max of the table will be calculated
% the linear equation will be calculated by these points
% -----------------------------------------------------
% [a,b]=max(V)
% a = [maxNumber :2 , maxNumber :1]
% b = [position in :2 , position in :1]
[y1,pos1]=max(Y);
x1=X(pos1);
[y2,pos2]=min(Y);
x2=X(pos2);
% solve equations to find parameters a and b
% y = a*x+b
Ya=[y1;y2];
Xa=[x1 1;x2 1];
A=Xa\Ya;
a=A(1);
b=A(2);
end
```

G. General: few topics related to multi-material objects

Assemblies consisting of different materials are often encountered in measurement tasks using X-ray CT. Multi-material assemblies are inherently problematic for X-ray CT, one often faces difficulties when selecting the scan parameters and it is in many cases impossible to optimize the X-ray power and filter settings for all material components within one single CT scan: low energy X-ray beams are essential for detecting small details and creating sufficient contrast especially for the lower density material; high energy X-ray beams are necessary for penetrating and revealing internal structures of denser parts. When light plastic and dense metal parts are involved (Fig A1), dual energy CT scan and data fusion (Fig A2) can be helpful in generating better 2D projection images, but it is more time consuming and the gain for dimensional metrology applications is yet to be justified. Some argues that for dimensional metrology, one can as well measure different material components on different scans (for example: measuring dimensions of the plastic parts on the low energy CT scan data, measuring dimensions of the metal parts on the high energy CT scan data), thus the data fusion step is unnecessary.

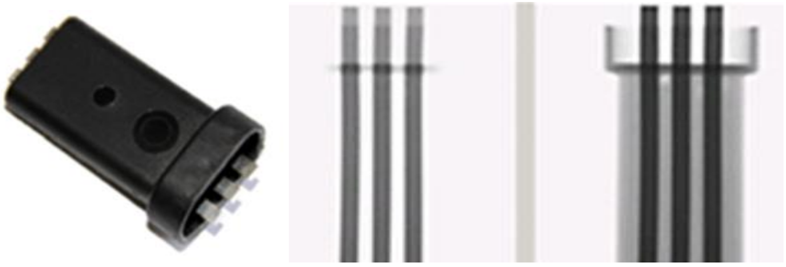

Figure A2 *Connector with encapsulated metal parts (left) and its 2D X-ray projection images acquired using high (middle) and low (right) X-ray energies [Krämer P. et al., 2010]*

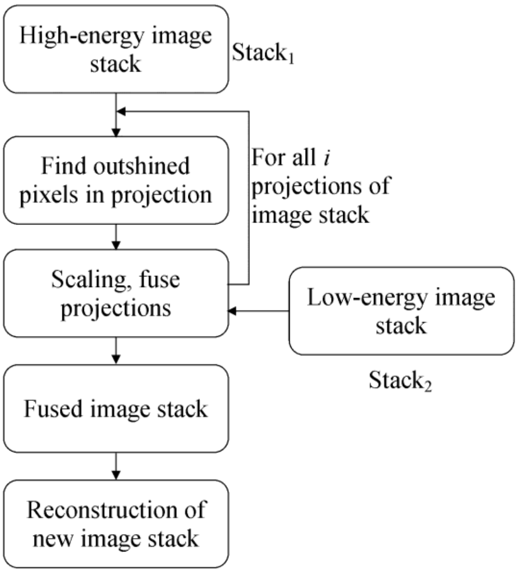

Figure A3 *Workflow of dual energy CT image stack fusion [Krämer Ph. et al., 2010]*

The basic rule of thumb for scanning multi-material objects is to get the most contrast between different materials; so that after the thresholding process, each material component has clear boundary, can be well separated and measured. Theoretically, one can make use of the linear attenuation coefficients to select the "best" X-ray photon energy when scanning objects consist of two materials. Few examples are shown in Fig A3 *[data source: http://physics.nist.gov]*: in order to produce the most contrast between Tungsten and Iron components, it can be seen that the maximum separation between the tungsten and iron curves occurs at around 100keV. At this energy the difference in attenuation between the two materials is the greatest so the contrast will be maximized. However, the X-ray source of most industrial CT scanners produces polychromatic beams with broad spectrum range; thus, setting the acceleration voltage to 100kV does not ensure the major energy of the generated X-ray beams is 100keV. This makes the above mentioned method much less practical. Nevertheless, the linear attenuation coefficients can still provide very useful information, it can be seen that certain material combinations are extremely hard to be distinguished using X-ray CT, for example: silicon and aluminum. Moreover, most iron, zirconium dioxide and copper objects are scanned at more than 100kV acceleration voltage to get sufficient X-ray transmission; as indicated in Fig A3, they are also difficult to be separated.

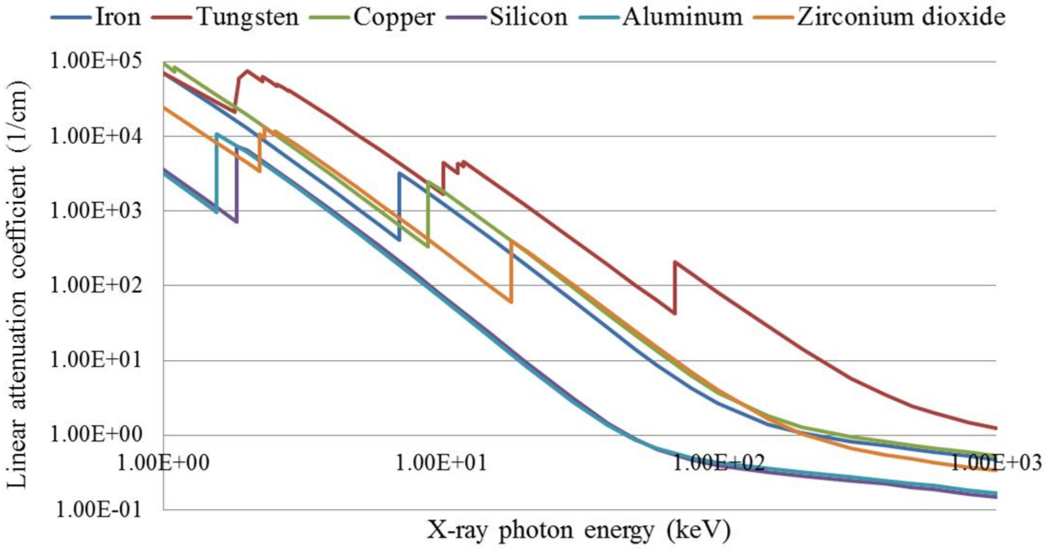

Figure A4 *Graphs of linear attenuation coefficients versus radiation energy*

Except for setting up the scanning parameters, the post-processing steps are also complicated when it comes to multi-material objects.

At the moment, no beam hardening correction algorithm has been reported which can successfully deal with multi-material objects in the aspect of improving dimensional measurement results for both materials.

Moreover, the accuracy and reliability of the thresholding process is decrease as well. As shown in Fig A4, an "imaginary" layer of less attenuating materials around the edge of more attenuating materials is created when applying global thresholding method. Applying local thresholding is not a guarantee either, unless the gray value gradient around the more attenuating material's edge is sufficiently higher than around the less attenuating material's edge. Nevertheless, if the peaks of different material are well separated in the histogram, "accurate" thresholding is possible by shifting the thresholding starting contour and only measure the material components that is optimized for the particular thresholding starting contour. In other words, threshold the same volume several times and measure different materials separately. This method is also applied in Chapter 6 to handle the industrial component.

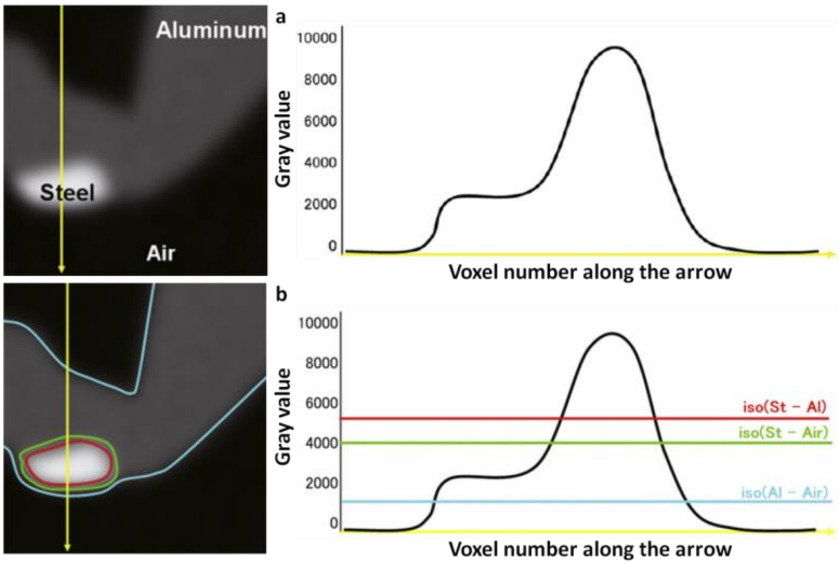

Figure A5 *Volumetric model and its corresponding histogram containing three materials: steel, aluminum and air. Due to the limitation of isosurface technique, an "imaginary" layer of aluminum is created at the bottom interface between steel and air [Shammaa M.H. et al., 2010]*

H. General: parameter optimization protocol for CT dimensional metrology

Based on the reported experimental and simulation results throughout this PhD research, an initial protocol is suggested for "optimizing" the operator dependent scanning parameters for CT dimensional metrology applications, as shown in Fig A6.

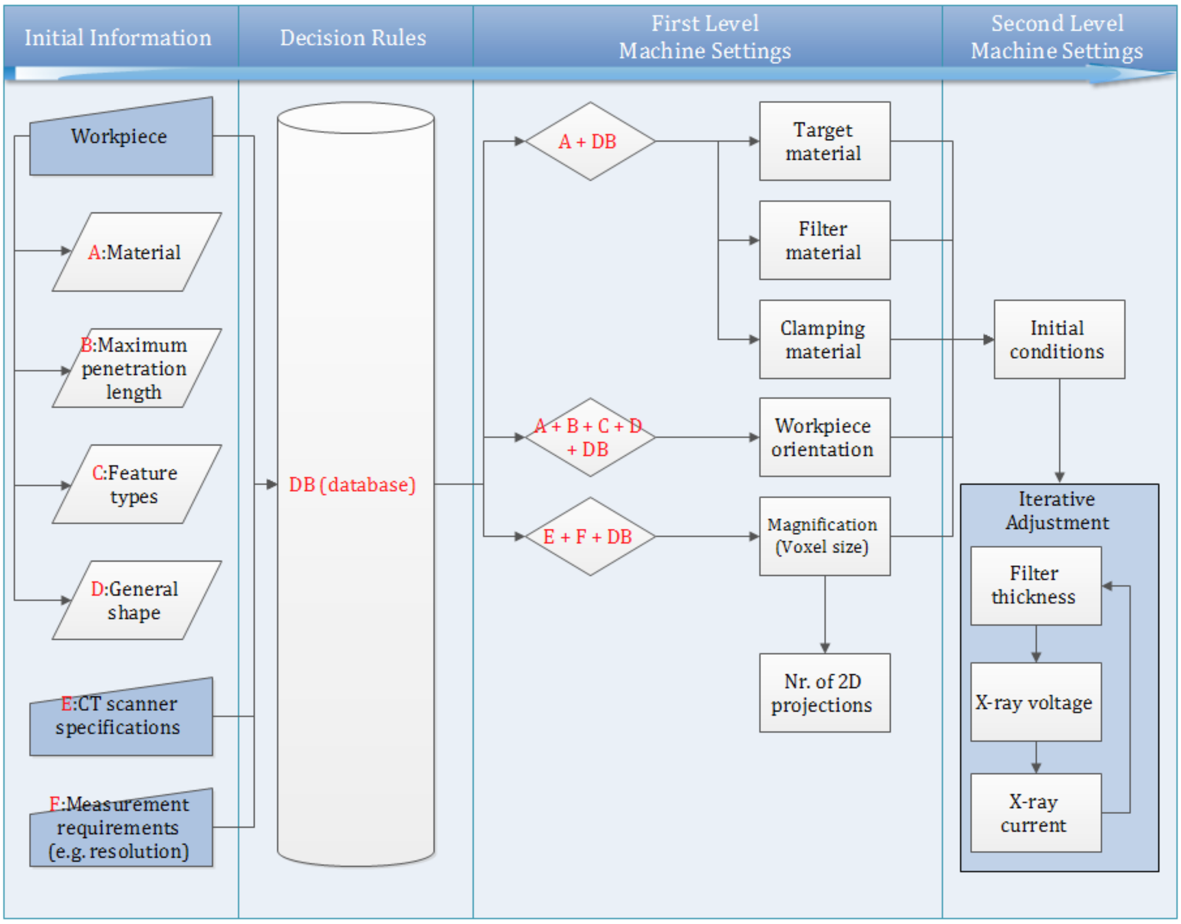

***Figure A6** Decision making flow chart for the major CT machine settings*

This protocol consists of four sequential steps:

1. Collect initial information, including: workpiece material compositions, estimation of its overall size and maximum penetration length. In addition, the specific goal should be clear (e.g. required accuracy range, desired resolution…). These conditions should be compared with the specifications of the CT scanner for selecting the most suitable equipment.

2. Step two is to optimize the scanning settings for the specific case. The optimization strategy is similar to a database which is gradually built up through experience. For example:

Target material

- Copper – scanning biological materials and carbon fiber, measuring porosity of polymers.
- Molybdenum – plastic objects
- Tungsten – suitable for CT dimensional metrology application and scanning higher density materials (metal, ceramic etc.)

Filter material: Filter material can significantly influence the accuracy and repeatability of CT dimensional measurements.

- Copper filter – mostly applied when scanning dense materials (steel, ceramic, brass etc.)
- Aluminum filter – can be applied for scanning medium density materials (aluminum, titanium, magnesium etc.)
- Tin filter – can be used when scanning very dense materials where copper filters are insufficient.

Clamping material: two important features for a good clamping material are low X-ray attenuation and stability

Workpiece orientation: the influence of the object's orientation becomes significant when scanning dense metals. Objects should be tilted to avoid a flat plane being parallel to the incident X-ray beam throughout the entire 360 degrees

Magnification (Voxel size): In practice, the magnification is selected so that the object occupies around 80% to 90% of the detector space

Nr. of 2D projections: taking too many 2D projection images is not always beneficial. Nevertheless, the minimum required number of images need to be ensured so that the achievable resolution is not affected due to under sampling

3. Step three is to combine the initial information and the existing decision rules in the database, so that the "first level" machine settings can be determined. The target material, filter material, clamping material, workpiece orientation and magnification are seen as the first level machine

4. The filter thickness, X-ray voltage and current are regarded as second level machine settings, because their determination process is more complex and typically requires several trial and error iterations. Moreover, it is recommended to adjust their order as: filter thickness → X-ray voltage → X-ray current.

I. General: case dependent calibration protocol for dimensional metrology applications

Furthermore, a case dependent calibration protocol (Fig. A7) is proposed. The core processes of this protocol are:

1. Combining CT and tactile CMM dimensional measurement data for calculating the voxel size correction factor using calibration object Nr.1 (adjacent steel spheres).

2. Combining CT and tactile CMM dimensional measurement data for iteratively calculating the "optimal" BHC polynomial coefficients and for obtaining the edge offset correction terms (different terms for inner and outer features). Calibration object Nr.2 (hollow step cylinder with a inner pin) can be used here.

3. After obtaining both voxel size correction term, the “optimal” coefficients of the BHC polynomial and the edge offset terms, the original scanned data should be treated as follows: beam hardening correction using predefined polynomial → voxel size correction → initial dimensional measurements → applying edge offset correction terms → final dimensional measurement results.

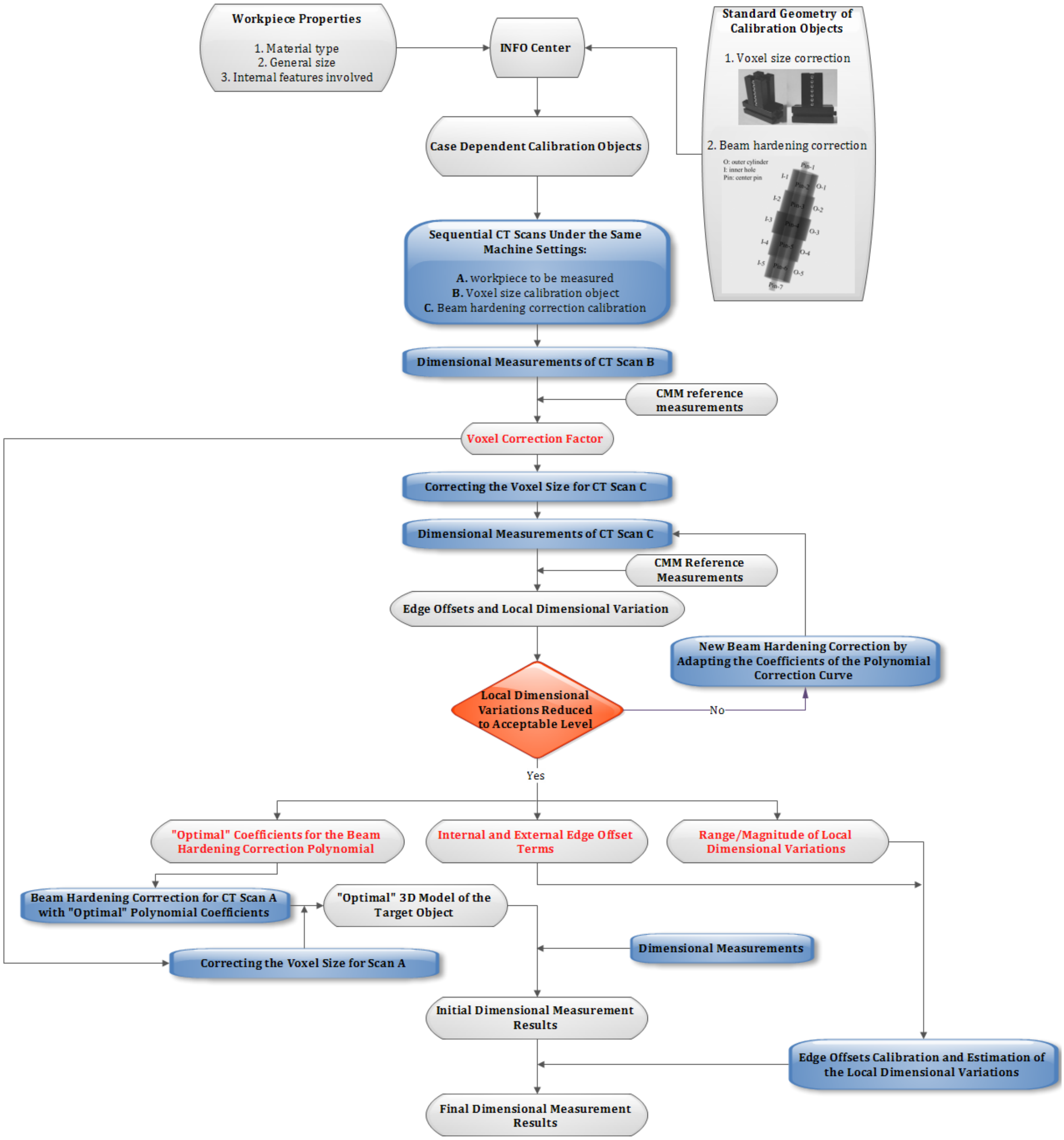

Figure A7 *Case dependent calibration procedures for CT dimensional metrology applications*

Curriculum Vitae

Date of Birth: 1986/01/22
Tel: +32487577508
E-mail: tanye.belgium@gmail.com

Professional Goal

To feel enthusiasm every morning when I go to work, and to develop my talents together with and for **YOU!**

Current Status

2009.10 – 2015.4	**Graduating PhD student**
University	Mechanical Engineering Department, KU Leuven
Promotor	Prof.dr.ir. Jean-Pierre Kruth, Prof.dr.ir. Wim Dewulf
Research topic:	Dimensional Metrology and Non-destructive Testing using Industrial CT Systems.

Working Experience

2009.10 – now	**Teaching Assistant**
University/College	Industrial Engineering Department, KU Leuven
Content	Coaching master theses, project courses and lab sessions
2005.3 – 2009.6	**Several student jobs**
	ICT service, CAD designer, China study trip organizer, trainer for home tutors

Educational Background

2008.9 – 2009.9	**Master in Advanced Manufacturing**
University/College	Industrial Engineering Department, KU Leuven
Promotor	Prof.dr.ir. Wim Dewulf, Prof.dr.ir. Kathleen Denis
Evaluation	Magna cum Laude
Master Thesis Topic	Surgery Guide Design Using 3D Printing Technology
Thesis Company	Materialise
2006.9 – 2008.7	**Bachelor, Electro-Mechanical Engineering**
University/College	Industrial Engineering Department, KU Leuven
Evaluation	Magna cum Laude
2004.9 – 2006.7	**Bachelor, Industrial Management**
University	Mechanical Engineering Department, Shanghai Jiaotong University
Evaluation	1st year : 83/100, 2nd year : 87/100
Remark	*Selected as exchange student for obtaining double bachelor degree*

Other Skills

Intercultural communication: quickly adapted to the Belgian way of life, including falling in love with a Belgian girl and marrying her

Entrepreneurship and team work: founding member of an engineering company in China

Started a business initiative together with 5 other Chinese colleagues and friends in 2013, and turned these ideas into a running engineering company in China. Being the leader in the process of company establishment, I have built up partnerships with several Belgian companies and convinced a German manufacturer to provide their support. Moreover, I submitted this business plan to the local Chinese government, successfully presented it and obtained their hardware facility and financial support.

Project management: leading student project to success

From 2010, I have been guiding a student project course (2nd Bachelor, Engineering Experience) at GroepT campus – KU Leuven, in which different teams of students design and manufacture a small scale solar car and participate in a competitive race (around 20 teams every year) by the end of the semester. Through my guidance, my teams have won the championship in 3 out of the 4 years.

Creative thinking: coaching my master thesis student to the level of getting a patent for the company

In the year 2013, I have successfully guided 4 master thesis topics. An innovative idea for product design came from brain storming with my student; it is much appreciated by the company. As a result, my student was immediately offered a R&D position in the company and this design is also going to be patented.

Coaching: guide my student in an efficient and effective way

Guided 2 project courses (1st and 2nd Bachelor), 2 lab sessions (3rd Bachelor and Master in electro-mechanical engineering) and more than 10 master theses since October, 2009. Good at explaining difficult to understand theories to students so that they can easily understand.

Organizational skill: organizing China study trip (2 weeks) for more than 50 students

In 2012, I have organized the China study trip for more than 50 students (3rd Bachelor, GroepT campus – KU Leuven). The study trip was scheduled during the Easter holiday and lasted 2 weeks. As an organizer, I contacted local companies for student visits, designed the travel schedule, and estimated the budget. This study trip turned out to be a great success, every student returned to Belgium soundly and all of them have enjoyed this experience.

Time management & self-motivation: combining various student jobs with studying

I came to study in Belgium as an exchange student in 2006. As a young student coming from China, I always wanted to be independent and did not want to add extra financial load to my parents. Although it was already difficult to suddenly study abroad, I motivated myself to combine studying with various student jobs. In addition, I still managed to obtain the best study results (81.9/100) among all students of the year.

Language

Native Chinese speaker; fluent oral English and professional English writing skill; middle level Dutch speaker (level 5/7 at ACE GroepT evening language school)

Professional Software

All kinds of Industrial CT related software; Autodesk Inventor, Solid Edge, Solid Works, UG NX, Matlab, Labview, ImageJ, Mimics and 3-Magics (Materialise), GOM Inspect, Microsoft office package

Reference

Jean-Pierre Kruth : full professor at Mechanical Engineering Department - KU Leuven.
E-mail : Jean-Pierre.Kruth@mech.kuleuven.be
Tel : +3216322490
Wim Dewulf : professor at Campus Group T, and at Mechanical Engineering Department - KU Leuven.
E-mail : wim.dewulf@kuleuven.be
Tel : +3216301030-1073

Publications

International Journals

1. **Tan Y.**, Kiekens K., Welkenhuyzen F., Angel J., De Chiffre L., Kruth J.P., Dewulf W., “Simulation-aided investigation of beam hardening induced errors in CT dimensional metrology”, Meas. Sci. Technol. 25 064014, doi:10.1088/0957-0233/25/6/064014, 2014
2. Dewulf W., Kiekens K., **Tan Y.**, Welkenhuyzen F., Kruth J. P., “Uncertainty determination and quantification for dimensional measurements with industrial computed tomography”, CIRP Annals-Manufacturing Technology, 62(1), p535-538, 2013
3. Dewulf W., **Tan Y.**, Kiekens K., “Sense and non-sense of beam hardening correction in CT metrology”, CIRP Annals-Manufacturing Technology, 61(1), 495-498, 2012
4. Kiekens K., Welkenhuyzen F., **Tan Y.**, Bleys P., Voet A., Kruth J.P., Dewulf W., “A test object with parallel grooves for calibration and accuracy assessment of industrial CT metrology” Meas. Sci. Technol. 22 115502 doi:10.1088/0957-0233/22/11/115502, 2011

International Conferences

1. Welkenhuyzen F., Boeckmans B., **Tan Y.**, Kiekens K., Dewulf W., and Kruth J.P., “Investigation of the kinematic system of a 450 kv CT scanner and its influence on dimensional CT metrology applications”, In Proceedings of the International Conference on Industrial Computed Tomography，Wels，Austria 2014.
2. **Tan Y.**, Kiekens K., Welkenhuyzen F., Angel J., De Chiffre L., Kruth J.P., Dewulf W., “Simulation-aided investigation of beam hardening induced errors in CT dimensional metrology” 11th International Symposium on Measurement Technology and Intelligent Instruments，Aachen，Germany，2013
3. **Tan Y.**, Kiekens K., Welkenhuyzen F., Kruth J.P., Dewulf W., “Defining the Optimal Beam Hardening Correction Parameters for CT Dimensional Metrology Applications” International Conference on Competitive Manufacturing，Stellenbosch，South Africa，2013
4. **Tan Y.**, Kiekens k., Welkenhuyzen F., Kruth J.P., Dewulf W., “Beam hardening correction and its influence on the measurement accuracy and repeatability for CT dimensional metrology applications” Conference on Industrial Computed Tomography，Wels，Austria，2012
5. Kiekens K., **Tan Y.**, Welkenhuyzen F., Kruth J.P., Dewulf W., “Uncertainty Determination for Dimensional Measurements with Computed Tomography” Conference on Industrial Computed Tomography， Wels，Austria，2012

6. **Tan Y.**, Kiekens K., Kruth J.P., Voet A., Dewulf W., “Material Dependent Thresholding for Dimensional X-ray Computed Tomography” International Symposium on Digital Industrial Radiology and Computed Tomography，Berlin，Germany，2011
7. Kiekens K., **Tan Y.**, Kruth J.P., Voet A., Dewulf W., “Parameter dependent thresholding for dimensional X-ray computed tomography” International Symposium on Digital Industrial Radiology and Computed Tomography，Berlin，Germany，2011
8. Kiekens K., Welkenhuyzen F., **Tan Y.**, Bleys P., Voet A., Dewulf W., Kruth J.P., “A test object for calibration and accuracy assessment in X-ray CT metrology” 10th International Symposium on Measurement and Quality Control，Osaka，Japan，2010